PETROGRAPHY, MINERALOGY, GEOCHEMISTRY AND GEOCHRONOLOGY OF THE DIAMONDIFEROUS DRYBONES BAY KIMBERLITE PIPE AND MUD LAKE KIMBERLITE DYKE, NORTHWEST TERRITORIES

By

Ankar Rockwell Sheng

A Thesis submitted to the Faculty of Graduate Studies of
The University of Manitoba
In partial fulfillment of the requirements of the degree of

MASTER OF SCIENCE

Department of Geological Sciences
University of Manitoba
Winnipeg

Abstract

The Drybones Bay and Mud Lake kimberlites are Ordovician kimberlites located in the Slave Geological Province. The Drybones Bay pipe formed by multiple discrete eruptions, producing several texturally distinct phases of kimberlite, including hypabyssal kimberlite (HK) autoliths, tuffisitic kimberlite (TK), pyroclastic kimberlite (PK) and resedimented volcaniclastic kimberlite (RVK). The recognition of TK suggests this pipe represents a Class 1 kimberlite. The nearby Mud Lake kimberlite is a dolomite-rich HK dyke characterized by macrocrystic and segregation textures. Although the kimberlites are proximal, U-Pb zircon dates indicate they were not emplaced contemporaneously, and geochemical discrepancies that cannot be explained by known magma evolution processes indicate that these rocks formed from distinct parental magmas. Mineralogical and geochemical data is used to evaluate crystallization conditions and diamond potential. New geochemical modeling of compatible trace elements reveals convincing evidence of magma evolution by olivine fractionation, adding substantially to the published research on kimberlite geochemistry.

Acknowledgements

This work is dedicated to my father and mother, Raymond Shindi Sheng (August 30, 1946 to April 4, 2006) and Diane Theresa Sheng (June 28, 1954 to July 3, 2014), who taught me that knowledge and happiness are the most valuable things in life.

I owe a debt of gratitude to my advisor, Dr. Anton Chakhmouradian, for recognizing my potential, introducing me to this esoteric field of geology, and guiding me on part of this path to becoming a man of knowledge.

I would like to thank Dr. Ekaterina Reguir of the University of Manitoba, for assisting with trace-element analysis and U-Pb dating, and Dr. Christian Böhm of the Manitoba Geological Survey and Mr. Barrett Elliot of the Northwest Territories Geological Survey for their valuable insights and feedback on this project.

The technical support for electron microprobe and LA-ICP-MS analysis provided by Dr. Panseok Yang and Dr. Ravinder Sidhu of the University of Manitoba is greatly appreciated.

This research would not have been possible without the support of the Northwest Territories Geological Survey.

Table of Contents

Abstract i
Acknowledgements ii
Chapter 1: Introduction 1
1.1 Introduction to kimberlites 1
1.2 Kimberlite nomenclature and classification 3
1.3 Kimberlite emplacement theory 5
1.3.1 Phreatomagmatic pipe model 6
1.3.2 Bottom-up embryonic pipe model 6
1.3.3 Downward explosive dyke model 1 7
1.3.4 Downward explosive dyke model 2 9
1.3.5 Downward exploding dyke model 3 10
1.4 Kimberlite geochemistry 11
1.4.1 Contamination 12
1.4.2 Parental kimberlite magma composition 12
1.4.3 Trace-element composition of kimberlites 14
1.5 The kimberlite-carbonatite connection 16
1.6 Scope and objectives of the present work 18
Chapter 2: Geological Setting 21
2.1 Geology of the Slave Province 21
2.2 Geology of the Mud Lake kimberlite dyke 24
2.3 Geology of the Drybones Bay kimberlite pipe 25
2.4 Exploration history 27
2.5 Previous work 30
Chapter 3: Methodology 32
3.1 Sample collection and preparation 32
3.2 Whole-rock geochemistry 32
3.3 Petrography 33
3.4 Electron-microprobe analysis 34
3.5 Laser-ablation inductively coupled plasma mass-spectrometry 34
3.6 Geochronology 35

Chapter 4: Petrography 36
4.1 Mud Lake 36
4.2 Drybones Bay 36
4.2.1 Unit K-1 40
4.2.2 Unit K-2 42
4.2.3 Unit K-3 47
4.2.4 Unit K-6 47
4.2.5 Unit K-7 47
4.2.6 Unit K-8 48
4.2.7 Unit KE 50
Chapter 5: Mineralogy and Mineral Chemistry 51
5.1 Olivine 51
5.1.1 Mud Lake olivine 51
5.1.2 Drybones Bay olivine 51
5.2 Phlogopite 51
5.2.1 Mud Lake phlogopite 51
5.2.2 Drybones Bay phlogopite 52
5.3 Ilmenite 58
5.3.1 Mud Lake ilmenite 58
5.3.2 Drybones Bay ilmenite 59
5.4 Spinel-group minerals 62
5.4.1 Mud Lake spinel-group minerals 62
5.4.2 Drybones Bay spinel-group minerals 67
5.5 Garnet 68
5.5.1 Mud Lake garnet 68
5.5.2 Drybones Bay garnet 73
5.6 Zircon 73
5.6.1 Mud Lake zircon 73
5.6.2 Drybones Bay zircon 75
5.7 Carbonate minerals 78
5.7.1 Mud Lake carbonate minerals 78

5.7.2 Drybones Bay carbonate minerals 80
5.8 Rutile 80
5.8.1 Mud Lake rutile 80
5.8.2 Drybones Bay rutile 80
Chapter 6: Geochemistry 82
6.1 Whole-rock geochemistry 82
6.1.1 Major elements 82
6.1.2 Trace elements 86
Chapter 7: U-Pb zircon geochronology 89
7.1 Sample description 89
7.2 Results 90
Chapter 8: Discussion and Conclusions 92
8.1 Geochemistry 92
8.1.1 Assimilation trends 93
8.1.2 Fractionation trends 95
8.2 Kimberlite crystallization conditions 98
8.2.1 Thermometry 98
8.2.2 Redox state 102
8.3 Facies interpretation 102
8.3.1 Hypabyssal kimberlite (HK) 103
8.3.2 Tuffisitic kimberlite (TK) 104
8.3.3 Pyroclastic kimberlite (PK) 105
8.3.4 Resedimented volcaniclastic kimberlite (RVK) 106
8.4 Unroofing 107
8.5 Emplacement of the Drybones Bay kimberlites 109
8.6 Relationship between Mud Lake and Drybones Bay 112
8.7 Diamond potential 113
8.8 Concluding remarks 116
References 118
Appendix I 126
Appendix II 129

List of Figures

Figure 1 The classic South African model of a kimberlite pipe showing old nomenclature (left side of figure) and revised nomenclature (right side of figure). Note: massive volcaniclastic kimberlite (MVK) is a non-genetic term for tuffisitic kimberlite (TK). Kjarsgaard (2007) modified after Mitchell (1986). Used with permission. 2

Figure 2 Schematic representation of the three main types of kimberlite pipes: (a) Class 2 (Canadian Prairies) kimberlite, with a shallow crater infilled with PK, and no diatreme or root zones; (b) Class 3 (Lac de Gras) kimberlite, with a steep-walled pipe infilled with (R)VK ± PK ± HK, the lack of TK is characteristic of both Class 2 and Class 3 pipes; and (c) Class 1 (South African) kimberlite, with well defined crater, diatreme and root zones (Scott Smith, 2008). Used with permission. 4

Figure 3 Chondrite-normalized REE diagrams for on- and off-craton (a) kimberlites and (b) orangeites. Diagram is from Becker and Le Roex (2006), normalized to values from Sun and McDonough (1989). Used with permission. 15

Figure 4 Primitive mantle-normalized trace-element patterns for on- and off-craton (a) kimberlites and (b) orangeites from South Africa, with highlighted trace element anomalies. Diagram from Becker and Le Roex (2006), normalized to values from Sun and McDonough (1989). Used with permission. 15

Figure 5 Schematic geologic map of the Slave craton showing the location of kimberlites and four age domains: (I) southern-western Siluro-Ordovician domain (~450 Ma); (II) south-eastern Cambrian domain (~540 Ma); (III) central Tertiary/Cretaceous domain (48–74s Ma); and (IV) northern mixed domain consisting of Jurassic and Permian kimberlite fields. Figure after Heaman et al. (2003). Used with permission. 19

Figure 6 Cross-sections showing the results of the Mud Lake drilling program. Drill holes are marked in red and labeled with their depth and identification number, kimberlite contacts are marked in blue on the drill holes, inferred contacts delineating the kimberlite are marked with blue dashed lines (Vivian, 2006). 24

Figure 7 Schematic illustration of the Drybones Bay kimberlite pipe. See text for description of kimberlite units (K1–6, KC, KE). Modified after Kretschmar (1995a)..... 26

Figure 8 Photographs of Mud Lake and Drybones Bay rocks: (A) Mud Lake HK; (B-J) Drybones Bay; (B) medium- and (C) fine-grained VCK; (D) clay-rich VCK showing desiccation cracks when dried; (E) well indurated VCK with an olive drab matrix; (F) thin basal unit with unusual blue hues and abundant serpentine veining. 37

Figure 9 Petrography of Mud Lake HK: (A) fresh and chloritized phlogopite macrocrysts and pseudomorphed olivine macrocrysts in a serpentine-dolomite segregated mesostasis; (B) diverse textural varieties of dolomite, including blocky segregations, lacey frills, and primary laths (rhombohedral dolomite not pictured; see text for details). Chl = chlorite; Dol = dolomite; GM = groundmass; M = (pseudomorphed) olivine macrocryst; Phl = phlogopite; Spl = spinel; Srp = serpentine. Photos captured in PPL. 39

Figure 10 Petrography of Drybones Bay kimberlite: (A) medium-grained K-1 composed of broken macrocrysts and chloritized phlogopite with thin green reaction rims in a serpentine matrix, compared to (B) fine-grained K-1 with fresh phlogopite, euhedral olivine (pseudomorphed) in an opaque matrix, note the parallel alignment of elongate crystals; (C) K-2 macrocrysts and magmaclasts (lower left) in a serpentine matrix; (D) K-3 broken angular macrocrysts with green reaction rims supported by a dark, mud-rich matrix; (E) K-6 abundant comminuted granitic xenoliths in a dark serpentine matrix with mud; (F) poorly-sorted kimberlite with crystal choked veins of serpentine. Photos captured in PPL. 43

Figure 11 Petrographic features of Drybones Bay kimberlite: (A) juvenile magmaclast with a super-thin, coherent rim, in K-1; (B) juvenile magmaclast with a very-thin, clastic rim, in K-1; (C) juvenile magmaclasts with a very-thin, clastic rim, in K-2; (D) abraded juvenile magmaclast with part of a clastic rim preserved in a concavity, in K-3; (E,F) BSE image and photomicrograph of a compound clast composed of phlogopite and groundmass spinel, interpreted as possible HK autoliths, in K-2. Magmaclasts are marked with dashed lines in A, C and D to enhance clarity. Optical photos captured in PPL. 44

Figure 12 Petrographic features of Drybones Bay kimberlite: (A) juvenile magmaclasts with a clastic rim next to a rounded olivine macrocryst in a carbonate-serpentine matrix, in K-7; (B) magnified view of the carbonate-serpentine matrix, in K-7; (C) juvenile magmaclasts with an ultra thin, coherent rim, interpreted as pelletal lapilli, in K-8, note the plastic deformation at grain contacts (white arrows); (D) juvenile magmaclasts with a super-thin, compound rim, in K-8; (E) compound clast in K-8 composed of parallel aligned grains in a

dark matrix, note the contrast in clast size and matrix composition with the host rock; (F) well-preserved magmaclasts with clastic rims, in KE (XPL). 45

Figure 13 Petrography of Drybones Bay kimberlite: (A) overview of the volcaniclastic material at the top of K-8 shows broken olivine crystals in a dark, mud-rich matrix; (B) an exotic siltstone xenolith from the same unit; (C,D) below 175 m unit K-8 appears very different, and is characterized by rounded macrocrystic olivine pseudomorphs and pelletal lapilli-like magmaclasts in a mud-free serpentine mesostasis; (E) shattered quartz grains in a dark, mud-rich matrix, from KE; (F) flow textures in KE defined by the alignment of phlogopite crystals. Photos A-E captured in PPL; photo F captured in XPL. 46

Figure 14 BSE images of Mud Lake minerals: (A) fresh phlogopite macrocryst and olivine pseudomorphs in a fine-grained groundmass; (B) poikilitic phlogopite with a mosaic texture and spinel inclusions; (C) intensely altered ilmenite macrocryst; (D) spinel macrocryst with gradational zoning; (E) groundmass spinel with sharp zoning; (F) atoll spinel. Cal = calcite; Dol = dolomite; GM = groundmass; Ilm = ilmenite; Phl = phlogopite; Rt = rutile; Spl = spinel; Srp = serpentine. 53

Figure 15 BSE images of Drybones Bay minerals: (A) fresh ilmenite macrocryst with corroded margins with a relatively fresh phlogopite macrocryst; (B) xenocrystic phlogopite associated with carbonate xenoliths, note the prismatic habit; (C) altered ilmenite macrocryst with an amoeboid-shaped core surrounded by rutile laths in a carbonate matrix with minor barite (high-AZ phase); (D) atoll-textured groundmass spinel with a zoned core; (E) peridotite garnet with a kelyphite rim; (F) zircon macrocryst rimmed with baddeleyite. Cal = calcite; Dol = dolomite; Grt = garnet; Ilm = ilmenite; Phl = phlogopite; Rt = rutile; Srp = serpentine; Zrn = zircon. 54

Figure 16 Comparison of trace-element compositions of phlogopite macrocrysts from Drybones Bay and Mud Lake with those of typical kimberlites and carbonatites (Reguir et al., 2009). 57

Figure 17 Major-element variation in ilmenite from (A,B) Mud Lake and (C,D) Drybones Bay, and (E) Zr/Nb vs. Nb/Ta plot for ilmenite from Siberian kimberlites (Carmody et al., 2014), Mud Lake (ML), and Drybones Bay (DBB). The dashed line at Zr/Nb = 0.37 separates the data corresponding to low diamond potential (D = 0–3) from those with high diamond potential (D = 6–10). 61

Figure 18 Compositional variations of spinel-group minerals from Mud Lake (A–E) and Drybones Bay (F–J). 65

Figure 19 Composition of spinels from Mud Lake (cones) and Drybones Bay (circles) in the oxidized spinel prism. Macrocrysts plot along the aluminous magnesian chromite trend (Trend 1). Groundmass spinels and the evolved rims of zoned macrocrysts plot along Trend 2. Trends referenced from Mitchell (1986)..... 66

Figure 20 BSE image of a Mud Lake pyrope garnet with an inset showing the texture of the kelyphite rim under higher magnification. Grt = garnet; Srp = serpentine; Dol = dolomite. 69

Figure 21 Composition of garnets from Mud Lake and Drybones Bay, shown in terms of atomic proportions of Fe + Mn (almandine + spessartine), Ca (grossular + andradite) and Mg (pyrope), compared with the compositional fields of garnets from eclogites and granulites. The shaded area is the field of granulites; field 1 is eclogites from kimberlite pipes; field 2 is eclogites from amphibolite-facies terrains; and field 3 is eclogites associated with glaucophane schist. Granulite and eclogite fields are from Chappell and White (1970). 70

Figure 22 G-number classification of pyrope garnets from Mud Lake and Drybones Bay (Grütter et al., 2004). 70

Figure 23 Compositional variation of garnet from Mud Lake (A–E) and Drybones Bay (G–J).. 71

Figure 24 BSE and CL images of a zircon macrocryst: (A) BSE image of a zircon macrocryst mantled with discrete baddeleyite; (C) CL image of the same zircon shows the grain is homogeneous, with illumination artifacts occurring as bright lines along fractures. Zrn = zircon; Bdy = baddeleyite. 74

Figure 25 Comparison of primitive mantle-normalized REE patterns of zircon (calculated from average analyses) from the Mud Lake (Mud-11, Snow-5-12) and Drybones Bay (DB) kimberlites, published kimberlitic zircon data (Belousova et al., 1998) and the Wekusko Lake (WL) carbonatite, (Chakhmouradian et al., 2009). Normalized to pyrolite (McDonough and Sun, 1995)..... 76

Figure 26 (pp. 79) BSE and CL images of Mud Lake carbonate minerals: (A) BSE image of groundmass composed of primary lath-shaped dolomite microphenocrysts, serpentine, spinel and apatite; (B) CL image of microphenocrystic dolomite laths; (C) BSE image of rhombohedral dolomite with a turbid inclusion-rich rim; (D) CL image of rhombohedral dolomite; (E) BSE and (F) CL images of lacey dolomite frills with turbid inclusion-rich

textures; (G) BSE image of clear, blocky segregationary dolomite; (H) CL image blocky segregations with concentric zoning. Ap = apatite; Dol = dolomite; Chl = chlorite; Srp = serpentine; FeO = iron oxide. 80

Figure 27 Incompatible element patterns for Mud Lake (ML), selected Drybones Bay (DBB) samples and average hypabyssal kimberlite (Chakhmouradian et al., 2013). Normalized to primitive mantle values of McDonough and Sun (1995)..... 88

Figure 28 Chondrite-normalized REE patterns for Mud Lake (ML), Drybones Bay (DBB) and hypabyssal kimberlites (Chakhmouradian et al., 2013). Normalized to C1 values of McDonough and Sun (1995)..... 88

Figure 29 CL image of a dated zircon macrocryst from Mud Lake. The six 55 μm and four 30 μm ablation pits correspond to geochronology and trace element measurements, respectively. 89

Figure 30 (A) U-Pb concordia diagram displaying the results for the Mud Lake zircons, all 11 analyses are concordant and yield an age of 469.6 ± 9.7 Ma. (B) Weighted mean of $^{207}Pb/^{235}U$ and $^{206}Pb/^{238}U$ isotopic ratios (right)..... 90

Figure 31 Relationship between SiO_2 and Al_2O_3 in the apparently uncontaminated Mud Lake HK and the contaminated Drybones Bay VK. The Mud Lake samples and units K-1, -2 and -3, form a trend towards the Defeat cluster, indicated by the dashed line. Solid lines are simple mixing lines between average HK (Chakhmouradian et al., 2013) Defeat granodiorite (Yamashita et al., 1999), quartzite, and serpentine. The field of "uncontaminated" compositions (dashed box) is from Mitchell (1986)..... 93

Figure 32 Relationship between Ga/Al and Nb/Ta for the Mud Lake and Drybones Bay kimberlites, the average HK (Chakhmouradian et al., 2013) and the Defeat granodiorite (Yamashita et al., 1999)..... 94

Figure 33 Bivariate plots of Ni vs. Co/Ni for (A) whole-rock data, (B) ilmenite, and (C) spinel from Mud Lake and Drybones Bay. The variation trend and Co-Ni budget are replicated by olivine fractionation paths ($^{Ol/L}D_{Ni}$ = 32 and $^{Ol/L}D_{Co}$ = 4). The solid line (A) models the composition of the residual melt evolving by olivine fractionation, while the dashed lines (B,C) model the composition of ilmenite ($^{Ilm/L}D_{Ni}$ = 5 and $^{Ilm/L}D_{Co}$ = 1.7) and spinel ($^{Spl/L}D_{Ni}$ = 7 and $^{Spl/L}D_{Co}$ = 4) crystallizing from the evolving melt. See text for details..... 97

Figure 34 Temperature of Mud Lake and Drybones Bay kimberlitic zircons projected onto the Drybones Bay Slave geotherm (Carbno and Canil, 2002). Modified after Carbno and Canil (2002), used with permission. 99

Figure 35 Summary of Zr-in-rutile thermometry measurements (BSE images and LA-ICP-MS line profiles). The red lines show where line profiles were taken, below each BSE image is the Zr response along the profile, from A to B. Note: the Zr concentration indicated in the first profile exceeds the range measured by spot analysis, while its possible that the values on the profile are accurate, the previously reported values are considered to be much more reliable..... 101

Figure 36 (pp. 111–112) Hypothetical eruption sequence to account for the internal pipe geology. See text for details..... 112

List of Tables

Table 1 Whole-rock composition of parental kimberlite magma proposed in the literature. 13
Table 2 Summary of post-Archean mantle magmatism in the Slave craton, from youngest to oldest. 23
Table 3 Catalogue of Drybones Bay samples used in this study. 33
Table 4 Summary of petrographic features of the Drybones Bay rocks. 41
Table 5 Representative major- and trace-element compositions of phlogopite from Mud Lake and Drybones Bay 55
Table 6 Representative major- and trace-element compositions of ilmenite macrocrysts from Mud Lake and Drybones Bay. 60
Table 7 Representative major- and trace-element compositions of spinel-group minerals from Mud Lake and Drybones Bay. 63
Table 8 Representative major- and trace-element compositions of garnet macrocrysts and xenocrysts from Mud Lake and Drybones Bay. 72
Table 9 Representative major- and trace-element compositions of zircon macrocrysts and xenocrysts from Mud Lake and Drybones Bay. 77
Table 10 Representative major- and trace-element composition of rutile, Mud Lake and Drybones Bay 81
Table 11 Whole-rock major-element compositions (wt.%) of the Mud Lake and Drybones Bay kimberlites 83
Table 12 Whole-rock trace-element compositions of the Mud Lake and Drybones Bay kimberlites 85
Table 13 U-Pb isotopic data for zircon from the Mud Lake and Drybones Bay kimberlites, and the Defeat pluton country rock. 91

Chapter 1: Introduction

1.1 Introduction to kimberlites

Kimberlites are mantle-derived ultramafic volatile-rich alkaline rocks that form (sub)volcanic pipes, with most bodies measuring less than 200 ha in surface area (Mitchell, 1986; Jennings, 1995). Kimberlites are invaluable both scientifically and economically. Their parental magmas are generated in the mantle and transport xenoliths from Earth's deep interior to the (near) surface; this material provides insights into mantle petrology, composition and processes, and includes peridotite- and eclogite-derived diamonds. Diamonds are the primary motivation for kimberlite exploration: in 2014 over US$ 14 billion worth of rough diamonds were produced (Kimberley Process, 2015), and global diamond jewelry sales exceeded US$ 80 billion (De Beers, 2015). Kimberlite magmatism has been recurrent through space and time: kimberlites have been emplaced in every continent (Janse and Sheahan, 1995), spanning a ~1600 Ma period, from the Proterozoic to the late-Cenozoic (Donnelly et al., 2011; Brown et al., 2012). There were 5000 known occurrences in 1995 (Janse and Sheahan, 1995), and recent estimates place the number at approximately 6800 (Manson, 2012).

The geology of kimberlites is complex, even their classification is problematic due to the difficulties involved in differentiating between these rocks and other alkaline rocks on a modal or geochemical basis (Le Maitre et al., 2002). Our understanding of kimberlite petrogenesis and emplacement processes has been hindered by the fact that there are no modern day kimberlite volcanoes to study; research is relegated to ancient examples that have been modified by intense chemical alteration and subjected to millions of years of erosion that has removed any shallow and near-surface features. Imperfect and incomplete study material has led researchers to contradictory conclusions, even with respect to the same kimberlite occurrences (e.g., the interpretation of diatreme-facies rocks in the Ekati kimberlites, NWT; Janse and Sheahan, 1995; Nowicki et al., 2007; Brown et al., 2012), making kimberlite geology a contentious field.

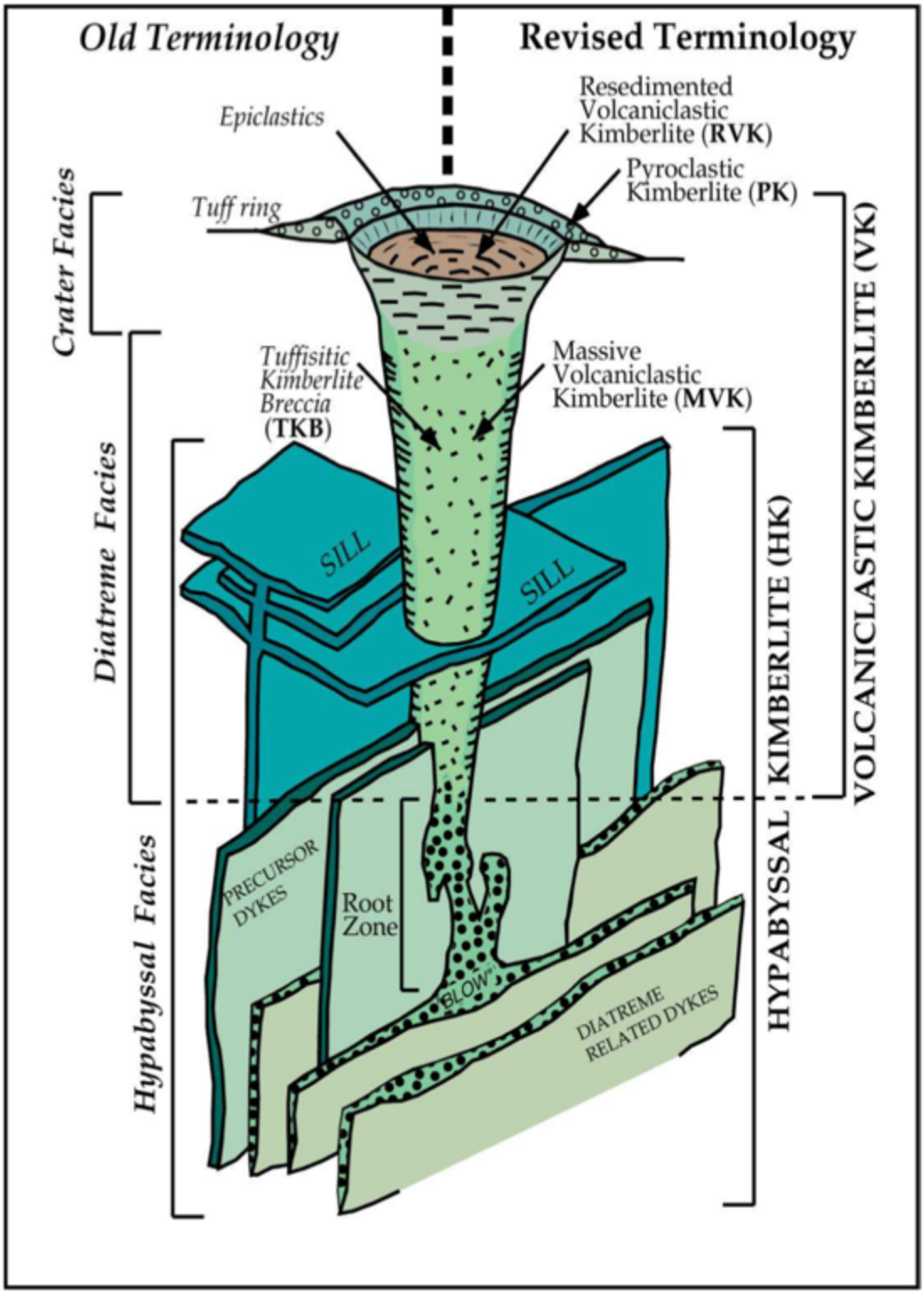

Figure 1 The classic South African model of a kimberlite pipe showing old nomenclature (left side of figure) and revised nomenclature (right side of figure). Note: massive volcaniclastic kimberlite (MVK) is a non-genetic term for tuffisitic kimberlite (TK). Kjarsgaard (2007) modified after Mitchell (1986). Used with permission.

1.2 Kimberlite nomenclature and classification

Kimberlites are distinct from other volcanic rocks in that they lack effusive or plutonic equivalents, and there is no evidence for magma reservoirs, calderas or ring faulting (Field and Scott Smith, 1999). Kimberlites are often typified by the classic South African model (Figure 1), comprising a pipe (vertical tapered body with steeply dipping sides) with a complex root zone and peripheral and cross-cutting dykes and sills. The pipe can be divided into crater, diatreme, and root zones, which contain texturally distinct kimberlite lithologies. The root zone is filled with competent igneous rocks known as hypabyssal kimberlite (HK); the diatreme zone contains a uniquely textured sub-volcanic rock called tuffisitic kimberlite (TK; alternatively termed Kimberly-type pyroclastic kimberlite, KPK; Scott Smith et al., 2013); the crater zone is infilled with various types of volcaniclastic kimberlite (VK) material, including pyroclastic kimberlite (PK) deposited directly from pyroclastic fallout, resedimented volcaniclastic kimberlite (RVK) formed by the reworking of PK, and less commonly epiclastic kimberlite formed from consolidated extra-crater material redeposited by surface processes (Scott Smith et al., 2013).

Not all kimberlites conform to the traditional South African model (Class 1). Two additional distinct types of kimberlite bodies have been recognized (Field and Scott Smith, 1999): the Canadian Prairies type (Class 2) and Lac de Gras type (Class 3), so named after kimberlite fields in Saskatchewan and the Northwest Territories, respectively. Figure 2 is a comparative illustration of Class 1, 2, and 3 kimberlites; note marked differences in the size and geometry of the pipes and the lithology of the infill material.

Class 1 kimberlites, based on the classical South African model, are characterized by deep, steep-sided (80–85^{o} contacts) pipes with well defined crater, diatreme and root zones, and associated dykes and sill complexes (Field and Scott Smith, 1999). The diatreme zone is filled with TK, which is recognized by cored magmaclasts (pelletal lapilli), microlitic diopside and the lack of carbonate in its matrix. Diatreme-zone TK grades into HK at the root zone; these transitional rocks are marked by a decrease in the proportion of magmaclasts and diopside microlites, and the presence of carbonate-serpentine segregation textures. Blind intrusions or embryonic pipes that failed to breach the surface are unique to Class 1 kimberlites (see Figure 13 of Barnett et al., 2011). Fully developed pipes are large and deep, with an original vertical extent of 1000–1500 m, and surface area on the order of 10–15 ha (Field and Scott Smith, 1999). Economic pipes have ranged in size from less than 0.4 ha up to 146 ha (Jennings, 1995).

Botswana is home to some of the largest pipes, such as Orapa A/K1 (112 ha), Mwadui (146 ha) and M1 (> 200 ha, Jennings, 1995).

Class 2 kimberlites are characterized by shallow (< 500 m) craters, with country rock contacts dipping at 0–60^{o} (usually between 15–45^{o}), and infilled with a texturally distinct variety of PK (Scott Smith, 2008). The PK from Class 2 kimberlites, referred to as Fort à la Corne-type PK, is distinguished by amoeboid-shaped magmaclasts with relatively thick, vesicular, compound selvages (juvenile lapilli in the terminology of Scott Smith et al., 2013). Class 2 kimberlites have no apparent diatremes or root zones, and contain no TK or HK. These bodies are comparatively large, with surface areas up to 250 ha.

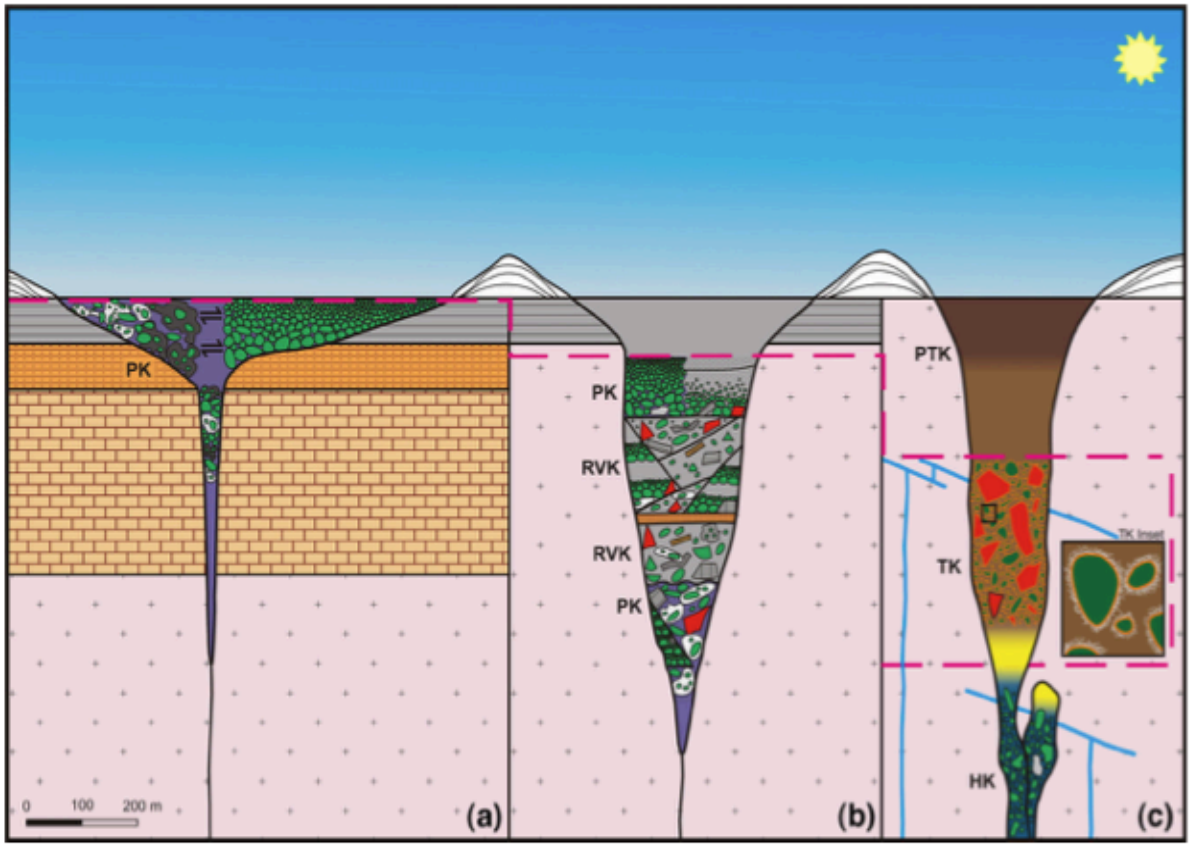

Figure 2 Schematic representation of the three main types of kimberlite pipes: (a) Class 2 (Canadian Prairies) kimberlite, with a shallow crater infilled with PK, and no diatreme or root zones; (b) Class 3 (Lac de Gras) kimberlite, with a steep-walled pipe infilled with (R)VK ± PK ± HK, the lack of TK is characteristic of both Class 2 and Class 3 pipes; and (c) Class 1 (South African) kimberlite, with well defined crater, diatreme and root zones (Scott Smith, 2008). Used with permission.

Class 3 kimberlites, typified by Cretaceous-Eocene pipes in the Lac de Gras area in the Slave craton, bear more resemblance to their South African counterparts than those in the Canadian Prairies due to their steep (> 70^{o}) sidewall contacts, but they are smaller, lack certain features of Class 1 pipes, and have distinct internal geology. They are typically < 15 ha in area, with many occurrences < 5 ha, and have an inferred vertical extent of 600–700 m (Field and Scott Smith, 1999). The pipes are infilled with volcaniclastic crater-facies material, including juvenile lapilli-rich PK and RVK contaminated with local surface sediments. Pipes infilled with HK are less common. Diatreme zones filled with TK do not occur, and their absence is considered a distinguishing feature of Class 3 pipes. Not all Slave craton kimberlites conform to this model though, because older (pre-Cretaceous) pipes containing TK and HK have been described at Jericho, Muskox, Rocking Horse Lake, Gahcho Kué, and Camsell Lake, and may represent lower diatreme and root zones comparable to southern African kimberlites (Field and Scott Smith, 1999).

The differences among Class 1, 2, and 3 kimberlites, and the general uniformity of pipes within individual fields are attributed to distinct near-surface conditions that affect the emplacement (Field and Scott Smith, 1999). Class 1 kimberlites were emplaced through country rock sequences of sedimentary units that contain competent barriers or cap rocks, such as diabase sills, whereas Class 2 pipes from the Canadian Prairies were emplaced into poorly consolidated sediments of varying thickness, and Class 3 were emplaced into competent Archean basement covered with a veneer of poorly consolidated sediment. Although the geometry of Class 1 and 3 pipes is similar, the absence of TK in the Lac de Gras kimberlites, even where HK is present, suggests these rocks formed by different processes.

1.3 Kimberlite emplacement theory

Several models of near-surface kimberlite emplacement with different mechanisms of magma ascent, pipe excavation and pipe filling are summarized below. This section, while seemingly inordinate in length, is relevant to the discussion on the emplacement of the Drybones Bay kimberlite (Chapter 8).

1.3.1 Phreatomagmatic pipe model

Phreatomagmatic processes, known to produce maar-diatreme complexes in other volcanic systems, were proposed as the primary mechanisms by which kimberlite pipes form (Lorenz, 1975). The phreatomagmatic model can be summarized in five stages:

Stage 1, initial cratering: Magma ascending along fissures near the surface encounters groundwater. The water flashes to steam, which erupts through the surface, ejecting fluids and pyroclastic debris and forming a small crater.

Stage 2, crater enlargement: The crater is enlarged through spalling of the wall rock due to pressure differences between the eruptive column and surrounding rock. The fissure becomes choked with wall-rock debris and the crater fills with water, allowing another cycle of phreatomagmatic eruptions. Pyroclastic material accumulates to form a rim of pyroclastic debris on the surface as it continues to be ejected.

Stage 3, crater filling: Enlargement of the crater and wall rock instability causes large-scale spalling and undermining. The wall rocks and overlying bedded pyroclastic material enclosed by the ring fault subside into the crater and become brecciated. Debris and water are again accumulated and the cycle of eruptions continues.

Stage 4, crater fill remixing: Continuous cycles of subsidence, brecciation and eruption cause the subsided material (i.e. fragmented wall rocks and slumped pyroclastics) to become intermixed with freshly ejected material. This remixing eliminates any pre-existing bedding and other internal structures.

Stage 5, late-stage modification: The faulted and fractured rocks and overlying tuffs are intruded with tuffisite. Migration of the ejection vent may produce several crosscutting columns of pyroclastic rock. Continuous intermixing with subsided material during this stage erases evidence of the central ejection column.

1.3.2 Bottom-up embryonic pipe model

The “bottom-up, embryonic pipe model”, first developed by Clement and Reid (1989) and built upon by Field and Scott Smith (1999), is based upon detailed investigation of southern African kimberlites, including petrographic studies, and takes into account the often neglected features such as complex root zones and blind pipes.

Stage 1, intrusion of kimberlite magma: Magma intrudes along joints in the country rock, ascending relatively slowly by stoping and wedging, aided by a gas cap of exsolved volatiles at

the head of the magma column (see Figure 8 in Field and Scott Smith, 1999). Geological barriers in the country rock (e.g., dolerite sills, basalt flows, etc.) temporarily stall the rising magma until sufficient pressure has built up to breach the barrier by explosive brecciation in an envelope around the head of the magma column (see Figure 4b in Field and Scott Smith, 1999). Gradual upward migration is re-established and the column grows as stoping and wedging become more efficient at shallower depths. The process is repeated when subsequent barriers are encountered, causing further sub-surface brecciation and preconditioning of the country rock.

Stage 2, country rock preconditioning and embryonic pipe development: As the magma column approaches the surface, the volume and pressure of exsolved volatiles increase. The reduced confining pressure permits larger volumes of country rock to be preconditioned by fracturing and intrusion of volatiles. At this stage, magma withdrawal will cause the infiltrated country rock to implode, assisting the brecciation process. Brecciation fronts that fail to breakthrough to the surface may result in embryonic pipes (see Figure 4c in Field and Scott Smith, 1999).

Stage 3, pipe formation and filling: Explosive breakthrough and crater excavation occurs when the volatile pressure exceeds the confining pressure. After breakthrough the upper part of the magma column degasses. In response to pressure drop, volatiles in the country rock move inward to escape, causing authigenic brecciation (see Figure 4d in Field and Scott Smith, 1999). Massive volatile streaming causes fluidization of the magma and the formation of magma droplets (pelletal lapilli) characteristic of TKB. The powerful and turbulent fluidization front moves downward through the ascending magma column, aiding implosion and eroding wall-rock contacts to smooth surfaces (see Figure 4e in Field and Scott Smith, 1999). Material above the degassing interface continues to be pneumatically transported upward, and diatreme excavation and widening proceed downward following the fluidization front. The fluidization event is short lived, as the system cools rapidly. Magma below the front crystallizes to form HK, while transitional or gradational zones between HK and TKB represent preserved degassing fronts (see Figure 4f in Field and Scott Smith, 1999).

1.3.3 Downward explosive dyke model 1

Sparks *et al.* (2006) consider the dynamic constraints on kimberlite volcanism, including the rheological properties of kimberlite magma, magma supply rates, and dyke propagation

velocities and volatile contents in their four-stage model for kimberlite emplacement (see Figure 16 in Sparks et al., 2006).

Stage 1, *initial cratering:* Rapid ascent of kimberlite magmas is facilitated by exsolved volatiles at the head of the magma column, which corrode the crustal rocks and create zones of weakness that can be exploited. Kimberlite magma travels along narrow fissures until it is within a few hundred meters of the surface, at which point it disintegrates into explosive flows. Explosive surface cratering results from high exit pressures in the narrow, choked vent, and can be augmented by phreatomagmatic explosions if groundwater is available.

Stage 2, pipe formation: Wall rock material in the crater along with juvenile kimberlite is ejected by explosive activity of sub-Plinian to Plinian intensity driven by degassing (i.e. producing a tall column of gas and volcanic ash). The pipe is widened and deepened by rock bursts that cause undermining, down faulting and crater-rim slumping (see Figure 15 in Sparks et al., 2006). Rock bursts are envisioned to occur in the deeper parts of the conduit (1-2 km) when under-pressurization causes the pressure differential to exceed the rock strength. This stage is largely erosive, with flow regimes remaining such that lithic fragments generated during the process are ejected. An abrupt halt to the eruption can leave a freshly excavated pipe empty, to be subsequently filled with surface sediments and breccia and epiclastic material from adjacent eruptions, as was the case at Lac de Gras, NWT and Jwaneng, Botswana.

Stage 3, pipe filling: Increasing cross-sectional area and decreasing gas velocities reduce the ability for flows to clear material from the conduit. Larger blocks of collapsed pipe margins can no longer be ejected and the pipe begins to fill. Reduced magma supply rates allow volatiles to segregate non-explosively and a fluidized bed starts to develop among the coarse clasts trapped in the pipe. The fluidized bed only permits gas and fine-grained debris to permeate and further suppresses explosive activity from new magma input. Trapped material is thoroughly mixed by the fluidization process and evolves into the VK infill. Late stage dykes and sills can intrude once magma supply rates have declined to the point that it can degas passively by bubbling. The transition between pipe formation and pipe filling is not proposed as a simple two-stage sequence, but involves alternating periods of pipe enlargement, emptying and filling.

Stage 4, post-emplacement metamorphism and alteration: The newly emplaced bodies are tens to hundreds of meters wide, and are expected to take decades to centuries to cool by conduction. Hydrothermal alteration resulting from meteoric water circulating through the hot

pipe principally produces serpentine at the expense of olivine. The serpentinization of olivine affects a significant volume change, causing original primary porosity to be filled with serpentine cement.

1.3.4 Downward explosive dyke model 2

Cas et al. (2008) proposed an emplacement model that shares similarities with that of Sparks et al. (2006) in terms of crater and pipe formation, but offers a markedly different interpretation for the formation of TKB and the nature of late-stage serpentine groundmass.

Stage 1, conduit formation: Rising magma and gas ascend to the surface through existing fractures expanded by tip crack propagation and by forming new passages by hydraulic and pneumatic fracturing (see Figure 6 in Cas et al., 2008). These processes produce a network of dykes and sills that act as a conduit to the surface, and zones of hydraulically fractured rock that are excavated during eruption.

Stage 2, vent opening: When the fractures breach the surface, abrupt decompression generates a prodigious gas overpressure that will trigger a high-energy ballistic gas explosion that will break through and open a roughly shaped vent. The initial explosions are Vulcanian in style (i.e. short-lived and discrete) and eject a volume of rock roughly equivalent to the size of the initial vent (see Figure 6b in Cas et al., 2008)

Stage 3, vent clearing, reaming and sculpting: Depressurization at the vent opening triggers an acceleration of volatile exsolution and explosive fragmentation of the magma that produces a waxing jet of ejecta, carrying lithic fragments and juvenile material and feeds a buoyant eruption column. The depth of vesiculation and explosive fragmentation migrates downwards through the magma column as it decompresses, excavating deeper portions of the pipe (see Figure 6c in Cas et al., 2008).

Stage 4, pyroclastic vent infilling: When the eruption begins to wane, the column of gas and particulate matter rising from the vent becomes too dense to remain buoyant and will collapse into the vent (see Figure 6d in Cas et al., 2008). The collapsing pyroclastic column deposits the uniquely textured lapilli tuff (i.e. TK) that is characteristic of diatreme facies. Fluidization processes are not considered to be involved in the formation of these rocks. Normal pyroclastic fallout produces much better sorted deposits due to hydraulic sorting from the buoyant eruption column, rather than column collapse.

Stage 5, late-stage filling of the pipe: Stratified crater deposits of RVK form from the collapse of crater rim debris, minor explosive events within the crater or pyroclastic fallout from nearby eruptions (see Figure 6e in Cas et al., 2008). Coherent kimberlite (HK) can intrude the base of the vent fill.

Stage 6, post-emplacement alteration: Hydrothermal alteration persists long after the eruption and emplacement stages are complete (see Figure 6f in Cas et al., 2008). In contrast to the previous model, Cas et al. (2008) considers groundmass serpentine as the replacement product of the fine ash matrix rather than cement from olivine serpentinization, and that original open pore spaces would have been largely absent.

1.3.5 Downward exploding dyke model 3

Wilson and Head (2007) offer an integrated model of kimberlite emplacement, from the ascent of magma from its mantle source to eruption. They propose that melts originate from a CO_2-rich mantle source and rise to the surface rapidly via dyke propagation.

Stage 1, dyke propagation, ascent and wall-rock fracturing: The tip of a dyke originating from a CO_2-rich mantle source at a depth of 250 km is able to propagate rapidly due to the formation of a supercritical fluid in the cavity behind the tip (see Figure 2 in Wilson and Head, 2007). Bubbles of CO_2 burst into the cavity from an underlying zone of magmatic foam, causing the pressure behind the dyke tip to decrease. Exsolved volatiles streaming from the degassing magma (initially containing up to 20 wt.% CO_2) constantly renew the supply of CO_2 to the dyke tip. The process causes an intense pressure gradient in the system, from ~8 GPa at the source to ~2 GPa at the foam layer to ~70 MPa in the cavity, which drives the turbulent rise of magma at tremendous speeds. The average ascent rate is estimated at 30–50 m/s, implying a transit time of roughly 1 hour. The low-pressure cavity behind the dyke tip produces tensional stress that causes fracturing in the surrounding rock. Fragments of country rock are torn from the walls to form xenoliths, which become entrained in the magmatic foam. Over the last several kilometers of magma rise, the stress across the dyke walls changes from tensile to compressive, and the decreasing overburden pressure may permit the intrusion of small dykelets.

Stage 2, vent opening: When the dyke tip breaks the surface, the chamber of supercritical fluid expands violently, producing an initial Vulcanian style explosion (see Figure 2c in Wilson and Head, 2007). The explosion generates an expansion wave that propagates downward,

imploding the wall-rock and ejecting the mixture of magma, gas and entrained particles in a Plinian to sub-Plinian eruption plume. This eruption empties a cavity typically 3 km deep.

Stage 3, depressurization: When the depressurization wave initiated by the vent opening propagates through the layer of magmatic foam, the bubbles expand and the foam is disrupted into magma droplets as the gas is released (see Figure 2d in Wilson and Head, 2007). As the wave continues, additional foam is generated and subsequently disrupted as bubble-free liquid degasses. The coalescing magma droplets will incorporate particles in the magma (i.e. xenocrysts and phenocrysts) and rapidly cool to produce the pelletal lapilli of TK.

Stage 4, upward fluidization: The combined effects of foam generation and disintegration produce an upward propagating fluidization wave that will cause sorting in the brecciated diatreme zone, and permit the downward displacement of large blocks of country rock to stratigraphically lower levels (see Figure 2e–f in Wilson and Head, 2007). When the fluidization wave hits the obstructed vent opening, a pressure wave is reflected back downward. This pressure wave causes instabilities in gas exsolution processes that can in turn generate a new fluidization wave, causing the system to reverberate through cycles of gas release, pressure change and venting. Magma deeper in the dyke will undergo "catastrophic adiabatic chilling" and cease to rise into the diatreme.

Stage 5, post-emplacement alteration: The resulting structure is characterized by a porous, cone-shaped diatreme with a crater rim of breccia and pyroclastic deposits. If groundwater is available, a crater lake may form, and the groundwater will permeate and rapidly alter the kimberlite infill (see Figure 2g–h in Wilson and Head, 2007).

1.4 Kimberlite geochemistry

The chemical composition and physical properties of parental kimberlite magma remain elusive due to the lack of material that unambiguously represents the melt phase, such as aphyric or glassy extrusive rocks (Mitchell, 1986; Price et al., 2000), and also because kimberlites invariably contain mantle and crustal material as xenoliths (Mitchell, 2008). The problem is further exacerbated by the intense post-emplacement alteration that is ubiquitous in kimberlites. The alteration inexorably changes the chemical composition of these rocks, while obliterating primary textural characteristics in the process. Consequently, whole-rock compositions of kimberlite samples *are not* representative of the magmas from which they formed.

1.4.1 Contamination

Crustal contamination is a serious issue complicating the interpretation of whole-rock geochemical data. Significant quantities of brecciated and disaggregated wall-rock material can be incorporated during the emplacement of kimberlite, drastically changing its bulk composition. Crustal contamination usually results in the addition of SiO_2, Al_2O_3 and Na_2O. A preliminary screening can be done to reject obviously contaminated samples a priori (e.g., $Al_2O_3 > 4.5$ wt.%), but more involved methods are required to properly evaluate the degree of crustal contamination. A widely used approach is the Contamination Index (C.I.), which can be calculated using the weight % of major oxides (Clement, 1982):

$$C.I. = \frac{(SiO_2 + Al_2O_3 + Na_2O)\ wt.\%}{(MgO + 2K_2O)\ wt.\%} \quad \textbf{(1)}$$

The index essentially compares the proportion of clay minerals and tectosilicates relative to olivine and phlogopite (Mitchell, 1986). Uncontaminated or 'fresh' kimberlite is indicated by C.I. values close to 1 (Clement, 1982; Nowicki et al., 2008; Kjarsgaard et al., 2009); however, values up to 1.5 have been reported for apparently uncontaminated phlogopite and/or diopside-rich kimberlites (Clement, 1982). Unfortunately, the sensitivity of this index is hampered by the effects of mantle contamination, which produces an opposite effect on the C.I., effectively obscuring the extent of crustal contamination (Kjarsgaard et al., 2009). For example, the addition of 20–30% peridotite plus 5% crust produces signatures that are difficult to distinguish from non-contaminated rocks (Kjarsgaard et al., 2009). Additional approaches have been utilized to better screen contaminated and non-contaminated kimberlite: bivariate plots of Yb (ppm) vs. Al_2O_3 (wt.%), ln(Mg/Yb) vs. ln(Si/Al), and C.I. vs. ln(Si/Al) have shown bimodal distributions of contaminated and non-contaminated rocks (Kjarsgaard et al., 2009), but there remains some overlap, and the bimodal distribution is not consistent across other elements expected to be similarly affected by crustal contamination.

1.4.2 Parental kimberlite magma composition

Nascent studies of kimberlite geochemistry paid little heed to the aforementioned problem of contamination, and early literature is rife with analyses of severely contaminated volcaniclastic rocks (Mitchell, 1986). Since then, researchers have taken different approaches to

overcoming these obstacles, such as: analyzing quenched aphanitic kimberlites, considered to be representative of their parental magmas (Price et al., 2000; Le Roex et al., 2003; Kopylova et al., 2007); modeling magma evolution trends of HK suites; and conducting experimental high-pressure studies to constrain the initial geochemistry of kimberlites (Le Roex et al., 2003; Harris et al., 2004; Becker and Le Roex, 2006; Sparks et al., 2006; Kjarsgaard et al., 2009; Patterson et al., 2009).

Proposed parental melts (Table 1) have a compositional range of 24.3–31.8 wt.% SiO_2, 15.2–30.8 wt.% MgO, 9.2–22.2 wt.% CaO, 5.4–9.7 wt.% FeO_{total}, 1.3–5.9 wt.% Al_2O_3, 0.5–3.2 wt.% TiO_2, 0.4–1.9 wt.% K_2O, 0.4–2 wt.% P_2O, 0.1–0.2 wt.% Na_2O, 6.1–12.3 wt.% H_2O and 5.1–17.3 wt.% CO_2 (Le Roex et al., 2003; Harris et al., 2004; Becker and Le Roex, 2006; Sparks et al., 2006; Cas et al., 2008; Kjarsgaard et al., 2009; Patterson et al., 2009). The different models proposed in the literature are consistently silica-deficient, have a high Mg# and are volatile-rich, but there is a marked lack of consensus in some areas. For example, the concentrations of TiO_2 and K_2O show a five-fold difference between the low and high estimates; and the volatile composition varies from CO_2-dominant to H_2O-dominant. The alkali content is strikingly low across all estimates, with $K_2O + Na_2O$ ranging from 0.55 to 2.06 wt.%, and $(Na + K)/Al < 1$, which is at odds with kimberlites being considered potassic rocks (Mitchell, 1986).

Table 1 Whole-rock composition of parental kimberlite magma proposed in the literature.

	Southern Africa			Canada						
	BLR[1]	Harris[2]	Le Roex[3]	Kjarsgaard[4]		Price[5]		Kopylova[6]		Patterson [7]
Oxide wt.%	Average group I	Uintjies-berg	Kimberly	low-Ti	hi-Ti	JD69	JD82	296G-C[8]	296G-C[9]	Renard[10]
SiO_2	26.15	24.99	26.50	31.79	27.46	27.00	28.13	28.54	26.7	24.33
TiO_2	2.58	3.23	2.20	0.72	1.12	0.51	0.71	1.62	1.73	2.91
Al_2O_3	2.76	2.32	2.20	3.08	2.54	1.33	1.61	1.60	1.57	5.92
FeOt	9.65	9.23	8.80	8.28	7.29	5.39	6.63	7.38	7.58	8.90
MnO	0.19	0.19		0.19	0.17	0.14	0.16	0.18	0.18	0.22
MgO	25.20	26.09	26.50	30.77	27.46	22.40	23.10	28.68	28.25	15.15
CaO	13.26	14.99	12.00	9.23	14.24	19.40	16.70	12.16	12.90	22.23
Na_2O	0.16	0.06		0.10	0.09	0.15	0.19	0.09	0.10	0.10
K_2O	0.83	1.06	1.50	1.03	0.61	0.40	0.50	1.19	1.26	1.96
P_2O	2.04	1.87		0.97	0.71	0.60	0.80	0.37	0.40	1.03
Cr_2O_3	0.18	0.22				0.13	0.18	0.37	0.36	
H_2O	7.33	5.18	12.30	8.72	6.10	7.10	6.70	8.52	9.07	
CO_2	8.19	8.63	7.00	5.13	12.20	14.01	12.10	9.29	9.88	17.25
Total	98.52	98.06	99.00	100.01	99.99	98.56	97.51	99.99	99.98	100.00

[1]Becker and Le Roex (2006); [2]Harris et al. (2004); [3]Le Roex et al. (2003); [4]Kjarsgaard et al. (2009); [5]Price et al. (2000); [6]Kopylova et al. (2007); [7]Patterson et al. (2009); [8]calculated composition at subsurface; [9]calculated composition at depth before orthopyroxene assimilation; [10]calculated composition by removal of orthopyroxene.

1.4.3 Trace-element composition of kimberlites

The trace-element geochemistry of kimberlites has been poorly characterized in the past due to the limitations of the analytical methods at the time (Mitchell, 1986). With the advent of readily available high-precision techniques, trace-element data are now providing a wealth of information on mantle sources and magma-evolution processes (Becker and Le Roex, 2006).

Trace elements in kimberlites can be grouped as compatible and incompatible elements. Compatible trace elements (e.g., Cr, Ni, Co) have solid/liquid distribution coefficients greater than unity ($^{S/L}D > 1$), they are therefore preferentially incorporated in rock-forming minerals such as olivine, during crystallization and become rapidly depleted from the magma during crystal fractionation (Mitchell, 1986). Compatible trace elements, as demonstrated in this work (see Section 8.2), can be used to model magma evolution processes.

Incompatible trace elements, including Ba, Sr, Zr, Hf, Nb, Ta, U, Th, rare earth elements (REE), alkalis, and volatiles, have infinitesimal distribution coefficients ($^{S/L}D << 1$) in common rock-forming minerals, and cannot be removed from the melt until the later stages of crystallization (Mitchell, 1986). Although their abundance can be diluted by crustal contamination or the presence of olivine macrocrysts, the ratios of geochemically similar incompatible trace elements (e.g., Zr-Hf, Nb-Ta, Th-U) largely remain unaffected and can provide valuable information on the source region of the melts (Mitchell, 1986).

A comparative geochemical study (Becker and Le Roex, 2006) of bona fide Group I kimberlites and micaceous Group II kimberlites (also known as orangeites), located on- and off-craton, indicates systematic differences in the source region of these rocks, which supports the recommendation of Mitchel (1995) to recognize Group II kimberlites as new rock type, distinct from kimberlites, known as orangeites. Chondrite-normalized REE patterns (Figure 3) show that Group I kimberlites are considerably enriched in light REE (LREE; La_{CN} = 300–1300) relative to heavy REE (HREE; Lu_{CN} = 3–8). The ratios of $(La/Yb)_{CN}$ and $(La/Sm)_{CN}$ are 45–267 and 4–7, respectively. Trace-element patterns normalized to primitive mantle (Figure 4) are generally smooth, except for strong enrichment in Nb and Ba, and relative depletions in Rb, K, Sr, and Ti in Group I kimberlites (Becker and Le Roex, 2006). The trace-element patterns for orangeites are characterized by slight depletion of K, Ta, and Nb and a *lack* of the negative Rb, K, Sr, and Ti anomalies seen in kimberlites.

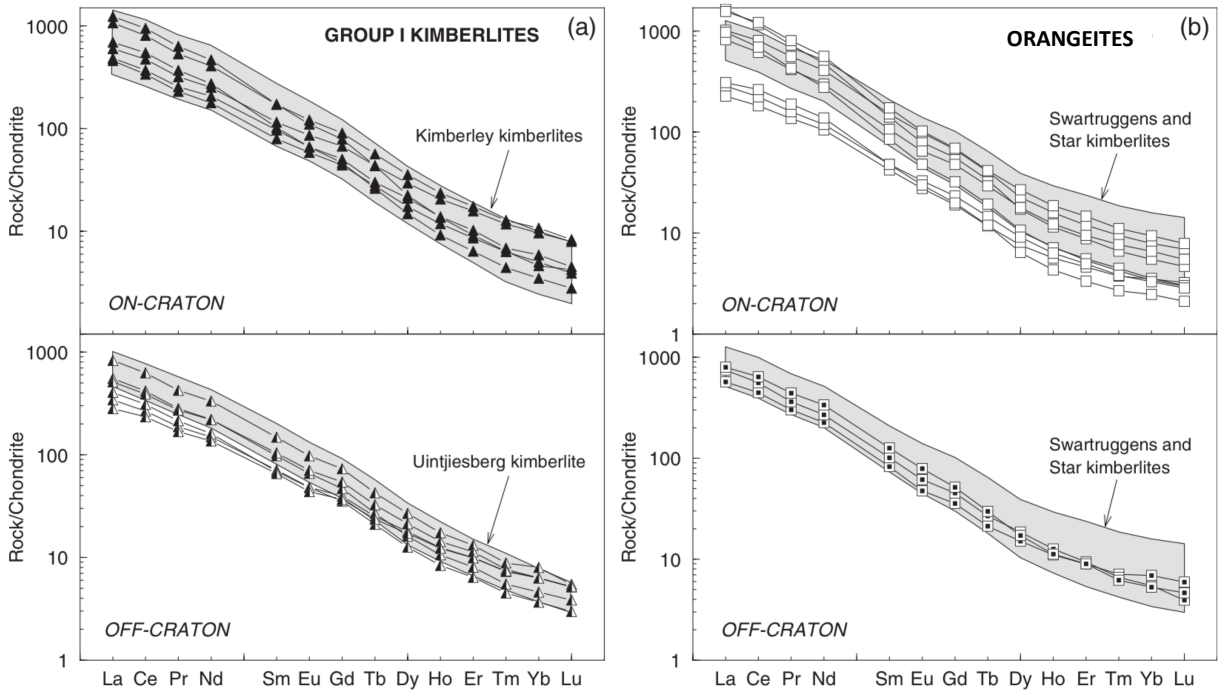

Figure 3 Chondrite-normalized REE diagrams for on- and off-craton (a) kimberlites and (b) orangeites. Diagram is from Becker and Le Roex (2006), normalized to values from Sun and McDonough (1989). Used with permission.

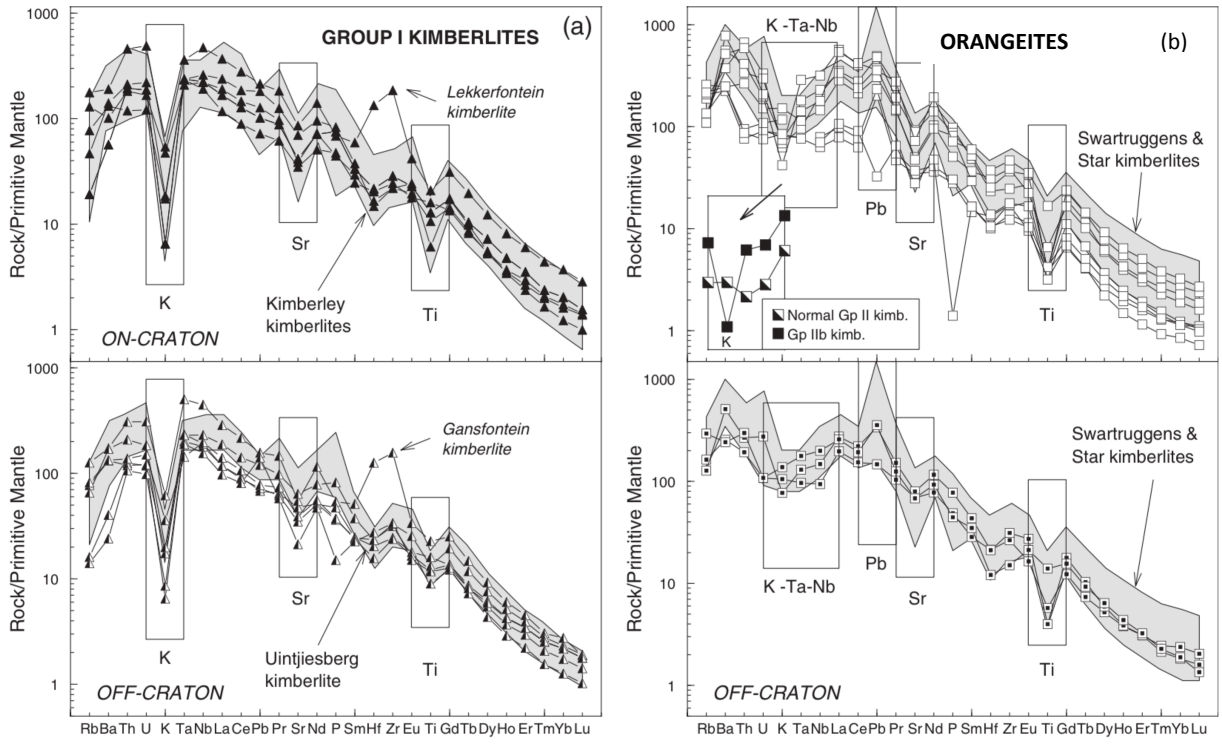

Figure 4 Primitive mantle-normalized trace-element patterns for on- and off-craton (a) kimberlites and (b) orangeites from South Africa, with highlighted trace element anomalies. Diagram from Becker and Le Roex (2006), normalized to values from Sun and McDonough (1989). Used with permission.

1.5 The kimberlite-carbonatite connection

Kimberlites and carbonatites share commonalities that have led many to view them as genetically related rocks. The view was initially predicated on the fact that both contain primary magmatic carbonate, and carbonatite and kimberlite-like rocks occur in association with alkaline complexes (Mitchell, 1979). The possibility that kimberlite and carbonatite magmas form a continuum of melts produced from a common source has been suggested by certain xenolith data, diamond inclusion studies, and experimental work (Dalton and Presnall, 1998; Moore and Wood, 1998; van Achterbergh et al., 2002; Gudfinnsson and Presnall, 2005; Araújo et al., 2009; Miller et al., 2013). The premise remains controversial and is not universally accepted by petrologists (Mitchell, 1986; Chakhmouradian et al., 2009).

Petrographically, kimberlite and carbonatite can be too similar to be reliably distinguished. Some evolved hypabyssal kimberlites contain CO_2-rich, SiO_2-poor mineral assemblages comprising over 50 vol.% carbonate (Mitchell, 1979; Gaspar and Wyllie, 1984), which satisfies the main criteria of the IUGS's non-genetic (modal) classification of carbonatites (Le Maitre et al., 2002). The overlapping mineral assemblage extends beyond carbonate phases and includes rock-forming minerals, such as apatite, Mg-Fe micas, and magnetite (Mitchell, 1986; 2005). Minerals common to both rocks are often compositionally distinct (Chakhmouradian et al., 2009; Reguir et al., 2009), and there are marked differences in trace-element geochemistry between kimberlites and carbonatites (Chakhmouradian et al., 2009), suggesting systematic differences in the mantle sources and parental melt chemistry. However, differences in mantle sources are not irreconcilable; occasionally carbonatites host diamonds (Chagatai, Uzbekistan; Jones et al., 2013) or diamond-indicator minerals that are typically associated with kimberlites (Wekusko Lake, Manitoba; Chakhmouradian et al., 2009).

The argument for a kimberlite-carbonatite continuum is supported by experimental melting of synthetic carbonated garnet lherzolite, represented by the $CaO–MgO–Al_2O_3–SiO_2–CO_2$ system (Dalton and Presnall, 1998; Moore and Wood, 1998; Gudfinnsson and Presnall, 2005). These researchers were able to produce a spectrum of melts ranging from carbonatitic to kimberlitic by varying the pressure and degree of partial melting. Initial experiments (Moore and Wood, 1998) conducted above and below the carbonate solidus at a pressure of 3 GPa (i.e. below the diamond stability field) generated a full compositional range from magnesiocarbonatite to volatile-free silicate melts. Carbonatite melts represent early melt fractions formed at the 1250

°C solidus. The SiO_2 content of these melts rapidly increases at 1475 °C, where clinopyroxene reacts out. At temperatures above 1550 °C, olivine melting further increases the SiO_2 content of the melt as the proportion of CO_2 decreases. Transitional carbonate-silicate melts are produced over a very narrow temperature interval (1475 °C to 1525 °C), explaining the absence of transitional rocks in nature. High-pressure experiments conducted on the same system, but within the diamond stability field, at 6 GPa (Dalton and Presnall, 1998) and 6–8 GPa (Gudfinnsson and Presnall, 2005), produced similar findings with respect to a possible kimberlite-carbonatite continuum.

Mineral and fluid inclusions with carbonatite to kimberlite compositions have been reported in diamonds and other mantle-derived material (van Achterbergh et al., 2002; Araújo et al., 2009; Miller et al., 2013), suggesting a link between carbonatites, kimberlites and diamond formation. Lherzolitic xenocrysts of Cr-rich diopside from the Diavik diamond mine, Lac de Gras area (van Achterbergh et al., 2002; Araújo et al., 2009), host abundant melt inclusions that range from carbonatitic (50–97 vol.% carbonate) to Ca-Mg-silicic (10–50 vol% carbonate) to Mg-silicic (<10 vol.% carbonate), and are similar in major-element composition to the range of melts produced experimentally (Dalton and Presnall, 1998). There is a lack of consensus on the origin of these carbonate-silicate inclusions and their implications: Van Achterbergh et al. (2009) have proposed that such inclusions form by quenching of entrapped mantle melts during xenolith transport in the kimberlite magma, whereas Araújo et al. (2009) have argued that melt differentiation after wall-rock interaction and fractionation from parental kimberlite melts is responsible for the carbonate-silicate segregation. Isotopic studies of the same melt inclusions found a subduction signature and a distinct lack of equilibrium between the inclusions and host mineral, suggesting that there is no genetic link, and that the carbonatitic fluids were trapped shortly before the xenoliths were entrained in the kimberlite (van Achterbergh et al., 2002). Araújo et al. (2009) found that the clinopyroxene host was enriched in LREE, Ba, alkali elements, high field-strength elements (HFSE), Th, and U, relative to inclusion-free grains, due to metasomatism by fluids that escaped from the melt inclusions. The composition of these metasomatising fluids (modeled from distribution coefficients) is similar to fluid inclusions in many of the Diavik diamonds, suggesting a genetic relationship between carbonate-silicate melts and the metasomatising fluids involved in diamond formation (Araújo et al., 2009).

1.6 Scope and objectives of the present work

The Drybones Bay pipe and the Mud Lake dyke (Figure 5), located approximately 45 km SE of Yellowknife (Northwest Territories, Canada), occur in the area of the Slave craton classified as Domain I by Heaman et al. (2003). Domain I kimberlites are Silurian–Ordovician in age, and thus far have received much less attention compared to other Slave craton kimberlites, which are more amenable to mining (i.e. Snap Lake, Diavik, Ekati, Gahcho Kué and Jericho) and represent either older (Cambrian) or younger (post-Permian) magmatism in the central and eastern parts of the craton (Figure 5; see Section 2.1 for additional information on Slave craton kimberlite domains). Prior to the present work, virtually nothing was known about the petrography or mineralogy of the Mud Lake kimberlite, and no detailed studies of this nature had been published on the Drybones Bay kimberlite. The main objectives of this study are:

1. Document the petrography and mineralogy;
2. Report on the whole-rock geochemistry and mineral compositions;
3. Establish the provenance of the rocks;
4. Classify the Drybones Bay rock units based on textural-genetic criteria (i.e. RVK, PK, TK, etc.);
5. Determine the age of the Mud Lake kimberlite;
6. Determine the relationship between the Drybones Bay and Mud Lake kimberlites;
7. Test the applicability of the common geothermometers to kimberlites;
8. Identify and model magma evolution trends.

In general, kimberlites share many similarities with other volatile-rich, silica-undersaturated mantle-derived rocks, such as carbonatites, olivine melilitites and ultramafic lamproites, in terms of their mineralogical, textural and geochemical characteristics (Mitchell, 1986). Some Mud Lake samples bear resemblance to dolomite carbonatite from Wekusko Lake, Manitoba, which was initially misclassified as a kimberlite (Chakhmouradian et al., 2009). While diamonds have been known to occur in other rock types, kimberlites and their associated placer deposits remain the principal source of diamond production. Therefore correctly classifying these rocks is essential in order to describe them in the proper context and assess their economic potential. In this work, the kimberlitic provenance of the rocks is established based on mantle-like geochemical signatures, the composition of kimberlite indicator minerals, and textural and mineralogical evidence.

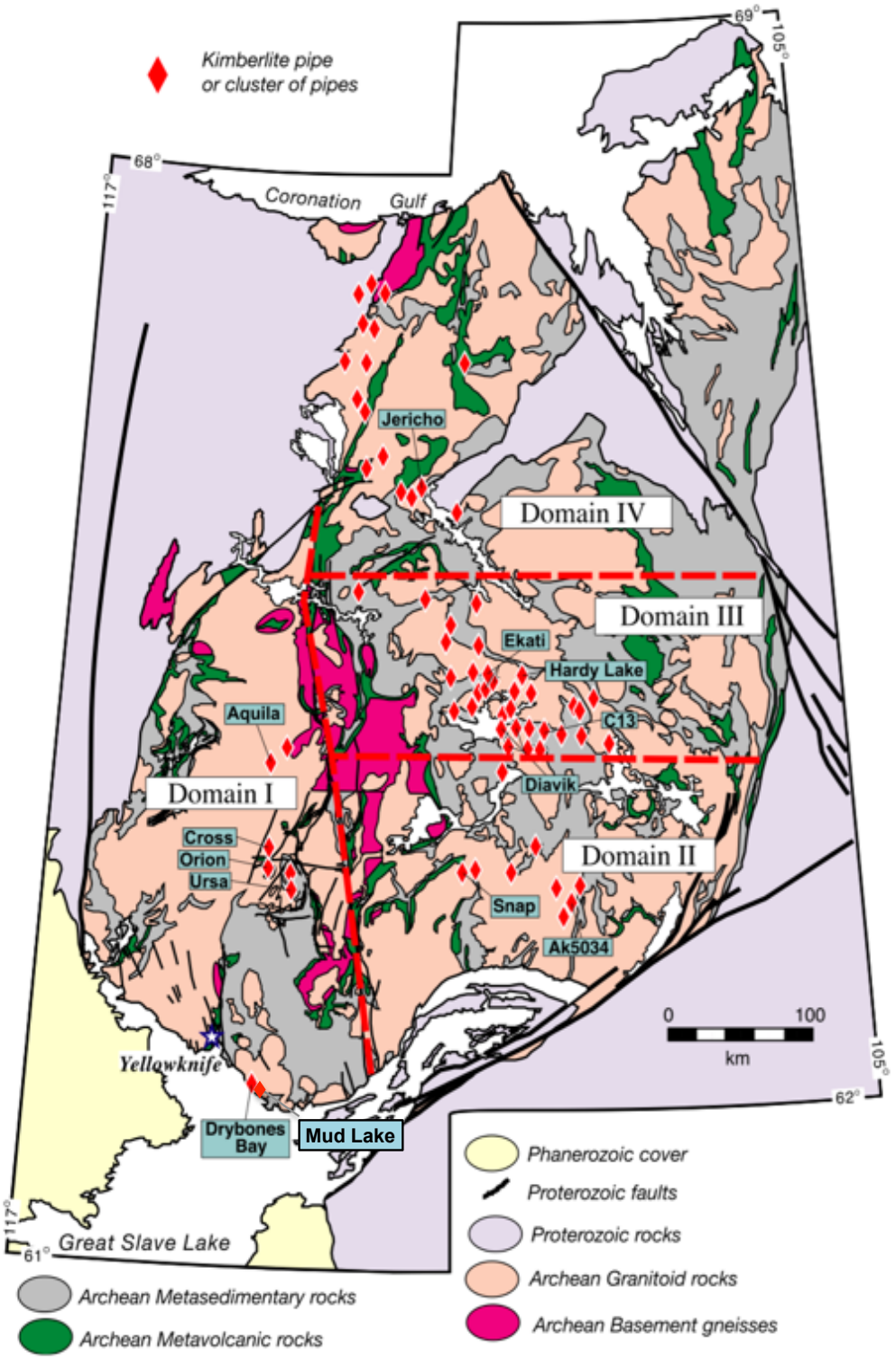

Figure 5 Schematic geologic map of the Slave craton showing the location of kimberlites and four age domains: (I) southern-western Siluro-Ordovician domain (~450 Ma); (II) south-eastern Cambrian domain (~540 Ma); (III) central Tertiary/Cretaceous domain (48–74s Ma); and (IV) northern mixed domain consisting of Jurassic and Permian kimberlite fields. Figure after Heaman et al. (2003). Used with permission.

Accurate textural-genetic interpretation of kimberlite pipe infill also has important economic implications. The application of facies models (i.e. Class 1, 2 or 3 pipes) allows for reasonable predictions and interpretations to be made about the geology of the pipe. In the seminal work of Field and Scott Smith (1999), the Drybones Bay pipe is briefly summarized as being infilled with juvenile-lapilli-bearing VK, with no evidence for the presence of TK, TKB or HK. The findings of our detailed petrographic investigation show the contrary, and we present evidence of TK and HK rocks.

Given the close proximity of Drybones Bay and Mud Lake (~4 km), it is possible that the two structures are related, and that the Mud Lake dyke could represent part of an intrusive complex associated with the formation of the Drybones Bay pipe, such as that depicted in Figure 1. This hypothesis is tested using geochronology and geochemistry. The relative timing of formation is established by U-Pb zircon dating, and the whole-rock geochemistry is used to assess whether the rocks are equivalent or could have evolved from a common parental magma.

The crystallization temperature and oxidation state are estimated from trace-element concentrations in minerals with well-calibrated, chemical substitutions that are sensitive to crystallization conditions. Geochemical data, including whole-rock and mineral compositions, reveal convincing evidence of olivine fractionation, adding substantially to the published research on kimberlite magma evolution.

Chapter 2: Geological Setting

2.1 Geology of the Slave Province

The Slave Geological Province of the Northwest Territories, northern Canada (Figure 5), is a relatively small (~200,000 km^2), well-exposed Archean craton that records a history of crustal growth, deformation, and magmatism, spanning from 4.05 to 2.55 Ga (Padgham and Fyson, 1992; Bleeker et al., 1999a; 1999b). The exposed bedrock comprises metasedimentary and metavolcanic supracrustal rocks of the Yellowknife Supergroup, dated 2.71–2.61 Ga, that have been extensively intruded by syn- to post-volcanic granitoid plutons from 2.64 to 2.58 Ga (Padgham and Fyson, 1992). Granitoid rocks constitute approximately 65% of the exposed bedrock, while supracrustal rocks cover the remaining 33% (Padgham and Fyson, 1992).

The Slave craton has been subdivided into distinct eastern and western domains, based primarily on the presence of a 4.05–2.85 Ga Mesoarchean basement, termed the Central Slave Basement Complex (CSBC), which is recognized only in the western half of the craton (Bleeker, 1999). The CSBC, formally known as the Anton Terrane (Kusky, 1989), is composed of a heterogenous assemblage of tonalitic to dioritic gneisses (Bleeker et al., 1999b). The eastern Slave Province is characterized by younger felsic to intermediate calc-alkaline volcanic rocks, typified by the Hackett River greenstone belt, and the absence of Mesoarchean basement (Padgham and Fyson, 1992). This structural boundary is further delineated on the basis of Pb- and Nd-isotopic studies, which show isotopically juvenile signatures in the eastern domain, relative to the western Slave (Davis and Hegner, 1992; Thorpe et al., 1992). The eastern extent of the CSBC at depth is unknown, however tectonic accretion models for the formation of the Slave craton propose that the CSBC continues beneath the juvenile arc terrane along an east dipping cryptic suture, which remains buried under supracrustal rocks (Kusky, 1989). Lower crustal xenoliths recovered from kimberlites in the Lac de Gras area have been dated at > 2.9 Ga, suggesting the presence of a Mesoarchean protolith at depth (Davis et al., 2003b).

The CSBC is overlain by a post-2.93 Ga autochthonous cover sequence known as the Central Slave Cover Group (CSCG), which forms the base of the Yellowknife Supergroup (Bleeker et al., 1999b). The CSCG is a thin, discontinuous cover sequence that is highly deformed and consists of (ultra)mafic and minor felsic volcanics, conglomerates, chromite-

bearing quartzites, and banded iron formations (Bleeker et al., 1999b). Overlying the CSCG are thick sequences of Neoarchean (2.73–2.70 Ga) tholeiitic basalts, which are well preserved in the Yellowknife greenstone belt, and do not correlate with any volcanic sequences documented in the eastern Slave (Padgham and Fyson, 1992; Davis et al., 2003b). Cover sequences that can be correlated across the entire craton begin with 2.69–2.66 Ga successions of felsic to intermediate calc-alkaline volcanic and subvolcanic units. The cessation of volcanism is marked by the deposition of thick turbidite sequences occurring across the entire craton, between 2.66–2.63 Ga (Bleeker et al., 1999a).

Syn- to late-kinematic granitoid plutons are voluminous and widespread, and account for most of the exposed bedrock (Padgham and Fyson, 1992). Early intrusions are of limited extent and confined to the southwest part of the craton, forming the tonalitic Anton and Suse Lake plutonic suites (ca. 2.65–2.64 Ga) north of Yellowknife, and the tonalitic to granodioritic Defeat suite (ca. 2.63–2.62 Ga) east and west of Yellowknife along the shore of Great Slave Lake (Davis and Bleeker, 1999). Widespread plutonism spanning the entire craton occurred from ca. 2.61 to 2.58 Ga, forming I-type granitoid (diorite to granodiorite) plutons dated at ca. 2.61–2.60 Ga, followed by syn- to late-kinematic S-type granitoid (biotite granite, two-mica leucogranite and extensive pegmatite) plutons emplaced ca. 2.60–2.58 Ga (Davis and Bleeker, 1999). Carbonatite-bearing alkaline complexes, consisting of five sequentially emplaced phases, occur at Grays Bay and Leith Lake, and have been dated at 2.605 Ga and 2.592 Ga, respectively (Villeneuve et al., 1998).

Proterozoic diabase dyke swarms, representing at least seven magmatic events, were associated with craton rifting or mantle-plume activity (LeCheminant and Van Breemen, 1994). The Mesoproterzoic Mackenzie dyke swarm, trending north-northwest in the Slave, is the largest known radiating mafic dyke swarm in the world (LeCheminant and Heaman, 1989).

Post-Archean mantle magmatism in the Slave (Table 2) spans a period of time over 2100 my in duration, from the Paleoproterzoic (2155 Ma) Big Spruce Lake carbonatite (Cavell and Baadsgaard, 1986) and Proterzoic lamprophyre dykes (LeCheminant, 1996) to the Eocene (47.5–56.0 Ma) kimberlite pipes in the Lac de Gras field (Heaman et al., 2003). Kimberlite magmatism, which represents the most significant mode of post-Archean mantle magmatism in the Slave after the Mackenzie dyke swarm, spans a shorter (~500 Ma) period, beginning with the emplacement of the Cambrian (542 Ma) Kennady Lake AK5034 pipe, until the time of the

aforementioned Lac de Gras kimberlites. There is a distinct correlation between the spatial distribution of Slave kimberlites, and the timing of kimberlite magmatism, and on this basis the Slave craton has been crudely subdivided into four kimberlite age domains (dashed lines in Figure 5): (1) a southwestern Slave domain characterized by Siluro-Ordovician kimberlites (459 Ma Ursa, 450 Ma Cross, 441 Ma Drybones Bay and 435 Ma Orion kimberlites); (2) a southeastern domain characterized by Cambrian kimberlites (542 Ma AK5034 and 523–535 Ma Snap Lake kimberlites); (3) a central domain representing Cretaceous and Eocene kimberlites (48–74 Ma Lac de Gras kimberlites); and (4) a northern mixed domain comprising Jurassic kimberlites (173 Ma Jericho pipe) and ~245–286 Ma Permian kimberlite fields on Victoria Island (Heaman et al., 2003).

The reason for the distinct domains is presently unknown, as there are no obvious explanations for the apparent pattern. The N-S trending eastern boundary of the Silurian-Ordovician domain (Figure 5) roughly coincides with the exposed margin of the CSBC, and the kimberlites of this domain (Drybones Bay, Mud Lake, Ursa, Orion, cross and possibly Aquila) define a linear N-S trend, which parallels the major trans-Slave crustal-scale Beniah Lake fault system (Heaman et al., 2003). Aside from the apparent trends in the Silurian-Ordovician domain, there are no obvious geological controls that correlate with the other age domains (ibid).

Table 2 Summary of post-Archean mantle magmatism in the Slave craton, from youngest to oldest.

Locality/Area	Type	Age (Ma)	Method
Lac de Gras[1]	Kimberlite	47.5–70.5	Rb-Sr phlogopite, U-Pb perovskite
Jericho[1]	Kimberlite	173.1 ± 1.3	Rb-Sr phlogopite
Victoria Island[1]	Kimberlite	256.0–286.0	U-Pb perovskite, Ar/Ar phogopite
Orion[1]	Kimberlite	435.4 ± 2.8	U-Pb perovskite
Drybones Bay[1]	Kimberlite	441.4 ± 0.8	U-Pb zircon
Cross[1]	Kimberlite	450.4 ± 2.2	U-Pb zircon
Ursa[1]	Kimberlite	459 ± 10	U-Pb zircon
Mud Lake	Kimberlite dyke	469 ± 9.7	See Chapter 7
Snap Lake[1]	Kimberlite dyke	522.9 ± 6.9	Rb-Sr phlogopite
Kennady Lake[1]	Kimberlite	542.2 ± 2.6	Rb-Sr phlogopite
Awry plutonic suite[2]	Lamprophyre dyke	post-2.0 Ga	Field relationships
Big Spruce Lake[3]	Alkaline intrusive complex	2155 ± 16	Pb-Pb zircon

[1]Heaman et al. (2003) and references therein; [2]LeCheminant (1996); [3]Cavell and Baagsgaard (1986).

2.2 Geology of the Mud Lake kimberlite dyke

Dolomite-rich macrocrystic HK was discovered near the southern extent of the Slave craton at Mud Lake, located at 62° 06’ 46.34” N, 113° 44’ 41.40" W, roughly 45 km southeast of the town of Yellowknife. The HK occurs as dykes and peripheral stringers over an area approximately 700 × 300 m. The country rock is a weakly foliated muscovite-bearing quartz monzonite pluton that is crosscut by a north-northwest striking vertically dipping diabase dyke of the Mackenzie dyke swarm (Vivian, 2006). Two faults intersect at Mud Lake, the northwest striking Cross fault and the east-northeast striking Mud Lake fault.

The main kimberlite body is a dyke that is up to 10 m thick, with a strike length of 110 m, located at a depth of 10 to 30 m (Figure 6; Vivian, 2006). The dyke is partly intruded along the lower contact of a gently southwest-dipping (13°), northwest-striking diabase dyke that is thought to be an appendage of a larger dyke of Mackenzie age. The kimberlite body is offset by a fault, and its geometry is irregular and only partially constrained.

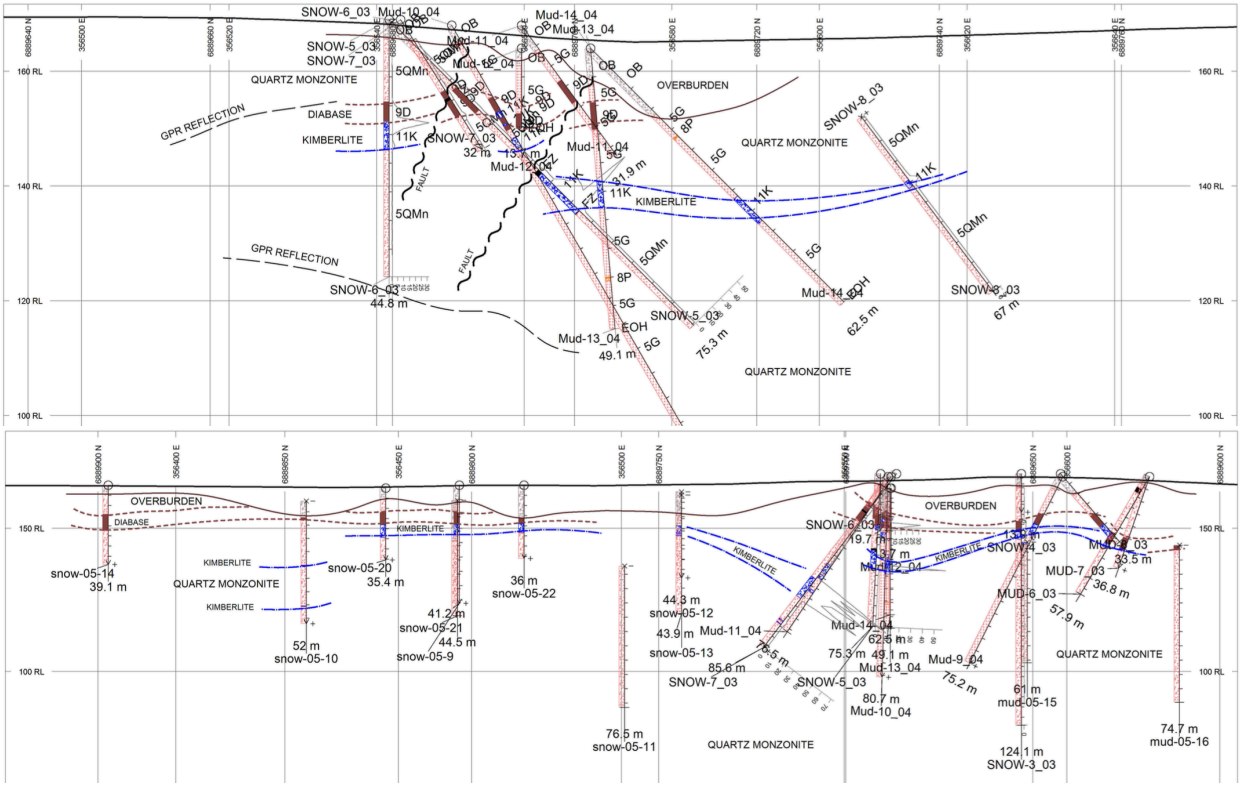

Figure 6 Cross-sections showing the results of the Mud Lake drilling program. Drill holes are marked in red and labeled with their depth and identification number, kimberlite contacts are marked in blue on the drill holes, inferred contacts delineating the kimberlite are marked with blue dashed lines (Vivian, 2006).

The dyke is closed to the south, appears open to the north and west and may intersect the surface to the east. Low counts of micro- and macro-diamonds were reported for the Mud Lake kimberlite (Snowfield Development Corp, 2008a; see Section 2.4 for more details).

2.3 Geology of the Drybones Bay kimberlite pipe

The Drybones Bay kimberlite occurs under ~38 m of water and 67 m of overburden, in a small enclave near the opening of Drybones Bay. The overburden consists of lacustrine clay, sand and a basal boulder conglomerate that thickens to the northeast in the up-ice direction (Kretschmar, 1996). The country rock is the Defeat plutonic suite, which consists predominantly of biotite tonalite and leuco-granodiorite with minor metasedimentary xenoliths of the Yellowknife Supergroup (Kretschmar, 1995a). The kimberlite body consists of a large crater-like formation that has been partially delineated by drilling and geophysical surveys (Kretschmar, 1995a; Power, 1998). It is unknown how the morphology and size of the body change with depth, as the deepest drill hole (302 m) was stopped in volcaniclastic kimberlite. Current geophysical models offer scant new insights due to the inherit limitations of potential field methods at resolving subtle variations with depth, and the lack of sharp seismic reflectors beyond areas explored by drilling (Power, 1998).

The crater is approximately 900 m long by 400 m wide, with an estimated area of 22 hectares (Kretschmar, 1996). It has a lobate shape in plan view (Figure 7) that bulges to the west and is narrower to the east. In cross section, the sidewall contacts dip at a lower angle in the western lobe than the in the eastern lobe. In terms of kimberlite pipe classification, the morphology imparted by the shallow dipping contacts and the large size of the crater causes the Drybones Bay body to resemble Class 2 kimberlites more than Class 3 kimberlites, which are typical of the central Slave (Field and Scott Smith, 1999; Scott Smith, 2008).

The kimberlite consists of several different phases that were initially defined on the basis of: contact relationships; textures and grain size; dominant xenolith size, abundance and composition (i.e. granitic, metasedimentary, peridotite, eclogite); degree of kimberlite alteration; and the nature of the groundmass. These phases include inferred crater-facies units K-1, -2, -3, -6, -7, a core intrusion (KC), and an epiclastic unit (KE). Several units (K-2, -3, -6) were described as probable diatreme-facies rocks (Kretschmar 1995, 1996), but are interpreted as crater-facies rocks in this work.

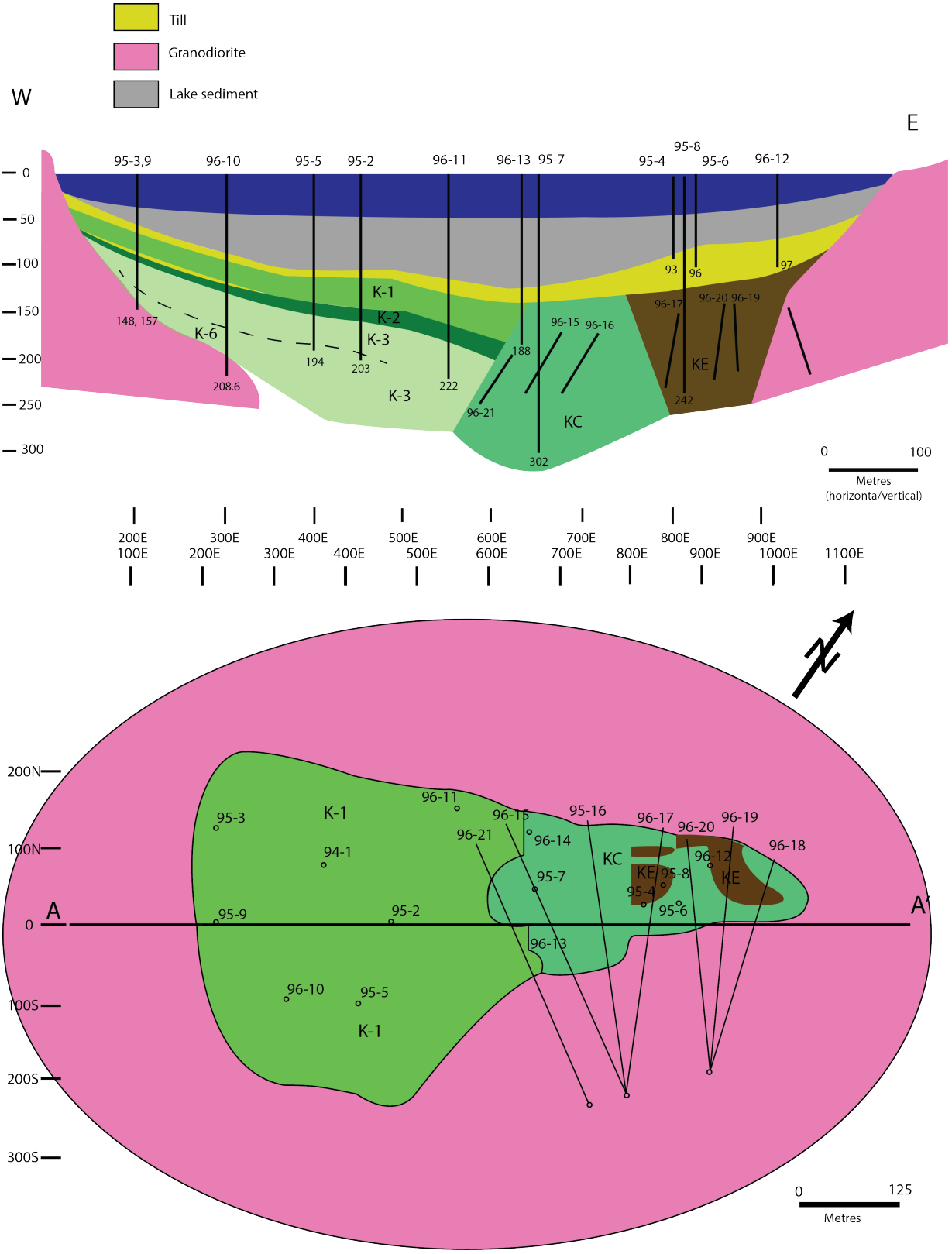

Figure 7 Schematic illustration of the Drybones Bay kimberlite pipe. See text for description of kimberlite units (K1–6, KC, KE). Modified after Kretschmar (1995a).

The western part of the crater is well stratified and consists of the crater-facies units (K-1, -2, -3, -6, -7). The upper unit (K-1) is a graded volcaniclastic kimberlite that disconformably overlies a thin (<10 m), relatively well-indurated unit (K-2). Beneath K-2 is a thick sequence of graded volcaniclastic kimberlite (K-3) that transition into a breccia (K-6) with an increasing proportion of country-rock fragments towards the contact with the Defeat pluton. A thin basal unit (K-7) overlies the shallow-dipping granodiorite country rock. The central intrusion comprises a massive, uniform unit (KC).

The eastern portion of the crater is infilled with an unusual sandy kimberlite, referred to as epiclastic kimberlite (KE), which is characterized by abundant rounded quartz grains with a distinct shattered texture. The KE is interbedded with volcaniclastic kimberlite described as being similar to K-3 (Kretschmar, 1996), however samples from hole 95-08 (Figure 7) examined in this work are found to be distinct, and are interpreted as a new unit: K-8. The interbedding occurs over an apparent thickness of > 150 m, in a cyclical, gradational fashion, with periods on the scale of meters to tens of meters. The cycles consist of basal kimberlite tuff that becomes progressively sandier, grading into sandy-kimberlite, kimberlite-sand and finally into semi- to unconsolidated sand (Kretschmar, 1996).

Diamonds have been recovered from each of these lithological units identified during exploration. The highest grades, ranging from 23.7 to 39.2 cpht, were yielded from the central section of unit KC (Kretschmar, 1996). However, the grades obtained cannot be considered representative due to insufficient sample sizes (see Section 2.4).

2.4 Exploration history

Diamond exploration on the north shore of Great Slave Lake began in February 1993 with the staking of Drybones Bay by local prospector Mr. David Smith (Kretschmar, 1995a). In April 1993, he conducted ground-based magnetic and very low frequency electro-magnetic surveys over Drybones Bay. In the winter of 1994, Drybones Bay was drilled and 24 m of kimberlite was intersected beneath 77 m of clay at the base of the bay. The discovery led Smith to partner with several other individuals and companies, and acquire additional land around Drybones Bay. In July 1994, Tradewinds Resources entered into an option agreement with Smith on the Drybones Bay claim.

Airborne and ground-based geophysical surveys were conducted over Drybones Bay and the peripheral claims during the summer, fall, and winter of 1994 (Kretschmar, 1995a). In the summer months, overlapping low-level airborne magnetic surveys were flown over Drybones Bay as part of a larger regional survey (Timmins, 2002). The first survey was conducted by High-Sense Geophysics Ltd., and consisted of 163.9 line-km, on a 50 m spacing, oriented at 340°. The second survey was flown by Geonex Aerodat Inc., and consisted of 80 line-km, on a 250 m line spacing, and an east-west orientation. In the fall, a third magnetic survey was flown by Geonex, covering 721 line-km with a line spacing of 50 m. During the winter of 1994, ground-based total magnetic field and vertical gradient magnetic surveys were conducted over the Drybones Bay pipe by Kalvick Mining Services of Yellowknife.

An advanced drill program at Drybones Bay was conducted from February to April 1995; it consisted of eight vertical holes (95-2 to 95-9) with a total length of 1546.9 m. The depth of the holes ranged from 131 to 302 m. Kimberlite was intersected in six holes (95-2, -3, -5, -7, -8 and -9), while two holes (95-4 and 95-6) were abandoned without recovering core due to difficulties penetrating the overburden. Drilling was halted in kimberlite in holes 95-2, -5, and -7, while holes 95-3 and 95-9 penetrated granodiorite before being stopped. The core was logged by Dr. Ulrich Kretschmar, who was later appointed Vice President of Exploration for Tradewinds Resources. Most of the kimberlite core recovered from the six holes was split and processed by alkali caustic fusion at Lakefield Research Ltd. in Ontario. The 641.3 kg of drill core yielded sixteen macro-diamonds (i.e. > 0.5 mm in at least one dimension).

The second drill program consisting of five vertical drill holes (96-10 to 96-14) was carried out during February to March 1996. A total of 887 m were drilled. From the recovered core, an 1873 kg sample was sent to Ashton Mining Ltd. Dense Media Separation processing facility in Vancouver, BC, to be processed for diamonds; 26 macro-diamonds were recovered. R.I. Barnett of London, ON, performed microprobe analysis on selected pieces of core and produced geochemical plots and backscattered electron images preserved on Polaroid (Timmins, 2002).

The last drilling was done in the summer of 1996, to provide a larger sample for diamond evaluation and to better define the geometry of the pipe. This final drill program consisted of seven holes (96-15 to 96-21), bringing the total number of holes drilled to 21 (including the discovery hole), and the total distance drilled to 5550 m. The holes were inclined and collared on

the southeastern shore of the bay. Both NQ and HQ drill cores were recovered. A 7.58 tonne sample was processed by Ashton Mining Ltd., and 48 macro-diamonds were recovered (Timmins, 2002).

Tradewinds Resources option was terminated following the 1996 summer drill program. Exploration work up to that point had demonstrated that the Drybones Bay pipe is a multi-phase, diamondiferous kimberlite body. However, a definitive diamond grade could not be established and no plans for production were brought to fruition. The project was eventually optioned to New Shoshone Ventures Ltd. in January 2002. They proposed further drilling and conducted an archeological assessment to satisfy the review process, but in April 2006, their application for a land use permit was rejected following the recommendations of the Mackenzie Valley Environmental Impact Review Board. The study material used in the present work consists of samples obtained from the 1995 and 1996 drill programs.

Exploration of the peripheral claims led to the discovery of kimberlite indicator minerals southeast of Drybones Bay at Mud Lake. In 2001, Smith optioned the Mud Lake property to Snowfield Development Corp. (Vivian, 2006). From 2002 to 2006, the Mud Lake area was explored with geophysical, geochemical, and biogeochemical methods, as well as diamond drilling. The exploration programs were designed to follow up on earlier surveys, which consisted of ground-based magnetic and horizontal loop EM surveys done in 1999, and various geochemical surveys done between 1999 and 2001 (Kerr and Smith, 2000; Dunn et al., 2001; Kerr et al., 2001).

The geophysical surveys available for the Mud Lake area consist of: an airborne magnetic and frequency-domain electro-magnetic survey flown in 2002; a ground penetrating radar survey conducted in 2003 by Aurora Geosciences; and a ground-based total magnetic field survey completed in 2004. The biogeochemical survey (Dunn et al., 2001) involved analyzing samples of bark from black spruce trees (*Picea Mariana*) for trace elements. The elements Rb, Cs, Zn, and Ni were considered to be kimberlite indicators, and tree bark from the Mud Lake area was found to have anomalous concentrations of these elements. Till samples, which were largely responsible for the Mud Lake kimberlite discovery, were collected in an area extending from Mud Lake northeast to Sipper Lake.

Drilling was carried out from 2002 to 2006; forty-four drill holes were collared and a total distance of 2907 m was drilled. The first discovery came in 2003, when kimberlite was

intersected along the base of a diabase dyke. Delineation drilling intersected the kimberlite along 110 m of strike, and identified numerous stringers forming a dyke complex with an areal extent of 700 × 300 m (Vivian, 2006).

Diamond grades were evaluated from drill core and a 500 tonne bulk sample that was excavated in 2007 and sent to De Beers Canada Exploration Ltd. for processing (MacFarlane et al., 2007). The results were not promising. The press release following the analysis of a 1044 kg sample of concentrates, representing the first 100 tonnes of material processed by De Beers, did not bother to report the number of diamonds recovered and instead speculated on deficiencies with the processing method that could be responsible for the paucity of diamonds (Snowfield Development Corp, 2008b). A subsequent press release announced that the 154 kg sample representing drill core material yielded only 23 micro-diamonds and 2 macro-diamonds, and no further work was planned as a result of the low diamond counts (Snowfield Development Corp, 2008a). Unfortunately, most of the drill core and main kimberlite body were consumed in the diamond evaluation process, leaving very little material for research. Only two hand specimens and a selection of polished thin sections, provided by B. Elliot (NWT Geological Survey), were available for the present work.

2.5 Previous work

Published work on Drybones Bay includes: summaries of the geology, diamond potential and exploration work (Kretschmar, 1995b; 1996); U-Pb dating of zircon (Heaman et al., 2003); geophysical studies using seismic and time-domain electromagnetic methods (Janse and Sheahan, 1995; Power, 1998; Kaminski and Oldenburg, 2012); and studies on the sub-cratonic mantle structure and the development of the Slave craton, based on mantle and lower crustal xenoliths, respectively (Carbno and Canil, 2002; Davis et al., 2003a). There have been no previous detailed studies of the petrography, mineralogy or geochemistry of the Drybones Bay rocks, whereas the Mud Lake dyke has not been studied at all, and its age or relation to the Drybones Bay body have not been determined.

Age dating of the Drybones Bay kimberlite (Heaman et al., 2003) was done using zircon macrocrysts selected from caustic fusion residues. Thirteen grains from three drill holes (7 from hole 95-7, 5 from hole 95-8 and 1 from hole 95-9) were analyzed for U-Pb isotopes using thermal ionization mass-spectrometry. The zircon from hole 95-7 had low U (3.0–9.9 ppm) and

Th (0.8–13.6 ppm) and Th/U ratios between 0.25 and 0.36. All zircon analyses from that sample were discordant (11–35%) and yielded a relatively imprecise upper intercept date of 472 ± 24 Ma. The zircon from holes 95-8 and 95-9 had low U (4.0–8.3 ppm) and Th (0.9–3.6 ppm) and intermediate Th/U ratios (0.33–0.68). Many of the grains were discordant (up to 24%); however, the two most precise analyses were concordant and yielded an age 441.8 ± 0.8 Ma (see Chapter 7 for additional details).

The seismic refraction survey (Power, 1998) consisted of three 115 m lines, situated on the western, central, and eastern parts of the crater, near holes 95-9, 95-7, and 96-12, respectively. The survey detected high- and low-velocity reflectors, interpreted as fresh and weathered kimberlite. The seismic velocity of the fresh kimberlite is approximately 4300 m/s, which is comparable to the velocity of PK from Fort à la Corne (4300 to 4700 m/s), whereas the weathered kimberlite has a seismic velocity of 1900 to 2200 m/s. The kimberlite has a definite velocity contrast with the surrounding country rock, which has a seismic velocity of 5400 m/s. Low-velocity returns were recorded on all three lines, however the high-velocity refractor was only detected on the eastern line (above unit KE). The absence of a high-velocity refraction in the western and central parts of the crater may be due to the brecciated nature of the contact (Power, 1998).

Chapter 3: Methodology

3.1 Sample collection and preparation

The samples used in this study were provided by the Northwest Territories Geological Survey and represent essentially all of the available material from the Drybones Bay and Mud Lake exploration programs. A small portion of the Drybones Bay drill core did not have proper provenance information and hence was not sampled. Representative drill core samples were chosen for thin sections and geochemical analysis. The Mud Lake samples consist of previously prepared set of thin sections and two rock samples used for the preparation of thin sections and whole-rock geochemical analysis. Polished thin sections were prepared by Vancouver Petrographics. The sample numbers, depth, drill hole and lithology are summarized in Table 3.

Note: sample DB-16-01, representing unit KC, was not initially available for this study. The receipt and analysis of this sample occurred at too late a juncture for the results to be incorporated into this work, however it is still listed in Table 3 for a matter of record.

3.2 Whole-rock geochemistry

Whole-rock geochemical analyses were done by the Bureau Veritas laboratory in Vancouver, BC. The samples were pulverized and mixed with a lithium metaborate/tetraborate flux and fused in a furnace. The cooled beads were dissolved in ACS grade nitric acid and analyzed by inductively coupled plasma mass-spectrometry (ICP-MS) to determine the concentration of major- and trace-elements. Aqua regia digestion was used to measure the concentrations of Cu, Pb, Zn, Ni, As, Cd, Sb, Bi, Ag, Au, Hg, Tl and Se. The pulverized samples were digested with a modified aqua regia solution composed of equal parts concentrated HCl, HNO_3 and H_2O for one hour in a heating block then analyzed by ICP-MS. Loss on ignition (LOI) was determined by igniting a split sample then measuring the weight loss. Total carbon and sulfur were determined using a LECO infrared carbon-sulfur analyzer. The following reference materials were used by Bureau Veritas for quality control: GS311-1, GS910-4, DS10, OREAS45EA, SO-18 and SO-19.

Table 3 Catalogue of Drybones Bay samples used in this study.

Hole	Sample #	Depth (m)	Lithology	Thin section	Whole-rock analysis
95-5	DB-05-02	126.5	K-1	x	x
	DB-05-03	133.8	K-1	x	
	DB-05-04	158.1	K-3	x	x
	DB-05-07	192.1	K-7	x	x
95-8	DB-08-02	132.3	K-8	x	
	DB-08-04	175.6	K-8	x	
	DB-08-05	184.0	K-8	x	x
	DB-08-09	205.0	K-8	x	x
	DB-08-11	219.4	K-8	x	x
	DB-08-14	237.5	K-8	x	x
	DB-08-16	241.0	K-8	x	x
96-16	DB-16-01	283.9	KC		
96-19	DB-19-02	285.5	KE	x	
	DB-19-04	298.0	KE	x	x
	DB-19-05	350.0	KE	x	x
	DB-19-06	404.0	KE	x	x
96-10	DB-10-01	105.2	K-1	x	x
	DB-10-03	115.3	K-1	x	x
	DB-10-05	127.4	K-1	x	
	DB-10-06	149.4	K-2	x	x
	DB-10-07	151.0	K-2	x	x
	DB-10-09	158.2	K-3	x	x
	DB-10-10	170.5	K-3	x	x
	DB-10-13	182.1	K-6	x	x
	DB-10-14	182.7	K-6	x	
	DB-10-16	187.5	K-6	x	x
	DB-10-17	203.7	K-7	x	
	DB-10-18	204.0	K-7	x	x

3.3 Petrography

The polished thin sections were studied using optical microscopy in polarized transmitted and reflected light, back-scattered electron (BSE) imaging, cathodoluminescence (CL) imaging and energy-dispersive X-ray spectrometry (EDS). The major constituent minerals and their textural characteristics were identified optically using a Nikon EPOL-600 microscope. The initial petrographic analysis was followed up with a detailed examination of the sections with a Cameca SX-100 electron microprobe equipped with a Princeton Gamma-Tech Prism 2000 EDS detector, to overcome the limited spatial resolution of the optical microscope and to identify minerals that cannot be reliably characterized based on their optical properties. Small-scale features and cryptic textures were documented with BSE images, and the identity of all constituent minerals

was confirmed on the basis of their characteristic X-ray emission spectra using EDS. The chemical homogeneity of zircon grains used for the geochronological study was confirmed using BSE and CL imaging on the Cameca SX-100. Coloured CL images, used to study the relationship of carbonate phases, were acquired with a Reliotron VII CL instrument (Relion Industries), operated at 8.5 eV and 400 mA. Optical photomicrographs presented in this work were captured in plane-polarized light (PPL), unless otherwise noted as being taken cross-polarized light (XPL).

3.4 Electron-microprobe analysis

The major-element compositions of the constituent minerals in the Mud Lake and Drybones Bay rocks were measured by wavelength-dispersive spectrometry (WDS) using a Cameca SX-100 automated electron microprobe operated at 15 kV and 20 nA with a beam size of 1-10 μm. The spectral lines, detectors, and standards used for each mineral or mineral group are listed in Appendix I.

3.5 Laser-ablation inductively coupled plasma mass-spectrometry

The trace element and isotope abundances were measured by laser-ablation inductively coupled plasma mass-spectrometry (LA-ICP-MS) using a 213-nm Nd-YAG Merchantek laser connected to a Thermo Finnigan Element 2 sector-field mass-spectrometer. The trace-element analyses were performed in situ using spot ablation. Areas suitable for analysis were selected on the basis of reflected-light, BSE, and CL images. Laser ablation was performed in Ar and He atmospheres. The rate of oxide production was monitored during instrument tuning by measuring the ThO-to-Th ratio and kept below 0.2%. The LA-ICP-MS operating and data-acquisition parameters, the isotopes chosen for trace-element analysis, and the lower limits of detection are listed in Appendix I. For all trace-element measurements, synthetic glass standard NIST SRM 610 (Norman et al., 1996) was employed for calibration and quality control. The concentrations of the following elements determined by WDS were used as internal standards: Si (for zircon, phlogopite, and garnet), Ti (for ilmenite), and Cr (for spinel-group minerals). All analyses were performed in a low- resolution mode (~300) using Pt skimmer and sample cones. Trace-element data reduction was done using Iolite for the Igor Pro software platform.

3.6 Geochronology

For U-Pb isotope geochronology, U, Th, Pb and Hg data were acquired in a time-resolved mode for the following isotopes: ^{202}Hg, ^{204}Pb, ^{206}Pb, ^{207}Pb, ^{208}Pb, ^{232}Th, ^{235}U, and ^{238}U. Zircon standard GJ-1 (609 Ma; Jackson et al., 2004) was employed for calibration. A natural zircon standard, UQ2-12 (1135 Ma), was used as a secondary standard. In order to monitor the instrument induced mass bias and laser induced element fractionation, four measurements of the calibration standard (GJ-1) were performed, two at the beginning and two at the end of each analytical session. The UQ2-12 standard was run at the start and the end of each analytical session, yielding accuracy and precision levels near 2%. The data reduction was done using the VisualAge DRS procedure (Petrus and Kamber, 2012) in the Iolite software. A concordia diagram showing 2σ error ellipses was produced using Isoplot/Ex 3.75 (Ludwig, 2012).

Chapter 4: Petrography

4.1 Mud Lake

The kimberlite rocks at Mud Lake are competent and greenish-grey in appearance with pronounced hematite staining (Figure 8a). Petrographically, they are characterized by macrocrystic and segregation textures. The macrocrysts comprise (in order of decreasing abundance): major serpentinized olivine; major phlogopite; and minor ilmenite, spinel, garnet, and, zircon, in a dolomite-serpentine matrix (Figure 9a). Fine-grained groundmass minerals include spinel, phlogopite, dolomite and apatite. In addition to primary dolomite laths, the rocks comprise a variety of secondary carbonates replacing olivine and ilmenite, filling fractures, and occurring in association with serpentine in segregations. Other late-stage minerals include serpentine (after olivine), chlorite (after phlogopite), rutile (after ilmenite) and baddeleyite (after zircon). Crustal xenoliths of diabase are common, and have round shapes resulting from digestion by the host magma. Based on petrography, the Mud Lake rocks can be classified as kimberlite sensu stricto (i.e. Group I kimberlite; Le Maitre et al., 2002). However some samples bear resemblance to the dolomite carbonatite from Wekusko Lake (Manitoba), which was initially misclassified as kimberlite; thus further evidence to support their provenance is presented in Chapters 5 and 6, along with the petrographic descriptions and chemistry of the constituent minerals.

4.2 Drybones Bay

The Drybones Bay kimberlite comprises a variety of rock types, which are outlined along with their structural relationships in Chapter 2. In general, the rocks are fragmented/volcaniclastic and characterized by macrocrystic and magmaclastic textures. The macrocryst assemblage comprises (in decreasing order of abundance): major serpentinized olivine; major phlogopite; minor ilmenite, spinel, and garnet; and trace zircon. Chromium diopside is noted in the core logs, but was not observed in this study. Fine-grained groundmass minerals comprise euhedral-to-subhedral serpentine pseudomorphs, poikilitic phlogopite, euhedral spinel, perovskite and apatite.

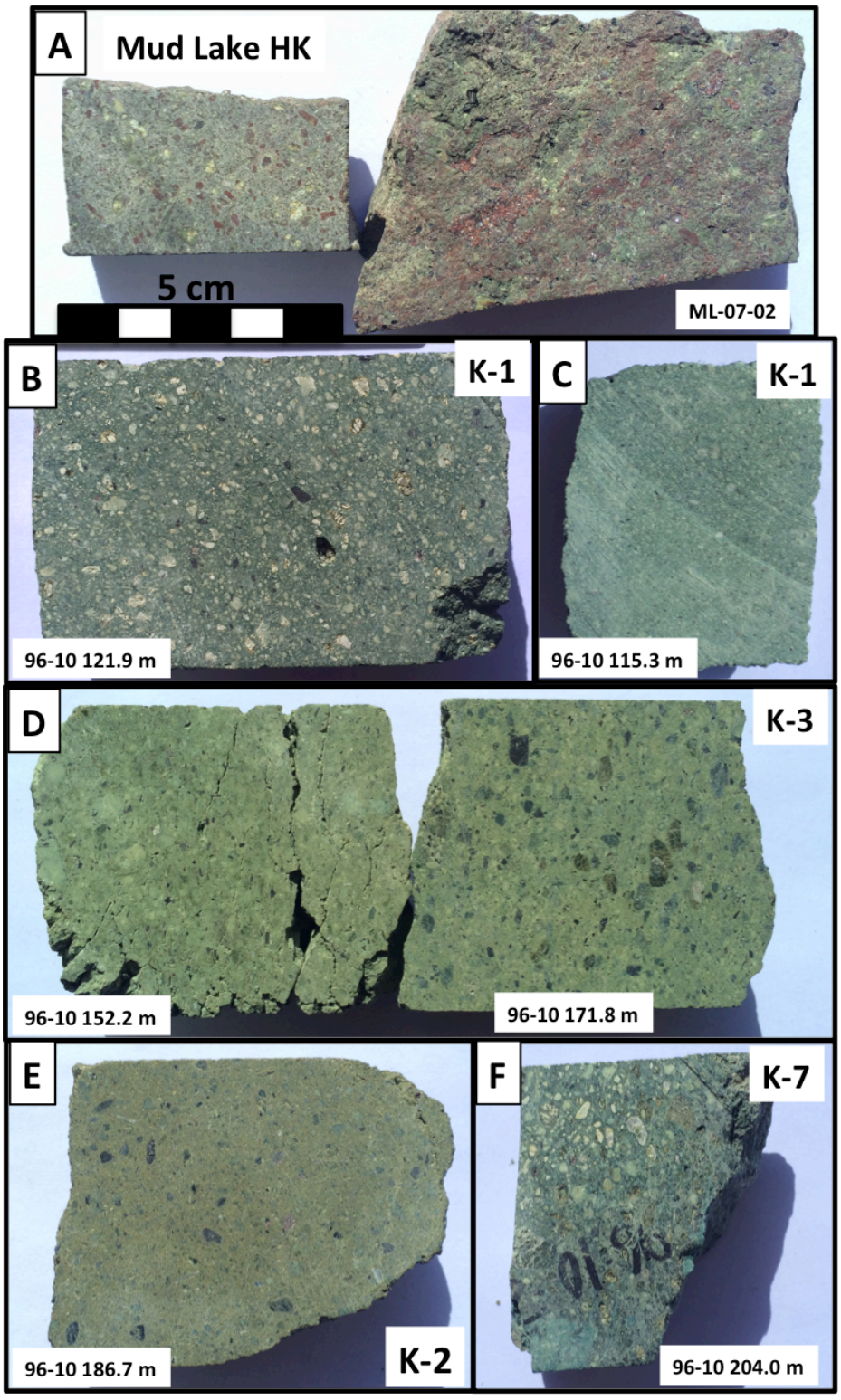

Figure 8 Photographs of Mud Lake and Drybones Bay rocks: (A) Mud Lake HK; (B-J) Drybones Bay; (B) medium- and (C) fine-grained VCK; (D) clay-rich VCK showing desiccation cracks when dried; (E) well indurated VCK with an olive drab matrix; (F) thin basal unit with unusual blue hues and abundant serpentine veining.

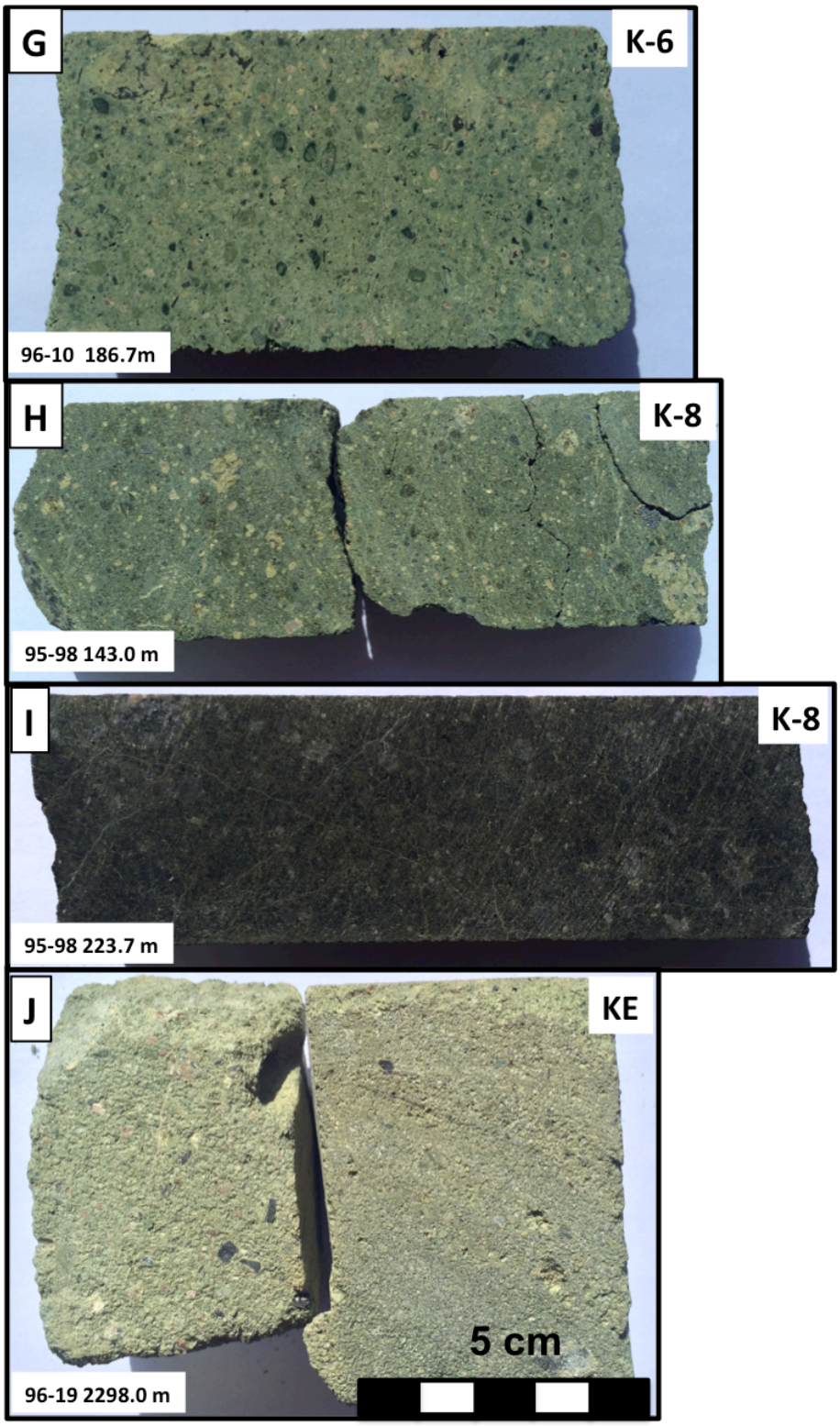

Figure 8 continued… (G) Granitic xenolith-rich VCK; (H) top of hole 95-08 resembling other VCK units; (I) competent and dark coloured rock with thin carbonate veins make up the bulk of hole 95-08, and is distinct from other lithologies; (J) light coloured, friable rock composed predominantly of rounded quartz sand.

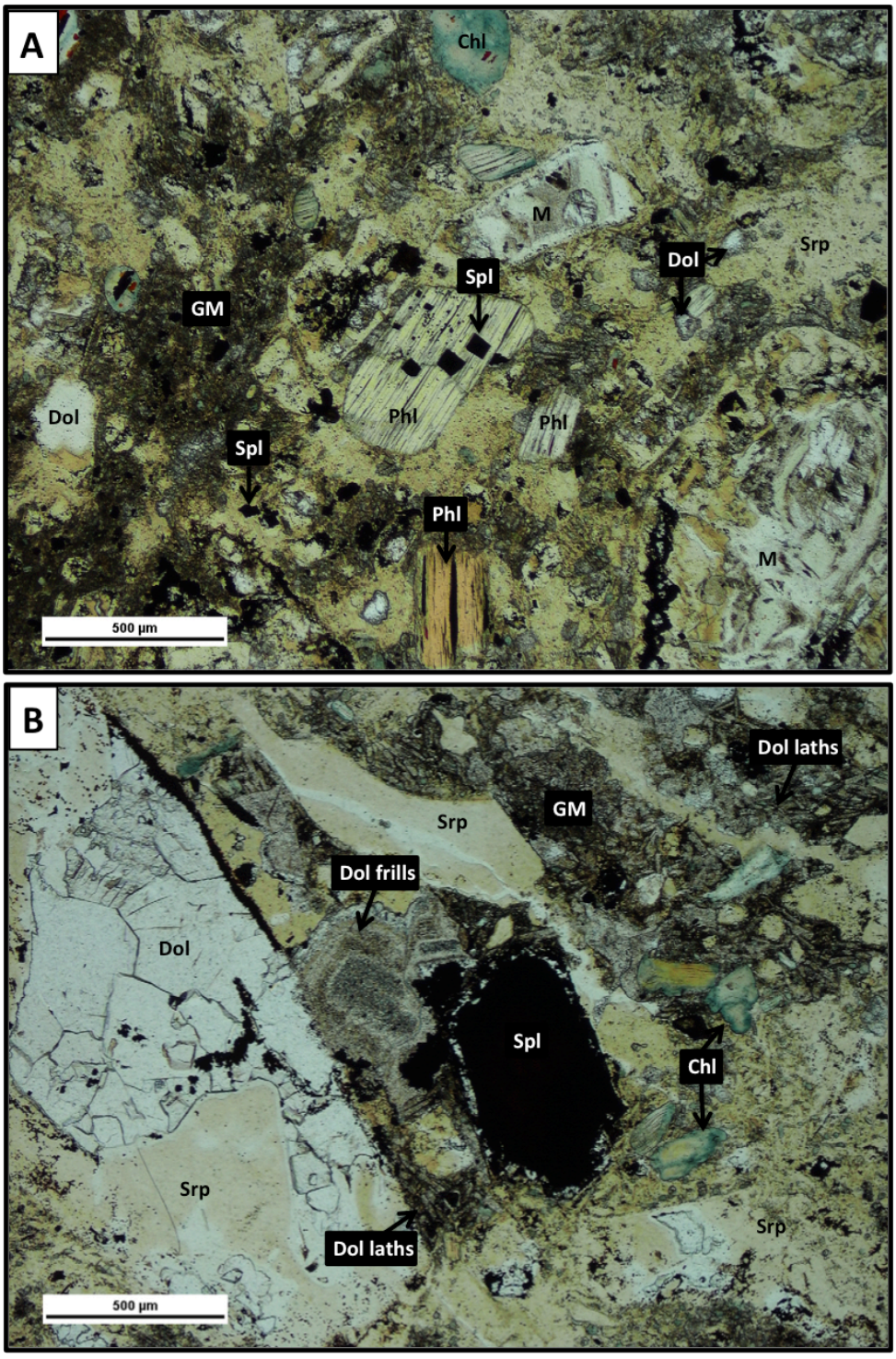

Figure 9 Petrography of Mud Lake HK: (A) fresh and chloritized phlogopite macrocrysts and pseudomorphed olivine macrocrysts in a serpentine-dolomite segregated mesostasis; (B) diverse textural varieties of dolomite, including blocky segregations, lacey frills, and primary laths (rhombohedral dolomite not pictured; see text for details). Chl = chlorite; Dol = dolomite; GM = groundmass; M = (pseudomorphed) olivine macrocryst; Phl = phlogopite; Spl = spinel; Srp = serpentine. Photos captured in PPL.

The replacement minerals comprise serpentine (after olivine), carbonates (after olivine and ilmenite), chlorite (after phlogopite), rutile (after ilmenite) and baddeleyite (after zircon). The interstitial matrix is composed of serpentine, carbonate, and variable amounts of disaggregated clay sediment in some samples.

Compound clasts include crustal xenoliths, mantle xenoliths, juvenile magmaclasts, and autoliths. Crustal xenoliths derived from the Defeat granodiorite host rock are the most abundant; they range in size from cobbles to disaggregated crystal fragments, but are typically pebble-sized. Other crustal contaminants include (disaggregated) sedimentary material, diabase, supracrustal rocks (most likely of the Yellowknife Supergroup), and lower crustal xenoliths of gneiss. Large mantle xenoliths of peridotite and eclogite are present, but not well represented in the thin sections. Carbonate-phlogopite aggregates containing euhedral zircon with oscillatory zoning occur in some samples; these clasts are of unknown provenance and could represent mantle xenoliths or perhaps cumulate autoliths. A variety of juvenile magmaclasts are observed in Drybones Bay, they are described below using the terminology of Webb (2006). Aggregates of super fine-grained phlogopite with spinel inclusions are interpreted as HK autoliths, and resemble the poikilitic groundmass phlogopite from Mud Lake.

The petrography of each unit is described in detail below. Important petrographic features are summarized in Table 4. Descriptions of important rock-forming minerals are presented along with mineral chemistry in the following chapters. The textural-genetic classification and genetic/process interpretation of the Drybones Bay rock types are discussed in Chapter 8.

4.2.1 Unit K-1

The K-1 rocks have a buff appearance with a pale green matrix and white crystals of serpentinized olivine (Figure 8b,c). The unit has well defined beds that grade on a scale of meters (Kretschmar, 1996) from coarse-grained and clast-supported to very fine-grained and variably matrix- to clast-supported. Fine-grained layers have subordinate bedding defined by sub-parallel alignment of phlogopite and elongate crystal fragments (Figure 10b).

Alteration is strong but not uniform: in coarse-grained beds (Figure 10a) olivine is completely pseudomorphed to serpentine and exhibit thin secondary rims of pale green serpentine, whereas the fine-grained beds (Figure 10b) vary from having olivine that is completely replaced by carbonate to samples that are uniformly altered to serpentine and oxides.

Phlogopite varies from chloritized (coarse beds) to fresh (fine beds). Ilmenite macrocrysts are fresh. Granodiorite xenoliths are disaggregated and intensely sericitized.

Table 4 Summary of petrographic features of the Drybones Bay rocks.

	K-1	K-2	K-3	K-6	K-7	K-8	KE
Appearance	pale green fragmented	olive drab uniform	pistachio fragmented	pistachio fragmented	teal fragmented	dark green uniform	light green sandy
Structure							
Massive	-	+	+	+	n.a.	+	-
Layered	+	+	+	+	n.a.	-	+
Graded	+	-	-	-	n.a.	-	+
Veined	-	-	-	-	+	+	-
Textures							
Overall grain size	fine	medium	medium	fine	medium	medium	v.f.–f.
Clast-supported	±	+	-	-	±	+	+
Matrix-supported	±	-	+	+	±	±	-
Carbonate segregations	-	-	-	-	-	+	-
Compound clasts							
Cored lapilli	+	+	±	±	±	±	+
Uncored lapilli	-	-	-	-	-	±	+
Pelletal lapilli	-	+	-	-	-	+	-
Autoliths	-	HK	-	-	TK	HK, VCK	-
Xenoliths							
Size	small	small	small	small	small	medium	micro
Abundance	low	low	low	high	low	low to int.	high
Sedimentary	-	-	-	-	-	+	+
Metasedimentary	-	-	-	-	-	+	-
Diabase	+	-	-	-	-	+	-
Granitic	+	+	+	+	+	+	+
Peridotite	+	+	+	+	+	+	-
Eclogite	+	+	+	+	+	+	-
Carbonatitic	+	-	-	-	-	-	-
Olivine macrocrysts							
Size	f.–med.	fine	v.fine	v.fine	med.	med.–c.	fine
Abundance	high	high	intermediate	intermediate	intermediate	high	low
Texture (roundness)	sub-ang.	sub-round	angular	sub-round	sub-round	round	round
Matrix							
Serpentine	+	+	±	±	+	+	+
Kimberlitic ash	+	+	±	±	±	-	n.a.
Unconsolidated mud	±	-	+	+	±	-	+

Size and abundance descriptors follow the classification scheme of Scott Smith et al. (2013). v.f. = very fine; f. = fine; med. = medium; c. = coarse; int. = intermediate; n.a. = not available.

Olivine forms broken, sub-angular macrocrysts (0.5–4.0 mm across), rare euhedral phenocrysts (0.12–0.25 mm) and comminuted angular fragments. Phlogopite crystals (0.2–2.5 mm) are broken and deformed in coarse beds; in fine beds, they are intact and have rounded margins. Granodiorite xenoliths are smaller and less abundant than in other units, and lower crustal and mantle xenoliths are scarce. Two types of juvenile clasts are observed:

(1) Sub-equant, sub-rounded, sub-irregular, with a single, coherent, super-thin (0.2–0.5 mm) rim surrounding a core. The cores consist of irregular, very fine-grained olivine and lithic

fragments. The rims are complete, asymmetrical, non-vesicular and do not conform to irregularities in kernel shape (Figure 11a).

(2) Rounded, smoothly curved, with a single, clastic, very-thin (0.5–1.0 mm) rim on a core grain. The cores consist of medium- to coarse-grained macrocrysts and xenoliths. The clastic rims are incomplete, asymmetrical and composed of super fine-grained olivine and minor phlogopite in a cryptocrystalline matrix (Figure 11b).

The inter-clast matrix is composed of ultra fine-grained (<0.125 mm) serpentine, minor amounts of unconsolidated mud, and ash-sized patches of brown material with hazy margins interpreted as kimberlitic ash.

4.2.2 Unit K-2

The K-2 rocks are more competent than the units above and below (K-1 and K-3), have a distinct olive drab matrix, and appear fresher and less fragmented due to the olivine having a similar colour to the matrix (Figure 8e). The unit consists of a single bed of massive clast-supported medium-grained material. Olivine macrocrysts and phenocrysts are round to sub-round and serpentinized (Figure 10c). Ilmenite macrocrysts are abundant and fresh. Xenoliths are predominantly small, disaggregated fragments of granodiorite; other varieties of xenoliths are scarce. Two types of juvenile clasts are present (Figure 11c):

(1) Sub-equant, rounded, and sub-irregular in morphology, with a single, coherent, ultra-thin, symmetrical rim around a core. The cores are very fine-grained irregular fragments and often have diffuse boundaries with their rims.

(2) Incomplete juvenile clasts consisting of a larger fragment with a rounded, irregular curvilinear, thin to very-thin clastic rim. The rims are composed of very fine-grained crystals of olivine ± phlogopite ± lithics in an unresolvable matrix; large protruding grains give rise to the irregular morphology of the rim.

Other compound clasts include aggregates of ultra fine-grained phlogopite and spinel (Figure 11e,f), which are interpreted as HK autoliths (see Section 8.3.1). The matrix is composed of serpentine and kimberlitic ash (slightly darker patches with diffuse margins, Figure 10c). Clay minerals and carbonates are scarce in this unit.

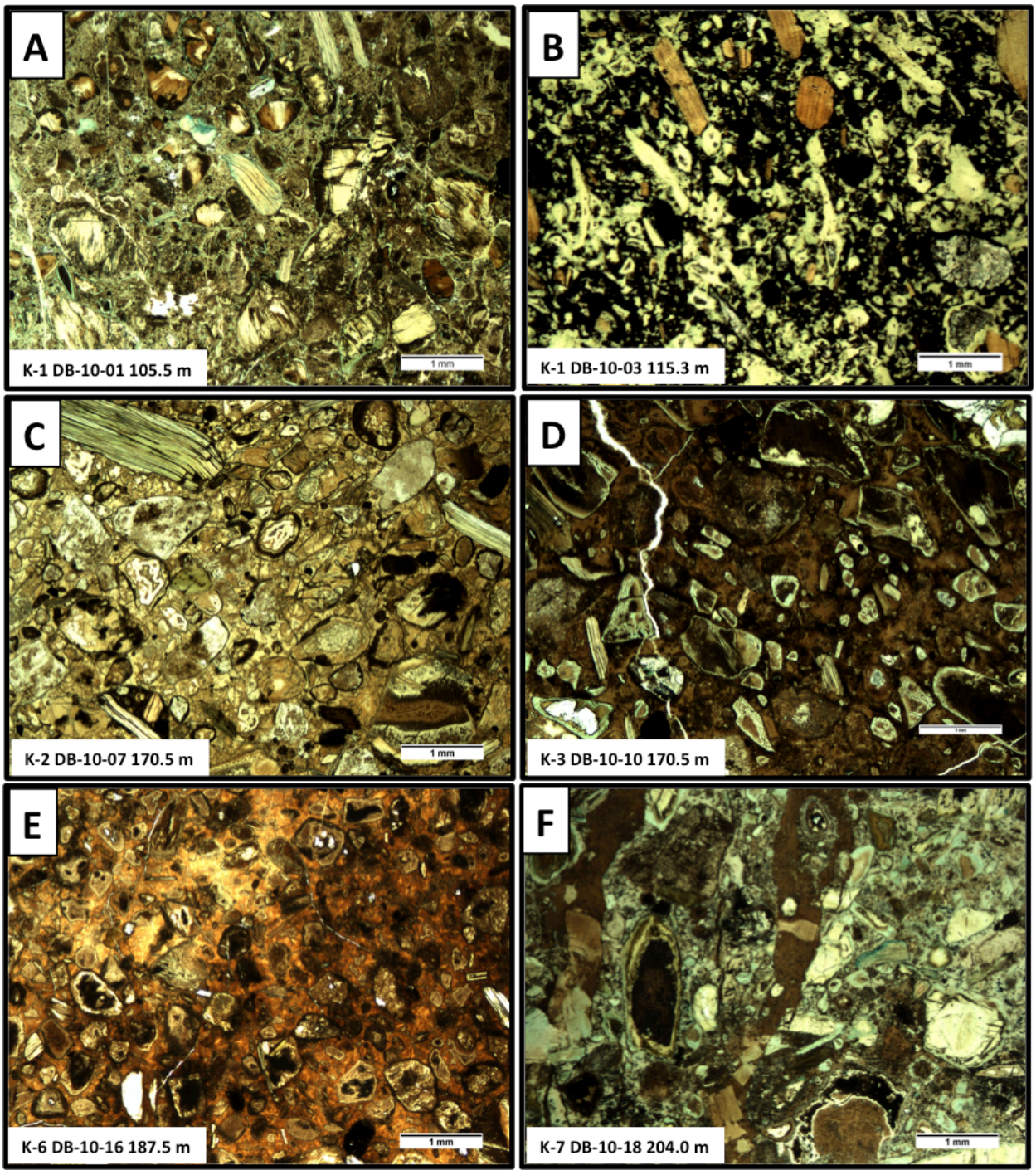

Figure 10 Petrography of Drybones Bay kimberlite: (A) medium-grained K-1 composed of broken macrocrysts and chloritized phlogopite with thin green reaction rims in a serpentine matrix, compared to (B) fine-grained K-1 with fresh phlogopite, euhedral olivine (pseudomorphed) in an opaque matrix, note the parallel alignment of elongate crystals; (C) K-2 macrocrysts and magmaclasts (lower left) in a serpentine matrix; (D) K-3 broken angular macrocrysts with green reaction rims supported by a dark, mud-rich matrix; (E) K-6 abundant comminuted granitic xenoliths in a dark serpentine matrix with mud; (F) poorly-sorted kimberlite with crystal choked veins of serpentine. Photos captured in PPL.

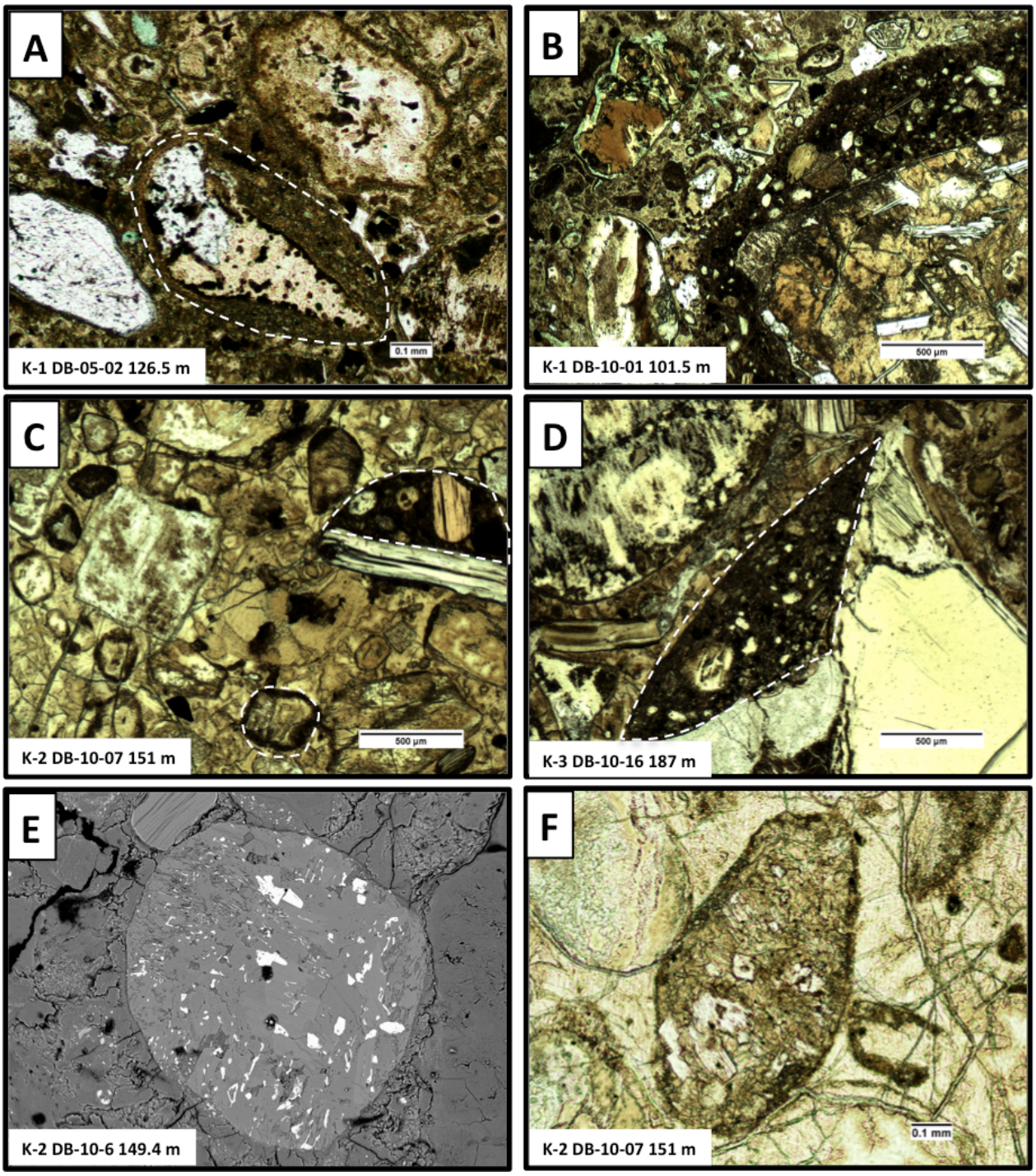

Figure 11 Petrographic features of Drybones Bay kimberlite: (A) juvenile magmaclast with a super-thin, coherent rim, in K-1; (B) juvenile magmaclast with a very-thin, clastic rim, in K-1; (C) juvenile magmaclasts with a very-thin, clastic rim, in K-2; (D) abraded juvenile magmaclast with part of a clastic rim preserved in a concavity, in K-3; (E,F) BSE image and photomicrograph of a compound clast composed of phlogopite and groundmass spinel, interpreted as possible HK autoliths, in K-2. Magmaclasts are marked with dashed lines in A, C and D to enhance clarity. Optical photos captured in PPL.

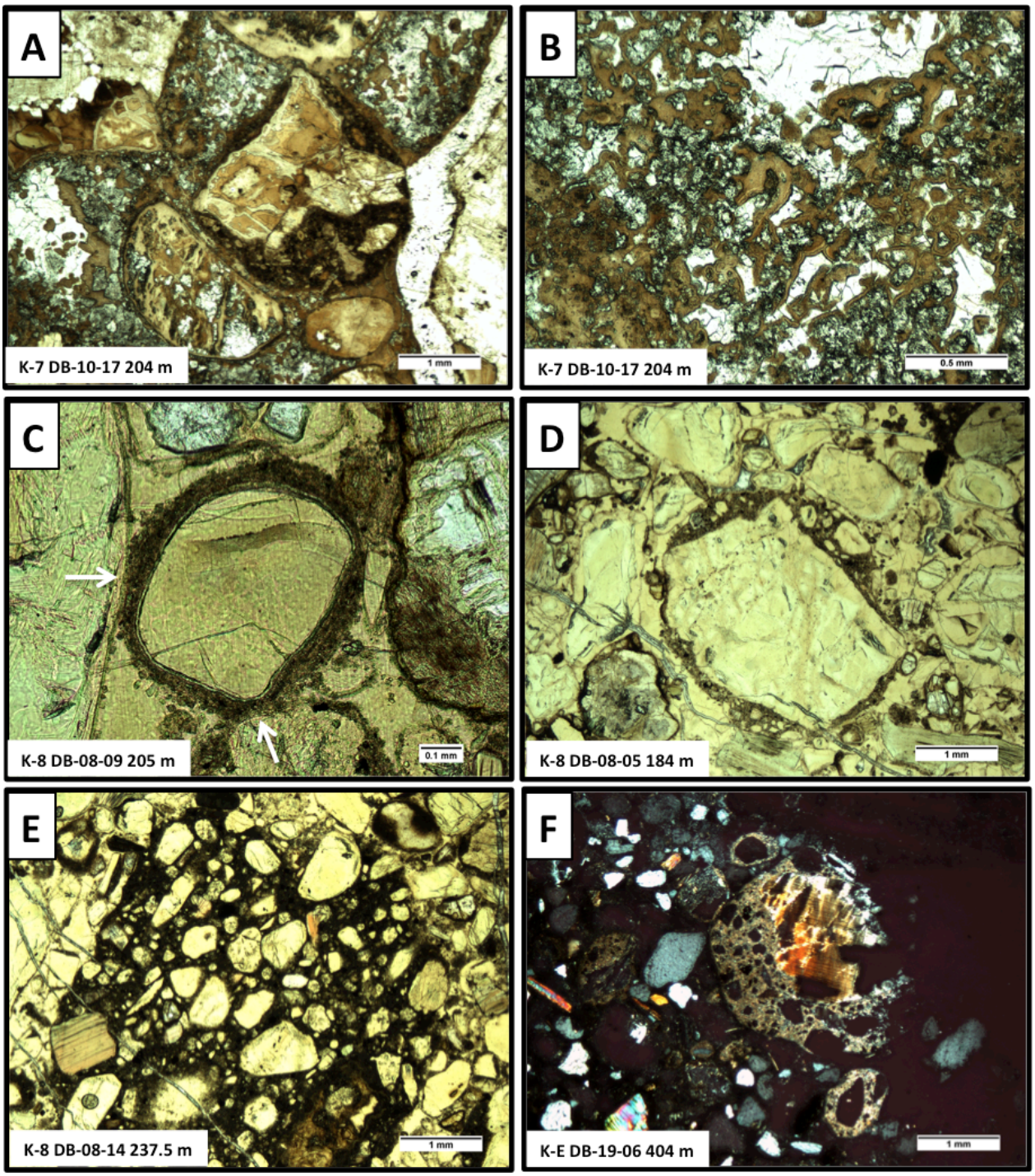

Figure 12 Petrographic features of Drybones Bay kimberlite: (A) juvenile magmaclasts with a clastic rim next to a rounded olivine macrocryst in a carbonate-serpentine matrix, in K-7; (B) magnified view of the carbonate-serpentine matrix, in K-7; (C) juvenile magmaclasts with an ultra thin, coherent rim, interpreted as pelletal lapilli, in K-8, note the plastic deformation at grain contacts (white arrows); (D) juvenile magmaclasts with a super-thin, compound rim, in K-8; (E) compound clast in K-8 composed of parallel aligned grains in a dark matrix, note the contrast in clast size and matrix composition with the host rock; (F) well-preserved magmaclasts with clastic rims, in KE (XPL).

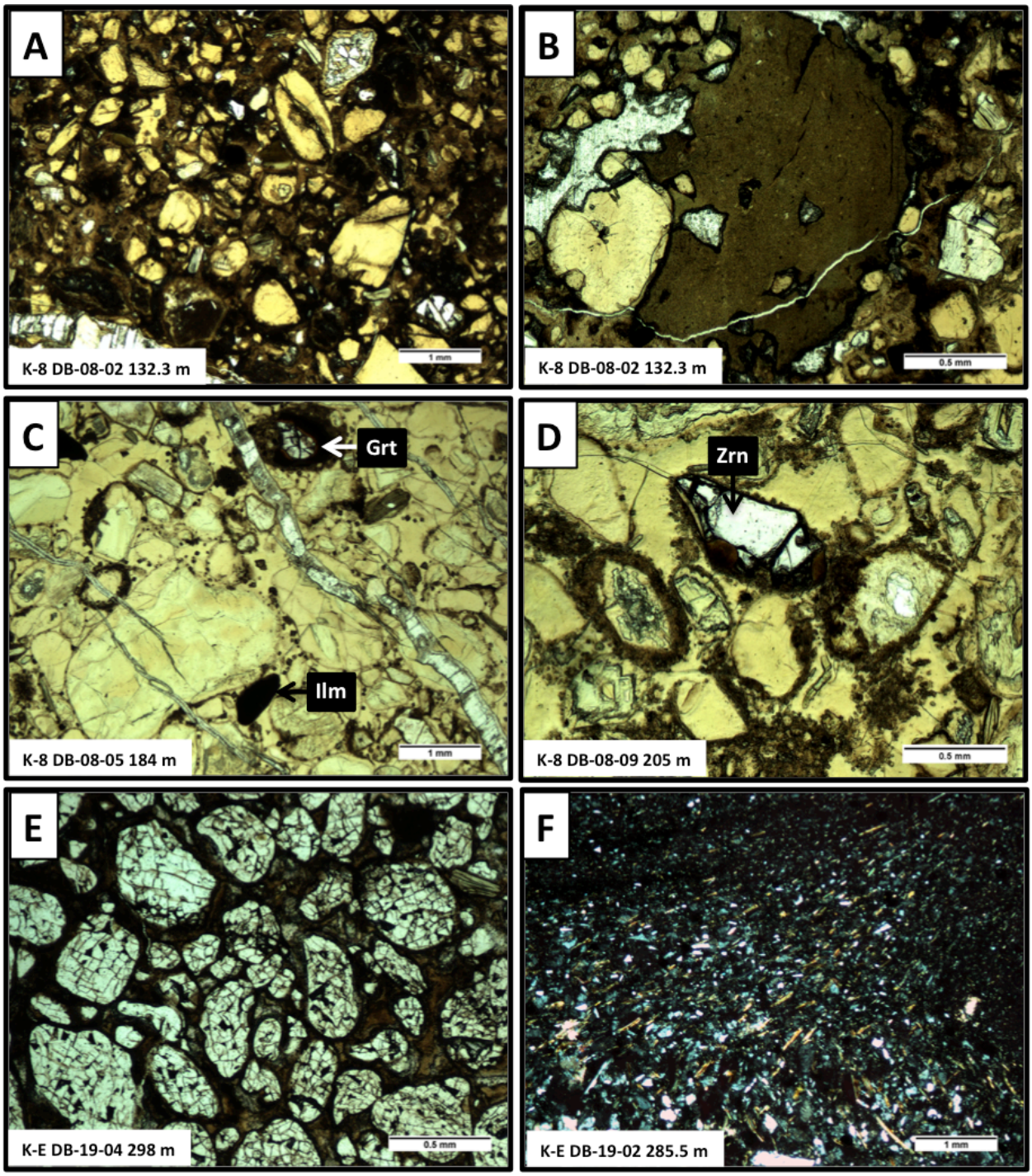

Figure 13 Petrography of Drybones Bay kimberlite: (A) overview of the volcaniclastic material at the top of K-8 shows broken olivine crystals in a dark, mud-rich matrix; (B) an exotic siltstone xenolith from the same unit; (C,D) below 175 m unit K-8 appears very different, and is characterized by rounded macrocrystic olivine pseudomorphs and pelletal lapilli-like magmaclasts in a mud-free serpentine mesostasis; (E) shattered quartz grains in a dark, mud-rich matrix, from KE; (F) flow textures in KE defined by the alignment of phlogopite crystals. Photos A-E captured in PPL; photo F captured in XPL.

4.2.3 Unit K-3

These rocks have greenish-grey olivine crystals and pistachio-green matrix that is soft, friable, absorbs water, and cracks upon desiccation (Figure 8d). The unit consists of a thick bed of poorly sorted, variably clast- to matrix-supported, fine- to medium-grained material (Figure 10d). Alteration is strong, pervasive, and similar to coarse beds in K-1, except that ilmenite is partially replaced with rutile. Olivine macrocrysts are broken, angular to sub-rounded and pseudomorphed to serpentine with a turbid appearance ± carbonate; euhedral olivine phenocrysts are rare, small crystals appear to be derived from larger fragments. Zircon macrocrysts are large and relatively abundant. Juvenile clasts are similar to the very-thin rimmed clastic variety described in K-1, but are abraded such that the rims are preserved mostly in concavities of the kernel grain (Figure 11d). The tendency of samples to absorb water and crack upon drying and the dark brown appearance of the matrix in transmitted light indicate that these samples contain considerable amounts of clay minerals.

4.2.4 Unit K-6

The K-6 rocks are dark green-grey with white olivine pseudomorphs in hand sample, and are relatively soft, but less friable than K-3 (Figure 8g). The unit is characterized by abundant country-rock xenoliths and fine-grained olivine fragments supported by a mud-rich matrix (Figure 10e). Olivine is pseudomorphed to serpentine that is dark brown in transmitted light, and is rimmed by a later generation of serpentine with a pale appearance, like in K-1; the macrocrysts are sub-round to sub-angular, whereas smaller crystals/fragments are sub-angular to angular. Large ilmenite macrocrysts are rimmed with rutile, while smaller grains are sometimes completely pseudomorphed to rutile. Granodiorite xenoliths are abundant, typically 1–2 cm across and rounded. Altered mantle xenoliths and bedded siltstone xenoliths are present. Juvenile clasts are as described in K-3, but less abundant. The matrix is also similar to that of K-3, but localized areas appear less inundated with clay.

4.2.5 Unit K-7

K-7 is described as a thin basal unit overlying the host granodiorite. The two samples of this unit are dissimilar. DB-10-18 is considered more representative based on descriptions in the core log (Kretschmar, 1995a), this sample is characterized by the chaotic distribution of broken macrocryst in a peculiar blue-green matrix (Figure 8f), and teal-coloured veins (~1 mm thick) of

serpentine. Serpentinized olivine and phlogopite macrocrysts are fine-grained and sub-angular. The serpentine veins are often clogged with relatively coarse material (Figure 10f). Overall this unit is similar to the coarser-grained variety of K-1 in terms of component size, distribution, alteration, and the fragmented texture. Juvenile magmaclasts are cored and have very-thin clastic rims (as described in K-1).

In contrast, sample DB-10-17 has (macroscopically) grey-coloured clasts in a light grey carbonate-rich matrix. Olivine crystals are round and pseudomorphed to serpentine and carbonate. Juvenile magmaclasts are of the clastic very-thin skinned variety seen in the previous sample and in unit K-1 (Figure 12a). Aggregates of carbonate and serpentine resembling globular segregation textures are prominent in this sample (Figure 12a,b). Given the contextual relationship with the magmaclasts, it is likely that these apparent carbonate-silicate segregations developed as a secondary texture, and are not related to a fluidization process thought to be involved in the formation of HK–TK transitional facies rocks, which are characterized by globular segregations (Field and Scott Smith, 1999).

4.2.6 Unit K-8

Two texturally distinct varieties of kimberlite are present in hole 95-8. The upper portion of the hole, down to a depth of 175 m, resembles the fragmented mud-rich units K-3 and K-6 (Figure 8h). The rocks are composed of fine- to medium-grained broken serpentinized olivine crystals in a dark brown, mud-rich matrix (Figure 13a). The serpentinized olivine is pale yellow in transmitted light, uniform, and lacks the rims seen in some other units (Figure 13a). Exotic siltstone xenoliths present in these samples are a probable source of the dark brown matrix material (Figure 13b). The transition between the mud-rich fragmented rocks sampled to a depth of 175 m, and the texturally distinct kimberlite occurring at 184 m and below, is described as gradational in the core logs (Kretschmar, 1995a), but no samples representing this contact were available for examination in this work.

Below 184 m, the rocks are significantly different from all of the previously described units: hand samples are very dark green, dense, have abundant thin (~0.05 mm) carbonate veins, and appear well crystallized (Figure 8i). The rocks are variably clast- to matrix-supported, dominated by serpentinized olivine macrocrysts, and contain a distinct type of juvenile clasts set in an unadulterated serpentine matrix (Figure 13c,d). The olivine macrocrysts are medium-grained (2–4 mm across), rounded, unbroken, and replaced by serpentine that has a wavy texture

and is more birefringent than in other units. Serpentinized groundmass olivine is common, and recognized by its euhedral habit fine grain size (0.25–1 mm). The inter-clast matrix is composed of ultra fine-grained (<0.125 mm) microlites of acicular apatite and an unidentified equant mineral set in a serpentine mesostasis. The matrix is free of surficial sediment or ash, and lacks carbonate. Crustal xenoliths comprise granodiorite as well as diabase and (meta)sandstone not observed in other units. The xenoliths tend to be sub-rounded to sub-angular, and larger and fresher than in the other units. Locally the abundance of xenoliths may be high enough to qualify as a breccia (> 15 vol.%).

The most abundant type of juvenile clasts is sub-elongate to sub-equant, well-rounded, smoothly curved, non-vesicular and cored mainly with very fine-grained olivine pseudomorphs. The rims of these magmaclasts are ultra-thin (<0.2 mm), uniform (i.e. non-clastic), complete, symmetrical, have a sharp boundary marking the contact with the kernel, and conform to irregular shapes of the kernel. The rims are composed of microcrystalline phlogopite, serpentine, opaque oxides and acicular apatite crystals, which protrude into the surrounding inter-clast matrix (Figure 12c; Figure 13d). Plastic deformation of the rim can be seen at grain contacts (Figure 12c, white arrows), indicating that the rim formed on solid grains in a crystal-liquid system, rather than by post-crystallization alteration. These ultra-thin rimmed juvenile clasts are ubiquitous throughout K-8 and are tentatively interpreted as pelletal lapilli, a characteristic feature of TK (Field and Scott Smith, 1999; Hetman, 2008; Masun and Scott Smith, 2008).

Different juvenile clast with thicker, clastic rims and sub-rounded, irregular curvilinear morphologies are cored by medium-grained olivine macrocrysts (Figure 12d). The clastic rims are asymmetrical, typically incomplete, and are composed of ultra fine- to super fine-grained olivine, phlogopite, and spinel, in a microcrystalline matrix. These juvenile clasts are a minor component in comparison to the pelletal lapilli.

Compound clasts that resemble uncored magmaclasts are sub-equant, sub-rounded, irregular curvilinear and are composed of very fine-grained euhedral to subhedral phenocrysts and ultra fine-grained, angular, fragmented olivine pseudomorphs, and minor phlogopite, in a dark cryptocrystalline matrix. One such magmaclast exhibits strong parallel alignment of elongate clasts (Figure 12e). The angular olivine fragments and dark matrix are inconsistent with the host rock, and the parallel alignment of grains suggests this compound clast maybe an autolith/xenolith of earlier-deposited VCK, rather than an uncored magmaclast. Fine-grained

aggregates of phlogopite, carbonate, and spinel, similar to those interpreted as HK autoliths in unit K-2, are also present.

4.2.7 Unit KE

The unit termed "epiclastic kimberlite" (Kretschmar, 1996) consists of a series of sandy graded beds. The beds grade upward with increasing amounts of sand from a volcaniclastic kimberlite (described as being similar to K-3) at the base of the sequence, to "sandy kimberlite", "kimberlitic sandstone" and finally semi- to unconsolidated sand. The material considered in this study (Figure 8j) is pale green, friable, and composed predominantly of quartz sand, most likely derived from near-surface material present at the time of eruption. The quartz grains composing the rock are typically rounded, super fine- to very fine-grained (0.12–1.0 mm), and intensely shattered but intact (Figure 13e). Flow textures are locally defined by the parallel alignment of phlogopite and elongate grains in an optically dark matrix composed of serpentine, clay, and probable ash (Figure 13f). Juvenile magmaclasts are sub-equant, well-rounded, smoothly curved, cored with a variety of very fine-grained material (olivine pseudomorphs, phlogopite or lithics), and have very-thin clastic rims (up to 1 mm). The clastic rims, composed of ultra fine- to very fine-grained olivine and phlogopite in a microcrystalline matrix, are complete, asymmetrical, and generally conform to the shape of the kernel. The juvenile clasts are well preserved (Figure 12f).

Chapter 5: Mineralogy and Mineral Chemistry

5.1 Olivine

5.1.1 Mud Lake olivine

Macrocrysts pseudomorphed to serpentine ± dolomite ± iron oxide (Figure 9b) comprise the bulk of the rock, and are interpreted as olivine. Although there are no fresh grains preserved, the original texture has not been completely overprinted, and macrocrystic and phenocrystic olivine can be discerned from the relict texture. Pseudomorphed macrocrysts are large, sub-rounded, tabular grains up to 4 mm in size, while phenocrysts are smaller (0.5–1 mm) and form equant, subhedral to euhedral crystals.

5.1.2 Drybones Bay olivine

Olivine macrocrysts (0.5–5 mm) and phenocrysts (0.1–0.5 mm) are completely pseudomorphed to serpentine ± carbonate ± iron oxide. The macrocrysts are anhedral and sometimes exhibit polycrystalline textures consistent with mantle-derived xenocrysts (Jones et al., 2014). Phenocrysts are subhedral to euhedral. Four textural varieties of serpentine replacing olivine are observed: (1) a yellow phase with a higher birefringence and wavy extinction texture (prominent in K-8); (2) a colourless to pale yellow, fine-grained phase with a felty texture and lower birefringence; (3) a beige to dark brown, cryptocrystalline phase that is very weakly birefringent to isotropic; and (4) a pale-green to beige, foliated phase that occurs as thin late-stage rims in K-1, -3, -6 and -7.

5.2 Phlogopite

5.2.1 Mud Lake phlogopite

Phlogopite occurs as fresh to chloritized macrocrysts (0.5–2.5 mm across) and groundmass crystals (0.05–0.5 mm). The macrocrysts are rounded or broken, anhedral, unzoned, strongly pleochroic crystals (Figure 14a). Occasionally they display kink banding, plastic deformation of grain margins, or dramatically expanded due to the growth of carbonate ± serpentine ± iron oxide along cleavage planes. Groundmass phlogopite is weakly pleochroic, subhedral to euhedral, and typically poikilitic. Broken disaggregated crystals are most common,

but the late-stage groundmass phlogopite also occurs as tightly packed mosaic-textured aggregates (Figure 14b). Inclusions of small spinel crystals (5–70 μm across) are present in significant quantities in some larger poikilitic crystals and intact aggregates of groundmass phlogopite. The groundmass crystals are more chloritized than the macrocrysts, which are generally fresh.

Phlogopite macrocrysts from Mud Lake are typically unzoned, with Mg# (Mg/[Mg + Fe], molar) ranging from 0.84 to 0.87 (Table 5). Uncommon zoned macrocrysts have higher Mg# that decreases from 0.94 in the core to 0.90 at the edge. Groundmass phlogopite has intermediate Mg# ranging from 0.88 to 0.91. The Mud Lake phlogopite has high levels of certain compatible and incompatible trace elements (up to 4360 ppm Ti, 1410 ppm Ni, 1860 ppm Cr, 1340 ppm Rb, and 1230 ppm Ba), but very low levels of Mn (< 300 ppm), Zr (< 7 ppm), Ta (< 1 ppm), Nb (≤ 4 ppm), Sc (< 3 ppm) and Sr (< 9 ppm). The measured variation is rather limited, defining a narrow range of values that can be attributed to inter-granular variations. The intra-granular variability is negligible; multiple analyses of the same grain gave uniform results, which is consistent with the absence of detectable zoning in BSE images. The Mud Lake micas plot almost entirely within the compositional range of kimberlitic phlogopite (Figure 16) and exhibit none of the trends observed in carbonatitic phlogopite (Reguir et al., 2009). The correlation is especially clear for the following element pairs: Mn vs. Cr (Figure 16a), Co vs. Ni (Figure 16b), Zr vs. Sr (Figure 16d), Nb vs. Ta (Figure 16e) and Mn vs. Nb (Figure 16f). The analytical results presented here thus offers convincing support for the classification of the Mud Lake dyke as kimberlite, rather than carbonatite.

5.2.2 Drybones Bay phlogopite

Phlogopite macrocrysts (0.5–4.0 mm) are typically tabular to sub-rounded single crystals that show little signs of plastic or brittle deformation, aside from minor bent or frayed grain margins (Figure 15a). Optically, the macrocrysts are beige to pale-green, moderately pleochroic, and have a uniform extinction. Varying degrees of chloritization are observed along cleavage planes, and many grains are fresh and amenable to trace-element analysis. Poikilitic phlogopite hosting euhedral spinel inclusions occurs in some samples. A distinct population of phlogopite, recognized by its unusual prismatic habit (elongate about the c-axis), plastic deformation, dark brown colour, strong pleochroism, and undulose extinction (Figure 15b), is probably derived from the phlogopite-calcite xenoliths observed in some samples.

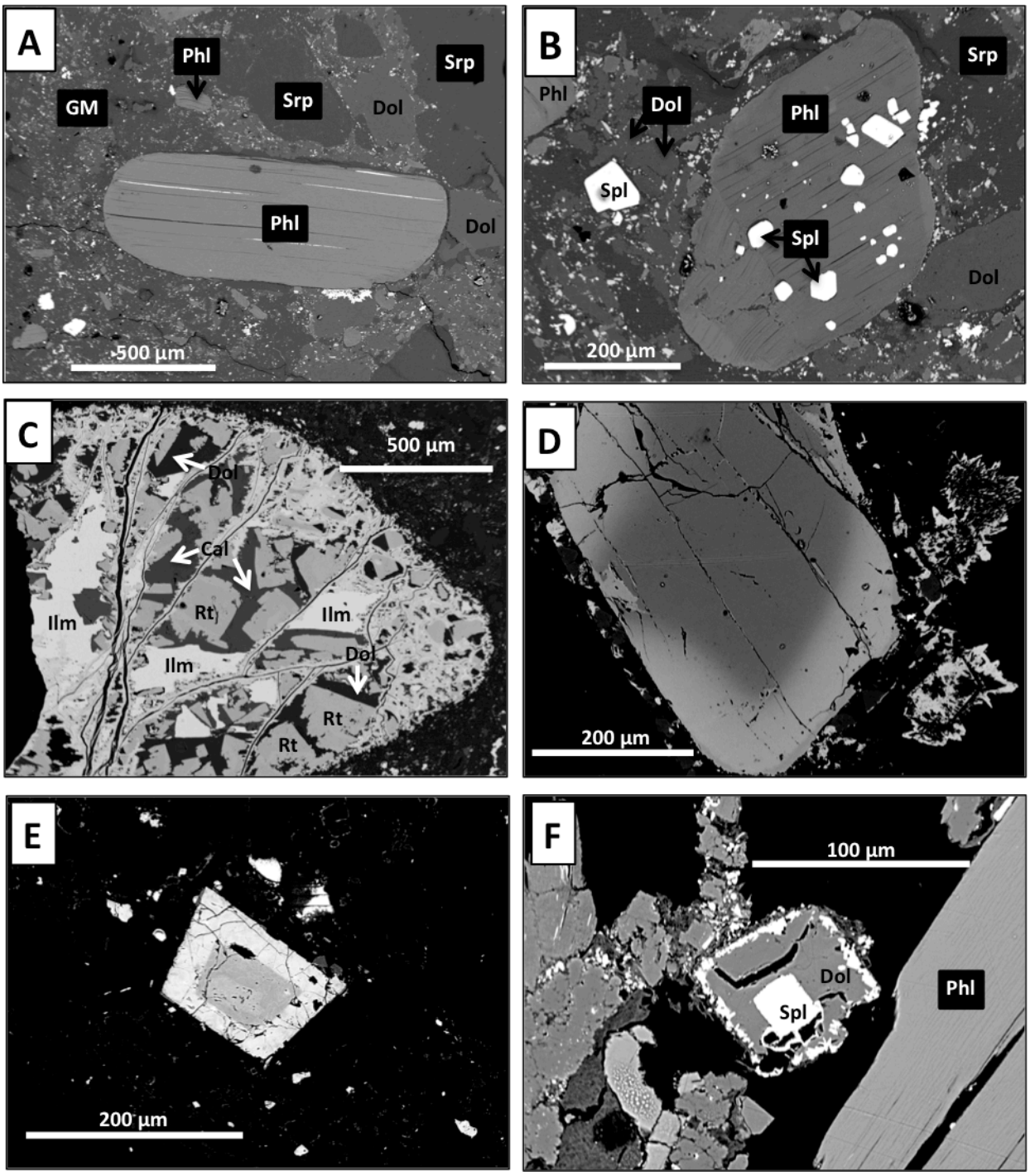

Figure 14 BSE images of Mud Lake minerals: (A) fresh phlogopite macrocryst and olivine pseudomorphs in a fine-grained groundmass; (B) poikilitic phlogopite with a mosaic texture and spinel inclusions; (C) intensely altered ilmenite macrocryst; (D) spinel macrocryst with gradational zoning; (E) groundmass spinel with sharp zoning; (F) atoll spinel. Cal = calcite; Dol = dolomite; GM = groundmass; Ilm = ilmenite; Phl = phlogopite; Rt = rutile; Spl = spinel; Srp = serpentine.

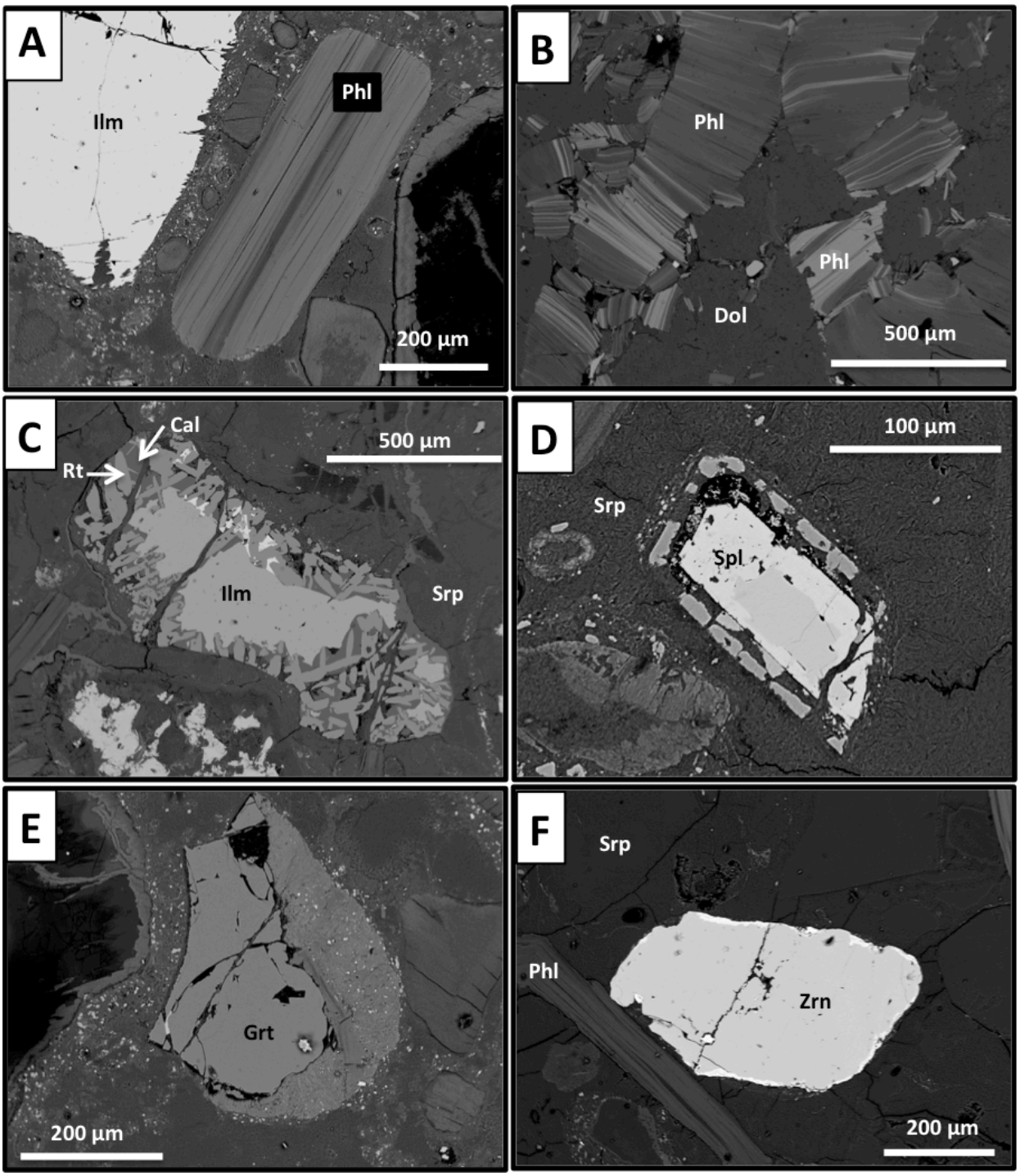

Figure 15 BSE images of Drybones Bay minerals: (A) fresh ilmenite macrocryst with corroded margins with a relatively fresh phlogopite macrocryst; (B) xenocrystic phlogopite associated with carbonate xenoliths, note the prismatic habit; (C) altered ilmenite macrocryst with an amoeboid-shaped core surrounded by rutile laths in a carbonate matrix with minor barite (high-AZ phase); (D) atoll-textured groundmass spinel with a zoned core; (E) peridotite garnet with a kelyphite rim; (F) zircon macrocryst rimmed with baddeleyite. Cal = calcite; Dol = dolomite; Grt = garnet; Ilm = ilmenite; Phl = phlogopite; Rt = rutile; Srp = serpentine; Zrn = zircon.

Table 5 Representative major- and trace-element compositions of phlogopite from Mud Lake and Drybones Bay.

	Mud Lake							Drybones Bay							
Oxide, wt.%	1	2	3	4	5	6	7	8	9	10	11	12	13	14	15
SiO_2	42.23	42.43	43.03	42.50	42.23	40.73	41.74	42.05	42.01	42.45	42.73	41.67	43.38	41.04	36.49
TiO_2	0.82	0.76	0.07	1.05	0.79	1.13	0.20	0.74	0.60	0.58	0.11	0.48	0.58	0.00	1.97
Al_2O_3	11.45	11.18	11.21	10.46	11.29	10.95	10.19	11.14	10.35	10.32	10.05	12.15	10.14	12.50	16.81
Cr_2O_3	0.22	0.24	0.32	0.54	0.05	0.26	0.19	0.07	0.03	0.05	0.14	1.23	0.29	0.74	0.01
FeO‡	6.27	6.17	2.76	5.10	7.59	6.52	3.22	7.20	7.60	7.86	2.76	3.44	5.04	2.82	21.08
Fe_2O_3‡	–	–	–	–	–	–	3.21	–	0.32	–	1.87	–	–	–	–
MnO	0.01	0.03	0.01	0.00	0.04	0.06	0.03	0.03	0.04	0.04	0.03	0.03	0.02	0.02	0.27
MgO	24.04	23.77	26.53	24.78	23.15	25.82	26.84	23.28	23.43	23.66	26.49	25.10	25.56	26.29	9.07
CaO	0.02	0.03	n.d.	n.d.	n.d.	0.29	n.d.	0.01	0.06	0.00	0.02	0.01	0.01	0.02	0.01
Na_2O	0.10	0.11	0.18	0.18	0.07	0.20	0.08	0.06	0.21	0.08	0.10	0.20	0.38	0.90	0.54
K_2O	10.02	9.75	10.39	9.93	10.31	7.37	9.33	10.69	10.02	10.20	10.22	10.56	9.70	7.64	9.85
BaO	0.08	n.d.	0.18	0.13	n.d.	0.07	n.d.	0.02	0.01	0.14	0.17	0.07	0.00	1.43	0.09
F	0.59	0.46	0.50	0.84	0.59	0.86	0.89	0.55	0.64	0.59	0.68	0.37	0.86	0.16	0.15
Cl	0.04	0.04	0.02	0.03	0.04	0.02	0.02	0.04	0.03	0.04	0.07	0.05	0.02	0.03	0.01
$–O=(F,Cl)_2$	-0.26	-0.20	-0.22	-0.36	-0.26	-0.37	-0.38	-0.24	-0.28	-0.26	-0.30	-0.17	-0.37	-0.07	-0.07
Total	95.63	94.84	94.98	95.19	95.89	93.91	95.57	95.64	95.08	95.75	95.13	95.19	95.61	93.52	96.28
mg#	0.87	0.87	0.94	0.90	0.84	0.88	0.89	0.85	0.84	0.84	0.91	0.93	0.90	0.94	0.43
Atoms per formula unit (APFU) calculated on the basis of 11 oxygen atoms															
Si	3.054	3.094	3.071	3.082	3.062	2.995	3.001	3.050	3.069	3.082	3.071	2.989	3.114	2.985	2.839
Ti	0.045	0.042	0.004	0.057	0.043	0.062	0.011	0.040	0.033	0.032	0.006	0.026	0.031	0.000	0.115
Al	0.976	0.961	0.943	0.894	0.965	0.949	0.863	0.952	0.891	0.883	0.851	1.027	0.858	1.071	1.541
Cr	0.013	0.014	0.018	0.031	0.003	0.015	0.011	0.004	0.002	0.003	0.008	0.070	0.016	0.043	0.001
Fe^{2+}	0.377	0.373	0.165	0.308	0.459	0.398	0.194	0.436	0.464	0.477	0.166	0.206	0.302	0.170	1.350
Fe^{3+}‡	–	–	–	–	–	–	0.173	–	0.018	–	0.101	–	–	–	–
Mn	0.001	0.002	0.001	0.000	0.002	0.004	0.002	0.002	0.002	0.002	0.002	0.002	0.001	0.001	0.018
Mg	2.592	2.584	2.823	2.679	2.502	2.830	2.877	2.517	2.552	2.561	2.838	2.684	2.735	2.851	1.052
Ca	0.002	0.002	0.000	0.000	0.000	0.023	0.000	0.001	0.005	0.000	0.002	0.001	0.001	0.002	0.001
Na	0.014	0.016	0.025	0.025	0.010	0.029	0.011	0.008	0.030	0.011	0.014	0.028	0.053	0.127	0.081
K	0.924	0.907	0.946	0.918	0.953	0.691	0.856	0.989	0.934	0.945	0.937	0.966	0.888	0.709	0.978
Ba	0.002	0.000	0.005	0.004	0.000	0.002	0.000	0.001	0.000	0.004	0.005	0.002	0.000	0.041	0.003
F	0.134	0.105	0.113	0.192	0.135	0.199	0.204	0.126	0.148	0.135	0.155	0.084	0.195	0.036	0.036
Cl	0.005	0.005	0.002	0.004	0.005	0.002	0.002	0.005	0.004	0.005	0.009	0.006	0.002	0.004	0.001

(1-2) representative unzoned macrocrysts; (3-4) core and rim of a high-mg# macrocryst; (5) high Co, Rb macrocryst; (6) mosaic-textured groundmass; (7) groundmass with spinel inclusions; (8-10) representative unzoned macrocrysts; (11) macrocryst with spinel inclusions; (12) poikilitic groundmass phlogopite with spinel inclusions; (13) mosaic-textured groundmass; (14) mosaic-textured autolith; (15) elongate mica xenocryst; ‡ Fe^{2+}/Fe^{3+} ratio calculated from stiochiometry; n.d. = not detected.

Table 5 continued…

	Mud Lake				Drybones Bay			
Element, ppm	1 (n = 5)	2 (n = 5)	3 (n = 3)	4 (n = 4)	5 (n = 4)	6 (n = 5)	7 (n = 6)	8 (n = 5)
Ca	388 (50)	244 (158)	313 (97)	468 (70)	193 (187)	220 (189)	433 (109)	110 (114)
Sc	0.71 (8)	1.6 (7)	0.9 (1)	1.05 (9)	1.0 (1)	1.45 (8)	1.2 (0.1)	1.3 (0.1)
Ti	787 (39)	787 (328)	4157 (72)	4285 (52)	735 (65)	4134 (544)	3543 (580)	2376 (166)
V	19 (2)	33 (5)	63 (1)	59 (1)	18.8 (6)	65 (4)	40 (5)	44 (2)
Cr	1000 (39)	1348 (594)	440 (13)	1638 (40)	980 (197)	335 (30)	380 (124)	211 (14)
Mn	213 (10)	200 (54)	278 (6)	276 (5)	248 (6)	333 (74)	323 (80)	313 (12)
Co	49 (1)	49 (8)	75 (1)	66 (1)	46 (3)	78 (8)	66 (7)	74 (3)
Ni	1298 (15)	1278 (137)	578 (4)	1305 (13)	1204 (53)	432 (34)	688 (89)	321 (23)
Zn	35.6 (9)	36 (18)	81 (4)	69 (4)	38.0 (9)	85 (13)	81 (13)	93 (7)
Rb	603 (14)	535 (59)	1286 (50)	884 (34)	530 (68)	760 (92)	692 (117)	693 (47)
Sr	6 (1)	5 (2)	3.9 (1)	8.1 (7)	5.4 (7)	6 (3)	11 (9)	4 (1)
Zr	3 (0.3)	5 (2)	3.4 (2)	3.5 (1)	3 (2)	3.1 (4)	3 (1)	2.8 (0.4)
Nb	6.8 (7)	22 (10)	8 (1)	5.5 (1)	8 (2)	5.3 (9)	7 (1)	5.2 (0.5)
Cs	4.9 (8)	6 (2)	7.8 (9)	7 (2)	4.2 (5)	3.7 (3)	4.6 (0.6)	3.7 (0.4)
Ba	608 (63)	786 (546)	316 (5)	300 (25)	1914 (1708)	190 (25)	160 (36)	121 (6)
Hf	0.06 (4)	0.19 (7)	0.19 (8)	0.15 (9)	0.18 (8)	0.15 (3)	0.2 (0.1)	0.12 (0.07)
Ta	0.54 (5)	0.7 (3)	0.56 (1)	0.46 (8)	0.8 (0.2)	0.45 (2)	0.5 (0.1)	0.45 (0.08)
Zr/Hf	76 (64)	28 (4)	20 (8)	33 (21)	17 (5)	21 (3)	25 (8)	28 (13)
Rb/Cs	125 (19)	106 (41)	166 (27)	136 (33)	127 (19)	205 (15)	149 (9)	191 (15)
Nb/Ta	13 (2)	29 (9)	14 (3)	12 (2)	9 (2)	12 (1)	14 (1)	12 (2)
Sr/Ba	0.010 (2)	0.010 (8)	0.0123 (5)	0.027 (3)	0.01 (1)	0.03 (2)	0.1 (1)	0.03 (7)
La/Rb	0.00002 (3)	0.001 (2)	0.0001 (1)	0.00002 (4)	0.001 (1)	0.00004 (6)	0.01 (1)	0.00004 (4)
Co/Ni	0.038 (1)	0.04 (1)	0.129 (3)	0.0507 (6)	0.039 (1)	0.179 (8)	0.096 (5)	0.23 (2)

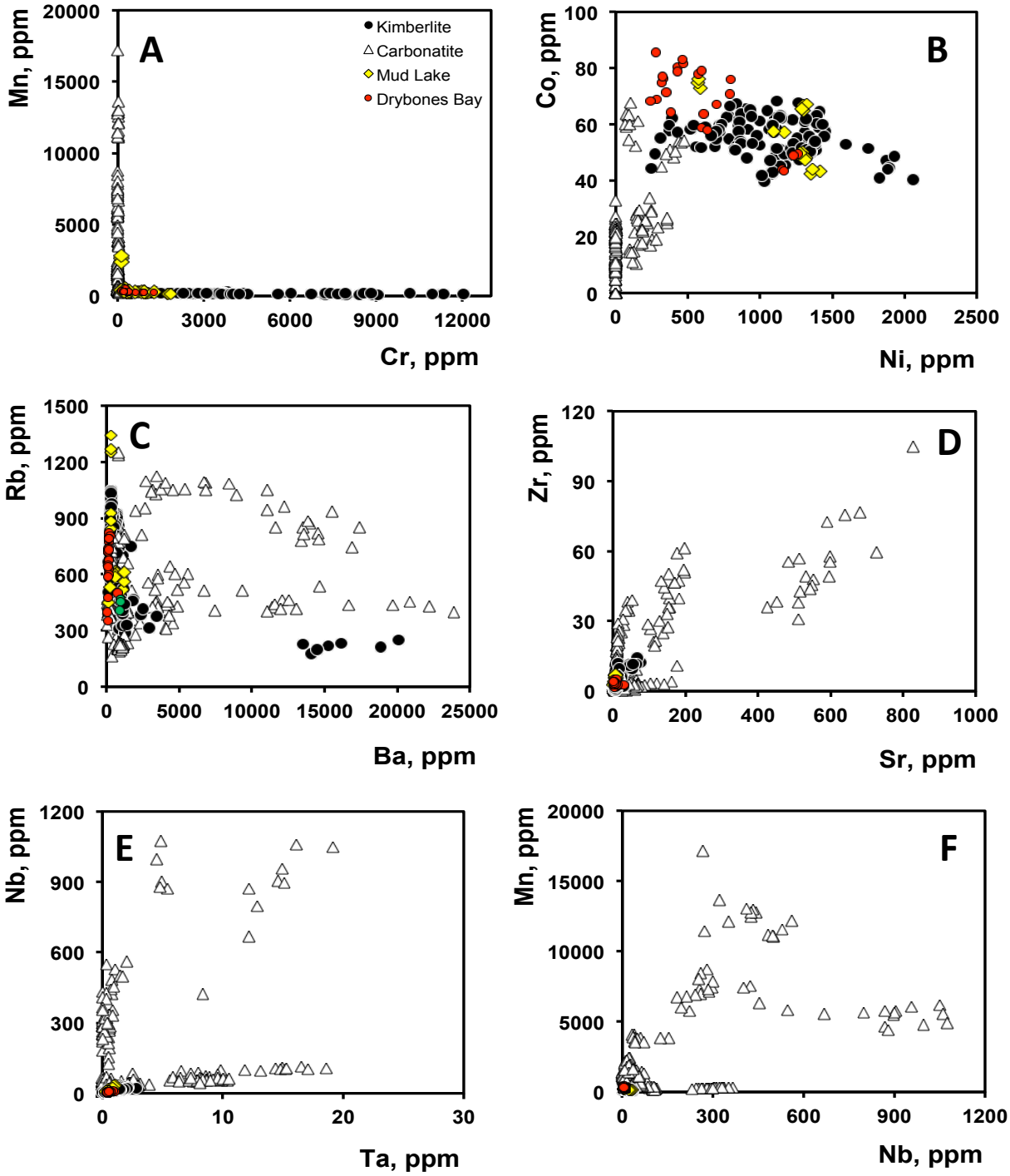

Figure 16 Comparison of trace-element compositions of phlogopite macrocrysts from Drybones Bay and Mud Lake with those of typical kimberlites and carbonatites (Reguir et al., 2009).

Phlogopite macrocrysts from the Drybones Bay are devoid of zoning and exhibit only minor inter-granular variations in their major-element composition, with Mg# ranging from 0.84 to 0.87 (Table 5). Groundmass phlogopite has appreciably higher levels of Mg, with Mg#

ranging from 0.90 to 0.94. Mica derived from the granodiorite country rock can be distinguished by low Mg# (0.44–0.47), and is classified as annite.

Trace elements in the Drybones Bay phlogopite macrocrysts are comparable to those at Mud Lake, and are characterized by consistently high levels of Ti (up to 4600 ppm), Ni (up to 1265 ppm), Cr (up to 911 ppm), Rb (up to 820 ppm) and Ba (up to 3480 ppm). Some discrepancies in the Ba contents determined by LA-ICP-MS and WDS could be potentially explained by alteration of phlogopite to chlorite. The elevated levels of REE and noticeable depletion in Ba observed in some of the phlogopite macrocrysts is most likely due to the presence of minute apatite inclusions below the sample surface ablated during the analysis.

The trace-element composition of the Drybones Bay and Mud Lake phlogopite macrocrysts plot within the kimberlite field on the discrimination diagrams of Reguir et al. (2009). The data shows significant overlaps on the Ba/Rb and Cr/Mn plots, and are clearly indistinguishable on the Sr/Zr, Ta/Nb, and Nb/Mn diagrams (Figure 16), further confirming the kimberlite provenance of the these rocks.

The trace-element characteristics of the Fe-rich xenocrysts differ significantly from the macrocrystic phlogopite. The xenocrysts contain much higher levels of Sc (up to 30 ppm), Ti (up to 10070 ppm), V (up to 343 ppm), Mn (up to 2810 ppm), Zn (up to 685 ppm), Nb (up to 9.3 ppm), and Cs (up to 40 ppm), but lower levels of Ni (≤ 135 ppm) and Sr (≤ 1 ppm).

5.3 Ilmenite

5.3.1 Mud Lake ilmenite

Ilmenite macrocrysts occur as large (0.5–2.5 mm) ellipsoidal grains that are intensely altered (Figure 14c), replaced by an assemblage of rutile, magnetite, barite, serpentine, and carbonates. The alteration imparts a variety of textures, including graphic aggregates, fragmented and symplectitic textures. Ilmenite rarely occurs in the groundmass as small (0.05–0.2 mm) irregular grains with eroded margins and discontinuous mantles of late forming iron oxide.

With the exception of one analysis of high-Fe (oxidized?) ilmenite, the major-element compositions of ilmenite from the Mud Lake kimberlite dyke fall within a narrow compositional range (45.1–47.5 wt.% FeO, 5.1–6.1 wt.% MgO, 42.7–45.6 wt.% TiO_2) (Table 6; Figure 17a,b). The mineral contains high levels of Al (1500–1770 ppm), V (1625–1770 ppm), Cr (0.5–0.9 wt.% Cr_2O_3), Mn (1860–1940 ppm), Zr (1120–1180 ppm), and Nb (0.2–0.4 wt.% Nb_2O_5), and also

shows appreciable Co, Ni, Zn and Ta (up to 145, 286, 192 and 200 ppm, respectively). The levels of Sc and Hf are below 36 ppm and 42 ppm, respectively. The abundances of REE are low and typically do not exceed 0.1 ppm. The mineral is poor in Y (< 0.3 ppm), U (< 0.15 ppm), Pb (< 0.5 ppm) and Th (< 0.1 ppm). The Zr/Nb value is high (~0.7) and consistent among the analyzed grains (Figure 17e). According to Carmody et al. (2014), kimberlitic ilmenite with Zr/Nb ratios exceeding 0.37 is indicative of high diamond potential.

5.3.2 Drybones Bay ilmenite

Ilmenite macrocrysts commonly occur as sub-rounded, crudely ellipsoidal crystals (0.4–4.0 mm across) with jagged or corroded grain margins, or as broken angular fragments with no alteration on the exposed internal surfaces. In reflected light, the crystals exhibit weak to moderate anisotropy. Most of the macrocrysts are fresh, although some grains exhibit intensely altered rims. The altered grains have amoeboid cores of ilmenite and rims composed of rutile laths and variable amounts of barite set in a carbonate matrix (Figure 15c).

Ilmenite from the Drybones Bay kimberlite shows a greater compositional variation (Table 6) relative to the Mud Lake material: 42.2–55.6 wt.% FeO, 3.8–7.4 wt.% MgO and 35.6–47.0 wt.% TiO_2 (Figure 17c,d). The majority of the Drybones Bay ilmenite macrocrysts are enriched in trace elements relative to the Mud Lake ilmenite, particularly in V (up to 2270 ppm), Cr (up to 3.5 wt.% Cr_2O_3), Mn (up to 2620 ppm) and Ni (up to 1860 ppm). The Al, Nb, Zn, Ta, Sc, and Hf levels are comparable in the two sets of samples. The bulk of the Drybones Bay ilmenites have Zr/Nb ratios exceeding 0.56 (with an average of 0.63), which, similar to the Mud Lake material and places them in the high diamond potential field on the discrimination diagram of Carmody et al. (2014) (Figure 17e). Only one grain of ilmenite is characterized by low Zr/Nb values (0.35–0.36) and plots at the boundary separating the high and low diamond potential fields (Figure 17e).

Table 6 Representative major- and trace-element compositions of ilmenite macrocrysts from Mud Lake and Drybones Bay.

	Mud Lake					Drybones Bay					
Oxide, wt.%	1	2	3	4	5	6	7	8	9	10	11
TiO_2	42.70	44.05	45.56	43.95	38.14	35.68	44.48	42.67	45.29	52.79	53.43
Al_2O_3	0.17	0.18	0.32	0.28	0.12	0.13	0.30	0.20	0.40	0.29	0.05
Cr_2O_3	0.48	0.55	0.76	0.71	0.86	0.93	0.83	0.54	1.79	3.78	3.52
FeO‡	35.75	35.91	35.52	34.59	36.55	36.29	35.13	35.73	33.15	25.68	27.98
Fe_2O_3‡	13.85	12.86	11.63	11.62	18.72	21.68	12.34	14.06	11.01	3.45	2.34
MgO	5.13	5.55	6.14	5.87	3.75	3.38	6.03	5.28	7.15	13.19	11.92
Nb_2O_5	0.24	0.27	0.22	0.21	0.42	0.36	0.26	0.28	0.19	0.12	0.11
Ta_2O_5	0.00	0.16	0.03	0.11	0.08	0.12	0.06	0.20	0.00	0.05	0.00
Total	98.33	99.53	100.18	97.34	98.63	98.57	99.43	98.96	98.98	99.36	99.35
APFU calculated on the basis of 3 oxygen atoms and 2 cations											
Ti	0.80	0.81	0.83	0.82	0.72	0.67	0.81	0.79	0.82	0.91	0.93
Al	0.00	0.01	0.01	0.01	0.00	0.00	0.01	0.01	0.01	0.01	0.00
Cr	0.01	0.01	0.01	0.01	0.02	0.02	0.02	0.01	0.03	0.07	0.06
Fe^{2+}	0.74	0.73	0.72	0.72	0.76	0.76	0.71	0.74	0.67	0.49	0.54
Fe^{3+}‡	0.26	0.24	0.21	0.22	0.35	0.41	0.23	0.26	0.20	0.06	0.04
Mg	0.19	0.20	0.22	0.22	0.14	0.13	0.22	0.19	0.26	0.45	0.41
Nb	0.00	0.00	0.00	0.00	0.00	0.00	0.00	0.00	0.00	0.00	0.00
Ta	0.00	0.00	0.00	0.00	0.00	0.00	0.00	0.00	0.00	0.00	0.00

(1-5) Mud Lake ilmenite macrocrysts; (6-9) Drybones Bay macrocrysts; (10,11) xenocrysts; ‡ Fe^{2+}/Fe^{3+} ratio calculated from stoichiometry

Element, ppm	1 (n = 5)	2 (n = 3)	3 (n = 3)	4 (n = 3)	5 (n = 6)	6 (n = 4)	7 (n = 4)	8 (n = 4)
Al	1606 (100)	1179 (61)	1601 (8)	1835 (35)	1887 (95)	1305 (43)	1370 (79)	1639 (31)
Ca	482 (229)	n.d.	n.d	n.d.	n.d.	n.d.	200 (400)	n.d.
Sc	35 (1)	39.8 (8)	34.1 (7)	21.1 (7)	27.6 (1)	31.0 (0.7)	42 (1)	34 (2)
V	1718 (60)	1926 (42)	1737 (26)	1089 (11)	1753 (17)	1749 (42)	2241 (45)	2039 (58)
Cr	4414 (129)	3234 (157)	4531 (26)	25127 (329)	5070 (201)	3733 (106)	4195 (129)	5120 (292)
Mn	1902 (45)	2018 (69)	2151 (22)	2590 (28)	1979 (72)	2015 (29)	2350 (58)	2270 (57)
Co	141 (3)	140 (8)	153 (2)	186 (2)	153 (7)	143 (4)	169 (9)	172 (6)
Ni	272 (9)	188 (6)	298 (6)	1827 (28)	382 (18)	258 (14)	247 (16)	351 (20)
Zn	181 (9)	207 (13)	219 (7)	167 (4)	183 (12)	173 (11)	215 (10)	199 (14)
Y	0.1 (1)	n.d.	n.d.	n.d.	0.03 (5)	0.02 (4)	0.12 (8)	0.08 (5)
Zr	1140 (24)	1231 (18)	1099 (18)	437 (6)	989 (72)	1127 (68)	1367 (63)	1219 (73)
Nb	1624 (57)	2148 (49)	1706 (16)	1226 (8)	1545 (122)	1805 (93)	2293 (78)	1838 (106)
Hf	40 (1)	43 (3)	41.8 (1)	14.2 (4)	34 (2)	36 (2)	48 (1)	42 (2)
Ta	191 (7)	259 (16)	214 (1)	183 (1)	181 (8)	196 (14)	265 (9)	208 (8)
U	0.10 (4)	0.05 (5)	0.07 (7)	n.d.	0.06 (3)	0.02 (3)	0.06 (4)	0.04 (5)
Nb/Ta	8.5 (3)	8.3 (6)	7.98 (0.1)	6.69 (5)	8.6 (5)	9.2 (5)	8.7 (1)	8.8 (3)
Zr/Hf	28.6 (4)	28 (2)	26 (1)	30.8 (5)	29 (2)	31 (3)	29 (1)	28.7 (7)
Zr/Nb	0.70 (2)	0.57 (2)	0.64 (0.01)	0.356 (5)	0.64 (2)	0.624 (8)	0.6 (2)	0.66 (1)
Co/Ni	0.52 (2)	0.74 (2)	0.51 (0.02)	0.102 (1)	0.4 (1)	0.56 (3)	0.69 (2)	0.49 (2)

(1) Mud Lake; (2-8) Drybones Bay; n.d. = not detected.

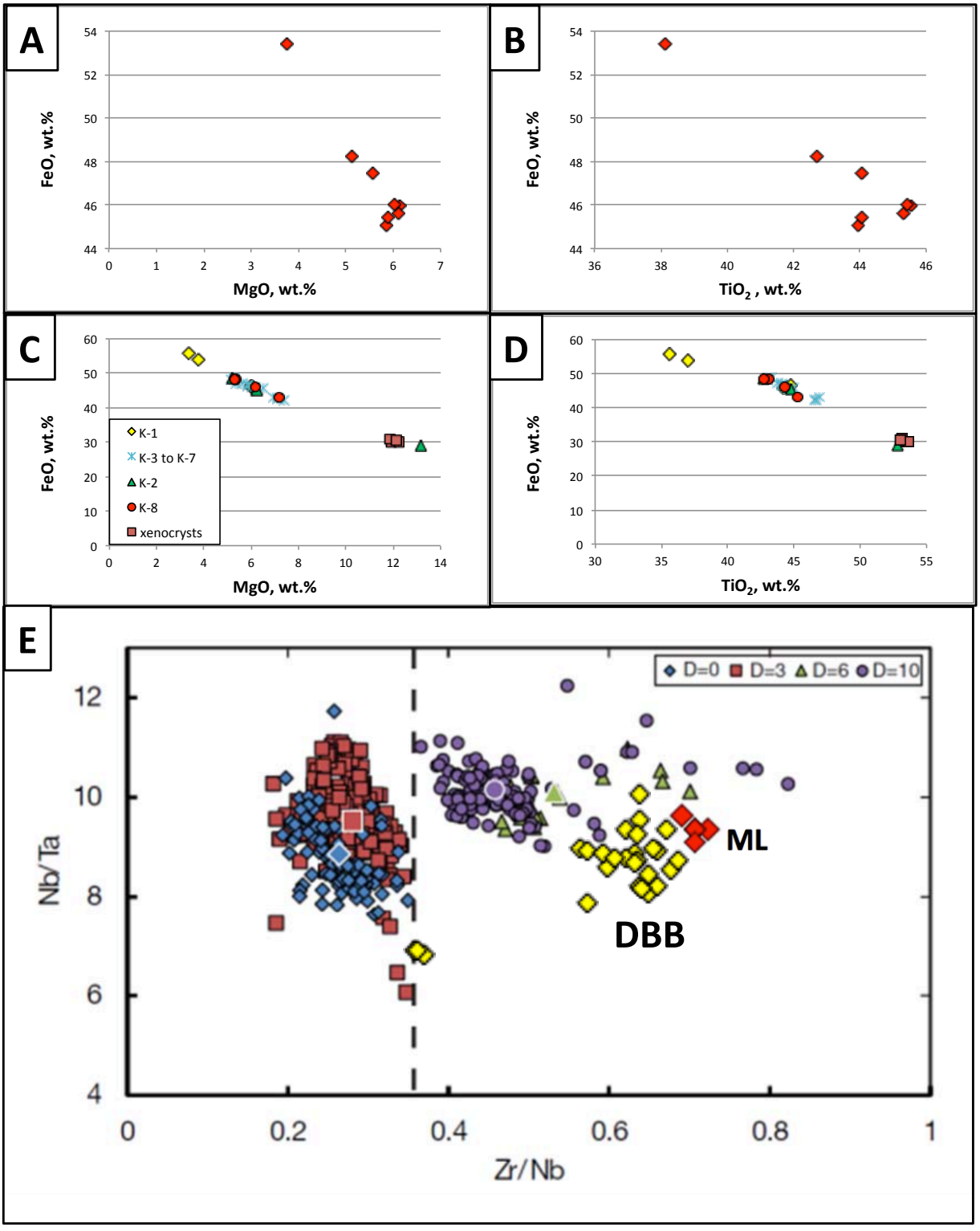

Figure 17 Major-element variation in ilmenite from (A,B) Mud Lake and (C,D) Drybones Bay, and (E) Zr/Nb vs. Nb/Ta plot for ilmenite from Siberian kimberlites (Carmody et al., 2014), Mud Lake (ML), and Drybones Bay (DBB). The dashed line at Zr/Nb = 0.37 separates the data corresponding to low diamond potential (D = 0–3) from those with high diamond potential (D = 6–10).

5.4 Spinel-group minerals

5.4.1 Mud Lake spinel-group minerals

Spinel-group minerals (referred to as spinels hereafter) occur as macrocrysts and as primary groundmass minerals. The macrocrysts are large (0.2–1.5 mm across), rounded crystals that are commonly rimmed with a discontinuous crust of late forming iron oxide. Optically they vary from opaque to translucent with a red colour. The translucent macrocrysts are homogeneous, whereas the opaque crystals exhibit continuous zoning in BSE images (Figure 14d). Groundmass spinels are small (0.01–0.1 mm) euhedral crystals with sharply defined, discrete zonation (Figure 14e). Atoll textured groundmass spinel is less common; atoll spinels are small (0.06–0.1 mm) complexly mantled spinels with euhedral cores that are separated by a 5–10 μm gap from a narrow (< 5 μm) discontinuous mantle (Figure 14f). Spinel inclusions in groundmass phlogopite are unzoned subhedral to euhedral crystals (Figure 14b).

The major-element composition (Table 7) of the macrocrystic spinel lacking zoning is comparable to the cores of the zoned macrocrysts, with slightly higher levels of MgO (up to 15 wt.%) and lower levels of Cr_2O_3 (as low as 30 wt.%) in some grains (Figure 18a,b). The large zoned macrocrystic spinel exhibits continuous compositional variations with MgO, Al_2O_3 and Cr_2O_3 decreasing from 10.8, 11.8 and 56.0 wt.% in the core to less than 0.2, 0.1 and 0.1 wt.% in the rims, respectively (Figure 18a,b). This decrease is accompanied by an increase in FeO (from 19 to 84 wt.%) and TiO_2 (from below the detection limit to 2.8 wt.%).

The cores of primary groundmass spinels are characteristically enriched in Mg (up to 10 wt.% MgO) and Cr (up to 55 wt.% Cr_2O_3), and depleted in Fe (21–41 wt.% FeO) relative to their rims (< 5 wt.% MgO, < 1.5 wt.% Cr_2O_3, and up to 78 wt.% FeO). Overall, the major-element core-to-rim variations observed in the macrocrystic spinel are comparable to those in the primary groundmass spinel (Figure 18a,b). The major-element characteristics of the cores of atoll spinels are also similar to those observed in the cores of zoned macrocrysts and groundmass spinels. In contrast, the rims of atoll spinels show lower levels of FeO relative to the rims of macrocrystic and groundmass spinels (Figure 18a,b). Unzoned spinel grains found as small inclusions in phlogopite have compositions comparable to those of the cores of groundmass spinels.

Table 7 Representative major- and trace-element compositions of spinel-group minerals from Mud Lake and Drybones Bay.

	Mud Lake							Drybones Bay						
Oxide, wt.%	1	2	3	4	5	6	7	8	9	10	11	12	13	14
SiO_2	0.01	0.01	0.04	0.03	0.18	0.03	0.02	0.05	0.11	0.07	0.05	0.11	0.06	0.10
TiO_2	0.15	1.03	0.01	3.16	11.20	0.22	4.02	0.05	1.47	0.02	1.01	0.18	1.32	1.56
Al_2O_3	11.59	1.90	16.04	0.49	0.66	24.53	0.52	21.97	7.52	10.04	1.22	10.89	0.64	10.89
Cr_2O_3	50.95	55.61	53.25	43.56	1.38	43.79	39.39	47.33	53.07	58.28	59.67	56.46	52.59	47.29
FeO‡	16.21	18.03	16.42	23.79	40.31	17.01	25.56	15.44	18.60	16.21	18.34	16.47	21.01	16.82
Fe_2O_3‡	6.57	9.87	0.17	19.28	42.24	0.17	21.56	0.92	8.16	3.43	8.64	3.46	13.14	10.12
MgO	10.82	8.93	11.40	6.08	0.22	12.07	5.84	0.55	0.63	0.55	0.71	0.59	0.89	0.66
MnO	n.d.	n.d.	n.d.	0.73	n.d.	n.d.	n.d.	12.51	9.78	10.89	8.78	10.78	6.57	11.22
NiO	n.a.	n.a.	n.a.	n.a.	n.a.	n.a.	n.a.	0.08	0.16	0.09	n.d.	0.08	0.06	0.07
ZnO	n.a.	n.a.	n.a.	n.a.	n.a.	n.a.	n.a.	0.11	0.16	0.12	0.14	0.16	0.07	0.08
Total	96.31	95.38	97.33	97.12	96.19	97.83	96.91	99.01	99.66	99.70	98.62	99.19	96.35	98.81
APFU calculated on the basis of 4 oxygen atoms and 3 cations														
Ti	0.004	0.028	0.000	0.087	0.331	0.005	0.112	0.001	0.037	0.000	0.027	0.004	0.037	0.039
Al	0.462	0.081	0.617	0.021	0.031	0.903	0.023	0.807	0.298	0.390	0.051	0.424	0.028	0.425
Cr	1.362	1.593	1.374	1.268	0.043	1.081	1.152	1.166	1.413	1.519	1.663	1.474	1.531	1.238
Fe^{2+}	0.459	0.546	0.447	0.732	1.325	0.444	0.791	0.402	0.524	0.447	0.541	0.455	0.647	0.466
Fe^{3+}	0.167	0.269	0.006	0.534	1.250	0.004	0.600	0.022	0.207	0.085	0.229	0.086	0.364	0.252
Mg	0.546	0.482	0.555	0.334	0.013	0.562	0.322	0.015	0.018	0.015	0.021	0.017	0.028	0.019
Mn	0.000	0.000	0.000	0.023	0.000	0.000	0.000	0.581	0.491	0.535	0.461	0.531	0.361	0.554
Ni	n.a.	n.a.	n.a.	n.a.	n.a.	n.a.	n.a.	0.002	0.004	0.002	0.000	0.002	0.002	0.002
Zn	n.a.	n.a.	n.a.	n.a.	n.a.	n.a.	n.a.	0.003	0.004	0.003	0.004	0.004	0.002	0.002
End-member composition														
$MgAl_2O_4$	12.55	1.90	17.04	0.33	0.01	25.21	0.33	23.49	7.10	10.47	1.14	11.22	0.48	11.34
$FeAl_2O_4$	10.55	2.15	13.77	0.71	1.51	19.93	0.81	16.27	7.57	8.74	1.34	9.62	0.87	9.53
$MgCr_2O_4$	37.01	37.35	37.95	19.42	0.02	30.19	16.67	33.95	33.59	40.76	37.50	39.03	26.66	33.03
$FeCr_2O_4$	31.11	42.29	30.66	42.63	2.12	23.86	40.92	23.51	35.82	34.03	43.93	33.45	47.82	27.78
$MgFe_2O_4$	4.55	6.31	0.11	8.18	0.60	0.11	8.69	0.63	4.92	2.29	5.17	2.28	6.34	6.73
$FeFe_2O_4$	3.82	7.15	0.09	17.96	61.89	0.09	21.32	0.43	5.24	1.91	6.05	1.95	11.37	5.66
Mg_2TiO_4	0.21	1.32	0.01	2.68	0.32	0.29	3.24	0.07	1.77	0.03	1.21	0.24	1.27	2.07
Fe_2TiO_4	0.17	1.49	0.01	5.88	32.81	0.23	7.95	0.05	1.89	0.02	1.41	0.20	2.28	1.74
$MnCr_2O_4$	0.00	0.00	0.00	1.60	0.00	0.00	0.00	1.43	1.57	1.45	1.86	1.56	2.24	1.54
$MnFe_2O_4$	0.00	0.00	0.00	0.67	0.00	0.00	0.00	0.03	0.23	0.08	0.26	0.09	0.53	0.31

(1-3) Macrocrysts: (1) core; (2) rim; (3) unzoned; (4-7) groundmass grains: (4) core; (5) rim; (6) atoll; (7) inclusions in Phl; ‡ Fe^{2+}/Fe^{3+} ratio calculated from stiochiometry; V was sought but not detected; n.d. = not detected; n.a. = not analyzed.

Table 7 continued…

	Mud Lake						Drybones Bay				
Element,	unzoned macrocrysts			zoned macrocryst			unzoned macrocrysts			groundmass	
ppm	1 (n = 4)	2 (n = 5)	3 (n = 4)	4 (n = 3)	5 (n = 2)	6 (n = 3)	7 (n = 5)	8 (n = 4)	9 (n = 4)	10 (n = 1)	11 (n = 1)
Sc,	2.1 (1)	2 (2)	1.8 (2)	0.9 (5)	3 (2)	6 (1)	2.6 (3)	0.7 (2)	0.5 (3)	3.63	0.96
Ti	59 (5)	670 (21)	595 (12)	196 (187)	6605 (9242)	17513 (5623)	210 (21)	434 (23)	225 (14)	4840	400
V	1137 (27)	1019 (19)	1151 (11)	1208 (16)	1474 (458)	2125 (426)	1594 (93)	2153 (90)	2325 (102)	1600	2060
Mn	1975 (53)	1924 (22)	2249 (49)	3359 (162)	3750 (537)	4447 (170)	1982 (60)	2253 (70)	2183 (70)	3710	2310
Co	470 (16)	414 (12)	459 (11)	281 (20)	265 (5)	281 (17)	406 (37)	415 (19)	394 (18)	412	404
Ni	169 (6)	400 (14)	640 (12)	389 (44)	845 (629)	1460 (224)	824 (86)	607 (23)	540 (27)	947	506
Zn	2154 (54)	1539 (18)	1408 (48)	4036 (1138)	2834 (688)	2487 (76)	1886 (134)	1845 (125)	1725 (17)	1520	2210
Zr	0.2 (1)	0.05 (10)	0.2 (2)	3 (5)	2 (3)	15 (14)	0.4 (3)	0.2 (2)	0.2 (1)	3.5	1.7
Nb	0.25 (1)	0.18 (8)	0.4 (2)	2 (2)	3 (3)	16 (16)	0.51 (9)	0.7 (1)	0.59 (8)	3.86	1.72
Hf	0.02 (3)	0.01 (2)	0.04 (2)	0.07 (6)	0.1 (1)	0.5 (5)	0.014 (1)	0.03 (4)	0.03 (3)	0.21	0.24
Ta	0.003 (5)	0.0002 (4)	0.010 (9)	0.2 (2)	0.4 (5)	1.4 (9)	0.01 (1)	0.008 (9)	0.04 (2)	0.54	0.106
Co/Ni	2.79 (4)	1.04 (5)	0.72 (1)	0.73 (8)	0.4 (3)	0.20 (3)	0.49 (1)	0.68 (2)	0.73 (2)	0.44	0.80

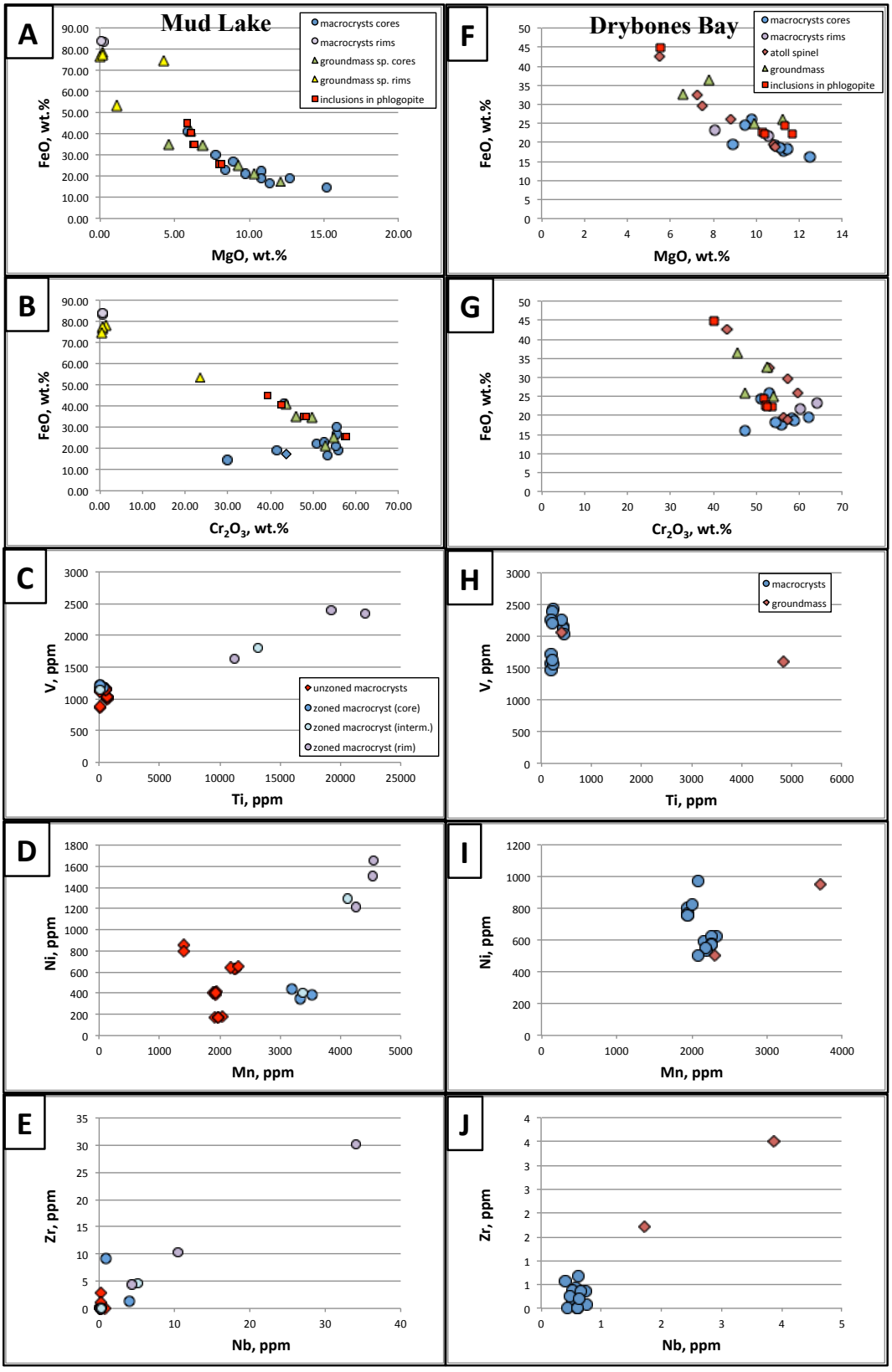

Figure 18 Compositional variations of spinel-group minerals from Mud Lake (A–E) and Drybones Bay (F–J).

The observed major-element variations in the zoned macrocrystic spinel are accompanied by a distinct trace-element trend, which involves a core-to-rim increase in V (from 1200 ppm to 2400 ppm), Mn (from 3200 ppm to 4550 ppm), Ni (from 350 ppm to 1650 ppm), Nb (from < 0.5 ppm to 34 ppm), and Zr (from below the detection limit to 30 ppm), and a decrease in Zn (from 5300 ppm to 2400 ppm; Figure 18c–e). Unzoned macrocrystic spinel shows little inter-granular trace-element variation and is comparable to the cores of the zoned macrocrysts (Figure 18c–e). The only noticeable difference is the lower levels of Mn and Zn in the unzoned macrocrysts relative to the zoned grains. The groundmass spinel, atoll spinel and inclusions in phlogopite were not analyzed for trace elements due to their small grain size.

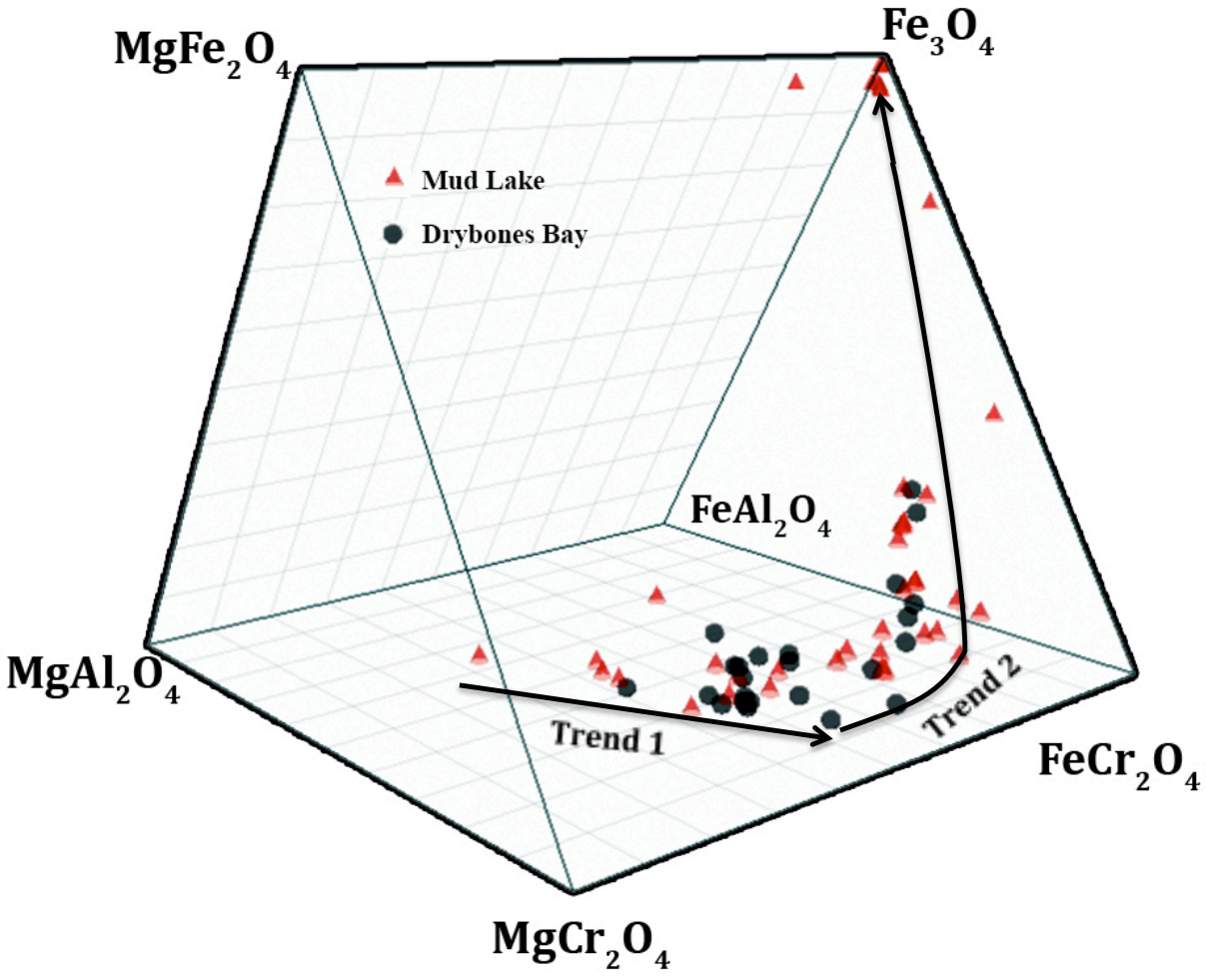

Figure 19 Composition of spinels from Mud Lake (cones) and Drybones Bay (circles) in the oxidized spinel prism. Macrocrysts plot along the aluminous magnesian chromite trend (Trend 1). Groundmass spinels and the evolved rims of zoned macrocrysts plot along Trend 2. Trends referenced from Mitchell (1986).

Plotting the spinel data on an oxidized spinel prism (Figure 19) shows that the composition of unzoned macrocrysts and the cores of zoned macrocrysts overlap, and plot along the aluminous magnesian chromite (AMC) trend (Mitchell, 1986). These AMC macrocrysts evolve towards higher Cr and Fe compositions at the expense of Al and Mg. Groundmass spinel and the rims of macrocrysts evolve along magmatic Trend 2 (Mitchell, 1986). Trend 2 defines the evolution of spinel along the $MgCr_2O_4$–$FeCr_2O_4$ edge of the prism, towards higher Fe/(Fe+Mg) ratios at low Fe^{3+} levels, followed by an increase in Fe^{3+} towards Fe_3O_4. The least evolved groundmass spinel (i.e. cores of zoned groundmass and atoll spinel) shows considerable overlap with the AMC macrocrysts, indicating a phenocrystic paragenesis (Mitchell, 1986).

5.4.2 Drybones Bay spinel-group minerals

Spinel macrocrysts range in size from 0.2 to 2.0 mm and form irregularly shaped grains with rounded to angular margins. Optically, they are dark red and translucent and appear to be homogeneous. A discontinuous crust of late-forming spinel mantles some macrocrysts. Groundmass spinel varies in size from 0.05 to 0.1 mm, and occurs as zoned, euhedral crystals with low-AZ (atomic mass) rims. The rims may be in contact with the cores or separated by a narrow gap, forming an atoll-type structure. The cores are most often homogeneous, but zoned cores have also been observed (Figure 15d).

Compositionally, the macrocrystic spinel from the Drybones Bay kimberlite is comparable to the macrocrysts from the Mud Lake kimberlite (Table 7; Figure 18). The spinel prism (Figure 19) shows they plot along the same evolutionary paths as the Mud Lake data; however, the least evolved Drybones Bay spinel is more enriched in Fe and Cr. The contents of MgO vary from 8.9 to 12.5 wt.%, Al_2O_3 from 7.2 to 22.0, FeO from 16.3 to 25.9 wt.%, and Cr_2O_3 from 47.3 to 62.2 wt.%. The narrow late-stage rims encrusting the macrocrysts do not deviate significantly from these values, showing similar levels of FeO, but slightly higher Cr_2O_3 contents and lower levels of MgO and Al_2O_3 (Figure 18f,g).

With the exception of two analyses, which are similar to the cores of spinel macrocrysts, atoll spinels are enriched in MgO and FeO, and depleted in Al_2O_3 relative to the macrocrystic spinel (Figure 18f,g). The Cr_2O_3 levels in both varieties are comparable. The major-element compositions of the groundmass spinel and spinel inclusions in phlogopite show some overlap with the atoll spinel, but the groundmass spinel shows a somewhat smaller variation in Mg, Fe, and Cr abundances (Figure 18f,g). The trace element composition of the macrocrystic spinel

from the Drybones Bay kimberlite is broadly similar to that of the unzoned macrocrysts and cores of the zoned macrocrystic spinel from Mud Lake. The bulk of the Drybones Bay material is relatively uniform in composition, with Ti ranging from 192 to 464 ppm, V from 1475 to 2430 ppm, Mn from 1940 to 2330 ppm, Co from 374 to 468 ppm, Ni from 500 to 970 ppm, and Zn from 1660 to 2090 ppm (Figure 18h,i). The two examined grains of atoll spinel are very different in terms of their trace element composition: one is compositionally similar to the bulk of the macrocrysts, whereas the other shows noticeably higher concentrations of Ti and Mn, and lower levels of Zn. Both grains of atoll spinel are characteristically enriched in Nb and Zr relative to the macrocrysts (Figure 18j).

5.5 Garnet

5.5.1 Mud Lake garnet

Garnet occurs as large fractured grains up to 1.5 mm across, and smaller irregular fragments with conchoidal fracture surfaces (Figure 20). Kelyphite rims composed of veins of serpentine anastomosing through a mass of radiating acicular phlogopite and chlorite crystals with disseminated iron oxides (Figure 20) occur on garnets with peridotitic compositions, and may be well preserved or removed during transport to reveal a characteristically etched surface. In heavily fractured garnet macrocrysts, discrete fragments are cemented together by dolomite and serpentine (if a kelyphite rim is present; Figure 20), or by quartz in non-pyrope garnets.

The major-element composition (Table 8; Figure 21; Figure 22; Figure 23a) suggests three sources of garnet. Large macrocrystic garnets with well-formed kelyphite rims correspond to Cr-Ca-rich pyrope (3.2–7.5 and 5.1–7.6 wt.% respective oxides). Such garnets are common in lherzolitic xenoliths from the S1 domain of the southern Slave craton (Grütter et al., 1999). Calcic pyrope-almandine garnets lack kelyphite rims and are 1.5 to 2 times richer in Fe relative to the pyrope macrocrysts, but very low in Cr ($\leq$ 0.1 wt.% Cr_2O_3). These are consistent with eclogite garnets from other kimberlite pipes (Figure 21; Chappell and White, 1970; Mottana, 1986). Non-eclogitic crustal garnets have an almandine composition, with three times as much Fe and up to 15 times as much Mn compared to the pyrope macrocrysts, and plot in the field of granulite garnets (Figure 21). The pyrope garnets can be further subdivided into lherzolitic (G9) and wehrlitic (G12) garnets (Figure 22), on the basis of their CaO and Cr_2O_3 contents, and Mg# (Grütter et al., 2004).

The macrocrystic garnets show significant inter-granular variations in their trace-element composition (Figure 23b–d). The abundances of Ti range from 8 to 325 ppm, V from 170 to 420 ppm, Sc from 85 to 200 ppm, LREE from 0.1 to 3.8 ppm, and HREE from 0.2 to 3.3 ppm. In terms of their REE budget, the macrocrysts vary from LREE- to HREE-dominant. Overall, the macrocrystic garnets are characteristically depleted in REE relative to the inferred crustal garnets, which contain up to 320 ppm REE. In addition to Cr (< 700 ppm), the crustal garnets are poorer in Ni, but richer in Mn and Zn with respect to the pyrope. One fragment of strained Cr-poor garnet is unusual in containing very low levels of Cr, Mn, Zn and REE at high Ni levels.

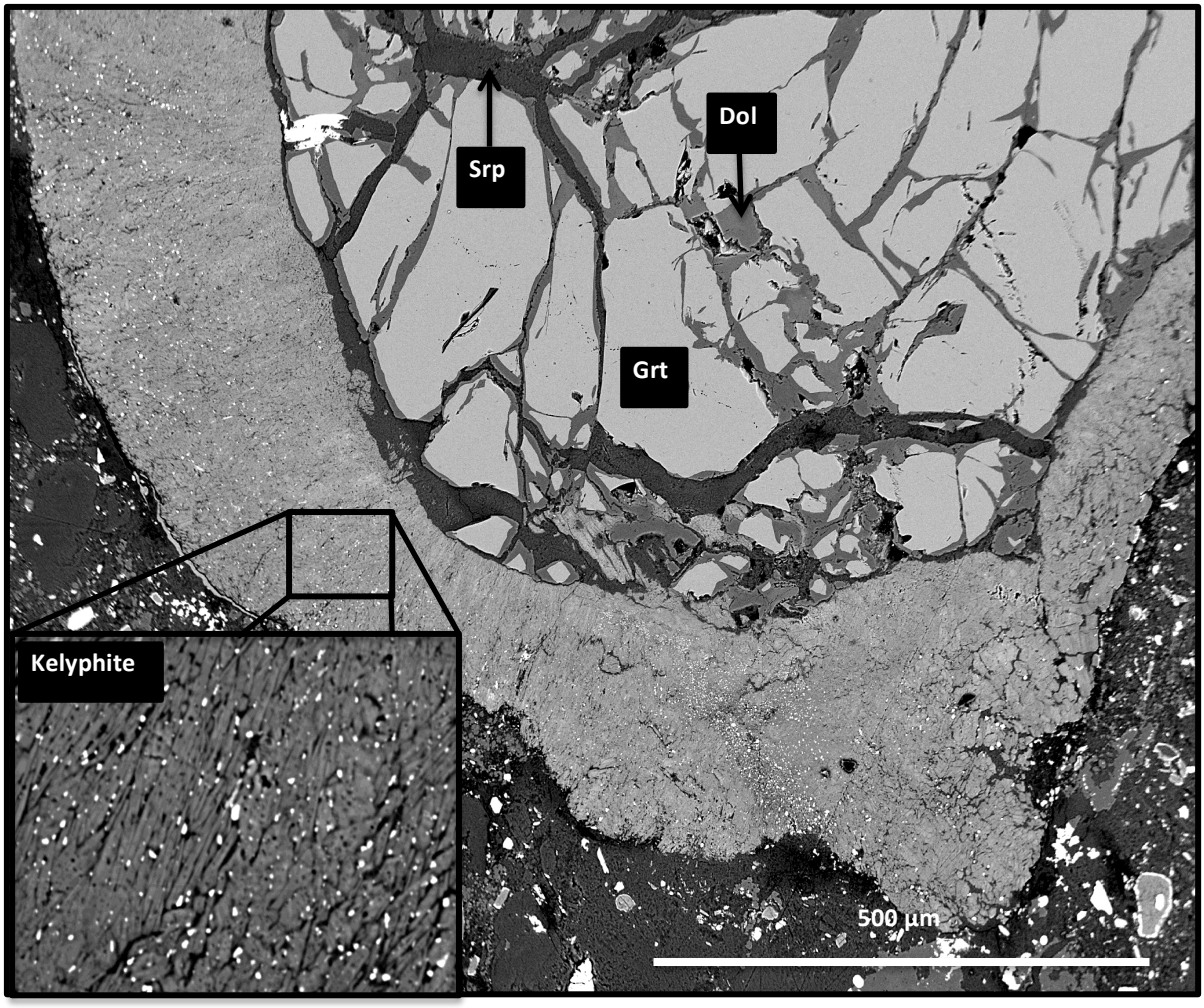

Figure 20 BSE image of a Mud Lake pyrope garnet with an inset showing the texture of the kelyphite rim under higher magnification. Grt = garnet; Srp = serpentine; Dol = dolomite.

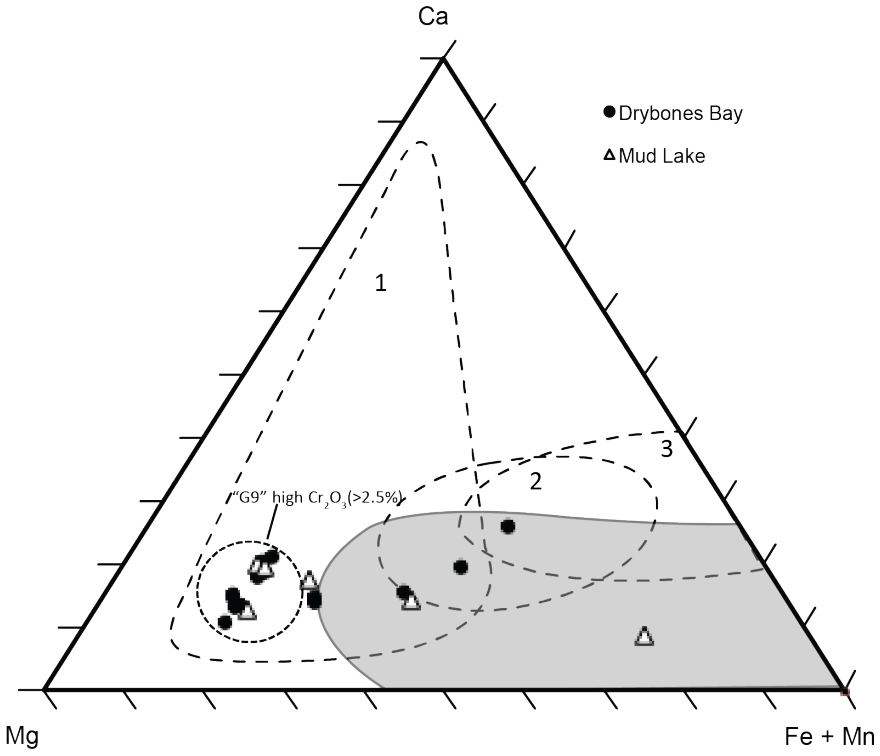

Figure 21 Composition of garnets from Mud Lake and Drybones Bay, shown in terms of atomic proportions of Fe + Mn (almandine + spessartine), Ca (grossular + andradite) and Mg (pyrope), compared with the compositional fields of garnets from eclogites and granulites. The shaded area is the field of granulites; field 1 is eclogites from kimberlite pipes; field 2 is eclogites from amphibolite-facies terrains; and field 3 is eclogites associated with glaucophane schist. Granulite and eclogite fields are from Chappell and White (1970).

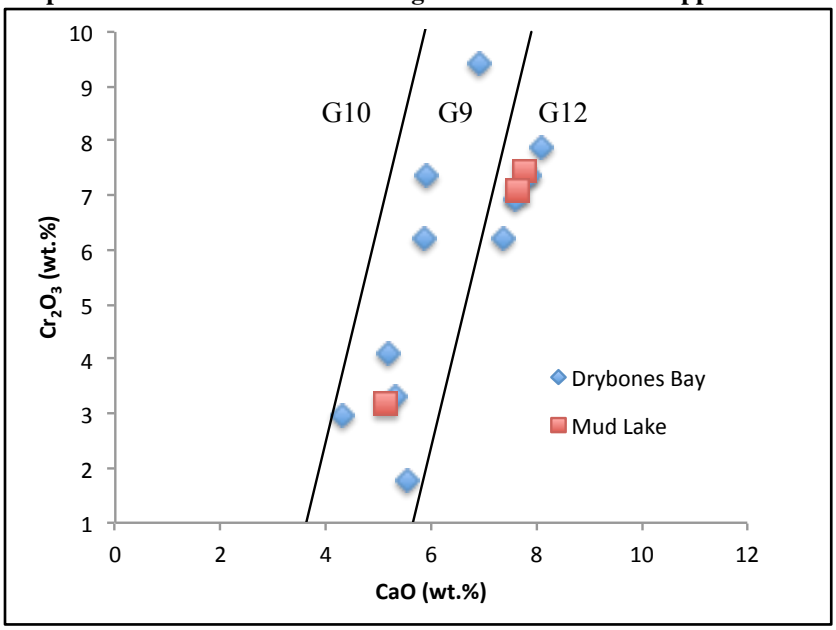

Figure 22 G-number classification of pyrope garnets from Mud Lake and Drybones Bay (Grütter et al., 2004).

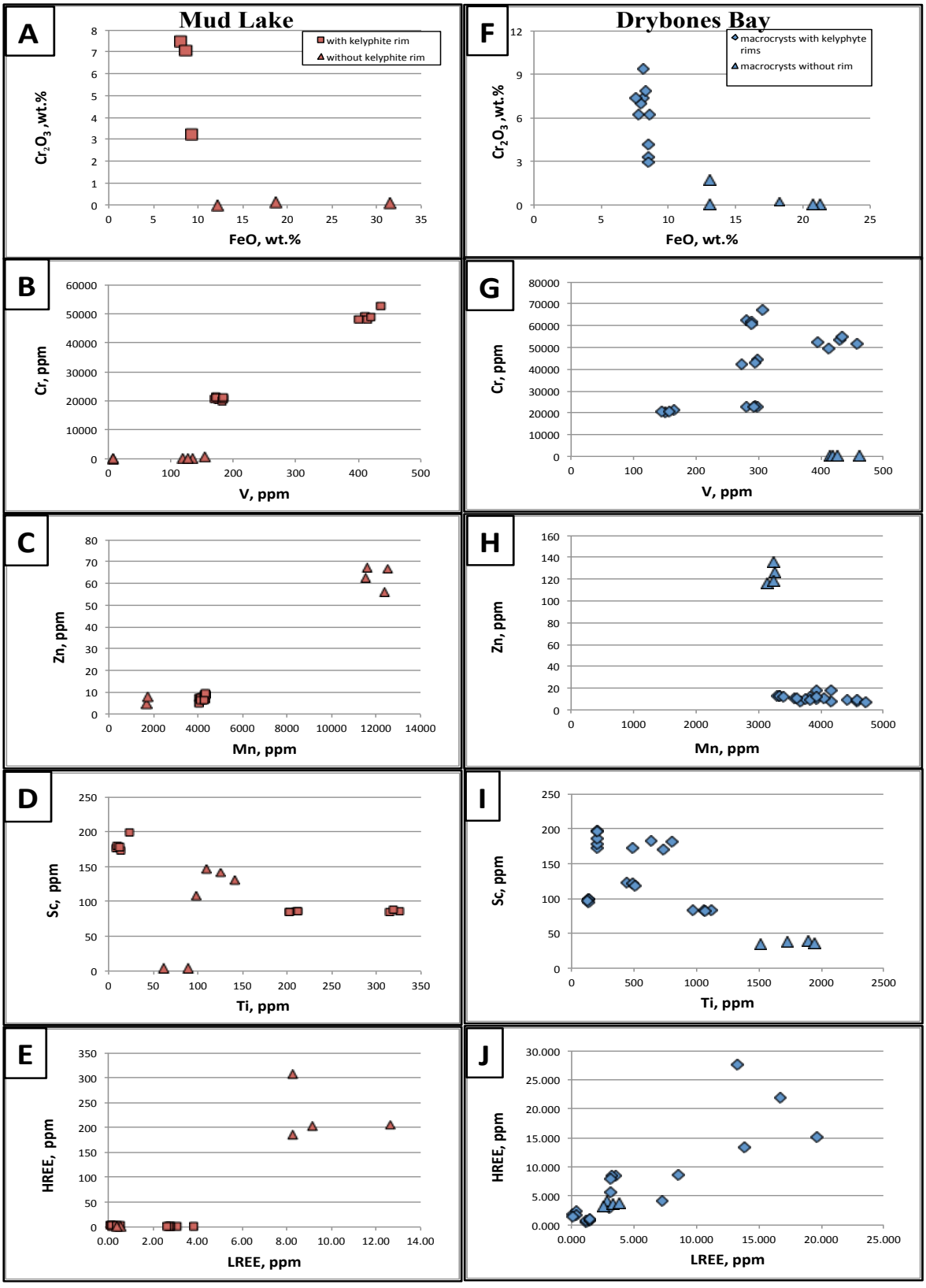

Figure 23 Compositional variation of garnet from Mud Lake (A–E) and Drybones Bay (G–J).

Table 8 Representative major- and trace-element compositions of garnet macrocrysts and xenocrysts from Mud Lake and Drybones Bay.

	Mud Lake						Drybones Bay					
Oxide, wt.%	1	2	3	4	5	6	7	8	9	10	11	12
SiO_2	42.21	41.15	40.17	40.64	42.31	38.57	41.31	42.84	41.64	41.92	39.63	39.95
TiO_2	n.d.	n.d.	n.d.	0.23	n.d.	n.d.	0.07	0.19	0.05	0.06	0.09	0.48
Al_2O_3	21.57	17.84	17.42	22.55	23.60	21.54	17.19	20.54	16.83	22.67	21.27	21.52
Cr_2O_3	3.02	7.47	7.08	0.11	n.d.	0.09	7.36	2.96	7.91	0.04	0.06	0.06
FeO	9.33	8.11	8.69	18.79	12.21	31.50	8.12	8.48	8.29	13.05	21.28	20.70
MnO	0.39	0.09	0.17	0.51	0.22	1.35	0.53	0.42	0.60	0.31	0.43	0.43
MgO	19.63	17.54	17.53	13.14	16.45	5.39	17.53	20.75	16.80	16.57	7.84	10.58
CaO	5.13	7.77	7.64	5.47	6.85	3.07	7.87	4.31	8.09	5.71	9.79	7.57
Total	101.56	100.12	98.96	101.44	101.65	101.61	99.98	100.49	100.21	100.33	100.39	101.29
End-member composition												
Almandine	18.19	16.41	17.42	37.78	24.16	67.88	62.52	71.94	60.86	58.82	28.98	37.95
Pyrope	68.22	63.26	62.62	47.09	58.03	20.70	16.24	16.49	16.84	25.98	44.12	41.66
Grossular	12.81	20.14	19.62	14.09	17.37	8.48	20.17	10.74	21.06	14.57	26.00	19.52
Spessartine	0.77	0.18	0.35	1.04	0.44	2.95	1.07	0.83	1.23	0.63	0.90	0.88

(1-3) Cr-rich pyrope with kelyphite rims; (4-6) garnets without kelyphite rims; (7-9) Cr-rich pyrope with kelyphite rims; (10-12) garnets without kelyphite rims; n.d. = not detected.

Element	Mud Lake				Drybones Bay			
ppm	1 (n = 5)	2 (n = 7)	3 (n = 4)	4 (n = 2)	5 (n = 5)	6 (n = 4)	7 (n = 4)	8 (n = 4)
S	182 (10)	86.2 (8)	132 (17)	4.2 (1)	186 (11)	177 (6)	83.3 (6)	37 (2)
Ti	13 (6)	255 (60)	119 (18)	75 (19)	203 (2)	668 (137)	1057 (62)	1774 (197)
V	416 (13)	177 (6)	134 (15)	7.3 (3)	426 (23)	291 (11)	155 (9)	430 (21)
Cr	9312 (1837)	20770 (495)	355 (214)	27 (5)	52360 (2040)	63000 (2981)	20685 (455)	257 (3)
Mn	4115 (67)	4287 (86)	12023 (527)	1733 (13)	4494 (213)	4021 (110)	3348 (36)	3228 (52)
Co	39.9 (3)	45.0 (9)	42 (2)	90 (1)	37.1 (8)	39.8 (7)	48 (1)	57 (2)
Ni	20.5 (9)	16 (2)	0.2 (4)	18 (4)	21 (1)	44 (3)	48 (2)	1.4 (7)
Zn	7 (1)	8 (1)	63 (5)	6 (2)	8.4 (9)	15 (4)	12.7 (0.8)	124 (9)
Y	0.06 (4)	4.9 (4)	428 (86)	0.51 (9)	0.67 (7)	23 (12)	11 (2)	3.6 (2)
Zr	0.1 (1)	1.1 (4)	11 (6)	1.17 (5)	0.11 (9)	292 (26)	53 (6)	10.9 (7)
Nb	0.5 (1)	0.01 (2)	0.002 (4)	0.11 (3)	0.33 (5)	1.3 (9)	0.25 (4)	0.005 (3)
La	0.36 (7)	0.01 (3)	0.5 (8)	n.d.	0.08 (2)	0.5 (5)	0.01 (1)	0.07 (6)
Ce	1.9 (2)	0.005 (8)	1 (1)	0.021 (1)	0.53 (7)	2.1 (1)	0.25 (3)	0.3 (3)
Pr	0.16 (6)	0.01 (1)	0.1 (2)	0.006 (6)	0.11 (1)	0.6 (2)	0.11 (1)	0.09 (7)
Nd	0.6 (4)	0.1 (1)	1.6 (3)	0.12 (6)	0.56 (9)	6 (1)	1.2 (2)	1.1 (2)
Sm	0.05 (6)	0.06 (5)	6.3 (6)	0.07 (5)	0.08 (5)	4.5 (2)	1.1 (1)	1 (1)
Eu	0.002 (4)	0.06 (3)	0.32 (5)	0.265 (4)	0.01 (1)	2.5 (2)	0.54 (8)	0.57 (5)
Gd	0.1 (2)	0.1 (2)	27 (2)	0.1 (1)	0.1 (1)	7.2 (9)	1.7 (3)	1.2 (1)
Tb	0.007 (5)	0.06 (3)	7.7 (8)	0.01 (2)	0.009 (7)	1.3 (3)	0.36 (7)	0.17 (1)
Dy	0.02 (2)	0.7 (1)	66 (11)	0.14 (2)	0.11 (5)	6 (3)	2.2 (4)	0.9 (2)
Ho	0.004 (8)	0.17 (2)	15 (4)	0.03 (3)	0.05 (2)	1.0 (5)	0.44 (7)	0.153 (8)
Er	0.07 (2)	0.61 (7)	45 (16)	0.09 (8)	0.09 (5)	2 (1)	1.2 (3)	0.5 (1)
Tm	0.02 (2)	0.11 (3)	7 (2)	n.d.	0.02 (2)	0.2 (1)	0.17 (3)	0.08 (1)
Yb	0.15 (5)	0.9 (2)	51 (19)	0.13 (1)	0.4 (1)	1.4 (7)	1.4 (3)	0.57 (5)
Lu	0.05 (1)	0.15 (3)	6 (3)	0.023 (4)	0.05 (1)	0.22 (9)	0.22 (6)	0.09 (2)
Hf	0.02 (2)	0.05 (4)	0.22 (8)	0.005 (6)	0.02 (2)	4.9 (8)	0.7 (1)	0.23 (4)
Ta	0.03 (2)	0.002 (4)	0.002 (4)	0.01 (1)	0.015 (8)	0.1 (7)	0.028 (4)	0.008 (2)
Pb	0.06 (7)	0.01 (1)	0.1 (2)	0.016 (2)	0.01 (1)	0.1 (1)	0.02 (1)	0.03 (2)
Th	0.09 (2)	0.008 (9)	0.01 (3)	0.06 (6)	0.04 (2)	0.08 (5)	0.02 (1)	0.03 (2)
U	0.06 (2)	0.009 (10)	0.05 (5)	0.3 (2)	0.01 (1)	0.07 (3)	0.008 (7)	n.d.
ΣLREE	3 (0.5)	0.2 (2)	10 (2)	0.5 (1)	1.4 (2)	16 (3)	3.2 (2)	3.1 (6)
ΣHREE	0.4 (0.2)	2.7 (3)	225 (55)	0.5 (1)	0.8 (2)	20 (7)	8 (1)	3.7 (4)

Mud Lake: (1-2) with kelyphite rims; (3-4) without kelyphite. Drybones Bay: (5-7) with kelyphite rims; (8) without kelyphite.

5.5.2 Drybones Bay garnet

Garnets occur as large rounded clasts, typically 1.0 to 8.0 mm in diameter, and as smaller irregular fragments (Figure 15e). Fractures are ubiquitous and infilled with serpentine and groundmass minerals (phlogopite, apatite, spinel). The garnets may be mantled with kelyphite rims, as seen in Mud Lake (Figure 20), or overgrown with phlogopite. These rims vary in their degree of preservation from intact to mostly removed, with only scant remnants left in concavities, to completely absent. Some garnets lacking kelyphite rims show evidence of strain. Polycrystalline garnet aggregates are rare.

The Drybones Bay garnets show similar compositional variations to those from Mud Lake (Table 8; Figure 21; Figure 22). The macrocrysts surrounded by the kelyphite rims correspond to Cr-Ca-rich pyrope, whereas those lacking kelyphitic rims are depleted in Cr and enriched in Fe (Figure 23f). The major-element compositions of the strongly resorbed anhedral macrocrysts overgrown by thick phlogopite rims are comparable to those of the macrocrysts rimmed by kelyphite (Figure 23f). Some grains lacking kelyphitic rims correspond to Ca-rich, but Cr-poor (6.0–9.8 and < 0.2 wt.% respective oxides) members of the pyrope-almandine series, and are similar to the eclogite garnets identified in the Mud Lake dyke. These eclogite garnets have a range of compositions that spans the overlapping fields of eclogite garnet from kimberlite, amphibolite and glaucophane schist (Figure 21). The pyrope garnets comprise G9 and G12 type garnets (Figure 22).

The macrocrysts rimmed by kelyphite are enriched in Sc (up to 200 ppm) and Mn (up to 4720 ppm), and depleted in Zn (≤ 18 ppm) and Ti (≤ 1124 ppm) relative to the macrocrysts lacking kelyphitic rims (35–39 ppm Sc, 3150–3260 ppm Mn, 116–136 ppm Zn and 1514–1950 ppm Ti; Figure 23g–j). Similar to the Mud Lake garnets, the Drybones Bay samples vary from LREE- to HREE-dominant. Notably, the Drybones Bay macrocrysts exhibit overall higher levels of ΣREE (up to 41 ppm) and Y (up to 39 ppm) relative the Mud Lake garnets (≤ 5 ppm ΣREE and ≤ 6 ppm Y).

5.6 Zircon

5.6.1 Mud Lake zircon

Zircon grains range in size from 0.1 to 1.1 mm and are present in most samples. The grains lack discernible crystal faces, being rounded to subrounded with eroded margins, and are

mantled with discrete crystals of baddeleyite (ZrO_2) resulting from reaction with the host magma. The large grain size, anhedral habit, and the baddeleyite reaction rim are features consistent with zircon from kimberlite (Kresten et al., 1975; Belousova et al., 1998; 2002). The grains appear homogeneous in BSE and CL images (Figure 24). On the basis of the petrographic features, the trace-element data, and isotopic composition (see Chapter 7), these zircons are interpreted as fragmented macrocrysts.

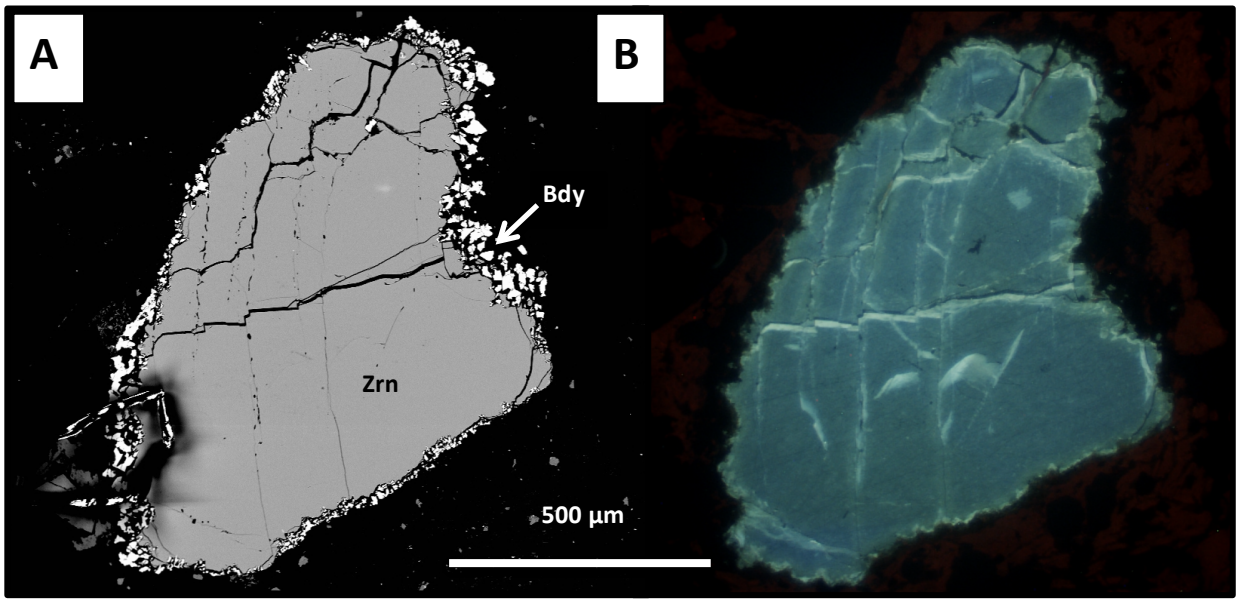

Figure 24 BSE and CL images of a zircon macrocryst: (A) BSE image of a zircon macrocryst mantled with discrete baddeleyite; (C) CL image of the same zircon shows the grain is homogeneous, with illumination artifacts occurring as bright lines along fractures. Zrn = zircon; Bdy = baddeleyite.

The trace-element composition of zircon can be used as an indicator of provenance (Belousova et al., 2002). The range of major- and trace-element concentrations in zircon from the Mud Lake kimberlite is given in Table 9. The mineral shows only minor variations in its major-element composition, with ZrO_2 levels ranging from 64.8 wt.% to 65.5 wt.% (WDS data). Hence, Zr was chosen as an internal standard for the LA-ICP-MS measurements. The Zr/Hf ratio varies from 46 to 62, which is somewhat higher than the average value of 36 reported by Belousova et al. (1998) for kimberlitic zircon, but within the range established by Kresten et al. (1975). The levels of Y, REE, Th and U in the Mud Lake zircon are consistently low, not exceeding 26, 18, 2 and 8 ppm, respectively. The concentration of these elements is considered to be a good indicator of the source rock, and results are in good agreement with the previously reported data for kimberlitic zircon (Kresten et al., 1975; Belousova et al., 1998; 2002). In comparison, granitic zircon on average has 2515 ppm Y, 368 ppm Th, 764 ppm U, and up to

several wt.% REE (Belousova et al., 2002). The Th/U ratio is consistently low (0.22 ± 0.05). The Y and REE abundances are much lower than those in zircon from the Wekusko Lake carbonatite, which were also analyzed in the present work for comparative purposes (Figure 25). Chondrite-normalized REE patterns show a steep positive slope leveling off at Ho, in accord with the greater structural affinity of this mineral for heavy REE (Belousova et al., 2002). The most remarkable feature of these zircons is a strong positive Ce anomaly (Ce/Ce* = 14 ± 4), coupled with the absence of Eu anomaly (Figure 25). The Ce anomaly indicates high O_2 fugacity in the parental magma (Trail et al., 2012). The Y/Ho ratio ranges from 24 to 35, averaging 28 ± 4, which is close to the primitive mantle value of 28.9 (McDonough and Sun, 1995), and effectively rules out equilibration of the zircon with any crustal fluids (Bau, 1996). The Mud Lake zircons are characterized by very low Nb/Ta ratios (1.1 ± 0.1), with Nb and Ta concentrations not exceeding 3.5 ppm each, which is typical for kimberlitic zircon (Belousova et al., 1998). While granitic zircon has Nb/Ta ratios that span the entire range measured in igneous zircon (from 0.3 to 48), they typically contain higher levels of Nb and Ta, and can be distinguished by higher levels of Y and REE (Belousova et al., 2002). The Mud Lake zircon consistently matches the criteria for kimberlitic zircon in the classification tree used for predicting source rock types (see Figure 7 in Belousova et al., 2002). This classification tree is based on statistical analysis, and has a 94% confidence rate for predicting kimberlite as the source rock. Overall, our data show that the trace-element budget of the analyzed grains is in accord with their proposed kimberlitic origin. Hence, we confidently interpret this zircon as macrocrysts, rather than xenocrysts derived from crustal rocks, and consider its age to represent the timing of kimberlitic magmatism (see Chapter 7).

5.6.2 Drybones Bay zircon

Zircon macrocrysts (0.2–0.5 mm) are present as angular fragments with rounded, embayed margins. Rims of baddeleyite occur as a thin discontinuous crust (Figure 15f) or as discrete crystals mantling some of the zircon macrocrysts. Cathodoluminescence images show the crystals are chemically homogeneous. Small (50–100 μm), concentrically zoned, euhedral zircons occur in the groundmass of some samples, and are suspected to be xenocrystic in origin based to the occurrence of very similar zircons in the phlogopite-calcite xenoliths.

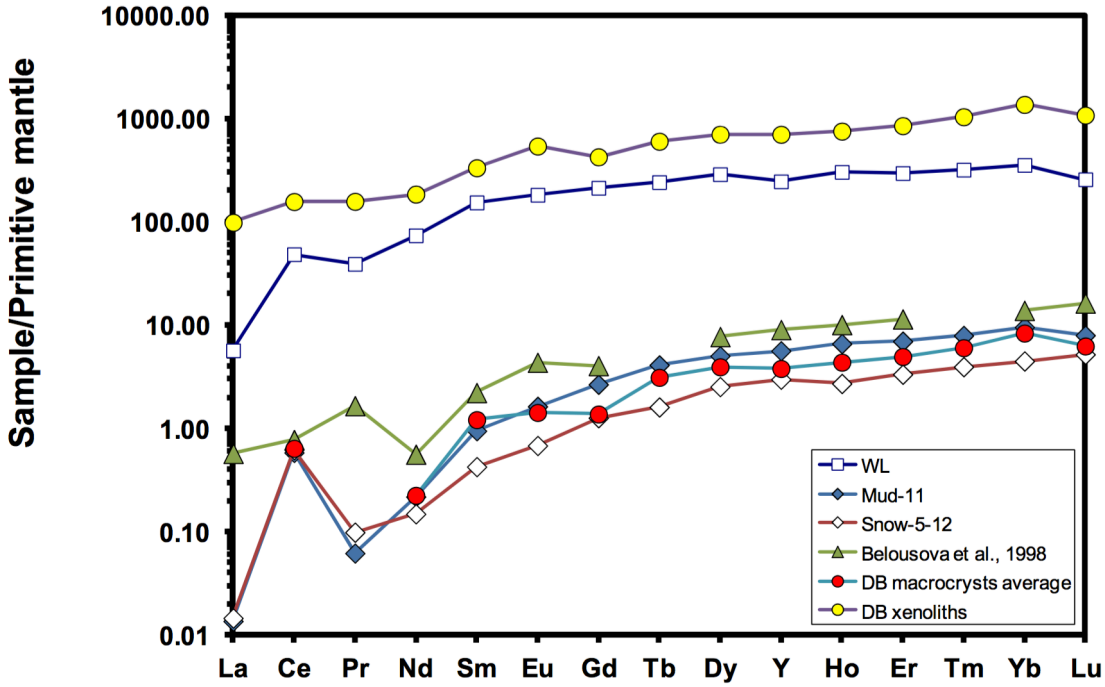

Figure 25 Comparison of primitive mantle-normalized REE patterns of zircon (calculated from average analyses) from the Mud Lake (Mud-11, Snow-5-12) and Drybones Bay (DB) kimberlites, published kimberlitic zircon data (Belousova et al., 1998) and the Wekusko Lake (WL) carbonatite, (Chakhmouradian et al., 2009). Normalized to pyrolite (McDonough and Sun, 1995).

As with the Mud Lake samples, zircon from Drybones Bay is relatively uniform in terms of its major-element composition (Table 9), with ZrO_2 levels ranging from 61.6 to 65.9 wt.% and Zr/Hf ratios (38–45) higher than the average value for kimberlitic zircon reported by Belousova et al. (1998). Overall, the chondrite-normalized patterns of the macrocrystic Drybones Bay zircon closely resemble those of the Mud Lake samples (Figure 25). Notably, the abundances of La and Pr in the Drybones Bay zircon are at or below the detection limits for these elements. Hence, the magnitude of positive Ce anomaly, evident from Figure 25, could not be calculated.

The Drybones Bay zircon macrocrysts show consistently low levels of ΣREE (≤ 3 ppm), Y (≤ 27 ppm), Th (≤ 2.9 ppm) and U (≤ 6.5 ppm). The mineral is characterized by low Th/U (0.32 ± 0.07) and Nb/Ta (0.96 ± 0.07) ratios, which is in agreement with the data for other kimberlitic zircons (Belousova et al., 1998). Based on the classification tree of Belousova et al. (2002), these grains fit the criteria for kimberlitic zircon.

Table 9 Representative major- and trace-element compositions of zircon macrocrysts and xenocrysts from Mud Lake and Drybones Bay.

	Mud Lake			Drybones Bay				
Oxide, wt.%	1	2	3	4	5	6	7	8
SiO_2	32.08	32.01	31.22	32.84	32.90	32.53	32.74	32.62
ZrO_2	65.49	65.52	64.84	61.64	64.97	62.03	65.91	60.20
HfO_2	1.50	1.57	1.62	1.63	1.67	1.39	1.70	1.25
Total	99.07	99.09	97.68	96.11	99.54	95.95	100.35	94.07
Zr/Hf	44	42	40	38	39	45	39	48

(1-3) Mud Lake macrocrysts; (4-7) Drybones Bay macrocrysts: (4) K-1; (5) K-2; (6) K-3; (7) K-8; (8) Drybones Bay euhedral zoned xenocryst.

	Mud Lake		Drybones Bay			
Element, ppm	1 (n = 4)	2 (n = 4)	3 (n = 3)	4 (n = 3)	5 (n = 6)	6 (n = 3)
Mg	83 (33)	106 (22)	n.d.	n.d.	5 (12)	2239 (2058)
Ca	180 (226)	270 (70)	n.d.	n.d.	n.d.	n.d.
Sc	812 (19)	695 (23)	787 (63)	794 (12)	792 (44)	927 (57)
Ti	15.2 (0.9)	14.3 (4)	14.3 (0.3)	4 (7)	12 (13)	83 (55)
V	n.d.	n.d.	n.d.	n.d.	n.d.	17 (5)
Mn	n.d.	n.d.	n.d.	n.d.	n.d.	81 (32)
Sr	n.d.	n.d.	n.d.	n.d.	n.d.	57 (9)
Y	24 (1)	13 (1)	18 (1)	12.1 (7)	18 (9)	2257 (751)
Nb	2.5 (1)	3 (3)	4.8 (2)	3.0 (3)	3.8 (2)	54 (48)
La	0.009 (6)	0.011 (9)	0.03 (2)	n.d.	n.d.	41 (14)
Ce	0.98 (3)	1.04 (5)	1.11 (2)	0.94 (5)	1.1 (2)	179 (76)
Pr	0.016 (5)	0.025 (1)	0.01 (2)	n.d.	n.d.	27 (12)
Nd	0.27 (3)	0.19 (4)	0.2 (4)	0.2 (2)	0.3 (4)	167 (74)
Sm	0.38 (3)	0.17 (8)	0.4 (2)	0.4 (1)	0.5 (3)	101 (48)
Eu	0.25 (6)	0.1 (3)	0.195 (2)	0.15 (2)	0.3 (2)	60 (27)
Gd	1.4 (2)	0.69 (3)	1.2 (2)	0.4 (6)	1 (1)	171 (64)
Tb	0.41 (3)	0.159 (2)	0.24 (5)	0.20 (1)	0.4 (2)	44 (15)
Dy	3.4 (3)	1.7 (2)	2.4 (1)	1.9 (1)	3 (2)	364 (137)
Ho	0.98 (4)	0.40 (7)	0.66 (3)	0.50 (3)	0.7 (4)	87 (28)
Er	3.1 (1)	1.5 (2)	2.3 (1)	1.7 (1)	2 (1)	281 (72)
Tm	0.54 (5)	0.27 (1)	0.40 (7)	0.31 (2)	0.5 (2)	57 (15)
Yb	4.2 (3)	2 (1)	3.7 (2)	2.9 (1)	4 (2)	487 (107)
Lu	0.54 (3)	0.35 (2)	0.50 (6)	0.40 (9)	0.4 (2)	60 (11)
Hf	8548 (533)	9925 (509)	12320 (416)	12290 (167)	11992 (605)	12400 (458)
Ta	2.16 (8)	3.1 (3)	5.00 (4)	3.5 (3)	3.8 (5)	3 (1)
Pb	0.19 (6)	0.12 (3)	0.11 (2)	0.06 (5)	0.09 (7)	24 (2)
Th	1.87 (9)	1.2 (2)	1.9 (3)	1.39 (7)	1.9 (8)	372 (215)
U	7.0 (5)	7 (2)	5.9 (4)	4.7 (3)	6 (1)	717 (333)
ΣLREE	1.91 (4)	1.5 (1)	2.0 (3)	1.7 (0.2)	2 (1)	575 (251)
ΣHREE	14.6 (8)	7 (5)	11.3 (5)	8.2 (0.9)	12 (6)	1551 (442)
Th/U	0.27 (2)	0.18 (3)	0.32 (7)	0.298 (0.002)	0.34 (8)	0.5 (3)
Nb/Ta	1.14 (7)	0.97 (8)	0.96 (6)	0.88 (0.09)	0.99 (8)	18 (9)
Y/Ho	24.6 (8)	32 (3)	27.5 (6)	24.3 (0.4)	27 (4)	25.7 (5)
Ce/Ce*	16 (4)	11 (3)	17 (17)	n.a.	n.a.	1.25 (6)

(1-2) Mud Lake macrocryst; (3-5) Drybones Bay macrocrysts; (6) Drybones Bay euhedral zoned xenocryst; n.d.=not detected; n.a.=not available.

The zoned euhedral zircon crystals observed in the groundmass (see petrographic description above) show significant enrichment in the majority of trace elements, including Mg (up to 1300 ppm), Ti (up to 144 ppm), V (up to 20 ppm), Mn (up to 104 ppm), Sr (up to 64 ppm), Y (up to 3000 ppm), Nb (up to 107 ppm), REE (up to 2750 ppm), Pb (up to 25 ppm), Th (up to 384 ppm) and U (up to 1080 ppm). This zircon exhibits a gently sloping positive chondrite-normalized REE profile resembling that of the Wekusko Lake material, but is characterized by appreciably higher REE levels (Figure 25). The classification tree predicts these grains originate from a granitic source rock (based on > 20.7 ppm Lu, > 38 ppm U, > 0.58 ppm Th, > 0.8 wt.% Hf, Ce/Ce* < 3.9 and < 170 ppm Nb). These euhedral zircons are interpreted as xenocrysts, though their source is not entirely clear. Although the classification scheme of Belousova et al. (2002) predicts these zircons were derived from the granodiorite host rock, their REE distribution pattern is very similar to carbonatitic zircon from Wekusko Lake (Figure 25) and these grains morphologically resemble zircon hosted in the phlogopite-calcite xenoliths. Further investigation of these xenocrysts is warranted.

5.7 Carbonate minerals

5.7.1 Mud Lake carbonate minerals

Dolomite is the principal carbonate mineral in the Mud Lake kimberlite dyke, it occurs in several different morphologies: lath-shaped microphenocrysts (100 × 20 μm; Figure 26a,b); rhombohedral crystals with clear cores and turbid rims (Figure 26c,d); lacy frill-like overgrowths (Figure 26e,f); blocky segregations (Figure 26g,h); and discrete rhombohedral crystals associated with altered minerals. The lath-shaped microphenocrysts occur as tightly packed masses in the groundmass, and are interpreted as a primary magmatic phase. The rhombohedral crystals are comparable in size to the lath-shaped dolomite and exhibit similar cathodoluminescence (cf. Figure 26b and d). It is probable that the laths and rhombs are the same phase, but viewed from different perspectives, with the short axis of the crystal either parallel to the viewing plane or normal to it. Dolomite associated with carbonate-serpentine segregations occurs as frill-like overgrowths lining pools of serpentine (Figure 26f) and as blocky segregations (Figure 26h). These dolomite segregations are sometimes clear but usually have a turbid appearance due to cryptocrystalline inclusions. These inclusions impart an apparent zoning that is noticeable in transmitted light, but barely perceptible in BSE images.

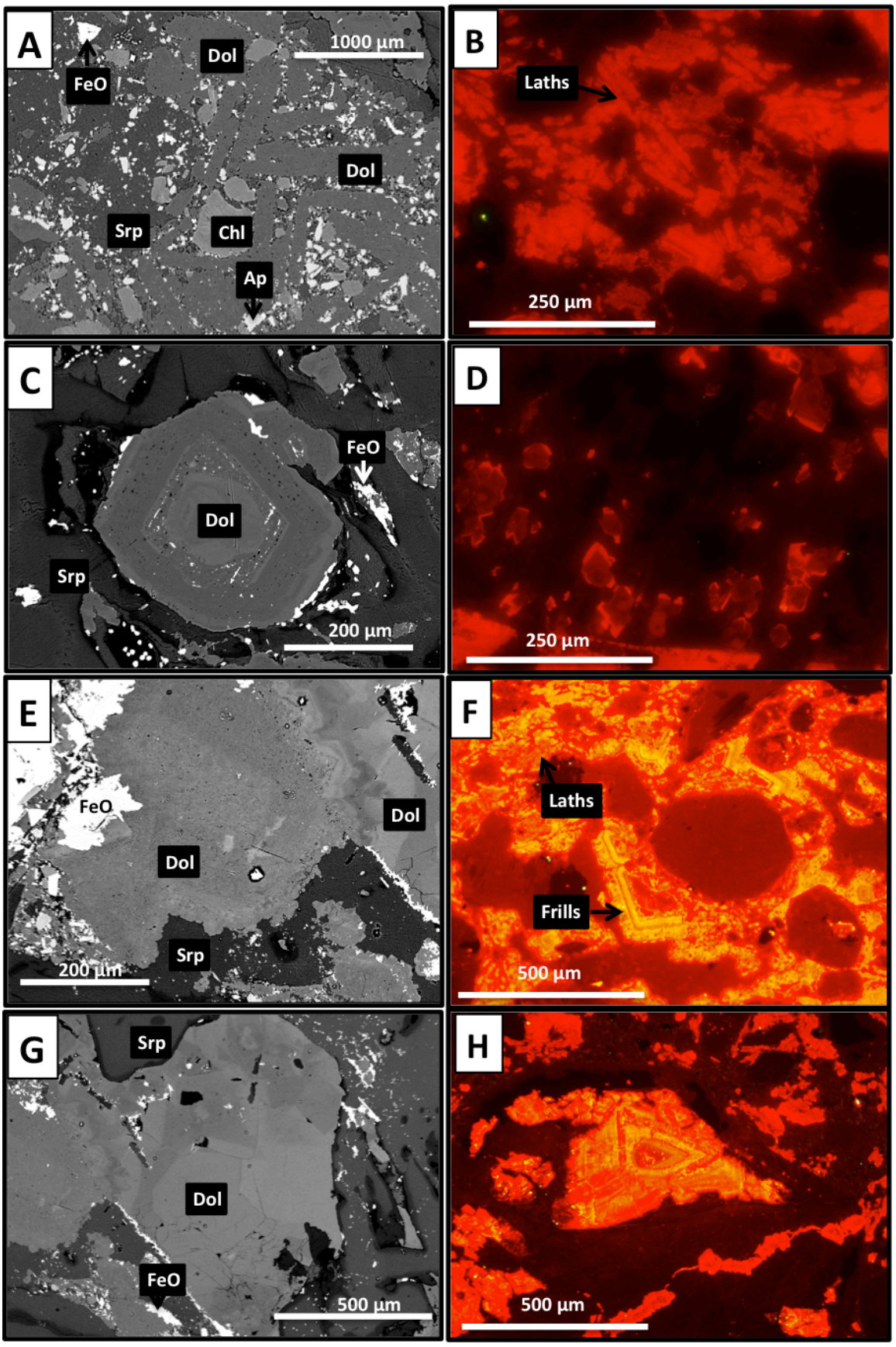
A
FeO
Dol
1000 µm
Dol
Srp
Chl
Ap
B
Laths
250 µm
C
FeO
Dol
Srp
200 µm
D
250 µm
E
FeO
Dol
Dol
Srp
200 µm
F
Laths
Frills
500 µm
G
Srp
Dol
FeO
500 µm
H
500 µm

Figure 26 (pp. 79) BSE and CL images of Mud Lake carbonate minerals: (A) BSE image of groundmass composed of primary lath-shaped dolomite microphenocrysts, serpentine, spinel and apatite; (B) CL image of microphenocrystic dolomite laths; (C) BSE image of rhombohedral dolomite with a turbid inclusion-rich rim; (D) CL image of rhombohedral dolomite; (E) BSE and (F) CL images of lacey dolomite frills with turbid inclusion-rich textures; (G) BSE image of clear, blocky segregationary dolomite; (H) CL image blocky segregations with concentric zoning. Ap = apatite; Dol = dolomite; Chl = chlorite; Srp = serpentine; FeO = iron oxide.

Dolomite in carbonated olivine pseudomorphs is clear and has a blocky segregation texture. Calcite is present as late-forming veins and occasionally as a minor component of replacement assemblages. Compositionally, all of the carbonate phases analyzed by WDS were found to be unremarkable stoichiometric dolomite or calcite, with MnO not exceeding 1 wt.%, and < 1 wt.% FeO on average, and Sr and Ba contents at or below the detection limit. Hence, no trace-element analyses were preformed. See Appendix II for the WDS data.

5.7.2 Drybones Bay carbonate minerals

Primary carbonate phases were not observed in the Drybones Bay kimberlite. Relevant occurrences of secondary carbonate are described in the context of the replacement assemblages and rock textures in Chapters 4 and 5. As was the case with the Mud Lake carbonate, there is nothing noteworthy to report about the composition of the Drybones Bay carbonate, thus the data is relegated to the Appendix II.

5.8 Rutile

5.8.1 Mud Lake rutile

The major- and trace-element composition of rutile is given in Table 10. The major-element composition shows little variation, with 98.09–98.95 wt.% TiO_2 and 0.21–0.49 wt.% FeO, whereas the trace-elements show considerable variation. The concentration of Cr ranges from 254 to 2720 ppm, Zr from 766 to 2630 ppm, Nb from 2667 to 5972 ppm and Ta from 135 to 443 ppm.

5.8.2 Drybones Bay rutile

Rutile from Drybones Bay shows similar major- and trace-element variations to the Mud Lake rutile (Table 10), but contains slightly less TiO_2 and almost twice as much Cr. The mineral contains 97.17–97.98 wt.% TiO_2 and 0.3–0.37 wt.% FeO. The trace-element abundance of Cr

ranges from 376 to 5000 ppm, Zr from 182 to 2890 ppm, Nb from 2040 to 5490 ppm and Ta from 71 to 492 ppm.

Table 10 Representative major- and trace-element composition of rutile, Mud Lake and Drybones Bay.

	Mud Lake			Drybones Bay		
Oxide, wt.%	1	2	3	4	5	6
TiO_2	98.95	98.56	98.09	97.17	97.48	97.98
Cr_2O_3	0.71	0.06	0.04	0.35	0.34	n.d.
FeO	0.21	0.42	0.49	0.30	0.37	0.30
Nb_2O_5	0.35	0.78	1.03	0.36	0.54	0.79
Total	100.22	99.82	99.65	98.33	98.84	99.50

(1-3) Mud Lake; (4-6) Drybones Bay. Sought but not detected: Mg, Al, Si, Mn, Ta

Element,	Mud Lake			Drybones Bay	
ppm	1 (n = 1)	2 (n = 1)	3 (n = 11)	4 (n = 5)	5 (n = 5)
Mg	392	414	391 (24)	n.d.	n.d.
Al	n.d.	n.d.	n.d.	14 (14)	31 (28)
Ca	n.d.	n.d.	n.d.	188 (271)	78 (174)
Sc	10.7	6.5	9 (4)	14 (4)	10 (8)
V	55.4	4.4	9 (16)	35 (11)	47 (48)
Cr	253	2720	1437 (1356)	2180 (1687)	1797 (969)
Mn	3.2	5.2	6 (5)	5 (2)	17 (31)
Y	1.6	1.5	2 (2)	0.8 (2)	2 (3)
Zr	2630	766	1766 (808)	1086 (392)	972 (1126)
Nb	3850	2667	4506 (1466)	3938 (1056)	3410 (1288)
La	1.6	0.9	2 (2)	1 (1)	2 (4)
Ce	4.8	2.8	3 (4)	2.0 (7)	6 (10)
Pr	0.49	0.39	0.6 (6)	0.2 (1)	0.6 (1)
Nd	1.4	1.9	3 (3)	1.0 (5)	2 (3)
Sm	0.4	n.d.	0.8 (7)	0.4 (3)	0.5 (0.7)
Eu	n.d.	0.18	0.3 (3)	0.11 (8)	0.2 (0.3)
Gd	n.d.	n.d.	1.4 (1)	0.2 (2)	0.5 (0.6)
Tb	n.d.	n.d.	0.25 (8)	0.043 (8)	0.1 (0.2)
Dy	0.4	0.3	0.5 (5)	0.3 (2)	1 (1)
Ho	0.08	0.05	0.1 (1)	0.05 (3)	0.1 (2)
Er	0.20	0.20	0.3 (2)	0.09 (6)	0.3 (5)
Tm	n.d.	n.d.	0.12	0.015 (1)	0.04 (7)
Yb	n.d.	n.d.	0.65	0.11 (6)	0.2 (4)
Lu	n.d.	n.d.	0.114	0.006 (9)	0.03 (4)
Hf	96.2	35.4	60 (23)	33 (9)	31 (29)
Ta	443.0	134.9	311 (131)	260 (127)	210 (166)
Pb	1.44	1.03	1.2 (9)	1.1 (3)	3 (5)
Th	0.29	0.47	0.7 (7)	2.9 (9)	5 (9)
U	0.5	0.7	0.7 (6)	2.6 (7)	3 (4)
Nb/Ta	9	20	15 (3)	17 (5)	20 (7)
Zr/Hf	27	22	28 (4)	32 (4)	29 (6)

(1-3) Mud Lake; (1-2) individual analyses to illustrate intra-grain variation; (3) average composition; (4-5) Drybones Bay. Sought but not detected: Co, Ni, Zn; n.d.= not detected.

Chapter 6: Geochemistry

6.1 Whole-rock geochemistry

6.1.1 Major elements

The whole-rock major-element composition of the Mud Lake and Drybones Bay samples is listed in Table 11, along with published analyses of rocks relevant to the forthcoming discussion. These data include the Defeat granodiorite country rock (Yamashita et al., 1999), hypabyssal kimberlite from Snap Lake, NWT (Kopylova et al., 2010a), Jericho, Nunavut (Kopylova and Hayman, 2008) and Wesselton, South Africa (White et al., 2012), world average HK (Chakhmouradian et al., 2013), and dolomite carbonatite from Wekusko Lake (Chakhmouradian et al., 2009).

High SiO_2, MgO and volatiles, moderate FeO_T, CaO, and low TiO_2, Al_2O_3 and P_2O_5 characterize the major-element composition of the Mud Lake rocks. Volatiles account for the 18.1–19.5 wt.% LOI, of which roughly half is CO_2, with the balance (LOI‡ = LOI – CO_2) inferred to be H_2O. The samples have Mg# between 0.69 and 0.80, and are relatively uncontaminated, with C.I. values of 1.1–1.2. The composition of these samples is remarkably consistent with the average composition of HK, as well as the specific examples provided (Table 11), and is clearly distinct from that of the Wekusko Lake carbonatite, which contains significantly less SiO_2 and MgO, and much higher levels of CaO and CO_2.

The Drybones Bay rocks are characterized by high SiO_2 and MgO, moderate FeO_T and volatiles (7–15 wt.% LOI), and low TiO_2, Al_2O_3 and CaO contents. The C.I. values range from 1.4 in unit K-1 to 5.1 in unit KE, reflecting the differences in crustal xenolith content between units. The Mg# is consistent across units, with the unit averages ranging from 0.71–0.73, and standard deviations within units typically < 0.02. The amount of volatiles and proportion of CO_2 shows considerable inter- and intra-unit variation, with the total volatile contents ranging from 7 to 15 wt.% (LOI), and the CO_2 values ranging from 1.9 to 7.8 wt.% CO_2.

Table 11 Whole-rock major-element compositions (wt.%) of the Mud Lake and Drybones Bay kimberlites.

Sample	SiO_2	TiO_2	Al_2O_3	FeO_{total}	MnO	MgO	CaO	Na_2O	K_2O	P_2O_5	CO_2	S	LOI	LOI‡	Total	C.I.	Mg#
Mud lake																	
ML-07-2	33.67	0.91	1.37	5.77	0.11	28.83	6.37	0.06	0.44	1.04	8.76	0.02	19.5	10.74	99.07	1.2	0.80
ML-07-13	31.35	1.64	1.35	9.53	0.12	27.77	6.33	0.04	0.44	1.01	8.57	<0.02	18.1	9.53	99.11	1.1	0.69
Average (n = 2)	33	1.3	1.36	8	0.12	28.3	6.35	0.05	0.44	1.03	8.7	0.02	18.8	10.13	99.09	1.2	0.74
Stdev	2	0.5	0.01	3	0.01	0.7	0.03	0.01	0	0.02	0.1	0	1	0.9	0.03	<0.1	0.07
K-1 Drybones Bay																	
DB-10-01	39.96	1.36	3.88	8.56	0.11	26.40	2.32	0.16	0.59	0.51	3.00	0.05	14.2	11.20	99.26	1.6	0.71
DB-10-03	39.83	1.50	3.37	8.41	0.13	27.75	2.44	0.20	0.56	0.64	3.26	0.04	13.1	9.84	99.08	1.5	0.72
DB-05-02	37.96	1.37	3.12	7.66	0.12	27.59	3.78	0.15	0.64	0.72	5.75	0.07	15.0	9.25	99.18	1.4	0.74
DB-10-06	43.54	1.48	6.31	7.33	0.08	24.26	1.11	0.52	0.85	0.19	2.93	0.04	12.6	9.67	99.31	1.9	0.72
Average (n = 4)	40	1.43	4	8.0	0.11	27	2	0.3	0.7	0.5	4	0.05	14	9.99	99.2	1.6	0.72
Stdev	2	0.07	1	0.6	0.02	2	1	0.2	0.1	0.2	1	0.01	1	0.84	0.1	0.2	0.01
K-2 Drybones Bay																	
DB-10-07	42.62	1.14	5.07	8.20	0.10	26.26	0.62	0.32	0.67	0.24	1.50	<0.02	13.0	11.50	99.39	1.7	0.71
K-3 Drybones Bay																	
DB-10-09	45.28	1.64	4.29	7.74	0.08	25.14	1.05	0.42	0.54	0.23	2.16	<0.02	11.9	9.74	99.42	1.9	0.72
DB-10-10	42.89	1.27	4.41	7.72	0.09	25.86	1.51	0.40	0.54	0.32	2.57	0.06	13.1	10.53	99.23	1.8	0.72
DB-05-04	44.72	1.58	4.67	6.53	0.09	25.28	1.77	0.48	0.67	0.31	2.24	0.12	12.2	9.96	99.23	1.9	0.75
Average (n = 3)	44	1.5	4.5	7.3	0.09	25.4	1.4	0.43	0.58	0.29	2.3	0.09	12.4	10.08	99.3	1.9	0.73
Stdev	1	0.2	0.2	0.7	0.01	0.4	0.4	0.04	0.08	0.05	0.2	0.04	0.6	0.34	0.1	0.1	0.02
K-6 Drybones Bay																	
DB-10-13	49.00	0.97	5.31	6.21	0.07	21.75	1.09	0.76	1.02	0.27	2.75	0.03	12.2	9.45	99.47	2.3	0.73
DB-05-07	51.61	1.22	5.98	6.04	0.07	20.14	1.18	0.82	1.99	0.19	2.13	0.03	9.3	7.17	99.46	2.4	0.72
DB-10-16	49.29	1.07	5.84	6.82	0.07	22.56	0.88	0.53	0.90	0.26	1.80	0.03	10.3	8.50	99.43	2.3	0.72
Average (n = 3)	50	1.1	5.7	6.4	0.07	21	1.1	0.7	1.3	0.24	2.2	0.03	11	8.38	99.45	2.3	0.72
Stdev	1	0.1	0.4	0.4	0	1	0.2	0.2	0.6	0.04	0.5	0	1	1.14	0.02	0.1	0.01
K-7 Drybones Bay																	
DB-10-18	42.74	1.72	3.91	8.37	0.08	27.27	0.91	0.20	0.45	0.39	1.28	0.03	11.9	10.62	99.16	1.7	0.72

‡: LOI-CO_2

Table 11 continued…

Sample	SiO_2	TiO_2	Al_2O_3	FeO_{total}	MnO	MgO	CaO	Na_2O	K2O	P_2O_5	CO_2	S	LOI	LOI‡	Total	C.I.	Mg#
K-8 Drybones Bay																	
DB-08-05	42.64	0.99	3.02	7.30	0.11	25.68	2.17	0.49	0.45	0.19	3.30	0.03	15.3	12.00	99.36	1.7	0.73
DB-08-09	41.20	1.65	3.74	7.45	0.11	25.12	2.98	0.40	0.55	0.36	3.11	0.03	14.7	11.59	99.35	1.7	0.72
DB-08-11	43.63	1.21	2.89	7.22	0.10	25.57	2.00	0.38	0.44	0.21	2.57	0.04	14.7	12.13	99.44	1.8	0.73
DB-08-14	42.76	0.94	2.29	7.19	0.11	26.18	2.21	0.31	0.47	0.24	2.53	0.03	15.6	13.07	99.42	1.7	0.74
DB-08-16	43.11	1.14	2.50	7.25	0.11	25.85	2.01	0.39	0.54	0.21	2.49	0.03	15.2	12.71	99.43	1.7	0.73
Average (n = 5)	42.7	1.2	2.9	7.3	0.11	25.7	2.3	0.38	0.49	0.24	2.8	0.03	15.1	12.30	99.40	1.7	0.73
Stdev	0.9	0.3	0.6	0.1	0.01	0.4	0.4	0.04	0.05	0.07	0.4	0.01	0.4	0.59	0.04	<0.1	0.01
KE Drybones Bay																	
DB-19-00	68.77	0.65	3.15	4.08	0.03	13.46	0.87	0.32	0.35	0.17	1.87	0.05	7.1	5.23	99.57	5.1	0.72
DB-19-04	64.25	0.70	2.36	3.88	0.06	14.64	1.93	0.5	0.42	0.13	4.18	0.05	10.1	5.92	99.56	4.3	0.75
DB-19-05	57.08	1.06	3.95	5.62	0.06	16.84	1.47	0.86	1.12	0.29	2.35	0.03	10.4	8.05	99.53	3.2	0.70
DB-19-06	55.66	0.96	3.24	5.05	0.12	14.02	5.39	0.41	0.53	0.31	7.81	0.05	13.1	5.29	99.56	3.9	0.68
Average (n = 4)	61	0.8	3.2	4.7	0.07	15	2	0.5	0.6	0.23	4	0.05	10	6.13	99.56	4.2	0.71
Stdev	6	0.2	0.7	0.8	0.04	1	2	0.2	0.4	0.09	3	0.01	2	1.32	0.02	0.8	0.03
Defeat granodiorite[1]																	
Y-1	72.82	0.225	15.10	1.85	0.024	0.66	2.08	5.40	1.78	0.059							
Y-29	74.46	0.172	14.18	1.87	0.024	0.60	1.34	4.54	2.75	0.057							
Y-30	70.72	0.419	15.28	2.96	0.038	1.33	2.72	3.98	2.45	0.107							
Hypabyssal kimberlite and carbonatite																	
HK average[2] (n = 77)	31.6	1.8	3.0	8.7	0.17	28.3	9.5	0.2	0.9	0.8						1.2	0.72
Stdev[2]	4.6	1.2	1.3	1.9	0.04	5.6	4.6	0.2	0.6	0.7							
Snap Lake, NWT[3]	36.92	0.74	2.88	7.64	0.12	33.35	1.98	0.06	0.89	0.37					84.93	1.1	0.77
Wesselton, S.A.[4]	32.49	2.84	2.33	9.85	0.21	20.53	12.73	0.52	3.47	1.90					86.87	1.3	0.62
Jericho, NU[5]	33.04	0.99	1.78	7.75	0.16	36.1	6.79	0.12	0.22	0.42					87.37	1.0	0.78
Wekusko, MB[6]	7.89	0.51	2.64	5.17	0.31	19.68	24.04	0.15	0.77	1.54					62.70	0.5	0.75

[1]Defeat granodiorite host rock (Yamashita et al., 1999); [2]average hypabyssal kimberlite (Chakhmouradian et al., 2013); [3]main hypabyssal kimberlite dyke, average (Kopylova et al., 2010); [4]hypabyssal macrocrystic kimberlite sill (White et al., 2012); [5]hypabyssal macrocrystic kimberlite dyke, average, (Kopylova & Hayman, 2008); [6]dolomite carbonatite (Chakhmouradian et al., 2009); ‡: LOI-CO_2.

Table 12 Whole-rock trace-element compositions of the Mud Lake and Drybones Bay kimberlites.

Element, ppm	Mud Lake (n = 2)	K-1 (n = 4)	K-2 (n = 1)	K-3 (n = 3)	K6 (n = 3)	K-7 (n = 1)	K-8 (n = 5)	KE (n = 4)	Average HK[1] (n = 78)	Defeat granodiorite[2] Y-1	Y-29	Y-30
Be	3.5 (7)	<1	3	1 (2)	4.5 (7)	<1	1	<1	n.a.			
V	89 (24)	77 (5)	59	72 (7)	59 (6)	88	63 (10)	48 (11)	117.38			
Cr	1454 (73)	848 (57)	738.936	837 (106)	661 (51)	1176.824	973 (182)	640 (194)	1370.67	4	3	6
Ni	1066 (59)	904 (65)	889	941 (80)	833 (44)	1080	1139 (152)	596 (43)	1130.12			
Co	68 (14)	81 (24)	62.1	86 (22)	65 (11)	87.6	78 (14)	42 (11)	80.26			
Sc	13	9.3 (1)	6	7	6	8	7 (0.7)	5 (1)	15.48	1	7	8
Cu	9 (2)	20 (29)	1.6	39 (34)	42 (43)	37.5	8 (4)	27 (22)	n.a.			
Zn	26	34 (7)	37	31 (6)	32 (2)	32	44 (3)	23 (7)	n.a.			
As	4.9 (8)	5 (6)	0.9	1.1 (2)	1.1 (3)	1.1	2 (1)	1.8 (5)	n.a.			
Ga	5.55 (7)	8 (1)	7.2	7.6 (4)	7.9 (5)	9.1	5 (1)	5.0 (6)	4.87	20	19	20
Rb	27.1 (2)	47 (7)	38.9	35 (4)	45.5 (4)	30.1	26 (4)	28 (13)	64.41			
Cs	0.75 (7)	1.7 (6)	2	1.2 (2)	1.8 (1)	1	1.4 (2)	1.7 (8)	2.05			
Sr	352 (5)	419 (214)	365	355 (56)	228 (37)	449.9	161 (25)	291 (110)	853.53			
Ba	1117 (86)	1276 (362)	233	1056 (721)	663 (242)	1249	321 (159)	671 (346)	1535.28			
Pb	8 (1)	2 (1)	0.6	9 (14)	2 (1)	0.8	2.4 (1)	8 (10)	10.09			
Y	19 (3)	11 (4)	7.8	6.1 (0.7)	6.5 (5)	6.9	5.2 (2)	6 (1)	14.07			
La	212 (44)	106 (44)	55	75 (20)	62 (9)	91.4	65 (9)	50 (18)	138.22			
Ce	389 (63)	195 (79)	102.9	138 (35)	113 (18)	164.1	116 (22)	94 (37)	250.56			
Pr	43 (3)	20 (8)	10.25	14 (3)	11 (2)	16.11	12 (2)	9 (4)	26.03			
Nd	144.6 (4)	68 (25)	33.9	45 (10)	39 (5)	52.7	37 (9)	31 (12)	89.09			
Sm	19 (2)	9 (4)	4.54	6 (1)	4.8 (8)	6.4	4 (1)	4 (1)	11.66			
Eu	5.0 (6)	2.3 (1)	1.4	1.4 (3)	1.2 (1)	1.57	1.1 (3)	0.9 (3)	2.95			
Gd	13 (1)	6 (3)	3.32	3.8 (7)	3.4 (4)	3.99	3 (0.7)	2.8 (8)	8.55			
Tb	1.3 (2)	0.7 (3)	0.43	0.39 (8)	0.35 (2)	0.41	0.30 (6)	0.29 (7)	0.82			
Dy	5.3 (8)	3 (1)	1.95	1.6 (2)	1.5 (1)	1.74	1.3 (2)	1.3 (4)	3.56			
Ho	0.7 (1)	0.4 (2)	0.31	0.21 (2)	0.24 (1)	0.23	0.19 (2)	0.20 (4)	0.52			
Er	1.4 (2)	0.9 (3)	0.71	0.54 (2)	0.537 (6)	0.62	0.41 (5)	0.5 (1)	1.24			
Tm	0.18 (4)	0.10 (4)	0.08	0.06 (1)	0.067 (6)	0.07	0.05	0.07 (2)	0.15			
Yb	1 (1)	0.6 (2)	0.47	0.38 (6)	0.43 (4)	0.37	0.33 (5)	0.44 (8)	0.78			
Lu	0.13	0.08 (2)	0.07	0.05 (2)	0.053 (6)	0.05	0.042 (4)	0.07 (2)	0.11			
Zr	812 (191)	476 (176)	351.3	383 (59)	226 (20)	741.7	391 (258)	345 (78)	201.89	104	143	172
Hf	22 (6)	12 (4)	9.5	11 (1)	6.3 (5)	20.7	11 (7)	9 (2)	4.53	2.26	4.07	3.74
Th	30.4 (1)	15 (7)	8.2	9 (1)	7.3 (8)	10.4	9 (2)	7 (2)	19.28	6.13	9.32	4.4
U	7.3 (3)	3 (1)	1.8	1.9 (5)	1.5 (1)	2.4	1.9 (3)	1.7 (4)	4.23	1.82	3.05	1.48
Nb	252 (24)	150 (53)	80.8	105 (2)	80 (3)	131.6	100 (20)	66 (20)	180.57	3.4	4.6	6.2
Ta	11 (1)	9 (2)	5.7	7.6 (9)	5.3 (4)	9.2	7 (1)	5 (1)	10.2	0.86	0.43	0.5

[1]Average HK (Chakhmouradian et al., 2013); [2]Defeat granodiorite (Yamashita et al., 1999).

Table 12 continued…

	Mud	K-1	K-2	K-3	K6	K-7	K-8	KE	HK[1]	Defeat granodiorite[2]		
Element	(n = 2)	(n = 4)	(n = 1)	(n = 3)	(n = 3)	(n = 1)	(n = 5)	(n = 4)	(n = 77)	Y-1	Y-29	Y-30
Ga/Al (x10^4)	7.70 (2)	3.80 (8)	2.7	3.10 (7)	2.60 (2)	4.3	3.00 (3)	3.00 (3)	3.9	2.5	2.5	2.5
Y/Ho	28 (1)	27 (3)	25.2	28.7 (8)	27 (3)	30	28 (2)	29 (2)	26			
Zr/Hf	37.6 (9)	39 (2)	37	36 (2)	36.0 (8)	35.8	37 (2)	38.9 (5)	42	46	35	46
Nb/Ta	23.6 (2)	17 (2)	14.2	14 (2)	15.0 (6)	14.3	14.2 (8)	14 (1)	17.7	4.0	10.7	12.4
Th/U	4.2 (2)	4.5 (4)	4.6	4.7 (6)	4.9 (7)	4.3	4.8 (7)	5 (1)	5	3.4	3.1	3.0
Sc/Cr (x10^3)	9.0 (4)	11 (2)	8	8 (1)	9.1 (7)	7	7 (1)	8 (1)	11	250	2333	1333
Zr/Nb	3 (1)	3.2 (3)	4.3	3.6 (0.5)	2.9 (4)	5.6	4 (4)	5 (2)	1.2	30.6	31.1	27.7

[1]Average HK (Chakhmouradian et al., 2013); [2]Defeat granodiorite (Yamashita et al., 1999).

6.1.2 Trace elements

The whole-rock trace-element abundance for Mud Lake and Drybones Bay, as well as published data on the average HK (Chakhmouradian et al., 2013) are presented in Table 12. Figure 27 shows the primitive mantle-normalized incompatible trace-element patterns for the average HK, Mud Lake, and representative samples of the least contaminated units from Drybones Bay (K-1, -2 and -8). The Mud Lake patterns are slightly elevated for most elements relative to the average HK, but show considerable enrichment in Th, U, Nb, Zr and Hf ($^{ML}Th_{CN}$ = 381; $^{ML}U_{CN}$=369; $^{ML}Nb_{CN}$ = 393; $^{ML}Zr_{CN}$ = 90; $^{ML}Hf_{CN}$ = 90) relative to the average HK ($^{HK}Th_{CN}$ = 242; $^{HK}U_{CN}$ = 208; $^{ML}Nb_{CN}$=264; $^{HK}Zr_{CN}$ = 19; $^{HK}Hf_{CN}$ = 16), and depletion in Rb ($^{ML}Rb_{CN}$ = 40 versus $^{HK}Rb_{CN}$ = 107) and Ba ($^{ML}Ba_{CN}$ = 147 versus $^{HK}Sr_{CN}$ = 232). Negative anomalies characteristic of kimberlites (Becker and Le Roex, 2006) are less conspicuous for K ($^{ML}K_{CN}$ = 16.3 versus $^{HK}K_{CN}$ = 5.5), but greater for Sr ($^{ML}Sr_{CN}$ = 18 versus $^{HK}Sr_{CN}$ = 43), and Ti ($^{ML}Ti_{CN}$ = 3.7 versus $^{HK}K_{CN}$ = 6.9). The Drybones Bay incompatible element patterns are generally lower than average HK (Figure 27). The patterns for K-1 and K-8 are parallel, with K-1 being relatively more enriched; the pattern for K-2 mirrors K-8 for the less compatible elements (Rb to Pr) then diverges to match the pattern of K-1 from Tb to Lu. Values of Rb are comparable to Mud Lake, as is Ba for K-1; however K-2 and K-8 are strongly depleted in Ba ($^{DB}Ba_{CN}$ = 35 versus $^{HK}Ba_{CN}$ = 232). Drybones Bay samples are also poorer in Th ($^{DB}Th_{CN}$ = 103–179 versus $^{HK}Th_{CN}$ = 243), U ($^{DB}U_{CN}$ = 90–148 versus $^{HK}U_{CN}$ = 208), Pb ($^{DB}Pb_{CN}$ = 27–55 versus $^{HK}Pb_{CN}$ = 67), Sr ($^{DB}Sr_{CN}$ = 6–18 versus $^{HK}Sr_{CN}$ = 43), and Nd ($^{DB}Nd_{CN}$ = 27 versus $^{HK}Nd_{CN}$ = 71). Zr and Hf are enriched ($^{DB}Zr_{CN}$ = 26–41; $^{DB}Hf_{CN}$= 27–33). The negative Ti anomaly seen in the Mud Lake material and average HK is absent from the Drybones Bay samples.

Chondrite-normalized REE patterns for the Mud Lake and Drybones Bay kimberlites (Figure 28) are consistent with published data on kimberlites (Chakhmouradian et al., 2013), showing strong enrichment in light REE (La_{CN} = 760–1027) relative to heavy REE (Lu_{CN} = 5). The Mud Lake rocks are particularly enriched in REE; sample ML-07-13 plots along the upper limit reported for HK, while ML-07-02 has lower levels of heavy REE, close to average HK values, and very high levels of light REE that exceed the typical range of kimberlitic values. The Drybones Bay data define a large field due to the diluting effect of crustal contamination. The least contaminated unit closely matches the average HK pattern; other samples share the same trend but with suppressed levels across the REE series.

The Drybones Bay samples have high Zr/Nb relative to average HK (Table 12), whereas the Ga/Al, Y/Ho, Zr/Hf, Th/U, Nb/Ta and Sc/Cr ratios are close to primitive mantle values (1.7×10^{-4}, 28.9, 37.1, 3.9, 18.5 and 6.2×10^{-3}, respectively). The unusually high Zr/Nb ratio (up to 5 times average HK) can be attributed to the abundance of zircon in the examined samples. The Mud Lake rocks have Y/Ho, Zr/Hf, Th/U and Sc/Cr ratios close to primitive mantle values, but high Ga/Al, Zr/Nb and Nb/Ta relative to average HK (Table 12). The high Zr/Nb ratio is comparable to that of the Drybones Bay rocks, and can be attributed to the same factors. The Ga/Al ratio (7.7×10^{-4}) is considerably higher than in the average HK (3.9×10^{-4}) and the Defeat granodiorite (2.5×10^{-4}), but is comparable to values reported for carbonatites (7.2×10^{-4}–2.6×10^{-3}; Chakhmouradian et al., 2009). The Nb/Ta ratio (23.6 ± 0.2) exceeds the range reported for HK (17.7 ± 4.7; Chakhmouradian et al., 2013), and is closer to values observed in carbonatites (21–32 for the Wekusko Lake carbonatite). The high Ga/Al and Nb/Ta ratios are also more consistent with carbonatites (Chakhmouradian, 2006; Chakhmouradian et al., 2009), whereas the other ratios are within the normal range of variability for kimberlites. To better understand the choice of elements selected, and their petrogenetic significance see the discussion in Section 8.1.

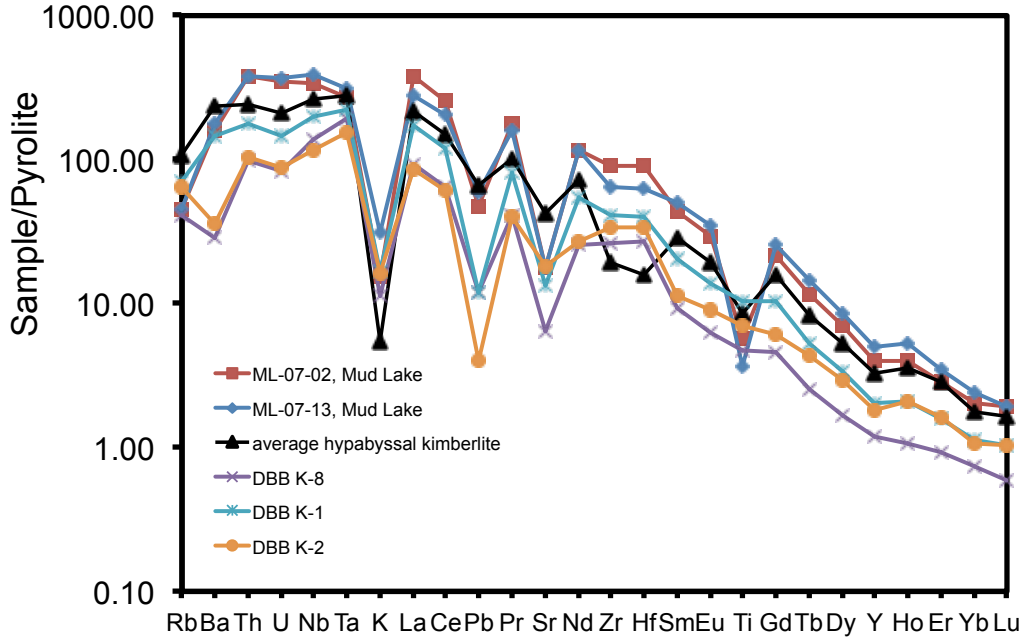

Figure 27 Incompatible element patterns for Mud Lake (ML), selected Drybones Bay (DBB) samples and average hypabyssal kimberlite (Chakhmouradian et al., 2013). Normalized to primitive mantle values of McDonough and Sun (1995).

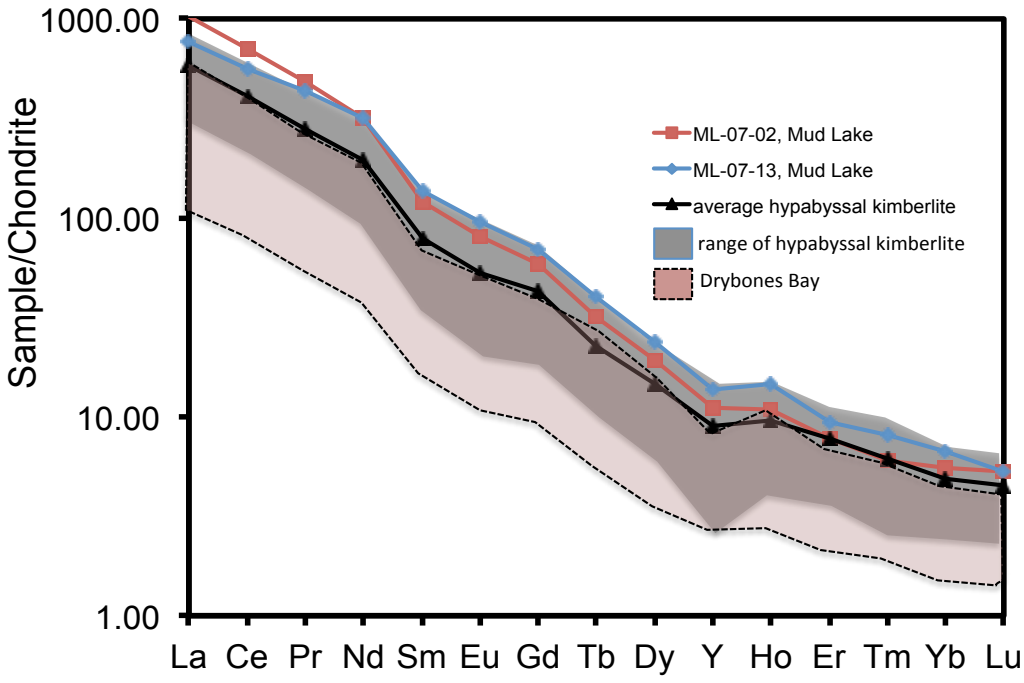

Figure 28 Chondrite-normalized REE patterns for Mud Lake (ML), Drybones Bay (DBB) and hypabyssal kimberlites (Chakhmouradian et al., 2013). Normalized to C1 values of McDonough and Sun (1995).

Chapter 7: U-Pb zircon geochronology

In this section, new U-Pb data are presented for zircon macrocrysts from the Mud Lake dyke, contributing to the published research on North American kimberlite emplacement ages. See Section 2.1 and 2.5 for more information on post-Archean magmatism in the Slave craton and Chapter 3 for LA-ICP-MS data acquisition and U-Pb geochronology methodology.

7.1 Sample description

Two relatively large anhedral, weakly fractured grains of zircon from different Mud Lake samples were selected for U-Pb dating. See Chapter 5 for the petrographic characteristics and mineral chemistry of the zircon macrocrysts, as well as evidence supporting their kimberlitic origin. The grains were examined for zoning and inclusions using BSE, CL, and optical imaging, and were found to be chemically homogeneous and free of visible inclusions (Figure 29). A total of 11 spot analyses were performed by LA-ICP-MS on unfractured areas of the crystals.

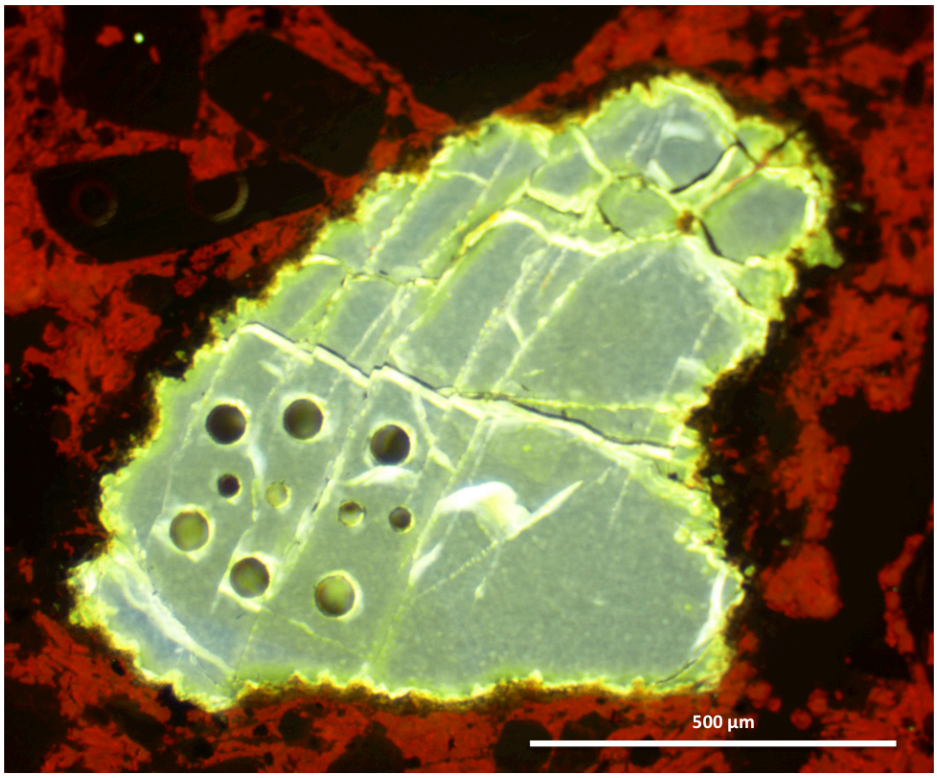

Figure 29 CL image of a dated zircon macrocryst from Mud Lake. The six 55 μm and four 30 μm ablation pits correspond to geochronology and trace element measurements, respectively.

7.2 Results

The isotopic ratios and calculated ages for the Mud Lake zircons are presented in Table 13, along with published U-Pb zircon data for the Drybones Bay kimberlite (Heaman et al., 2003) and Defeat granodiorite (MacLachlan and Davis, 2002). The data reported for zircon from the Defeat pluton is very different from those measured in the present work for the Mud Lake samples or the Drybones Bay zircon reported in the literature, providing further evidence that the grains analyzed here could not have been derived from the country rock. All of the analyzed grains are concordant, with 11 data points forming a cluster at 469.6 ± 9.7 Ma (Figure 30a), and all calculated ages are within the analytical error of one another. The weighted means of $^{207}Pb/^{235}U$ ages are shown in Figure 30b. By comparison, the emplacement age of the Drybones Bay kimberlite is 441.4 ± 0.8 Ma (Heaman et al., 2003), and the oldest age determined for the Defeat plutonic suite is 2632 ± 3 Ma. Thus, our results show that the Mud Lake dyke is broadly coeval with, but older than, the Drybones Bay kimberlite. Factoring in error, the Mud Lake dyke predates Drybones Bay by 20–40 Ma, which is comparable to the timespan of kimberlitic magmatism at Lac de Gras kimberlite further north in the Slave craton (ibid). The difference in error reported for the ages of the Mud Lake and Drybones Bay zircons is due to the analytical technique; the Drybones Bay zircons were analyzed by thermal ionization mass spectrometry, which yielded more precise data compared to LA-ICP-MS (Heaman et al., 2003).

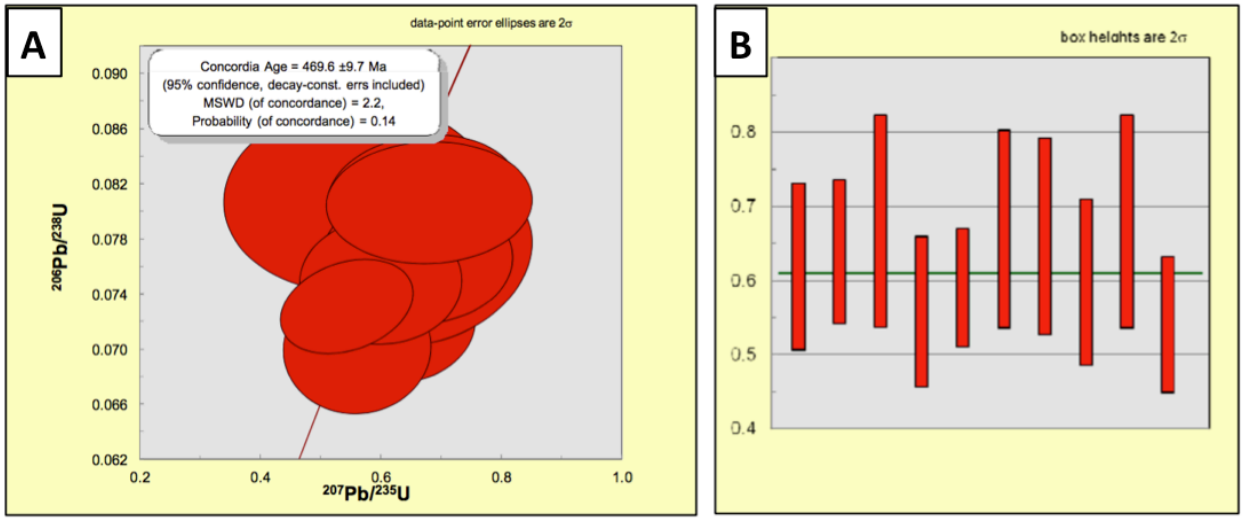

Figure 30 (A) U-Pb concordia diagram displaying the results for the Mud Lake zircons, all 11 analyses are concordant and yield an age of 469.6 ± 9.7 Ma. (B) Weighted mean of $^{207}Pb/^{235}U$ and $^{206}Pb/^{238}U$ isotopic ratios (right).

Table 13 U-Pb isotopic data for zircon from the Mud Lake and Drybones Bay kimberlites, and the Defeat pluton country rock.

Analyses	Measured ratios						Age (Ma)	
	$^{207}Pb/^{235}U$	± 2σ	$^{206}Pb/^{238}U$	± 2σ	$^{207}Pb/^{206}Pb$	± 2σ	$^{206}Pb/^{238}U$	± 2σ
Mud Lake								
1	0.620	0.110	0.0751	0.0035	0.0620	0.0110	466	21
2	0.640	0.095	0.0716	0.0033	0.0656	0.0098	450	20
3	0.560	0.100	0.0701	0.0039	0.0600	0.0130	437	23
4	0.543	0.090	0.0731	0.0028	0.0562	0.0083	455	17
5	0.592	0.078	0.0750	0.0026	0.0578	0.0075	468	15
6	0.680	0.140	0.0764	0.0050	0.0630	0.0120	474	30
7	0.670	0.130	0.0810	0.0037	0.0530	0.0110	500	22
8	0.660	0.130	0.0766	0.0039	0.0580	0.0130	478	24
9	0.600	0.110	0.0749	0.0037	0.0580	0.0110	465	22
10	0.680	0.140	0.0806	0.0036	0.0580	0.0120	498	21
11	0.560	0.180	0.0810	0.0056	0.0560	0.0170	501	33
Drybones Bay[1] (Hole 95-7)								
12	0.540	0.006	0.06902	0.0026	0.05679	0.00066	430.3	1.6
13	0.444	0.008	0.05661	0.0026	0.05690	0.00084	354.9	1.6
14	0.566	0.020	0.07174	0.0038	0.05718	0.00196	446.6	2.4
15	0.434	0.016	0.05441	0.0042	0.05787	0.00212	341.5	2.6
16	0.464	0.006	0.05898	0.0026	0.05701	0.00068	369.5	1.6
17	0.562	0.016	0.07065	0.0038	0.05765	0.00162	440.1	2.2
18	0.618	0.034	0.07333	0.0052	0.06117	0.00318	456.2	3.2
Drybones Bay[1] (Hole 95-8)								
19	0.545	0.004	0.07085	0.0036	0.05576	0.00016	441.3	2.2
20	0.573	0.018	0.07032	0.0042	0.05908	0.00174	438.1	2.4
21	0.556	0.006	0.07179	0.0034	0.05613	0.00058	446.9	2.0
22	0.609	0.022	0.07520	0.0042	0.05872	0.00194	467.4	2.4
23	0.553	0.010	0.07011	0.0032	0.05723	0.00098	436.8	2.0
24	0.553	0.010	0.07011	0.0032	0.05723	0.00098	436.8	2.0
Drybones Bay[1] (Hole 95-9)								
25	0.600	0.024	0.07288	0.0054	0.05972	0.00242	453.5	3.2
Defeat pluton[2]								
26	11.471	0.018	0.4742	0.0007	0.17545	0.00009	2502	2
27	11.627	0.030	0.4792	0.0012	0.17596	0.00012	2524	2
28	10.826	0.018	0.4457	0.0008	0.17616	0.00014	2376	3
29	11.903	0.015	0.4889	0.0006	0.17659	0.00009	2566	2
30	11.928	0.016	0.4896	0.0005	0.17671	0.00009	2569	2
31	12.050	0.133	0.4937	0.0054	0.17702	0.00009	2587	2

[1]U-Pb zircon data (Heaman et al., 2003); [2]U-Pb zircon data (MacLachlan and Davis, 2002).

Chapter 8: Discussion and Conclusions

8.1 Geochemistry

In order to understand the choice of element ratios presented in this work, their petrogenetic significance needs to be explained. Trace-element distribution patterns are not always sufficient to discriminate between chemically similar rocks. For example, kimberlites and magnesiocarbonatites may show very similar distribution patterns (see Figure 3a in Chakhmouradian et al., 2009). The ratios of certain isovalent trace elements provide a more reliable basis for discrimination. In magmatic systems characterized by CHArge-and-RAdius-Controlled (CHARAC) trace-element behavior, elements with similar charge and ionic radius, such as Y-Ho and Zr-Hf, tend to behave extremely coherently and retain their respective chondritic ratios (Bau, 1996). Basic to intermediate igneous rocks, including kimberlite, have Y/Ho and Zr/Hf ratios close to chondrite values, indicating CHARAC behavior of these elements in silicate melts (ibid). In contrast, aqueous solutions and highly evolved magmas rich in components such as H_2O, Li, B, F, P and/or Cl, and their precipitates, often show non-chondritic ratios for these elements and modified REE patterns, indicating non-CHARAC trace-element behavior in these systems. Fractionation of these twin pairs is caused by chemical complexing. Chemical complexing behavior is not dictated solely by charge and ionic radius; the electron configuration and type of complexing ligands determine the character of chemical bonding in the various complexes involving these elements (ibid). Thus, anomalous non-CHARAC behavior of certain isovalent trace elements is a reflection of specific physicochemical properties of the magma (ibid). In kimberlites, the ratios of Ga/Al, Sc/Cr, Zr/Hf and Nb/Ta are close to (or slightly above) primitive-mantle values, whereas these values are significantly higher in carbonatites (Chakhmouradian et al., 2009). Studies of Ga/Al fractionation in the Hawaiian volcanic rocks, which represent the entire range of nephelinitic, alkalic and tholeiitic lava series, found that systematic variations in Ga/Al could not be due to different pressure regimes or degrees of partial melting, and attributed the variations to mantle heterogeneities (De Argollo and Schilling, 1978).

8.1.1 Assimilation trends

Due to extensive crustal contamination, major elements are of limited use for modeling the relationship and evolution of the Mud Lake and Drybones Bay rocks. Bivariate plots of most major elements are dominated by contamination trends, and reveal little about the nature of the original material. Trace elements are less susceptible to direct contamination, but the dilution effects are strong enough to impose a dominant trend on the data. However, as discussed previously, the *ratios* of certain trace elements are largely unaffected by this process. This section will examine the extent and character of crustal contamination and assess the possible relationship between the Mud Lake and Drybones Bay kimberlites.

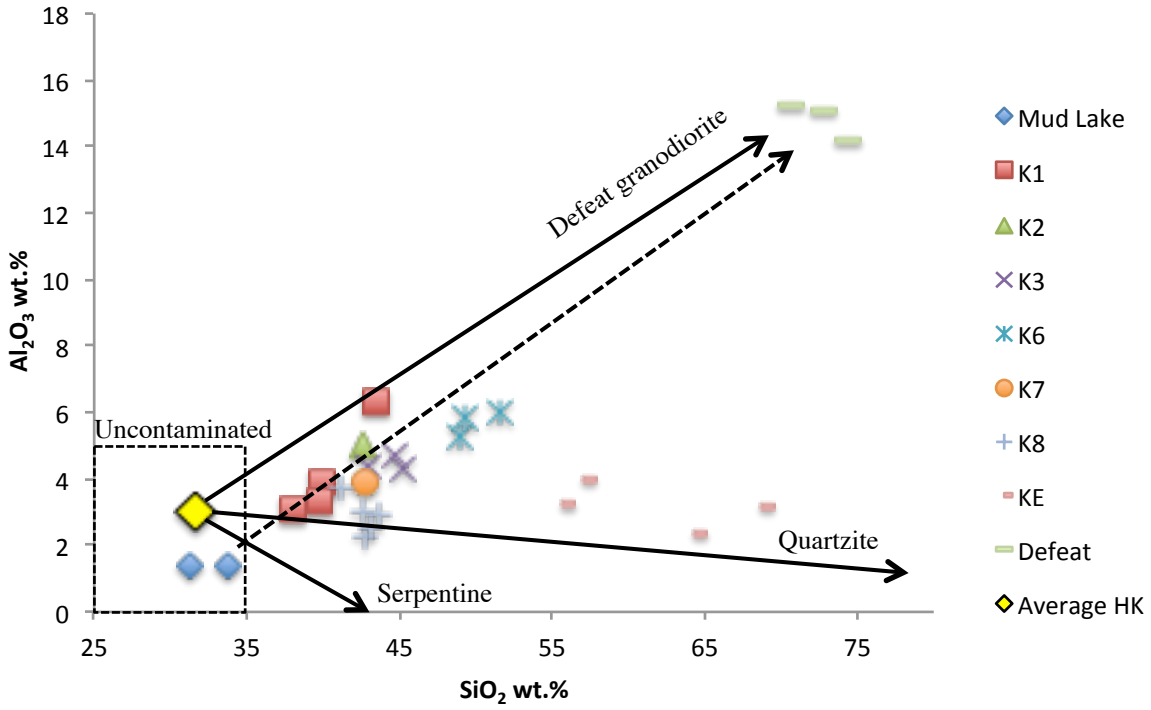

Figure 31 Relationship between SiO_2 and Al_2O_3 in the apparently uncontaminated Mud Lake HK and the contaminated Drybones Bay VK. The Mud Lake samples and units K-1, -2 and -3, form a trend towards the Defeat cluster, indicated by the dashed line. Solid lines are simple mixing lines between average HK (Chakhmouradian et al., 2013) Defeat granodiorite (Yamashita et al., 1999), quartzite, and serpentine. The field of "uncontaminated" compositions (dashed box) is from Mitchell (1986).

The Drybones Bay rocks are contaminated, with C.I. values ranging from 1.4 in the least contaminated unit (K-1) to 5.1 in the most contaminated unit (KE). The relationship between SiO_2 and Al_2O_3 (Figure 31) shows that the Drybones Bay contamination trend can be explained by the assimilation/contamination of kimberlite magma with ~12–40 vol.% Defeat granodiorite

country rock. Samples of the sandy unit (KE) plot along the contamination trend towards quartzite/sandstone, but are offset due to the contribution of Al_2O_3 from granodiorite. Unit K-8 has lower Al_2O_3 and diverges from the granodiorite mixing line towards serpentine, which is consistent with the serpentine-rich matrix of these samples. The relatively uncontaminated Mud Lake samples and units K-1, -2 and -3 form a linear trend towards the Defeat cluster (dashed line in Figure 31). This trend seems to suggest that the Drybones Bay rocks could have evolved from a parental magma not dissimilar from the Mud Lake kimberlite by crustal contamination. This possibility is explored using trace-element compositions below (Figure 32).

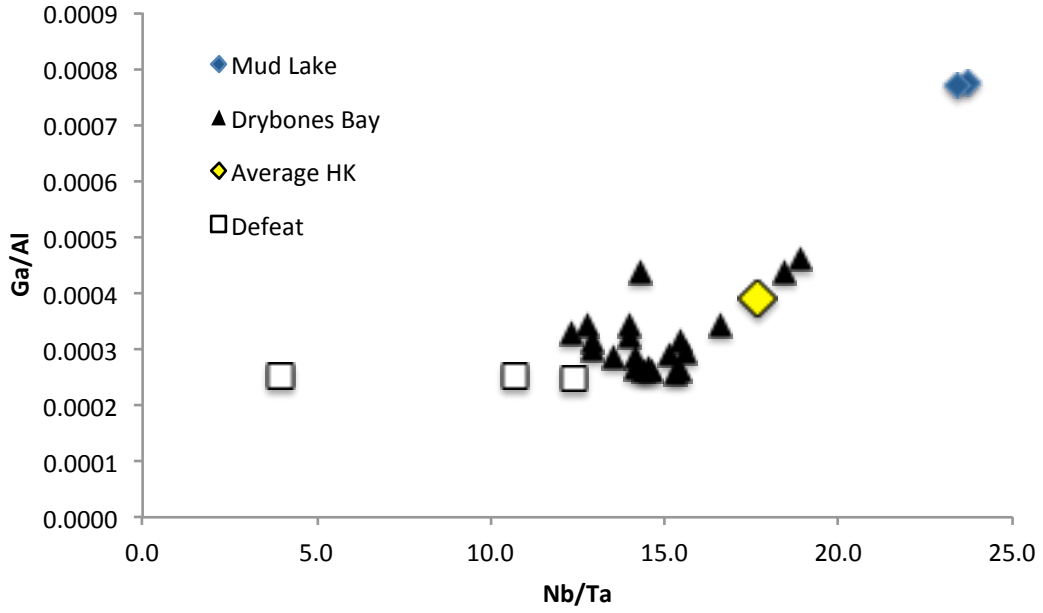

Figure 32 Relationship between Ga/Al and Nb/Ta for the Mud Lake and Drybones Bay kimberlites, the average HK (Chakhmouradian et al., 2013) and the Defeat granodiorite (Yamashita et al., 1999).

Using isovalent trace-element ratios, the Mud Lake and Drybones Bay rocks are best differentiated by their Nb/Ta and Ga/Al ratios, which are at normal kimberlitic values in the Drybones Bay samples, but significantly elevated in the Mud Lake samples. The plot of Nb/Ta vs. Ga/Al (Figure 32) shows that the Drybones Bay rocks are more enriched in Al relative to Ga and Ta relative to Nb compared to Mud Lake. The Drybones Bay samples have Ga/Al values ranging from 2.6×10^{-4} to 4.6×10^{-4} and Nb/Ta values ranging from 12 to 19, and plot between the average HK (Ga/Al = 3.9×10^{-4}; Nb/Ta = 18) and the Defeat granodiorite (Ga/Al = 2.5×10^{-4}; Nb/Ta = 4–12), whereas the Mud Lake rocks have Ga/Al = 7.7×10^{-4} and Nb/Ta = 24. This may

appear to be an assimilation trend at first glance, with the Mud Lake data representing uncontaminated samples and the Drybones Bay compositions approaching the Defeat granodiorite in their Nb/Ta and Ga/Al ratios. However, the granodiorite has an order of magnitude less Nb and Ta than kimberlite magmas, so the kimberlite magma would have to assimilate roughly ten times its mass to achieve the low levels of Nb/Ta seen in the Drybones Bay suite. Thus, crustal assimilation can be ruled out as the cause of the apparent trends in the Al_2O_3 vs. SiO_2 and Ga/Al vs. Nb/Ta data.

8.1.2 Fractionation trends

The evolution of magmas undergoing fractionation can sometimes be tracked using the ratio of two compatible trace-elements that have different affinities for a given mineral, that is elements A and B have different distribution coefficients (D) between mineral X and the liquid L (i.e. $^{X/L}D_{Element\ A} \neq {}^{X/L}D_{Element\ B}$). Below, we show compelling evidence for olivine fractionation through the evolution of Ni and Co abundances in ilmenite and spinel.

The whole-rock Co-Ni budget can be modeled by simple Rayleigh fractionation, however the ilmenite and spinel data require a more intricate model. In this work we uses a custom model (Equation 1) derived from the Rayleigh fractionation and mass balance models (Equations 2 and 3, respectively). The derived equation relates the mineral composition (C_S), rather than the residual liquid composition (C_L; cf. Equations 1 and 2), to the parental melt composition (C_0), crystal fraction (F), and distribution coefficient (D).

$$C_0 = \frac{C_S(1-F)}{(1-F^D)} \quad \textbf{(1)}$$

$$\frac{C_L}{C_0} = F^{(D-1)} \quad \textbf{(2)}$$

$$C_0 = C_L F - C_S(1-F) \quad \textbf{(3)}$$

Modeling the mineral data by crystallizing only ilmenite or spinel requires ludicrous amounts of these minerals to form. Instead we constrain the crystal fraction of ilmenite/spinel to a realistic range based on petrographic observations, and fit the model by substituting the constant C_0 with a variable (C_L from Equation 2) to represent a parental melt that is evolving by the precipitation of another mineral, in this case olivine.

The whole-rock trace-element data shows only a weak correlation between the Ni content and Co/Ni ratios (Figure 33a), but if the effects of contamination are considered, we can see that the points with maximum Ni for a given Co/Ni value define a locus with a negative slope. This

trend is consistent with crystal fractionation of Mg-rich olivine, which has a greater affinity for Ni than Co (Adam and Green, 2006). The whole-rock concentration of Ni and Co and the Co/Ni ratios can be modeled by 2–3% olivine fractionation (Figure 33a) from a primitive kimberlite melt, using published distribution coefficients. Initial concentrations 2641 ppm Ni and 135 ppm Co were used for the parental melt (C_0), these values represent the upper range reported for HK (Chakhmouradian et al., 2013), and are considered to represent a primitive kimberlite melt. The olivine distribution coefficients used in this work ($^{Ol/L}D_{Ni}$ = 32 and $^{Ol/L}D_{Co}$ = 4) are based on experimental data for basanite (Adam and Green, 2006).

The ilmenite and spinel data show a much stronger correlation between Ni and Co/Ni than the whole-rock data (Figure 33b,c), and exhibit well-defined trends that can be modeled to demonstrate the effects of olivine fractionation. The entire range of Ni and Co in ilmenite from Drybones Bay and Mud Lake (Ni = 182 to 378 ppm; Co = 132 to 180 ppm; Co/Ni = 0.4 to 0.72) can be modeled by the co-precipitation of olivine with ilmenite, using the same olivine fractionation parameters used previously, and published distribution coefficients for ilmenite: $^{Ilm/L}D_{Ni}$ = 5 and $^{Ilm/L}D_{Co}$ = 1.7 (Ewart and Griffin, 1994; Zack and Brumm, 1998). The model shows that ilmenite began to form at F_{Ol} = 10.5% and crystallized until F_{Ol} = 12.5%. The F_{Ol} values represent the total fraction of olivine crystallized from the parental melt, including the 2–3 vol.% removed from the system to produce the whole-rock Ni and Co values. Modeling this by crystallizing only ilmenite would require the precipitation of 40 vol.% ilmenite.

The spinel data show a wider range of values and a discontinuous distribution (Figure 33c). The bulk of the data has Ni = 370 to 970 ppm, Co = 260 to 470 ppm and Co/Ni = 0.44 to 1.1, while a small subset representing the late-forming rims of zoned macrocrysts from Mud Lake have high Ni (1290–1655 ppm), low Co (270–300 ppm) and a low Co/Ni ratios (0.16–2.2). The compositional range of the larger subset of spinel can be modeled in the same manner as the ilmenite data. Using $^{Spl/L}D_{Ni}$ = 7 and $^{Spl/L}D_{Co}$ = 4, which are within experimental values (Righter et al., 2005), the model indicates that spinel crystallized from F_{Ol} = 9% to 12%. Modeling the data by only crystallizing spinel results in an inferior fit and requires unrealistic amounts of spinel to fractionate (F_{Spinel} > 20 vol.%).

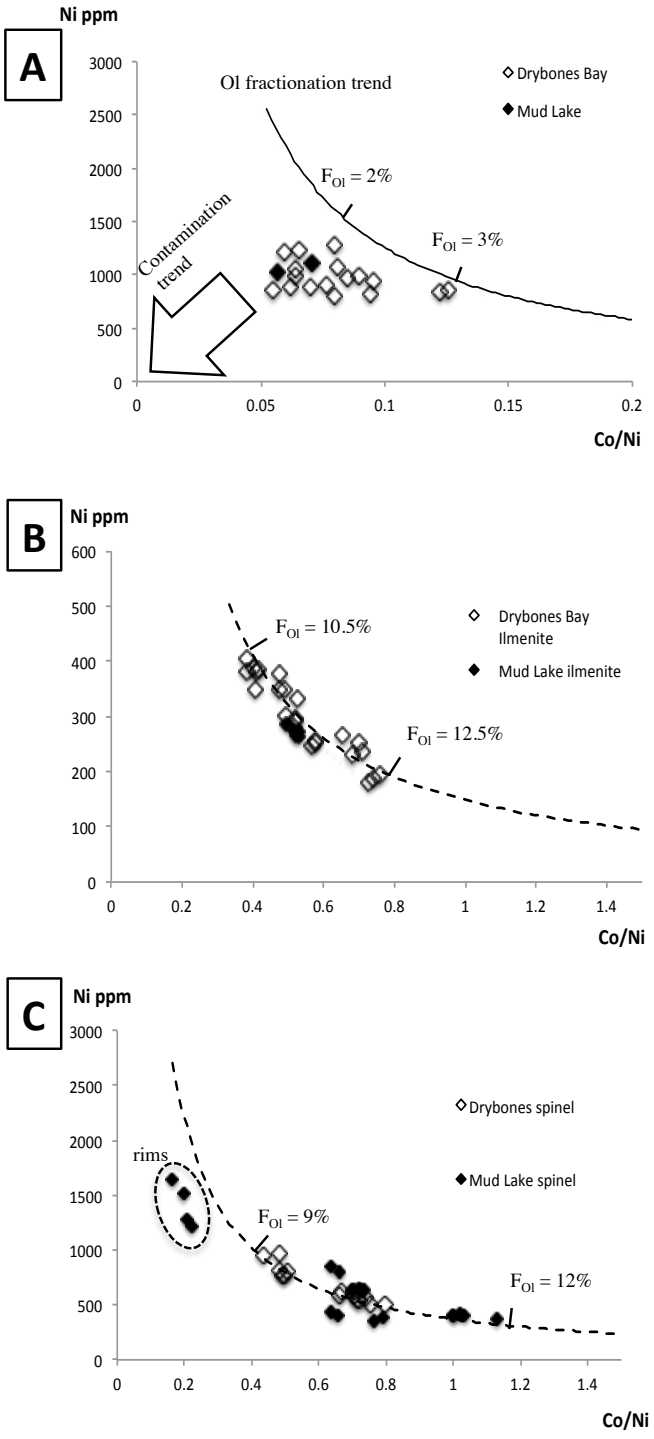

Figure 33 Bivariate plots of Ni vs. Co/Ni for (A) whole-rock data, (B) ilmenite, and (C) spinel from Mud Lake and Drybones Bay. The variation trend and Co-Ni budget are replicated by olivine fractionation paths ($^{Ol/L}D_{Ni}$ = 32 and $^{Ol/L}D_{Co}$ = 4). The solid line (A) models the composition of the residual melt evolving by olivine fractionation, while the dashed lines (B,C) model the composition of ilmenite ($^{Ilm/L}D_{Ni}$ = 5 and $^{Ilm/L}D_{Co}$ = 1.7) and spinel ($^{Spl/L}D_{Ni}$ = 7 and $^{Spl/L}D_{Co}$ = 4) crystallizing from the evolving melt. See text for details.

The small subset of spinel data with high Ni and low Co/Ni may appear to be part of the fractionation trend, representing the least evolved spinel, but these analyses are of late-forming rims on macrocrysts. The unexpectedly high Ni content in these rims can be attributed to the liberation of Ni from olivine during serpentinization (Mitchell, 1986; 2008). This is supported by the presence of trace amounts of nickel sulfide (confirmed by EDS) in the Drybones Bay samples. Fluctuating distribution coefficients may also play a role; experimental studies of Ni and Co partitioning in spinel demonstrated the dependence of $^{Spl/L}D_{Ni}$ and $^{Spl/L}D_{Co}$ on temperature, oxygen fugacity, and spinel composition, and that $^{Spl/L}D_{Ni}$ is more sensitive to these variations and ranges from 3.1 to 79.4, while $^{Spl/L}D_{Co}$ varies within a much narrower range, from 1.3 to 6.4 (Righter et al., 2005).

8.2 Kimberlite crystallization conditions

8.2.1 Thermometry

The Zr content in rutile and the Ti content in zircon have been proposed as potential geo-thermometers, which were calibrated using a suite of natural and synthetic samples (Watson and Harrison, 2005; Watson et al., 2006; Ferry and Watson, 2007). Zircon crystallization temperatures were estimated for the Mud Lake and Drybones Bay samples using the Ti-in-zircon thermometer (Watson et al., 2006), with revised calibration constants (Equation 4; Ferry and Watson, 2007).

$$log(Ti_{zircon}) = (6.01 \pm 0.03) - \frac{5080 \pm 30}{T(K)} - log(aSiO_2) + log(aTiO_2) \qquad \textbf{(4)}$$

No adjustments were made for the activity of Si or Ti (i.e. $a(SiO_2) = a(TiO_2) = 1$). Six zircons were analyzed for trace elements (Table 9), including two macrocrysts from Mud Lake, three macrocrysts from Drybones Bay, and one euhedral xenocryst from Drybones Bay. The Mud Lake zircon has a uniform Ti content of 14.7 ± 0.8 ppm (n = 8), whereas the Drybones Bay crystals are more variable: the three macrocrysts have Ti contents of 14.3 ± 0.3 ppm (n = 3), 4 ± 7 ppm (n = 3), and 12 ± 13 ppm (n = 6), and the euhedral xenocryst has 83 ± 55 ppm Ti (n = 3). Both Mud Lake macrocrysts and one Drybones Bay zircon were amenable to thermometry calculations; the two grains with high intragranular variations were discarded. The Mud Lake zircon yields a temperature of 783 ± 67 °C, while the Drybones Bay zircon yields a temperature

of 780 ± 41°C. The zoned xenocryst yields much higher values and a much wider temperature range (885–1078 °C).

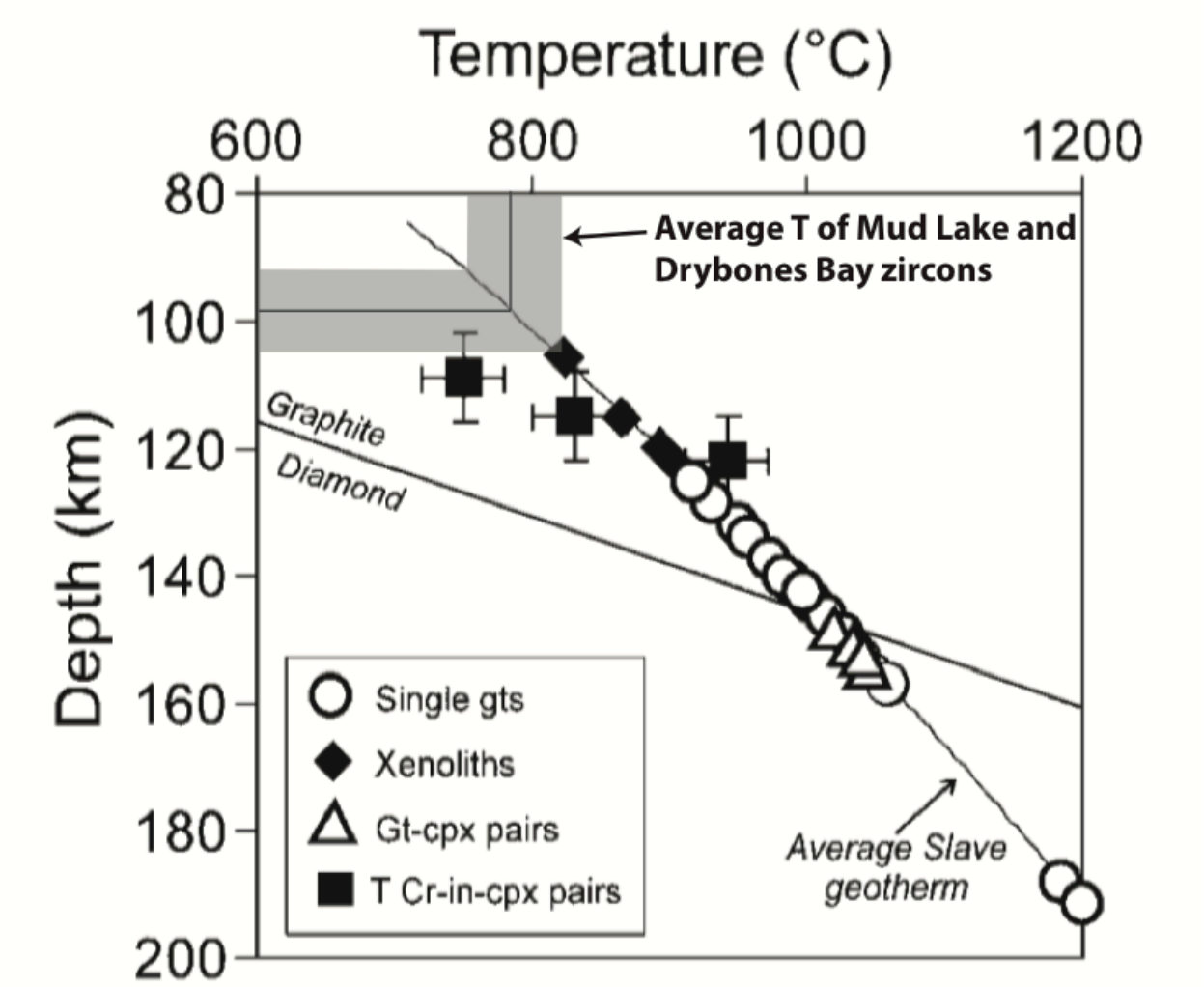

Figure 34 Temperature of Mud Lake and Drybones Bay kimberlitic zircons projected onto the Drybones Bay Slave geotherm (Carbno and Canil, 2002). Modified after Carbno and Canil (2002), used with permission.

The zircon macrocrysts from Mud Lake and Drybones Bay have Ti contents and formation temperatures (~780 °C) that are consistent with kimberlitic zircon from South Africa (13 ± 8.4 ppm Ti, 750 ± 63 °C, n = 114), Siberia (10 ± 8.1 ppm Ti, 717 ± 73 °C, n = 17), and Brazil (18 ± 11 ppm Ti, 778 ± 68 °C, n = 61), but higher values than in kimberlites from the Midwestern US (4.8 ± 4.3 ppm Ti, 664 ± 78 °C, n = 5; Page et al., 2007). The low crystallization temperature implies formation at relatively shallow depths in the lithospheric mantle (Page et al., 2007). When projected onto the Slave geotherm (Figure 34), the calculated temperature corresponds to a depth of ~100 km and a formation pressure of ~3 GPa, which is outside of the

diamond stability field. However, the ascending kimberlitic melt was obviously hotter than mantle rocks lining the magma conduit; i.e. the crystallization of zircon must have occurred at shallower levels than the geotherm temperatures determined from xenoliths.

The low crystallization temperature has implications for the timing of zircon formation relative to kimberlite eruption, and as a corollary, on the meaning of U-Pb zircon ages (Page et al., 2007). Zircon ages have been interpreted to represent the age of kimberlite eruption; zircon formation at mantle temperatures would be above the U-Pb closure temperature, therefore U-Pb isotopes would record the cooling age (Davis et al., 1980). On the contrary, the low crystallization temperature derived from Ti-thermometry would be insufficient to reset the isotopic equilibrium by Pb diffusion (Page et al., 2007), thus if these temperatures are accurate, the U-Pb ages would record the crystallization age.

The unexpectedly low temperature estimate raises the question of whether the Ti-in-zircon thermometer accurately reflects the crystallization conditions of kimberlitic zircon. The activities of TiO_2 and SiO_2 play an important role in the calibration of this thermometer (Ferry and Watson, 2007; Page et al., 2007); if $a(TiO_2) < 1$, the thermometer will reflect the minimum temperature (assuming all other components are at their saturation levels), whereas $a(SiO_2) < 1$ has the opposite effect and increases the equilibrium concentration of Ti in zircon (Page et al., 2007). In our calculations, we did not compensate for the activities of Ti or Si, (i.e. $a(TiO_2) = a(SiO_2) = 1$). Given the abundance of late-stage rutile, magma saturation with respect to TiO_2 seems likely. Textural features suggest the activity of Si may be less than unity: zircon macrocrysts show signs of resorption, with irregular, embayed grain margins, and are typically mantled with baddeleyite (ZrO_2; Figure 15e and 24a), indicating a desilication reaction with the host melt (Page et al., 2007). Page et al. (2007) have indicated that these disequilibrium features argue against kimberlite being the parental magma of zircon, and suggested that zircon in kimberlites forms in a more silica-saturated or lower-temperature environment, perhaps in eclogite domains in the mantle. However, perfectly euhedral zircon xenocrysts found in the Drybones Bay samples show no signs of resorption, even when fully isolated from their host xenolith and immersed in kimberlite matrix, suggesting that zircon was at equilibrium with the melt when the xenolith became disaggregated. It is therefore plausible that the conditions of kimberlite emplacement straddled the ZrO_2–$ZrSiO_4$ equilibrium. The crystallization temperature of 780 °C corresponds to an $a(SiO_2)$ value of ~0.15 (Barker, 2001). Because this value is <<1,

we consider the calculated Ti-in-zircon data to delineate the upper temperature limit of kimberlite crystallization.

Attempts to calculate the temperature of ilmenite-to-rutile conversion using the Zr-in-rutile thermometer (Equation 5; Watson et al., 2006) were unsuccessful due to the inhomogeneous distribution of Zr.

$$log(Zr_{rutile}) = (7.36 \pm 0.10) - \frac{4470 \pm 120}{T(K)} \quad \textbf{(5)}$$

Thirteen euhedral rutile crystals were selected on the basis of their homogeneous appearance in BSE images; major elements used for internal standards were measured by WDS. The LA-ICP-MS data consisted of 16 spot analyses and three line profiles. Although the grains appear homogeneous in BSE images, their Zr content is highly variable, ranging from 485 to 6410 ppm (average = 2525 ± 1885 ppm), with intra-granular variations exceeding 200% in some cases. The inhomogeneous Zr distribution indicates that the rutile was not in equilibrium with its parental fluid while it crystallized, and is not amenable to thermometric analysis.

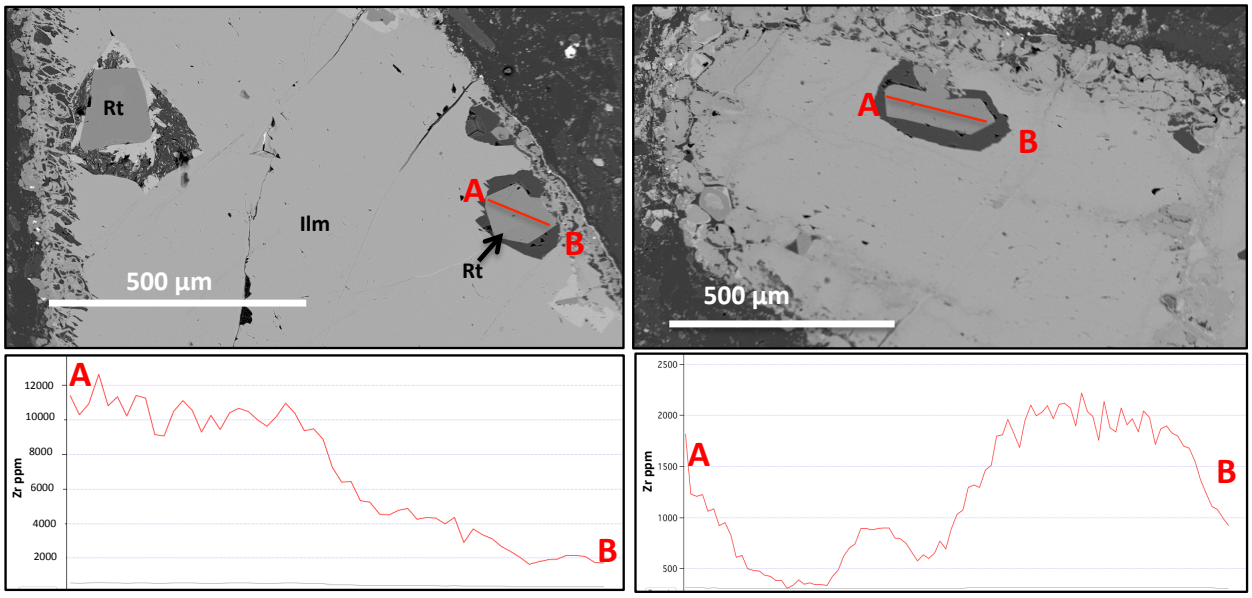

Figure 35 Summary of Zr-in-rutile thermometry measurements (BSE images and LA-ICP-MS line profiles). The red lines show where line profiles were taken, below each BSE image is the Zr response along the profile, from A to B. Note: the Zr concentration indicated in the first profile exceeds the range measured by spot analysis, while its possible that the values on the profile are accurate, the previously reported values are considered to be much more reliable.

The line profiles (Figure 35) show an overall step-wise decrease in Zr, with higher concentrations towards the ilmenite host. The second profile (Figure 35b) shows further complexities, the Zr content has a sigmoidal profile that increases at 'A' and decreases at 'B',

and has a small peak in the middle of the profile. The irregular pattern could be due to the long axis of the rutile being oriented parallel to the host ilmenite margin, or the presence of acicular ilmenite inclusions not resolvable with BSE images due to limitations in resolution and contrast.

8.2.2 Redox state

Chondrite-normalized REE patterns of zircon (Figure 25) show appreciably higher levels of Ce relative to La and Pr. The extent of Ce enrichment is represented as a Ce anomaly (Ce/Ce*), which is the ratio of the *measured* chondrite-normalized cerium concentration (Ce_{CN}) to the cerium concentration interpolated from the chondrite-normalized La and Pr abundances (La_{CN} and Pr_{CN}). Anomalously high Ce concentrations (i.e. Ce/Ce* > 1) are the result of Ce^{3+} being oxidized to a tetravalent state. Because the charge and ionic radius of Ce^{4+} are closer to that of Zr^{4+}, the compatibility of Ce in zircon under oxidizing conditions increases relative to the neighboring trivalent REE (i.e. La^{3+} and Pr^{3+}). Cerium anomalies therefore imply oxidizing conditions, and may serve as a proxy for the redox state of the magma at the time of zircon crystallization. Experiments with synthetic melts have established the following empirical relationship between Ce/Ce*, temperature, and oxygen fugacity, for melts with molar Al/(Na + K) ratios of 0.85 and 1.25 (Trail et al., 2012):

$$ln\left(\frac{Ce}{Ce^*}\right) = (0.0433 \pm 0.008) \times ln\left(f_{O_2}\right) + \frac{7123 \pm 1309}{T(K)} - (3.113 \pm 1.072) \quad \textbf{(6)}$$

A strong positive cerium anomaly ($Ce/Ce^* = \frac{Ce_{CN}}{\frac{1}{2}(La_{CN}+Pr_{CN})} = 14 \pm 4$) was calculated for the Mud Lake zircon. Although similarly high Ce concentrations were measured in the Drybones Bay zircon, La and Pr were at or below their detection limit, which precluded the calculation of the Ce/Ce* value. Using the oxygen fugacity proxy calibrated for alkali-rich compositions (Equation 6; Trail et al., 2012), and the Ti-in-zircon temperature estimate of 783 °C (see Section 8.2.1), the Mud Lake zircon yields $\log(f_{O2})$ values between –5.5 and –15.0, with an average $\log(f_{O2}) = -10 \pm 3$.

8.3 Facies interpretation

In Chapter 4, the petrographic features of the rocks were described, in Chapters 5 and 6 their identity as bona fide (i.e. Group I) kimberlite was established on the basis of the chemistry of indicator minerals and whole-rock geochemical signature. Thus far, textural-genetic classifications have been applied to the studied material in a limited extent to avoid premature

process interpretations (as recommended by Scott Smith et al., 2013). In this section, we will build upon previous observations to classify the rock units in terms of kimberlite facies and formation processes using the standard terminology (Field and Scott Smith, 1999). The interpretations presented here are based primarily on petrographic observations and supported by geochemical evidence when applicable. Geochemical trends resulting from volcanic and resedimentation processes (Nowicki et al., 2008) were evaluated, but no meaningful correlations were found.

It must be noted that these interpretations rely on a relatively small number of samples considering the large size of the Drybones Bay body. Earlier work on this locality is marred by inconsistency and premature interpretation (i.e. schematic diagram of the pipes internal geology shows K-8 as KE; units demonstrated in this work to be crater facies VK were classified as diatreme facies; etc.). The unavailability of the full drill core and lack of core logs for the 1996 drilling program limit our ability to fully integrate macroscopic structural features into the present interpretation. In cases where the textural evidence is ambiguous or contradictory, multiple hypotheses may be proposed for the reader's consideration.

As an overview, the stratified volcaniclastic rocks infilling the western-lobe of the Drybones Bay crater can be subdivided into RVK (K-3, -6 and -7) and PK (K-1 and -2); the dense rocks examined in the eastern lobe (K-8) are classified as TK; and the quartz-rich "epiclastic kimberlite" (KE) is reclassified as RVK.

8.3.1 Hypabyssal kimberlite (HK)

The Mud Lake rocks, once established as bona fide kimberlite, can be classified as HK a priori by virtue of their occurrence as an intrusive dyke. The competent, well-crystallized character of the rocks, and textural features such as carbonate-serpentine segregations, primary magmatic carbonate (as indicated by the tabular, lath-shaped habit of dolomite crystals; Kopylova et al., 2007), and the absence of lapilli or ash-sized particulate matter are consistent with such interpretation. Thus, the textural-genetic classification of these samples is macrocrystic dolomite HK.

The petrographic characteristics of the Drybones Bay samples reported in this work and by Kretschmar (1995, 1996), indicate that none of the drill holes at this locality intersected HK. However, well-crystallized compound clasts composed of phlogopite, serpentine, calcite, and

spinel (Figure 11e,f), which are distinct from the zircon-bearing carbonate-phlogopite xenoliths, are interpreted as HK autoliths.

8.3.2 Tuffisitic kimberlite (TK)

Tuffisitic kimberlite is the most controversial textural variety of kimberlite as (Hetman, 2008), largely because of the lack of consensus on its emplacement and some disagreements on terminology (Field and Scott Smith, 1999; Sparks et al., 2006; Cas et al., 2008). The accurate identification of TK is essential to the classification of a particular body as a Class 1 kimberlite, and has important implications for diamond exploration because it allows geologists to make reasonable predictions regarding the shape, vertical extent and internal geology of areas of the pipe not explored by drilling (Hetman, 2008). In contrast to South African Class 1 kimberlites, TK is not considered an essential feature in the models ascribed to Canadian kimberlites (i.e. Class 2 and 3 pipes; Scott Smith, 2008). While TK has been identified in Canadian kimberlites at Camsell Lake and Gahcho Kué (NWT), Quilalugaq and Aviat (NU), and Renard (QC) (for details, see Field and Scott Smith, 1999; Hetman et al., 2004; Hetman, 2008; Scott Smith, 2008), the suggested presence of TK in the Fox pipe (Ekati property, Lac de Gras kimberlite field, NWT; Nowicki et al., 2004; Porritt et al., 2006) has been met with criticism (Scott Smith, 2008).

The pelletal lapilli-bearing rocks in hole 95-08 (unit K-8) are distinct from the other Drybones Bay lithotypes in terms of their texture (see Chapter 4). In comparison to the stratified and graded volcaniclastic units, K-8 has clearly undergone less textural modification, and must therefore have a different mode of formation. Unit K-8 has many features that are similar to TK (Wilson and Head, 2007; Hetman, 2008; Scott Smith, 2008): uniform, massive structure; matrix-supported textures; complete replacement of olivine by serpentine; uncontaminated inter-clast matrix with microlitic textures; olivine distribution that resembles HK; abundant thin-skinned pelletal-shaped juvenile clasts, interpreted here as pelletal lapilli (Figure 12c); and common, relatively fresh granitic xenoliths. Magmaclasts with thick, clastic selvages (Figure 12d) and uncored clastic magmaclasts (Figure 12e) are atypical of TK (Scott Smith, 2008), but these uncommon features do not preclude the classification of unit K-8 as TK, and have been documented in other bona fide examples of TK in Canada (Hetman, 2008). Furthermore, the uncored magmaclasts pictured in Figure 12e most likely represent kimberlite autoliths/xenoliths derived from a previously deposited bedded volcaniclastic unit.

The features that dissuaded Scott Smith (2008, p.12) from accepting the interpretation of TK in the Fox pipe are: “chaotic, clast-supported and close-packed textures; olivine distributions that do not resemble those of HK; paucity of fine-grained olivine grains; some fresh olivine; common olivine lacking selvages; olivine grains with thick relatively well-crystallized kimberlite selvages; some carbonate in the inter-clast matrix; and clasts of shale or mixed shale and olivine”. Baring the well-crystallized magmaclasts, which have been addressed, the Drybones Bay TK does not exhibit any of these controversial features.

Based on petrographic characteristics, it is reasonable to propose that K-8 represents TK associated with Class 1 kimberlites. This interpretation is hampered somewhat by the unexpected stratigraphic position of these rocks laterally adjacent to crater-facies VK. Alternatively, these rocks could be interpreted as massive VK, as has been suggested for the TK-like material described in some of the Lac de Gras kimberlites, however it is clear that these rocks had a different mode of formation and are not merely a massive variety of the adjacent VK.

8.3.3 Pyroclastic kimberlite (PK)

Pyroclastic kimberlite comprises textural varieties of volcaniclastic kimberlite deposited by primary pyroclastic processes. Pyroclastic kimberlite technically includes diatreme-facies TK (Kimberley-type PK; Scott Smith et al., 2013) formed by fluidization (Clement and Reid, 1989; Field and Scott Smith, 1999) or column collapse (Cas et al., 2008), but is more commonly thought of as crater facies Fort à la Corne-type PK deposited from a pyroclastic cloud or base surge (Scott Smith et al., 2013). In this work PK refers specifically to the latter crater-fill variety. The characteristic textural features of crater-fill PK are juvenile lapilli magmaclasts and a lack of evidence of resedimentation.

Units K-1 and K-2 are interpreted as pyroclastic kimberlite. Their bedded nature indicates that they formed by deposition of fragmented volcanic material, and the textural evidence does not suggest significant reworking by sedimentary processes. Unit K-2 is the clearest example of PK; petrographically, the unit bears some resemblance to TK, in that it appears to be considerably less texturally modified than the other volcaniclastic units: olivine pseudomorphs are rounded, rather than angular; magmaclasts are prominent and well preserved; and the texture is less chaotic. Magmaclasts are an important diagnostic feature of these rocks; they are variable, and in some cases unit specific (see Chapter 4), but the type with thicker, clastic rims is common

among the PK samples (Figure 11b,c). The term juvenile lapilli has been thus far avoided in describing these magmaclasts due to the genetic connotations of the term, and because they do not exhibit the characteristic amoeboid morphology and vesicle content (Berryman et al., 2004; Wilson and Head, 2007; Mitchell et al., 2008; Scott Smith, 2008). Compared to typical juvenile lapilli, the Drybones Bay magmaclasts are noticeably rounder, but this is not unheard of; for example, juvenile lapilli with comparable morphologies are documented in PK from Lac de Gras, Fort à la Corne, and Attawapiskat (Webb et al., 2004; Webb, 2006; Wilson and Head, 2007; Nowicki et al., 2008). The absence of vesicles may be due to a number of reasons, such as: intense post-depositional alteration; low volatile contents during eruption; or low viscosity of the ejected material (i.e. high escape probability of any trapped gas phase), which would depend on a multitude of parameters. It is possible that some of these magmaclasts formed prior to eruption and are derived from an antecedent unit; the coarse-grained rim of the magmaclast in Figure 11c is texturally similar to the uncored magmaclast in unit K-8 (Figure 12c), whereas the material comprising the rim of magmaclasts in unit K-1 (Figure 11b) is noticeably finer-grained and more angular. It is proposed that the magmaclasts depicted in Figure 11a-c (units K-1 and K-2) represent juvenile lapilli.

The well-developed graded bedding in K-1 is suggestive of resedimentation. However, the interpretation of this unit as PK is favored for several reasons: the magmaclasts do not show evidence of significant abrasion (cf. Figure 11a,b to Figure 11d); the whole-rock geochemistry shows that K-1 is considerably less contaminated and contains significantly more volatiles than RVK units, with C.I. as low as 1.4 and up to 5.8 wt.% CO_2, compared to the minimum C.I. of 1.8 and 2.3 for units K-3 and K-6, respectively, and CO_2 not exceeding 2.8 wt.% in the RVK (Table 11). Euhedral olivine pseudomorphs are relatively common in both fine- and coarser-grained beds, suggesting that sorting was accompanied by minimal abrasion, effectively ruling out resedimentation.

8.3.4 Resedimented volcaniclastic kimberlite (RVK)

Resedimented volcaniclastic kimberlite is formed by the transportation and reworking of primary pyroclastic deposits. Units K-3, K-6, K-7, KE and the rock composing the top portion of hole 95-08, are interpreted as RVK. They are composed of a mixture of pyroclastic and non-kimberlitic material derived from the near-surface rocks present at the time of emplacement, and have the highest contamination indices (Table 11). The xenoliths comprise a significant

proportion of disaggregated sedimentary material in addition to granitic fragments. Exotic siltstone fragments are observed in thin section (Figure 13b), and the presence of expanding clay in the inter-clast matrix is evidenced by the desiccation cracks in some core samples (Figure 8d). Olivine pseudomorphs have undergone noticeable textural modification: crystals are finer-grained, angular, fragmented, and euhedral phenocrysts are rare. Magmaclasts are similar to the juvenile lapilli variety seen in PK, but less common and poorly preserved; their clastic rims are abraded and rarely retained outside of sheltered concavities in their kernels (Figure 13d).

The quartz-rich kimberlitic sandstone (KE) occurring in the eastern lobe was initially classified as epiclastic kimberlite, and this name has thus far been retained for consistencies sake. However, the petrographic evidence presented in Chapter 4 is not consistent with epiclastic kimberlite, which describes rocks formed by the consolidation of detritus and composed of epiclasts of lithified kimberlite that has been eroded by surface processes (Scott Smith et al., 2013). The unit is inter-bedded with an RVK over a thickness of 150 m; thus both materials must have been exposed at the same time and disaggregated at similar rates. It is extremely unlikely that normal surficial processes could erode lithified kimberlite and redeposit this eroded material locally in the crater at the same rate as unconsolidated VK material. A more feasible explanation is that these inter-bedded units formed by quartz-rich, vent-proximal pyroclastic material (possibly crater-rim deposits) slumping into the crater, while the typical RVK crater-fill was being deposited. A pyroclastic origin (prior to resedimentation) is indicated by the presence of magmaclasts resembling juvenile lapilli (Figure 12f). The crater-rim or vent-proximal spatial context is inferred from the well-preserved state of these juvenile lapilli, and the fact that the shattered quartz grains are essentially intact rather than comminuted to small angular fragments.

8.4 Unroofing

In Chapter 1, the important role that local geology plays in kimberlite emplacement was underlined. The country rock largely determines the style of kimberlite emplacement, and the geometry and nature of the infill material, corresponding to one of the three distinct classes. In the study area, the country rock consists of competent, intrusive Archean rocks; however, the xenoliths observed at Drybones Bay indicate that the upper portion of the kimberlite was emplaced into a sedimentary cover that has since been completely removed by unroofing.

The Phanerozoic surface history of the Slave craton has been modeled using apatite [U-Th]/He thermo-chronometry data and geologic constraints from sedimentary xenoliths in kimberlites (Ault et al., 2013). During the early Cambrian, the craton lacked substantial sedimentary cover, as suggested by the lack of sedimentary xenoliths in the Gahcho Kué pipes (Hetman et al., 2004; Ault et al., 2009). Limestone xenoliths in the 450 Ma (i.e. coeval with the Drybones Bay kimberlite) Cross pipe indicate that the western Slave craton was at sea level at the time of its emplacement. A thickness of several hundred meters for the marine sedimentary rocks is inferred from the depth of diatreme-facies rocks (Pell, 1997; Ault et al., 2013). By ~375 Ma, the unroofing model shows the craton was buried beneath at least 2.8 km of predominantly Devonian marine sedimentary rocks. Unroofing of the Paleozoic units began in the eastern Slave craton and progressed westward. Erosion to within 2.3 km of the present-day surface occurred by ~340 Ma in the east and ~270 Ma in the west. The majority of the Paleozoic sedimentary cover was lost by ~170 Ma, and by 100 Ma, it was entirely removed. The unroofing was followed by the burial under ≤1.4 km of Cretaceous marine sedimentary rocks. The Cretaceous cover was unroofed by 45 Ma, and Cenozoic terrestrial sediments have since been deposited.

While the Phanerozoic unroofing model (Ault et al., 2009; summarized above) does not detail the surface cover at Drybones Bay, or the extent of bedrock erosion during periods of exposure, the approach used to constrain the total post-emplacement erosion can be applied. The method is rather basic, and should be used with caution: crater, diatreme and hypabyssal facies are found to be representative of the upper ~250 m, 250-600 m and 600-700 m depth ranges in Class 1 kimberlite pipes (Field and Scott Smith, 1999), thus, exposed diatreme facies rocks of Paleozoic kimberlite pipes indicate greater post-emplacement erosion than the crater facies exposures of Late Cretaceous pipes (Ault et al., 2013). This approach presumes that the Class 1 kimberlite model can be directly applied to TK-bearing kimberlites from the Slave craton, and that development of pelletal lapilli textured TK is restricted to a depth of ~250-600 m by some mechanism, which would be the case in the fluidization model (Field and Scott Smith, 1999), but not necessarily so if TK is formed by pyroclastic column collapse, as has been alternatively proposed (Cas et al., 2008). Taking these requirements as met, and provided the K-8 rocks below ~140 m are correctly interpreted as diatreme-facies TK, the post-emplacement erosion must be at least 110 m. This estimate should be used cautiously; pipes in the Gahcho Kué cluster show that the depth of diatreme-facies rocks can be variable. In the Tuzo pipe, TK occurs at a depth of 22

m and completely transitions to HK by 300 m, whereas in the Hearne pipe, TK starts at 25 m and transitions to HK at 153 m, and in the central lobe of the 5034 pipe, TK is absent and HK is intercepted at a depth of 15 m (Caro and Kopylova, 2004; Hetman et al., 2004).

8.5 Emplacement of the Drybones Bay kimberlites

The Drybones Bay kimberlite pipe is evidently much more complex than initially thought. The summary of Drybones Bay by Field and Scott Smith (1999) describes a crater with shallow-dipping contacts, infilled with generally structureless, uniform, juvenile lapilli-bearing VK, with no evidence of TK(B) or HK. Based on the morphology of the pipe and the scant published work, one could reasonably assume that Drybones Bay is some kind of anomalous Class 2 kimberlite emplaced into a crystalline basement. However, the findings in this work suggest a more complex emplacement, and perhaps leave more unanswered questions than were initially proposed. Drybones Bay has features similar to the TK-bearing kimberlites from Canada (e.g., Gahcho Kué), with well-expressed crater- and diatreme-facies rocks, and a possible HK root zone inferred from autoliths. The structure of the Drybones Bay body is complex and incompatible with a single-stage emplacement model: diatreme-facies rocks are situated within the crater zone at the same stratigraphic depth as VK; and within the VK units we find primary PK overlaying RVK, instead of the other way around. However, in nature kimberlites do not necessarily conform to the neat geometry of schematic diagrams (Figure 1), and the atypical arrangement of units is not unprecedented. For example, the Misery pipe (Ekati property, Lac de Gras) comprises multiple overlapping intrusions, and has HK at the same depth as crater-facies VK (Nowicki et al., 2004); the 140/141 kimberlite at Fort à la Corne comprises smaller, younger craters nested within a larger, older crater (Berryman et al., 2004). Given the incompleteness of the available data (i.e. no drill core below a depth of 300 m; limited selection of material available for study; missing original core logs), a detailed evaluation of emplacement processes is not possible within the scope of this work. The hypothesis presented below is admittedly simplistic, but offers one possible explanation for the internal geology of the Drybones Bay pipe.

In the initial vent opening and crater excavation stage, phreatomagmatic processes likely played some role in the formation of the crater, particularly in the upper portion, which included the sedimentary strata that have since been removed by unroofing. Phreatomagmatism is inferred from the shattered quartz grains, which characterize the RVK in the eastern lobe of the crater.

The sandstone unit that the quartz was derived from must have been buried and served as an aquifer, as it is unlikely that the shattered texture could have developed without some confining pressure. Shoulderblade Island in Manitoba, which is a breccia structure hypothesized to be related to mantle magmatism, contains texturally identical shattered, round quartz grains at a depth of ~120 m from the present-day surface (Sheng, 2014). At Shoulderblade, the quartz was derived from the Winnipeg Formation sandstone, which is presently overlain by ~250 m of Ordovician-Silurian dolomite. In both cases, the quartz must have been shattered when hot magma encountered the aquifer and conditions were such that compressional forces prevailed over sheer forces, allowing the quartz to be fractured without being comminuted into small angular fragments. The role of phreatomagmatism in the portion of the crater situated in granitic bedrock is unknown, and we do not suggest phreatomagmatic processes are solely or principally responsible for the sculpting of the preserved portions of the pipe.

The proposed model (Figure 36) focuses on how subsequent magma pulses could produce the complex internal geology of the Drybones Bay body. The initial emplacement is based on the Class 1 kimberlite model (Field and Scott Smith, 1999; Wilson and Head, 2007), the geology of the lower sections of the pipe not explored by drilling is largely speculative and provided for the novelty of the reader. The schematic model starts after the initial kimberlite emplacement as a Class 1 pipe (Figure 36a); at this stage, the RVK units (K-7, K-6, K-3, KE) have been deposited, the strata are more or less continuous, and the crater is only partially filled. Primary PK deposits below the RVK are probable, a TK filled diatreme zone and a root zone comprising HK are inferred from the pelletal lapilli-like thin-skinned magmaclasts and autoliths in the subsequently deposited PK (K-2), as discussed in Sections 8.3.1 and 8.3.2. A second magma pulse (Figure 36b) entrained pipe-fill material during ascent and deposited PK (K-2, K-1; Figure 36c). Overlying RVK is probable, as crater-rim deposits slumped back into the crater. Units K-1 and K-2 may represent two separate magma pulses, as suggested by the structural, textural and geochemical differences, but a single pulse is shown for simplicity.

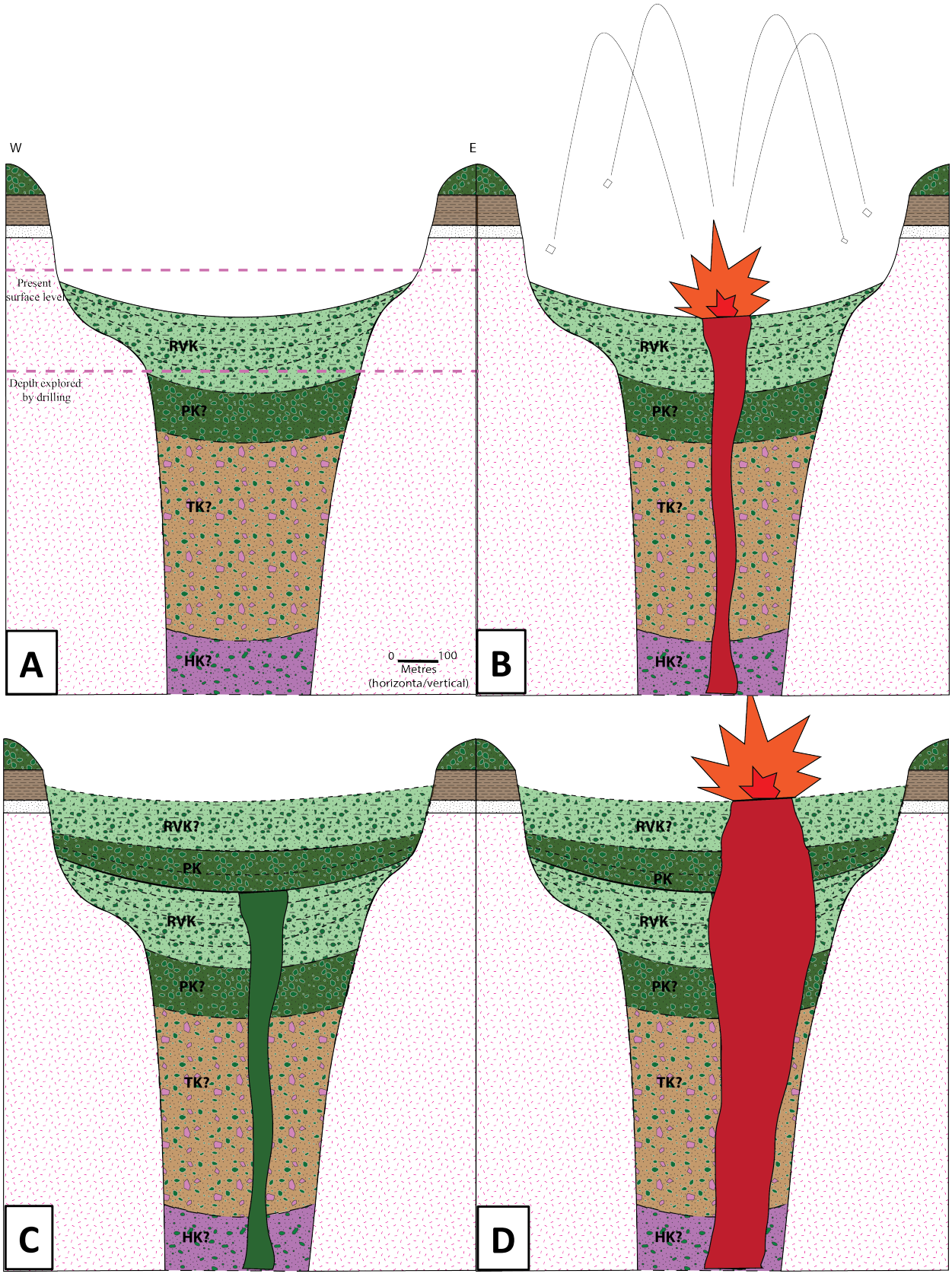
W
E
Present surface level
Depth explored by drilling
RVK
PK?
TK?
HK?
A
0
100
Metres
(horizonta/vertical)
B
RVK?
PK
RVK
PK?
TK?
HK?
C
D

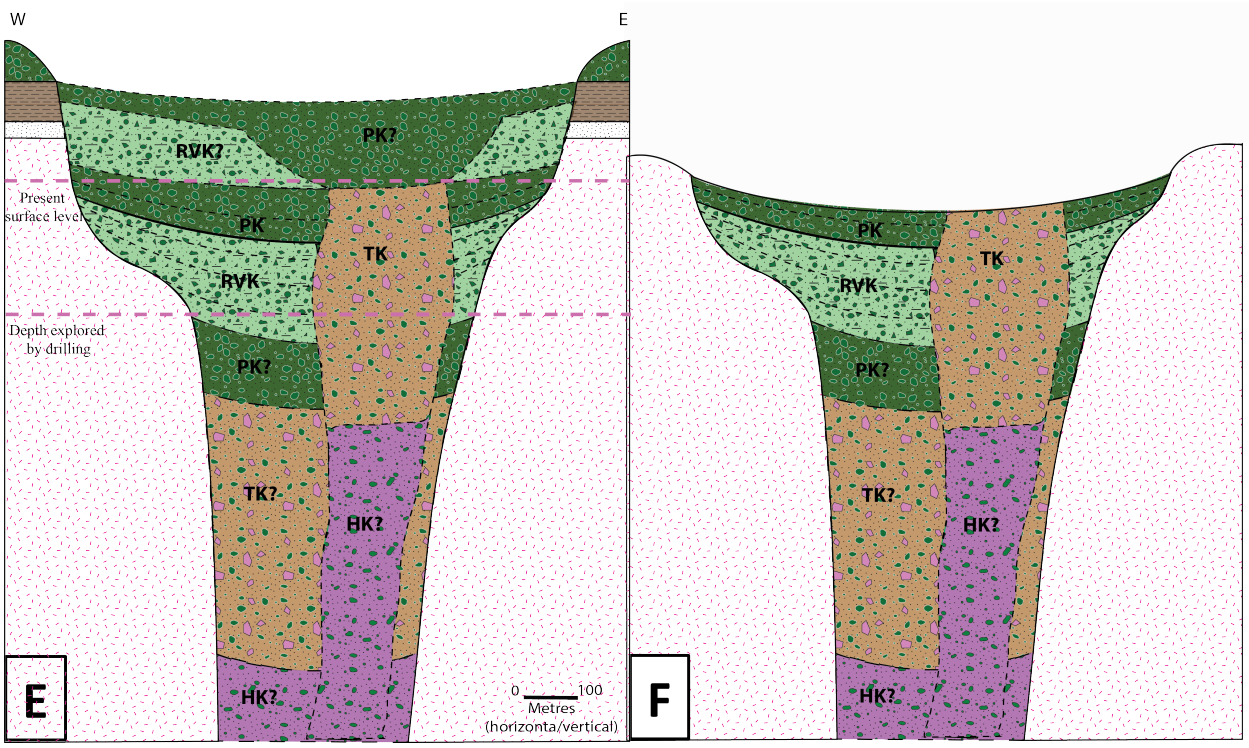

Figure 36 (pp. 111–112) Hypothetical eruption sequence to account for the internal pipe geology. See text for details.

Tuffisitic kimberlite (K-8 and perhaps the unexamined unit, KC) is emplaced by another magma pulse that erupted through the existing crater deposits, incorporating VK material as autoliths with aligned mineral grains (Figure 12e), and overprinting the previous conduit (Figure 36d,e). Additional volcaniclastic deposits were most likely associated with this event. The subsequent ~440 Ma of unroofing removed the younger VK, and what remains is consistent with drill core observations (cf. Figure 7 and Figure 36f).

8.6 Relationship between Mud Lake and Drybones Bay

Comparison of geochemical and geochronological data shows that the Mud Lake and Drybones Bay kimberlites are not genetically related. Radiometric U-Pb zircon dating yielded an age of 469 ± 9.7 Ma for Mud Lake (this work) compared to 441.8 ± 0.8 Ma for Drybones Bay (Heaman et al., 2003). Factoring in error, the difference in ages could be as little as 17 million years or as much as 38 million years. At any rate, the discrepancy is too great for these kimberlites to be related to a single magmatic event. Kimberlite magmas are thought to ascend from the mantle at high velocities (4–20 m/s), making it possible for a melt to traverse 150 km of

lithosphere in less than 15 minutes, and once emplaced, they cool in a matter of decades to centuries (Sparks et al., 2006). Given these dynamic constraints on kimberlite volcanism, it is clear that there is no possible overlap of the Drybones Bay and Mud Lake events. Furthermore, whole-rock geochemical data shows significant difference in the ratios of Ga/Al and Nb/Ta, even when the least-contaminated compositions are examined (Figure 32). The difference cannot be accounted for by usual mechanisms of magma modification affecting ascending kimberlite melts, such as crustal assimilation or crystal fractionation. Thus, the Drybones Bay and Mud Lake rocks are unlikely to have evolved from a common parental melt.

8.7 Diamond potential

The Drybones Bay and Mud Lake kimberlites are both diamondiferous, but not equally so (see Chapter 2). A total of 96 macro-diamonds were recovered from 10.1 tonnes of Drybones Bay kimberlite, and every lithological unit identified during exploration was found to be diamondiferous. The highest grades, ranging from 23.7 to 39.2 cpht, were obtained from a 1025 kg sample of the central unit KC (Kretschmar, 1996). In comparison, only two macro-diamonds were recovered from the Mud Lake drill core, and the results from the first 100 tonnes of excavated material processed for diamond evaluation were not promising (Snowfield Development Corp, 2008a; 2008b).

Before discussing the diamond potential of kimberlites, it is important to understand the relationship between kimberlites and diamonds. Diamonds do not crystallize from kimberlite magmas as phenocrysts; rather they are derived from the mantle and transported by the kimberlite magma to the near surface as xenocrysts. The principal source of diamonds are peridotitic (approximately 2/3 of diamonds) and eclogitic (1/3) domains, at depths of 130–200 km, in the sub-cratonic lithosphere (Stachel and Harris, 2008; 2009; Shirey et al., 2013), though diamond petrogenesis can extend to the 660 km transition zone (Kaminsky et al., 2001; 2009). Carbon in the upper mantle can occur as carbonate-silicate melts, exsolved vapor phases, carbonate minerals, or as graphite or diamond (Frost and Wood, 1997). Diamonds are a metastable high-pressure allotrope of carbon that is prone to re-equilibrate, either graphitize or more likely oxidize, unless conditions are conducive to its preservation (Frost and Wood, 1997; Shirey et al., 2013). Furthermore, diamond formation is proposed to be intimately linked to metasomatising carbonatitic fluids (Araújo et al., 2009; Stachel and Harris, 2009; Kopylova et

al., 2010b; Shirey et al., 2013), and irrespective of the contentious relationship between carbonatites and kimberlite petrogenesis (see Section 1.5), the carbonatitic fluids involved in diamond formation impart a geochemical signature that can be inherited by kimberlites.

Therefore, the diamond potential of a kimberlite depends on whether the ascending magma transects diamond-bearing lithosphere, and the magmas ability to rapidly transport diamonds to the low-pressure, oxidized environment of the near surface without the diamonds converting to graphite or being resorbed by the melt.

The approach used to evaluate diamond potential depends on the stage of the project. During initial exploration, tectonic considerations are paramount, as the diamond potential will depend first and foremost on whether the pressure and temperature conditions of the underlying lithosphere are favorable for diamond preservation (Boyd et al., 1985; Jelsma et al., 2009; Faure et al., 2011). The diamond potential of kimberlites occurring in tectonically prospective terrains can be further evaluated on the basis of their mineralogy and mineral chemistry. Diamond indicator minerals are used in exploration programs to elucidate the nature of the sub-cratonic lithosphere (Gurney and Zweistra, 1995).

Garnet is arguably the most important diamond indicator mineral. It has been demonstrated that certain types of mantle-derived garnets have a strong association with diamonds (Gurney, 1984), and these distinct populations can be easily discriminated on the basis of their major-element compositions (Grütter et al., 2004): hazburgitic (G10) garnets, characterized by low-Ca and high-Cr contents, represent 85% of peridotitc garnet inclusions in diamonds, whereas lherzolitic (G9) garnets account for only 15%, and wehrlitic (G12) garnets are only very rarely found as inclusions (Gurney, 1984; Grütter et al., 2004). Ilmenite has recently been proposed as a diamond indicator, based on the correlation between trace elements and diamond grades (Carmody et al., 2014). Ilmenite associated with high-grade diamond deposits are characterized by high Zr/Nb ratios, inferred to have been inherited from the metasomatising carbonatitic fluid involved in diamond formation. Ilmenite is also known to influence diamond resorption: high Fe_2O_3 contents in ilmenite have a negative correlation with diamond contents (Gurney and Zweistra, 1995).

The findings of this work have important implications on the diamond potential of the Drybones Bay pipe, and provide valuable insights regarding the paucity of diamonds in the nearby Mud Lake kimberlite. The pyrope garnets analyzed correspond to G9 and G12

compositions (Figure 22). While the G9 garnets have a weak association with diamonds, the G12 garnets are not particularly prospective, however the limited number of analyses must be acknowledged, and this data may not be representative of the actual garnet population present in these rocks: to wit, unpublished reports indicate the presence of G10 garnets (personal communication with B. Elliot, NWT Geological Survey, 2016). The Zr/Nb and Nb/Ta ratios of ilmenite from the Mud Lake and Drybones Bay kimberlites (see Chapter 5; Figure 17) correspond to the high diamond potential field of Carmody et al. (2014). If the reasoning behind the diamond potential and Zr/Nb relationship in ilmenite can be extended to bulk compositions, then one would plausibly expect the Mud Lake kimberlite to have higher diamond grades than the Drybones Bay kimberlite, as the Mud Lake rocks are considerably more enriched in Zr and Nb (Table 12), suggesting increased interaction with the metasomatizing agent assumed to favor diamond formation. Why then were the diamond counts from Mud Lake so dismal?

The poor diamond yields from the Mud Lake kimberlite, in spite of good indicators and respectable grades in the nearby Drybones Bay pipe, can be attributed to unfavorable conditions for preservation. Mineralogical and petrographic evidence indicate oxidizing conditions in the magma that could lead to the resorption of diamonds. Ilmenite has appreciable amounts of Fe_2O_3 (12.6–18.7 wt.%; Table 6), however these values are not unlike those seen in the Drybones Bay ilmenite. The oxygen fugacity calculated from zircon ($\log(f_{O2})$ = –5.5 to –15.0; see Section 8.2.2), corresponds to a redox state at or above the magnetite-hematite redox buffer, at the calculated temperature of 780 °C. The oxygen fugacity estimated from zircon is consistent with petrographic observations: ilmenite is pervasively altered to rutile (Figure 14c), to a greater extent than the Drybones Bay ilmenite, and the Fe_2O_3 released by this reaction can even be seen macroscopically as prominent hematite staining (Figure 8a). Given these oxidizing conditions, it is little wonder that there is a paucity of diamonds in the Mud Lake kimberlite.

The Drybones Bay kimberlite appears to have been emplaced under conditions more favorable for diamond preservation. Although no estimate of the redox state was made (see Section 8.2.2), the lack of hematite staining, less intense alteration of ilmenite, and higher diamond counts suggest the Drybones Bay magma was less oxidized than Mud Lake. The economic implications of the recognition of TK and the subsequent interpretation of Drybones Bay as a Class 1 kimberlite are of far greater significance than the indicator mineral results at this stage, considering the favorable diamond counts. The highest grades were obtained from unit

KC (23.7–39.2 cpht; Kretschmar, 1996). While this unit was not reported on due to the unavailability of study material, a sample (listed in Table 3) was eventually uncovered and analyzed, albeit at too late a juncture to be incorporated into the present work. The KC sample has a bulk composition that is very similar to that of unit K-8, and macroscopically bears more resemblance to K-8 than the other units. It is suspected that these units are closely related and might only differ in alteration; therefore we will assume this material also represents TK for the sake of this discussion.

The diamond resource of Drybones Bay was most likely greatly underestimated. High grades were only obtained from material localized in the central and eastern part of the crater (Figure 7), while the vast western lobe yielded fewer diamonds. Recognizing Drybones Bay as a Class 1 kimberlite has the implication that below the diluted low-grade VK material could be a significant volume of potentially high-grade TK, comprising a vertically extensive diatreme, and below that, a hypabyssal root zone. These findings could profoundly affect the economic viability of this kimberlite.

8.8 Concluding remarks

The findings of this work confirm that the Mud Lake and Drybones Bay rocks represent bona fide Group 1 kimberlites. The Mud Lake rocks can be classified as macrocrystic dolomite HK. Although primary dolomite is somewhat unusual in this type of rock, the whole-rock geochemistry and mineral chemistry of the examined samples are comparable to other well-studied occurrences of HK. The Drybones Bay kimberlite is a multiphase pipe, infilled with juvenile lapilli-bearing PK, mud-rich RVK and pelletal lapilli-bearing TK. Autoliths composed of calcite, phlogopite, and spinel indicate well-crystallized HK at depth, possibly forming a hypabyssal root zone. The presence of TK sets Drybones Bay apart from Canadian kimberlites found at Fort á la Corne, Attawapiskat, and Lac de Gras (Field and Scott Smith, 1999), and makes it more akin to the Gahcho Kuè kimberlite (Hetman et al., 2004) and southern African Class 1 kimberlites. The close proximity of the Mud Lake to the Drybones Bay kimberlite is coincidental; radiometric dating and geochemical evidence preclude the possibility that they were derived from a common parental melt.

The trace-element composition of ilmenite from Mud Lake and Drybones Bay suggests these kimberlites should have high diamond contents, however this is not the case at Mud Lake.

The paucity of diamonds recovered from Mud Lake can be explained by the high oxygen fugacity of the magma, leading to the resorption of the diamonds. The recognition of TK at Drybones Bay has significant economic implications on the diamond potential of this kimberlite.

Attempts to determine the temperature of ilmenite to rutile conversion were thwarted by the inhomogeneous distribution of Zr in rutile, indicating disequilibrium. Although unsuccessful, the effort was not entirely fruitless, and the findings show that care must be taken when applying the Zr-in-rutile thermometer to rutile that optically appears to be homogeneous. The suitability of a rutile crystal cannot be evaluated on the basis of electron microprobe analysis; a statistically significant number of trace-element analyses are necessary to first assess the inter- and intra-granular compositional variations.

The effects of olivine fractionation are clearly expressed by the evolutionary trend of Ni and Co/Ni in spinel and ilmenite macrocrysts. The variations in Ni and Co/Ni can be modeled by the crystallization of olivine, using published distribution coefficients and an initial melt with the upper range of published Ni and Co concentrations for HK. From this starting point, the whole-rock geochemical signature can be produced by Rayleigh fractionation of 2–3% olivine (F_{Ol} = 2–3 %). Spinel and ilmenite began to crystallize at F_{Ol} = 9% and F_{Ol} =10.5%, respectively, and co-precipitate with olivine until F_{Ol} = 12 –12.5%. Olivine is found to be the dominant control on the evolutionary trend; disregarding olivine would necessitate fractionation of spinel or ilmenite on an unrealistic scale. These data show the importance of looking at the trace-element composition of accessory minerals from the standpoint of major magma-evolution processes.

References

Adam, J., Green, T., 2006. Trace element partitioning between mica- and amphibole-bearing garnet lherzolite and hydrous basanitic melt: 1. Experimental results and the investigation of controls on partitioning behaviour. Contributions to Mineralogy and Petrology 152, pp. 1–17.

Araújo, D.P., Griffin, W.L., O'Reilly, S.Y., 2009. Mantle melts, metasomatism and diamond formation: Insights from melt inclusions in xenoliths from Diavik, Slave Craton. Lithos 112S, pp. 675–682.

Ault, A.K., Flowers, R.M., Bowring, S.A., 2009. Phanerozoic burial and unroofing history of the western Slave craton and Wopmay orogen from apatite (U–Th)/He thermochronometry. Earth and Planetary Science Letters 284, pp. 1–11.

Ault, A.K., Flowers, R.M., Bowring, S.A., 2013. Phanerozoic surface history of the Slave craton. Tectonics 32, pp. 1066–1083.

Barker, D.S., 2001. Calculated silica activities in carbonatite liquids. Contributions to Mineralogy and Petrology 141, pp. 704–709.

Barnett, W.P., Kurszlaukis, S., Tait, M., Dirks, P., 2011. Kimberlite wall-rock fragmentation processes: Venetia K08 pipe development. Bulletin of Volcanology 73, pp. 941–958.

Bau, M., 1996. Controls on the fractionation of isovalent trace elements in magmatic and aqueous systems: evidence from Y/Ho, Zr/Hf, and lanthanide tetrad effect. Contributions to Mineralogy and Petrology 123, pp. 323–333.

Becker, M., Le Roex, A.P., 2006. Geochemistry of South African on-and off-craton, Group I and Group II kimberlites: petrogenesis and source region evolution. Journal of Petrology 47, pp. 673–703.

Belousova, E.A., Griffin, W.L., O'Reilly, S.Y., Fisher, N., 2002. Igneous zircon: trace element composition as an indicator of source rock type. Contributions to Mineralogy and Petrology 143, pp. 602–622.

Belousova, E.A., Griffin, W.L., Pearson, N.J., 1998. Trace element composition and cathodoluminescence properties of southern African kimberlitic zircons. Mineralogical Magazine 62, pp. 355–366.

Berryman, A.K., Scott Smith, B.H., Jellicoe, B.C., 2004. Geology and diamond distribution of the 140/141 kimberlite, Fort à la Corne, central Saskatchewan, Canada. Lithos 76, pp. 99–114.

Bleeker, W., Ketchum, J.W., Davis, W.J., 1999a. The Central Slave Basement Complex, Part II: age and tectonic significance of high-strain zones along the basement-cover contact. Canadian Journal of Earth Sciences 36, pp. 1111–1130.

Bleeker, W., Ketchum, J.W., Jackson, V.A., Villeneuve, M.E., 1999b. The Central Slave Basement Complex, Part I: its structural topology and autochthonous cover. Canadian Journal of Earth Sciences 36, pp. 1083–1109.

Boyd, F.R., Gurney, J.J., Richardson, S.H., 1985. Evidence for a 150–200-km thick Arcaean lithosphere from diamond inclusion thermobarometry. Nature. URL (http://www.nature.com.uml.idm.oclc.org/nature/journal/v315/n6018/pdf/315387a0.pdf) [Aug. 2016].

Brown, R.J., Manya, S., Buisman, I., Fontana, G., Field, M., Niocaill, C.M., Sparks, R.S.J.,

Stuart, F.M., 2012. Eruption of kimberlite magmas: physical volcanology, geomorphology and age of the youngest kimberlitic volcanoes known on earth (the Upper Pleistocene/Holocene Igwisi Hills volcanoes, Tanzania). Bulletin of Volcanology 74, pp. 1621–1643.

Carbno, G.B., Canil, D., 2002. Mantle structure beneath the SW Slave craton, Canada: constraints from garnet geochemistry in the Drybones Bay kimberlite. Journal of Petrology 43, pp. 129–142.

Carmody, L., Taylor, L.A., Thaisen, K.G., Tychkov, N., Bodnar, R.J., Sobolev, N.V., Pokhilenko, L.N., Pokhilenko, N.P., 2014. Ilmenite as a diamond indicator mineral in the Siberian craton: A tool to predict diamond potential. Economic Geology 109, pp. 775–783.

Caro, G., Kopylova, M.G., 2004. The hypabyssal 5034 kimberlite of the Gahcho Kue cluster, southeastern Slave craton, Northwest Territories, Canada: a granite-contaminated Group-I kimberlite. The Canadian Mineralogist 42, pp. 187–207.

Cas, R.A.F., Hayman, P., Pittari, A., Porritt, L.A., 2008. Some major problems with existing models and terminology associated with kimberlite pipes from a volcanological perspective, and some suggestions. Journal of Volcanology and Geothermal Research 174, pp. 209–225.

Cavell, P.A., Baadsgaard, H., 1986. Geochronology of the Big Spruce Lake alkaline intrusion. Canadian Journal of Earth Sciences 23, pp. 1–10.

Chakhmouradian, A.R., 2006. High-field-strength elements in carbonatitic rocks: Geochemistry, crystal chemistry and significance for constraining the sources of carbonatites. Chemical Geology 235, pp. 138–160.

Chakhmouradian, A.R., Böhm, C.O., Demény, A., Reguir, E.P., Hegner, E., Creaser, R.A., Halden, N.M., Yang, P., 2009. “Kimberlite” from Wekusko Lake, Manitoba: Actually a diamond-indicator-bearing dolomite carbonatite. Lithos 112S, pp. 347–357.

Chakhmouradian, A.R., Reguir, E.P., Kamenetsky, V.S., Sharygin, V.V., Golovin, A.V., 2013. Trace-element partitioning in perovskite: Implications for the geochemistry of kimberlites and other mantle-derived undersaturated rocks. Chemical Geology 353, pp. 112–131.

Chappell, B.W., White, A.J.R., 1970. Further data on an “eclogite” from the Sittampundi complex, India. Mineralogical Magazine 37, pp. 555–560.

Clement, C.R., 1982. A comparative geological study of some major kimberlite pipes in the Northern Cape and Orange Free State. Unpublished Ph.D. thesis, University of Cape Town pp. 423.

Clement, C.R., Reid, A.M., 1989. The origin of kimberlite pipes: an interpretation based on a synthesis of geological features displayed by southern African occurrences, in: Ross, J. (Ed.), Kimberlites and Related Rocks. Geological Society of Australia, pp. 632–646.

Dalton, J.A., Presnall, D.C., 1998. The continuum of primary carbonatitic–kimberlitic melt compositions in equilibrium with lherzolite. Journal of Petrology 29, pp. 1953–1964.

Davis, G.L., Sobolev, N.V., Khar'kiv, A.D., 1980. New data on the age of Yakutian kimberlites obtained by the uranium-lead method on zircons. Doklady Akademii Nauk SSSR 254, pp. 175–179.

Davis, W.J., Bleeker, W., 1999. Timing of plutonism, deformation, and metamorphism in the Yellowknife Domain, Slave Province, Canada. Canadian Journal of Earth Sciences 36, pp. 1169–1187.

Davis, W.J., Canil, D., MacKenzie, J.M., Carbno, G.B., 2003a. Petrology and U–Pb geochronology of lower crustal xenoliths and the development of a craton, Slave Province, Canada. Lithos 71, pp. 541–573.

Davis, W.J., Hegner, E., 1992. Neodymium isotopic evidence for the tectonic assembly of Late Archean crust in the Slave Province, northwest Canada. Contributions to Mineralogy and Petrology 111, pp. 493–504.
Davis, W.J., Jones, A.G., Bleeker, W., Grütter, H.S., 2003b. Lithosphere development in the Slave craton: a linked crustal and mantle perspective. Lithos 71, pp. 575–589.
De Argollo, R., Schilling, J.G., 1978. Ge-Si and Ga-Al fractionation in Hawaiian volcanic rocks. Geochimica et Cosmochimica Acta 42, pp. 623–630.
De Beers, 2015. The diamond insight report. De Beers UK LTD. URL (http://www.debeersgroup.com/content/dam/de-beers/corporate/images/insight-report/pdf/DeBeers_Insight_Report_2015.pdf) [May 2016].
Donnelly, C.L., Griffin, W.L., O'Reilly, S.Y., Pearson, N.J., Shee, S.R., 2011. The Kimberlites and related rocks of the Kuruman Kimberlite Province, Kaapvaal Craton, South Africa. Contributions to Mineralogy and Petrology 161, pp. 351–371.
Dunn, C.E., Smith, D., Kerr, D.E., 2001. Biogeochemical survey of the Drybones Bay area, Northwest Territories (NTS 851I/4) using outher bark of black spruce (No. Open File D3919). Geological Survey of Canada.
Ewart, A., Griffin, W.L., 1994. Application of proton-microprobe data to trace-element partitioning in volcanic rocks. Chemical Geology 1, pp. 251–284.
Faure, S., Godey, S., Fallara, F., 2011. Seismic architecture of the Archean North American mantle and its relationship to diamondiferous kimberlite fields. Economic Geology.
Ferry, J.M., Watson, E.B., 2007. New thermodynamic models and revised calibrations for the Ti-in-zircon and Zr-in-rutile thermometers. Contributions to Mineralogy and Petrology 154, pp. 429–437.
Field, M., Scott Smith, B.H., 1999. Contrasting geology and near-surface emplacement of kimberlite pipes in Southern Africa and Canada. Proceedings of the 7th International Kimberlite Conference 1, pp. 217–231.
Frost, D.J., Wood, B.J., 1997. Experimental measurements of the fugacity of C02 and graphite/diamond stability from 35 to 77 kbar at 925 to 1650°C. Geochimica et Cosmochimica Acta 61, pp. 1565–1574.
Gaspar, J.C., Wyllie, P.J., 1984. The alleged kimberlite-carbonatite relationship: evidence from ilmenite and spinel from Premier and Wesselton mines and the Benfontein sill, South Africa. Contributions to Mineralogy and Petrology 85, pp. 133–140.
Grütter, H.S., Apter, D.B., Kong, J.M., 1999. Crust-mantle coupling: evidence from mantle-derived xenocrystic garnets. Proceedings of the 7th International Kimberlite Conference 1, pp. 307–313.
Grütter, H.S., Gurney, J.J., Menzies, A.H., Winter, F., 2004. An updated classification scheme for mantle-derived garnet, for use by diamond explorers. Lithos 77, pp. 841–857.
Gudfinnsson, G.H., Presnall, D.C., 2005. Continuous gradations among primary carbonatitic, kimberlitic, melilititic, basaltic, picritic, and komatiitic melts in equilibrium with garnet lherzolite at 3-8 GPa. Journal of Petrology 46, pp. 1645–1659.
Gurney, J.J., 1984. A correlation between garnets and diamonds, in: Glover, J.E. (Ed.), Kimberlite Occurrence and Origin: a Basis for Conceptual Models in Exploration. University of Western Australia, pp. 143–148.
Gurney, J.J., Zweistra, P., 1995. The interpretation of the major element compositions of mantle minerals in diamond exploration. Journal of Geochemical Exploration 53, pp. 293–309.
Harris, M., Le Roex, A.P., Class, C., 2004. Geochemistry of the Uintjiesberg kimberlite, South

Africa: petrogenesis of an off-craton, group I, kimberlite. Lithos 74, pp. 149–165.
Heaman, L.M., Kjarsgaard, B.A., Creaser, R.A., 2003. The timing of kimberlite magmatism in North America: implications for global kimberlite genesis and diamond exploration. Lithos 71, pp. 153–184.
Hetman, C.M., 2008. Tuffisitic Kimberlite (TK): A Canadian perspective on a distinctive textural variety of kimberlite. Journal of Volcanology and Geothermal Research 174, pp. 57–67.
Hetman, C.M., Scott Smith, B.H., Paul, J.L., Winter, F., 2004. Geology of the Gahcho Kué kimberlite pipes, NWT, Canada: root to diatreme magmatic transition zones. Lithos 76, pp. 51–74.
Jackson, S.E., Pearson, N.J., Griffin, W.L., Belousova, E.A., 2004. The application of laser ablation-inductively coupled plasma-mass spectrometry to in situ U–Pb zircon geochronology. Chemical Geology 211, pp. 47–69.
Janse, A.J.A.B., Sheahan, P.A., 1995. Catalogue of world wide diamond and kimberlite occurrences: a selective and annotative approach. Journal of Geochemical Exploration 53, pp. 73–111.
Jelsma, H., Barnett, W.P., Richards, S., Lister, G.S., 2009. Tectonic setting of kimberlites. Lithos 112, pp. 155–165.
Jennings, C., 1995. The exploration context for diamonds. Journal of Geochemical Exploration 53, pp. 113–124.
Jones, A.P., Genge, M., Carmody, L., 2013. Carbonate Melts and Carbonatites. Reviews in Mineralogy and Geochemistry 75, pp. 289–322.
Jones, T.J., Russell, J.K., Porritt, L.A., Brown, R.J., 2014. Morphology and surface features of olivine in kimberlite: implications for ascent processes. Solid Earth 5, pp. 313–326.
Kaminski, V., Oldenburg, D., 2012. The geophysical study of Drybones kimberlite using 3D Time Domain EM Inversion and 3D ZTEM inversion algorithms. ASEG Extended Abstracts.
Kaminsky, F.V., Khachatryan, G.K., Andreazza, P., Araújo, D.P., Griffin, W.L., 2009. Super-deep diamonds from kimberlites in the Juina area, Mato Grosso State, Brazil. Lithos 112, Supplement 2 IS -, pp. 833–842.
Kaminsky, F.V., Zakharchenko, O., Davies, R., Griffin, W.L., Khachatryan-Blinova, G., Shiryaev, A., 2001. Superdeep diamonds from the Juina area, Mato Grosso State, Brazil. Contributions to Mineralogy and Petrology 140, pp. 734–753.
Kerr, D.E., Kjarsgaard, I.M., Smith, D., 2001. Chemical characteristics of kimberlite indicator minerals from the Drybones Bay area (NTS85I/4), Northwest Territories (No. Open File D3942), Geological Survey of Canada. Geological Survey of Canada.
Kerr, D.E., Smith, D., 2000. Anomalous kimberlite indicator mineral and gold grain abundances, Drybones Bay and Yellowknife area, Northwest Territories (No. Open File D3861). Geological Survey of Canada.
Kimberley Process, 2015. Annual global summary: 2014 production, imports, exports and KPC counts. Kimberly Process Certification Scheme, public statistics. URL (https://kimberleyprocessstatistics.org/static/pdfs/public_statistics/2014/2014GlobalSummary.pdf) [May 2016].
Kjarsgaard, B.A., 2007. Kimberlite pipe models: Significance to exploration. Proceedings of Exploration 07: Fifth Decennial International Conference on Mineral Exploration, pp. 667–677.

Kjarsgaard, B.A., Pearson, D.G., Tappe, S., Nowell, G.M., Dowall, D.P., 2009. Geochemistry of hypabyssal kimberlites from Lac de Gras, Canada: Comparisons to a global database and applications to the parent magma problem. Lithos 112, Supplement 1, pp. 236–248.
Kopylova, M.G., Hayman, P., 2008. Petrology and textural classification of the Jericho kimberlite, northern Slave Province, Nunavut, Canada. Canadian Journal of Earth Sciences 45, pp. 701–723.
Kopylova, M.G., Matveev, S., Raudsepp, M., 2007. Searching for parental kimberlite melt. Geochimica et Cosmochimica Acta 71, pp. 3616–3629.
Kopylova, M.G., Mogg, T., Scott Smith, B.H., 2010a. Mineralogy of the Snap Lake kimberlite, Northwest Territories, Canada, and compositions of phlogopite as records of its crystallization. The Canadian Mineralogist 48, pp. 549–570.
Kopylova, M.G., Navon, O., Dubrovinsky, L., Khachatryan, G., 2010b. Carbonatitic mineralogy of natural diamond-forming fluids. Earth and Planetary Science Letters 291, pp. 126–137.
Kresten, P., Fels, P., Berggren, G., 1975. Kimberlitic zircons — A possible aid in prospecting for kimberlites. Mineralium Deposita 10, pp. 47–56.
Kretschmar, U., 1995a. Drybones Bay kimberlite: 1995 spring drill report. NWT Geological Survey, open file 83627 pp. 1–50.
Kretschmar, U., 1995b. Geology and diamond potential of the Drybones Bay kimberlite. Exploration Overview 1995: Northwest Territories Mining, Exploration and Geological Investigations, NWT Geological Mapping Division pp. 3.23–3.25.
Kretschmar, U., 1996. Drybones Bay kimberlite: Summary and exploration update. Exploration Overview 1996: Northwest Territories Mining, Exploration and Geological Investigations, NWT Geological Mapping Division pp. 3.27–3.28.
Kusky, T.M., 1989. Accretion of the Archean Slave province. Geology 17, pp. 63–67.
Le Maitre, R.W., Streckeisen, A., Zanettin, B., Le Bas, M.J., Bonin, B., Bateman, P., 2002. Igneous Rocks: A Classification and Glossary of Terms.
Le Roex, A.P., Bell, D.R., Davis, P., 2003. Petrogenesis of Group I Kimberlites from Kimberley, South Africa: Evidence from Bulk-rock Geochemistry. Journal of Petrology 44, pp. 2261–2286.
LeCheminant, A.N., 1996. Lamprophyre dykes in the Awry plutonic suite, North Arm, Great Slave Lake, Northwest Territories, in: Current Research 1996-C, Canadian Shield. Geological Survey of Canada, pp. 11–18.
LeCheminant, A.N., Heaman, L.M., 1989. Mackenzie igneous events, Canada: Middle Proterozoic hotspot magmatism associated with ocean opening. Earth and Planetary Science Letters 96, pp. 38–48.
LeCheminant, A.N., Van Breemen, O., 1994. U-Pb ages of Proterzoic dyke swarms, Lac de Gras area, NWT: evidence for progressive break-up of an Archean supercontinent. Geological Association of Canada/Mineralogical Association of Canada Annual Meeting 19, pp. 62.
Lorenz, V., 1975. Formation of phreatomagmatic maar-diatreme volcanoes and its relevance to kimberlite diatremes. Physics and Chemistry of the Earth 9, pp. 17–27.
Ludwig, K.R., 2012. Isoplot 3.75: A geochronological toolkit for Microsoft Excel. Berkely Geochronology Center Special Publication. URL (http://www.bgc.org/isoplot_etc/isoplot/Isoplot3_75-4_15manual.pdf) [May 2016].
MacFarlane, K.E., Goff, S.P., Irwin, D., 2007. 2007 Northwest Territories Mineral Exploration Overview. Northwest Territories Geoscience Office pp. 16.
MacLachlan, K., Davis, W.J., 2002. Uranium-lead ages of Defeat granitoid rocks near the Con

mine, Yellowknife, Northwest Territories. Geological Survey of Canada Current Research 2002-F1, pp. 9.
Manson, M., 2012. Interview with Stornoway Diamond CEO Matt Manson. Pure Funds. URL (http://www.pureetfs.com/media/pdfs/Interview_121312.pdf) [May 2016].
Masun, K.M., Scott Smith, B.H., 2008. The Pimenta Bueno kimberlite field, Rondônia, Brazil: Tuffisitic kimberlite and transitional textures. Journal of Volcanology and Geothermal Research 174, pp. 81–89.
McDonough, W.F., Sun, S.S., 1995. The composition of the Earth. Chemical Geology 120, pp. 223–253.
Miller, C.E., Kopylova, M.G., Smith, E., 2013. Mineral inclusions in fibrous diamonds: constraints on cratonic mantle refertilization and diamond formation. Mineralogy and Petrology 108, pp. 317–331.
Mitchell, R.H., 1979. The alleged kimberlite-carbonatite relationship; additional contrary mineralogical evidence. American Journal of Science 279, pp. 570–589.
Mitchell, R.H., 1986. Kimberlites: Mineralogy, Geochemistry and Petrology. Plenum Press, New York.
Mitchell, R.H., 2005. Carbonatites and carbonatites and carbonatites. The Canadian Mineralogist 43, pp. 2049–2068.
Mitchell, R.H., 2008. Petrology of hypabyssal kimberlites: Relevance to primary magma compositions. Journal of Volcanology and Geothermal Research 174, pp. 1–8.
Mitchell, R.H., Skinner, E.M.W., Scott Smith, B.H., 2008. Tuffisitic kimberlites: Mineralogical characteristics relevant to their formation. 9th International Kimberlite Conference Extended Abstracts pp. 3.
Moore, K.R., Wood, B.J., 1998. The transition from carbonate to silicate melts in the CaO—MgO—SiO_2—CO_2 system. Journal of Petrology 39, pp. 1943–1951.
Mottana, A., 1986. Second International Eclogite ConferenceCrystal-chemical evaluation of garnet and omphacite microprobe analyses: Its bearing on the classification of eclogites. Lithos 19, pp. 171–186.
Norman, M.D., Pearson, N.J., Sharma, A., Griffin, W.L., 1996. Quantitative analysis of trace elements in geological materials by laser abblation ICPMS: Instrumental operating conditions and calibration values of NIST glasses. Geostandards and Geoanalytical Research 20, pp. 247–261.
Nowicki, T.E., Crawford, B., Dyck, D., Carlson, J., McElroy, R., Oshust, P., Helmstaedt, H.H., 2004. The geology of kimberlite pipes of the Ekati property, Northwest Territories, Canada. Lithos 76, pp. 1–27.
Nowicki, T.E., Moore, R.O., Gurney, J.J., Baumgartner, M.C., 2007. Diamonds and associated heavy minerals in kimberlite. Developments in Sedimentology 58, pp. 1235–1267.
Nowicki, T.E., Porritt, L.A., Crawford, B., Kjarsgaard, B.A., 2008. Geochemical trends in kimberlites of the Ekati property, Northwest Territories, Canada: Insights on volcanic and resedimentation processes. Journal of Volcanology and Geothermal Research 174, pp. 117–127.
Padgham, W.A., Fyson, W.K., 1992. The Slave Province: a distinct Archean craton. Canadian Journal of Earth Sciences 29, pp. 2072–2086.
Page, F.Z., Fu, B., Kita, N.T., Fournelle, J., Spicuzza, M.J., Schulze, D.J., Viljoen, F., Basei, M.A., Valley, J.W., 2007. Zircons from kimberlite: new insights from oxygen isotopes, trace elements, and Ti in zircon thermometry. Geochimica et Cosmochimica Acta 71, pp. 3887–

3903.
Patterson, M., Francis, D., McCandless, T.E., 2009. Kimberlites: Magmas or mixtures? Lithos 112, pp. 191–200.
Pell, J.A., 1997. Kimberlites in the Slave Craton, Northwest Territories, Canada. Geoscience Canada 24, pp. 77–90.
Petrus, J.A., Kamber, B.S., 2012. VizualAge: A novel approach to laser ablation ICP-MS U-Pb geochronology data reduction. Geostandards and Geoanalytical Research 36, pp. 247–270.
Porritt, L.A., Cas, R.A.F., Crawford, B., 2006. The origin and implications of the TK-like infill of the Fox kimberlite, Ekati Diamond Mine, NWT, Canada. 8th International Kimberlite Conference.
Power, M.A., 1998. Seismic signature of the Drybones Bay kimberlite pipe, N.W.T. CIM Bulletin 91, pp. 66–69.
Price, S.E., Russell, J.K., Kopylova, M.G., 2000. Primitive magma from the Jericho pipe, N.W.T., Canada: Constraints on primary kimberlite melt chemistry. Journal of Petrology 41, pp. 789–808.
Reguir, E.P., Chakhmouradian, A.R., Halden, N.M., Malkovets, V.G., Yang, P., 2009. Major- and trace-element compositional variation of phlogopite from kimberlites and carbonatites as a petrogenetic indicator. Lithos 112, pp. 372–384.
Righter, K., Leeman, W.P., Hervig, R.L., 2005. Partitioning of Ni, Co and V between spinel-structured oxides and silicate melts: Importance of spinel composition. Chemical Geology 227, pp. 1–25.
Scott Smith, B.H., 2008. Canadian kimberlites: Geological characteristics relevant to emplacement. Journal of Volcanology and Geothermal Research 174, pp. 9–19.
Scott Smith, B.H., Nowicki, T.E., Russell, J.K., Webb, K.J., Mitchell, R.H., Hetman, C.M., Harder, M., Skinner, E.M.W., Robey, J.A., 2013. Kimberlite Terminology and Classification. Proceedings of the 10th International Kimberlite Conference 2, pp. 1–17.
Sheng, A., 2014. Structure and Origin of the Shoulderblade Breccia Dome, Central Manitoba. Unpublished B.Sc (hons.) thesis, University of Manitoba.
Shirey, S.B., Cartigny, P., Frost, D.J., Keshav, S., Nestola, F., Nimis, P., Pearson, D.G., Sobolev, N.V., Walter, M.J., 2013. Diamonds and the geology of mantle carbon. Reviews in Mineralogy and Geochemistry 75, pp. 355–421.
Snowfield Development Corp, 2008a. Snowfield news release (NR 08-21). 24hgold.com. URL (http://www.24hgold.com/english/news-company-gold-silver-mud-lake-drill-results.aspx?articleid=281998) [Feb. 2016a].
Snowfield Development Corp, 2008b. Snowfield news release (NR 08-09). 24hgold.com. URL (http://www.24hgold.com/english/news-company-gold-silver-updates-bulk-sample-results.aspx?articleid=232529) [Feb. 2016b].
Sparks, R.S.J., Baker, L., Brown, R.J., Field, M., Schumacher, J.C., Stripp, G., Walters, A., 2006. Dynamical constraints on kimberlite volcanism. Journal of Volcanology and Geothermal Research 155, pp. 18–48.
Stachel, T., Harris, J.W., 2008. The origin of cratonic diamonds — Constraints from mineral inclusions. The Genesis of Gem Deposits 34, pp. 5–32.
Stachel, T., Harris, J.W., 2009. Formation of diamond in the Earth's mantle. Journal of Physics: Condensed Matter. URL (http://iopscience.iop.org.uml.idm.oclc.org/article/10.1088/0953-8984/21/36/364206/meta) [Aug. 2009].
Thorpe, R.I., Cumming, G.L., Mortensen, J.K., 1992. A significant Pb isotope boundary in the

Slave Province and its probable relation to ancient basement in the western Slave Province, in: Richardson, D.G., Irving, M. (Eds.), Project Summaries, Canada-Northwest Territories Mineral Development Subsidiary Agreement. Geological Survey of Canada, pp. 179–184.
Timmins, W.G., 2002. Report on the Drybones Bay property. Unpublished report pp. 24.
Trail, D., Bruce Watson, E., Tailby, N.D., 2012. Ce and Eu anomalies in zircon as proxies for the oxidation state of magmas. Geochimica et Cosmochimica Acta 97, pp. 70–87.
van Achterbergh, E., Griffin, W.L., Ryan, C.G., O'Reilly, S.Y., Pearson, N.J., Kivi, K., Doyle, B.J., 2002. Subduction signature for quenched carbonatites from the deep lithosphere. Geology 30, pp. 743–746.
Villeneuve, M.E., Relf, C., (null), (null), 1998. Tectonic Setting of 2.6 Ga Carbonatites in the Slave Province, NW Canada. Journal of Petrology 39, pp. 1975–1986.
Vivian, G., 2006. Report on diamond drilling: Mud Lake property. Unpublished report pp. 1–113.
Watson, E.B., Harrison, T.M., 2005. Zircon thermometer reveals minimum melting conditions on earliest Earth. Science 308, pp. 841–844.
Watson, E.B., Wark, D.A., Thomas, J.B., 2006. Crystallization thermometers for zircon and rutile. Contributions to Mineralogy and Petrology 151, pp. 413–433.
Webb, K.J., 2006. Juvenile clasts in kimberlites: standardised comprehensive description towards unravelling emplacement mechanisms. 8th International Kimberlite Conference Long Abstracts.
Webb, K.J., Scott Smith, B.H., Paul, J.L., Hetman, C.M., 2004. Geology of the Victor Kimberlite, Attawapiskat, Northern Ontario, Canada: cross-cutting and nested craters. Lithos 76, pp. 29–50.
White, J.L., Sparks, R.S.J., Bailey, K., Barnett, W.P., Field, M., Windsor, L., 2012. Kimberlite sills and dykes associated with the Wesselton kimberlite pipe, Kimberly, South Africa. South African Journal of Geology 115, pp. 1–32.
Wilson, L., Head, J.W., III, 2007. An integrated model of kimberlite ascent and eruption. Nature 447, pp. 53–57.
Yamashita, K., Creaser, R.A., Stemler, J.U., Zimaro, T.W., 1999. Geochemical and Nd-Pb isotopic systematics of late Archean granitoids, southwestern Slave Province, Canada: constraints for granitoid origin and crustal isotopic structure. Canadian Journal of Earth Sciences 36, pp. 1131–1147.
Zack, T., Brumm, R., 1998. Ilmenite/liquid partition coefficients of 26 trace elements determined through ilmenite/clinopyroxene partitioning in garnet pyroxene. Proceedings of the 7th International Kimberlite Conference pp. 986–988.

Appendix I

I.1: Summary of instrumental conditions and calibration standards used for WDS analysis.

Oxides

Element	Line	Crystal	Standard
Si	Kα	TAP	Diopside
Fe	Kα	LLIF	Fayalite
Mn	Kα	LLIF	Spessartine
Al	Kα	TAP	Andalusite
Mg	Kα	LTAP	Olivine
Ti	Kα	LPET	Titanite
Cr	Kα	LLIF	Chromite
V	Kα	LLIF	VP_2O_7
Nb	Lα	LPET	$Ba_2NaNb_5O_{15}$
Ta	Lα	LLIF	$Mn(Ta_{1.7}Nb_{0.3})O_6$

Phlogopite

Element	Line	Crystal	Standard
Na	Kα	TAP	Albite
Si	Kα	TAP	Diopside
Ca	Kα	LPET	Diopside
Mn	Kα	LPET	Spessartine
Fe	Kα	LLIF	Fayalite
F	Kα	LTAP	Fluoro-Riebeckite
Mg	Kα	LTAP	Olivine
Ti	Kα	LLIF	Titanite
Al	Kα	TAP	Albite
Cl	Kα	LPET	Tugtophite
K	Kα	LPET	Orthoclase
V	Kα	LLIF	VP_2O_7
Cr	Kα	LLIF	Chromite
Ba	Lβ	LLIF	$Ba_2NaNb_5O_{15}$

Zircon

Element	Line	Crystal	Standard
Si	Kα	TAP	Diopside
Zr	Kα	LPET	Zircon
Hf	Mα	TAP	Hf metal
Ti	Kα	LPET	Titanite

Carbonates

Element	Line	Crystal	Standard
Mg	Kα	LTAP	Olivine
Ca	Kα	LPET	Diopside
Mn	Kα	LLIF	Spessartine
Fe	Kα	LLIF	Fayalite
Sr	Lα	LPET	$SrTiO_3$
Ba	Lα	LPET	Barite

Garnets

Element	Line	Crystal	Standard
Na	Kα	TAP	Albite
Si	Kα	TAP	Diopside
Ca	Kα	LPET	Diopside
Mn	Kα	LPET	Spessartine
Fe	Kα	LLIF	Fayalite
Mg	Kα	LTAP	Olivine
Ti	Kα	LLIF	Titanite
Al	Kα	TAP	Albite
V	Kα	LLIF	VP_2O_5
Cr	Kα	LLIF	Chromite

Apatite

Element	Line	Crystal	Standard
F	Kα	LPC_0	Apatite
Na	Kα	TAP	Albite
Si	Kα	TAP	Diopside
P	Kα	LPET	Apatite
Ca	Kα	LPET	Apatite
Sr	Lα	LPET	$SrTiO_3$
Cl	Kα	LPET	Tugtupite
S	Kα	LPET	Pyrite
Fe	Kα	LLIF	Fayalite
La	Lα	LLIF	$LaPO_4$
Ce	Lα	LLIF	$CePO_4$
Nd	Lβ	LLIF	$NdPO_4$
Pr	Lβ	LLIF	$PrPO_4$
Sm	Lβ	LLIF	$SmPO_4$
F	Kα	LTAP	Apatite

Spinels

Element	Line	Crystal	Standard
Mg	Kα	LTAP	Olivine
Si	Kα	TAP	Diopside
Mn	Kα	LPET	Spessartine
Cr	Kα	LLIF	Chromite
Fe	Kα	LLIF	Pyrite
Ni	Kα	LLIF	Pentlandite
Al	Kα	TAP	Albite
Zn	Kα	LLIF	Gahnite
Ti	Kα	LPET	Titanite

I.2: LA-ICP-MS operating and data-acquisition parameters.

ICP-MS:			**Data Acquisition Parameters:**	
Model		Element 2	***U-Pb dating***	
Plasma power		1100 Watts	Sample time	0.01 s
Gas flows:	Plasma (Ar)	~15.59 L min^{-1}	Samples per peak	100
	Auxiliary (Ar)	~1.21 L min^{-1}	Segment duration	0.1 s
	Sample (He)	~1.013/0.308 L min^{-1}	Integration window	10%
			Scan method	EScan
LA:				
Model		Merchantek LUV 213	***Trace-element analysis***	
Beam diameter		30 µm (trace-elements)	Data acquisition protocol	time-resolved analysis
		55 µm (U-Pb dating)	Detector mode	analogue and counting
Repetition rate		10 Hz	Resolution	low
Power level		80–100%	Data acquisition	50 s background level
Incident pulse energy		~0.030 mJ		50 s sample ablation
Energy density on sample		3.08–4.00 J cm^{-2}		

I.3: Isotopes used for LA-ICP-MS trace-element analysis of various minerals.

Phlogopite		Garnet		Spinel	Ilmenite		Zircon	
^{25}Mg	^{140}Ce	^{23}Na	^{143}Nd	^{25}Mg	^{25}Mg	^{143}Nd	^{25}Mg	^{151}Eu
^{29}Si	^{141}Pr	^{29}Si	^{147}Sm	^{29}Si	^{27}Al	^{147}Sm	^{29}Si	^{157}Gd
^{43}Ca	^{143}Nd	^{43}Ca	^{151}Eu	^{45}Sc	^{43}Ca	^{151}Eu	^{43}Ca	^{159}Tb
^{45}Sc	^{147}Sm	^{45}Sc	^{157}Gd	^{49}Ti	^{45}Sc	^{157}Gd	^{45}Sc	^{163}Dy
^{49}Ti	^{151}Eu	^{49}Ti	^{159}Tb	^{51}V	^{49}Ti	^{159}Tb	^{49}Ti	^{165}Ho
^{51}V	^{157}Gd	^{51}V	^{163}Dy	^{53}Cr	^{51}V	^{163}Dy	^{51}V	^{167}Er
^{53}Cr	^{159}Tb	^{53}Cr	^{165}Ho	^{55}Mn	^{53}Cr	^{165}Ho	^{55}Mn	^{169}Tm
^{55}Mn	^{163}Dy	^{55}Mn	^{166}Er	^{57}Fe	^{55}Mn	^{166}Er	^{88}Sr	^{172}Yb
^{59}Co	^{165}Ho	^{59}Co	^{169}Tm	^{59}Co	^{59}Co	^{169}Tm	^{89}Y	^{175}Lu
^{60}Ni	^{166}Er	^{60}Ni	^{173}Yb	^{60}Ni	^{60}Ni	^{173}Yb	^{93}Nb	^{178}Hf
^{66}Zn	^{169}Tm	^{66}Zn	^{175}Lu	^{66}Zn	^{68}Zn	^{175}Lu	^{139}La	^{181}Ta
^{85}Rb	^{173}Yb	^{89}Y	^{178}Hf	^{90}Zr	^{89}Y	^{178}Hf	^{140}Ce	^{208}Pb
^{88}Sr	^{175}Lu	^{90}Zr	^{181}Ta	^{93}Nb	^{90}Zr	^{181}Ta	^{141}Pr	^{232}Th
^{89}Y	^{178}Hf	^{93}Nb	^{208}Pb	^{178}Hf	^{93}Nb	^{208}Pb	^{143}Nd	^{238}U
^{90}Zr	^{181}Ta	^{139}La	^{232}Th	^{181}Ta	^{139}La	^{232}Th	^{147}Sm	
^{93}Nb	^{206}Pb	^{140}Ce	^{238}U		^{140}Ce	^{238}U		
^{133}Cs	^{232}Th	^{141}Pr			^{141}Pr			
^{137}Ba	^{238}U							
^{139}La								

I.4: Average limit of detection (LOD) for elements analyzed by WDS and LA-ICP-MS.

WDS		LA-ICP-MS			
Element	**LOD (ppm)**	**Element**	**LOD (ppm)**	**Element**	**LOD (ppm)**
Na	257.9	Na	40.1	Nd	0.4
Mg	161.4	Mg	26.9	Sm	0.2
Al	200.8	Al	212.5	Eu	0.1
Si	215.0	Ca	786.3	Gd	0.7
P	212.3	Sc	2.3	Tb	0.1
K	147.3	Ti	29.7	Dy	0.2
Ca	191.3	V	0.5	Ho	0.1
Ti	311.6	Cr	8.5	Er	0.1
V	270.1	Mn	1.1	Tm	0.1
Cr	452.5	Co	1.2	Yb	0.3
Mn	236.0	Ni	4.3	Lu	0.1
Fe	537.8	Zn	5.0	Hf	0.3
Ni	624.2	Rb	0.4	Ta	0.1
Zn	1032.6	Sr	1.0	Pb	0.1
Sr	540.6	Y	0.1	Th	0.1
Zr	1340.6	Zr	0.8	U	0.1
Hf	828.3	Nb	0.1		
Nb	551.7	Cs	0.2		
Ta	2424.2	Ba	0.9		
Ba	1275.5	La	0.2		
F	1252.1	Ce	0.1		
Cl	132.1	Pr	0.1		

II.1: Major-element composition of carbonate minerals from Drybones Bay.

Oxide wt.%	1	2	3	4	5	6	7	8	9	10	11	12	13	14	15	16
MgO	0.46	0.08	0.09	0.30	0.00	18.69	18.78	20.01	0.02	0.07	16.79	18.73	0.27	20.02	20.16	19.40
CaO	55.29	56.77	56.65	55.76	56.58	30.31	30.37	30.32	56.27	55.52	33.08	30.07	56.60	30.23	30.10	29.92
MnO	0.49	0.10	0.12	0.90	0.28	1.36	1.00	0.54	0.08	0.27	0.75	1.04	0.54	0.49	0.43	0.64
FeO	0.17	0.10	0.11	0.15	0.02	2.45	2.70	1.51	0.02	0.04	1.97	2.45	0.21	1.47	1.50	2.30
SrO	0.06	0.06	0.03	0.00	0.02	0.00	0.00	0.02	0.00	0.06	0.02	0.02	0.03	0.00	0.00	0.00
BaO	0.00	0.00	0.00	0.00	0.00	0.00	0.00	0.00	0.00	0.01	0.00	0.00	0.00	0.03	0.00	0.00
CO_2	43.52	42.88	43.00	42.89	43.09	47.20	47.15	47.59	43.61	44.04	47.39	47.69	42.35	47.76	47.81	47.74
Total	100	100	100	100	100	100	100	100	100	100	100	100	100	100	100	100

II.2: Major-element composition of carbonate minerals from Mud Lake.

Oxide wt.%	1	2	3	4	5	6	7	8	9	10	11	12	13	14	15	16
MgO	21.54	20.31	0.45	22.27	21.47	21.54	21.90	21.63	22.16	21.92	22.50	22.24	21.68	2.14	20.47	1.41
CaO	29.92	30.82	56.34	30.52	31.24	31.23	31.09	31.37	31.19	30.95	31.13	30.89	30.91	51.65	30.18	0.52
MnO	0.64	1.00	1.11	0.54	0.56	0.38	0.36	0.39	0.31	0.38	0.18	0.25	0.93	0.92	0.62	0.02
FeO	0.37	0.44	0.28	0.51	0.44	0.26	0.20	0.32	0.49	0.44	0.02	0.08	0.23	2.46	1.80	0.29
SrO	0.01	0.00	0.14	0.04	0.02	0.02	0.00	0.00	0.00	0.00	0.00	0.04	0.00	0.23	0.01	0.00
BaO	0.00	0.00	0.00	0.00	0.00	0.00	0.00	0.00	0.00	0.00	0.00	0.00	0.00	0.03	0.00	0.00
CO_2	47.52	47.43	41.68	46.13	46.28	46.56	46.45	46.28	45.84	46.30	46.16	46.49	46.24	42.57	46.93	97.76
Total	100	100	100	100	100	100	100	100	100	100	100	100	100	100	100	100